Doklady Physics, Vol. 47, No. 1, 2002, pp. 1–4. Translated from Doklady Akademii Nauk, Vol. 382, No. 1, 2002, pp. 31–33.

PHYSICS

Observation of the Initial Stage in the Development of an Avalanche of Relativistic Runaway Electrons under Normal Atmospheric Conditions

L. P. Babich*, E. N. Donskoy*, K. F. Zelenskiĭ*, Corresponding Member of the RAS R. I. Il'kaev*, I. M. Kutsyk*, T. V. Loĭko*, and R. A. Roussel-Dupré**

Received August 7, 2001

INTRODUCTION

High-altitude above-cloud optical phenomena occupying volumes on the order of 1000 km^3 were repeatedly observed [1], high-intensity radio-emission pulses being associated with them [2, 3]. Thunderstorm electric fields are responsible for the generation of hard penetrating radiation of atmospheric origin [4–6]. In [7–9], a mechanism for ascending atmospheric discharges, which is based on the concept of an avalanche of relativistic runaway electrons, is proposed. This mechanism makes it possible to explain in a unified manner the entire totality of electromagnetic phenomena proceeding in a relatively weak electric field above thunderstorm clouds. For adequately treating field measurements, we need to know the *e*-fold amplification length l_e, which determines the exponential development of an avalanche of runaway relativistic electrons, or the corresponding time scale $t_e = \frac{l_e}{c}$ (c is the speed of light). Both were recently calculated with good accuracy [10, 11].

In this paper, we report the results of a straightforward laboratory experiment in which the initial stage for the development of an avalanche of runaway relativistic electrons in a dense gas medium (air at pressure P = 1 atm and temperature T = 300 K) was directly observed for the first time. In this experiment, we obtained the first experimental confirmation for the calculated value of l_e.

EXPERIMENTAL CONDITIONS

The experiment performed is similar to the classical Townsend experiment [12]. However, in this case we deal with relativistic electrons, and electric-field strengths are considerably smaller than $E_{br} \approx 3$ MV/m, which is required for a self-breakdown by electrons with energies close to the ionization threshold. The execution of this experiment is an extremely complicated task, since in actual laboratory conditions l_e is much longer than any reasonable length L of an accelerating gap that can be realized in practice. Values of the runaway threshold ε_{th}; the time t_e; the length $l_e = ct_e$, which were calculated for three values of the overvoltage $\delta = \frac{eE}{F_{min}}$ with respect to the minimum frictional force F_{min} = 2.18 (keV/cm)/atm in atmospheric air at P = 1 atm [10]; and the corresponding voltages U for $L \approx$ 1 m are presented in Table 1. Here, $\delta = 5$ corresponds to our experimental conditions.

As is seen, it is possible to realize in a laboratory only the initial stage for the avalanche of runaway relativistic electrons. The measurements under conditions of low amplification are hampered for a number of reasons. We have to select secondary relativistic electrons in the above-threshold region against the background of a huge number of electrons produced with energies much lower than ε_{th}. There are also other obstacles, e.g., the escape of relativistic electrons from the acceleration region due to scattering in air, noise of the electromagnetic origin, etc. Therefore, the development of an avalanche of runaway relativistic electrons in a dense gas medium and for electric fields much lower than E_{br} is confirmed by comparing measured spectra of relativistic electrons passing through the accelerating gap with spectra calculated by the Monte Carlo method. These calculations were performed using the same ELIZA

Table 1

δ	U, MV	ε_{th}, keV	t_e, ns	$l_e = ct_e$, m
2	0.44	650	400	120
5	1.10	120	50	15
8	1.74	65	26	7.8

* *Russian Federal Nuclear Center All-Russia Scientific Research Institute for Experimental Physics, pr. Mira 37, Sarov, Nizhni Novgorod oblast, 607188 Russia*

E-mail: babich@expd.vniief.ru

** *Los Alamos National Laboratory, USA*

1028-3358/02/4701-0001$22.00

Table 2

Collector no.	Collector thickness, mm	Experimental results, U = 1 MV	Monte Carlo calculation: 8.7% secondary and 91.3% primary electrons	Monte Carlo calculation: 0% secondary and 100% primary electrons
1	0.2	0.055	0.031	0.013
2	0.4	0.13	0.10	0.07
3	0.6	0.21	0.23	0.2
4	0.8	0.37	0.39	0.36
5	1.0	0.50	0.55	0.53
6	1.2	0.67	0.71	0.69
7	1.5	0.78	0.85	0.85
8	5	1	1	1

code [13], which had been used previously for calculating characteristics of an avalanche of runaway relativistic electrons. The corresponding data are given in Table 1.

The experiments were carried out in a conic chamber with planar electrodes into which relativistic electrons [with the initial number $N_e(0)$] had been injected. The diameter of the upper (high-voltage) and lower (grounded) electrodes were equal to 0.6 and 1.0 m, respectively. The interelectrode-gap length was L = 1 m. The forced distribution of the potential between a sectioned insulator provided a high degree of field uniformity. The breakdown along the insulator surface limited the operating voltage by the value of 1.2 MV. The chamber was fed by microsecond-duration voltage pulses from a high-voltage generator of an ORION-1 accelerator [14]. The voltage pulse satisfied the requirement of quasi-steadiness with respect to the injected beam. A MIN-1 accelerator generating a weakly diverging electron beam uniform across the cross section was used as an injector [15]. The total number of beam electrons at the anode of the injector accelerating tube, the beam width, and the duration of the pulse current were ~9×10^{13}, ~16 mm, and ~7 ns, respectively. Electrons were distributed in a wide energy region up to 0.7 MeV. The beam was injected through a circular window 20 cm in diameter cut out in the high-voltage electrode of the chamber. In order to avoid beam locking due to the magnetic field of the electric current of the secondary gas plasma generated by the beam in the chamber interior, the injector tube was positioned at a distance of 0.45 m from the window. Owing to this fact, the flux density of relativistic electrons injected into the chamber and, eventually, the magnetic field produced by the plasma electric current were strongly decreased without a noticeable decrease in $N_e(0)$.

In order to measure energy distributions of relativistic electrons, we employed the modified method of range spectrometers. In this case, electrons were detected by aluminum collectors with different thickness, which, at the same time, selected the electrons according to their energy and without shielding each other. The advantage of this method is a considerably weaker effect of measurement errors compared to that inherent in the traditional method of absorbing filters. The collectors were enclosed in thick-walled steel detector cases. In each case, there was a window covered with aluminum foil 50 μm thick with an area of 329 cm^2, equal to that of the collector area. The foil served as a screen against the noise and did not perturb the distribution of electrons within the region of energies exceeding ε_{th}. In this modified method, the detectors registered the charge accumulated in the collector. This charge was then determined with an accuracy of 1% according to the voltage at a capacitor connecting the collector and the detector case. To realize the method described, eight detectors with collectors of different thickness were manufactured (Table 2).

MONTE CARLO CALCULATIONS

In order to analyze the experimental results obtained, we have calculated using the ELIZA code [13] expected detector readings after the injected beam had passed through the chamber. In this case, we allowed for electron absorption and scattering in the injector accelerating-tube output window and in the air layer 45 cm thick ahead of the chamber input window. Electrons passed through the air layer with the thickness L = 0.92 m (the distance between the accelerating-chamber window and the detector window located at the chamber anode) in the uniform electric field $E = \dfrac{1\text{ MV}}{0.92\text{ m}} = 10.9$ kV/cm. Then, they penetrated the 50-μm aluminum layer that modeled the detector window. The transverse sizes of all layers are not limited. Therefore, of all the electrons passing through the detector window, only those that hit a circle 1 m in diameter centered on the symmetry axis, i.e., with a size equal to that of the chamber anode, were taken into account. The electrons impinged upon the aluminum disk with a diameter of 1 m, which modeled the collector of the given thickness. The calculations

are performed for the values of the disk thickness that were equal to those of the collectors. The reflection of electrons from a 5-mm-thick aluminum disk that modeled the anode was also taken into account. The charge being accumulated in the disk of the given thickness was calculated as $e(N_{e,\,inc} - N_{e,\,pass})$, where $N_{e,\,inc}$ and $N_{e,\,pass}$ are, respectively, numbers of electrons incident onto and passing through the disk that modeled the collector. Trajectories were traced for all electrons with energies exceeding 1 keV. The electron energy distributions in the disk modeling the collector is shown in Fig. 1. The distributions are normalized to the fraction (0.115) of the total number (9×10^{13}) of incoming electrons at the injector anode. In these distributions, the fraction of secondary electrons equals 8.7% (Table 2). As is seen, the spectra of primary (injected) and secondary (high-energy) electrons are weakly overlapped and the energy distribution of secondary electrons is rather uniform. This considerably simplified their selection by the collectors. Calculations have also been carried out testifying to the fact that the actual variations of the injected-electron spectrum virtually do not affect the value of the gas amplification.

It was important to adequately arrange the detectors on the anode surface in order to allow for both the radial nonuniformity of the electron flux and the degree of its amplification. We also took into account the fact that the expected collector readings had been obtained by averaging over a circle with a diameter of 1 m, whereas the actual area of the collectors was significantly smaller. Therefore, we performed calculations of the distribution of the local electron flux along the disk radius for the above-described geometry that corresponded to the experimental conditions. The positions of the detectors were shown to be reasonable to choose between the radii r = 15 and 40 cm, which correspond to the majority of electrons, and where the electron flux is rather uniform. In this case, a weak radial dependence of the ratio for the numbers of primary and secondary electrons on the anode considerably simplifies performing the measurements and interpreting the results obtained.

THE RESULTS OBTAINED AND THEIR DISCUSSION

In Table 2, the measurement results for charges accumulated in the collectors per one pulse and the results of the Monte Carlo numerical simulations, which were normalized to the readings of the thickest collector, are presented. The measurement error is estimated to be approximately ±10%. It is seen that the results of the measurements and the calculations performed with allowance for the generation of secondary relativistic electrons (whose fraction is 8.7%) are close to each other, except for the thinnest collector. The calculations performed with allowance for the contribution of only primary relativistic electrons in the expected detector readings (zero fraction of the secondary relativistic electrons) lowered the degree of agreement with the experimental data. Hence, we may conclude that the generation of a rather large number of secondary electrons with energies exceeding the runaway threshold ε_{th} took place. The following reasons probably explaining the discrepancy are possible. The calculation results are not corrected for the fact that a part of the reflecting anode surface was occupied by the steel detector cases. In addition, in actual experiments, there exists a contribution of electrons scattered from the chamber walls. It is also necessary to keep in mind that the measurement error was maximal in the case of thin collectors. In order to minimize the effect of errors, we intend to carry out new experiments with considerably higher voltages applied. For this purpose, we have constructed a new experimental setup with an operating voltage up to 2.5 MV and without a solid insulator between electrodes.

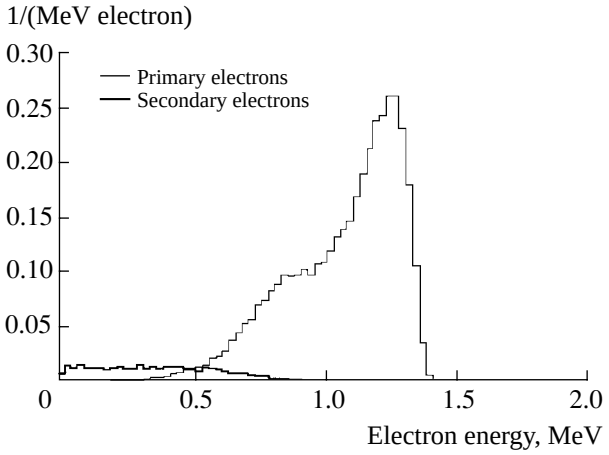

Calculated electron-energy distributions.

CONCLUSION

In this study, a satisfactory agreement between the results of a laboratory experiment on the multiplication of relativistic electrons in air at atmospheric pressure and theoretical predictions is obtained. In the experiment, electric-field strengths considerably lower than the self-breakdown value were used. The results obtained testify to the observation of the initial stage for the development of an avalanche of runaway relativistic electrons.

ACKNOWLEDGMENTS

The authors consider it a pleasant obligation to express their gratitude to Mrs. S. Voss and Dr. S. Gitomer for their invaluable contribution in the organization of collaboration between the Russian Federal Nuclear Center, All-Russia Scientific Research Institute of Experimental Physics and the Los Alamos National

Laboratory in the field of studies of giant ascending atmospheric discharges.

The authors also are grateful to V.A. Balakin, G.G. Gevorkyan, V.I. Gusakov, N.I. Zavada, N.V. Kamyshev, P.L. Komarov, V.S. Maĭornikov, V.L. Maĭornikova, Yu.M. Nedoĭkash, V.A. Obshivalov, M.S. Ovchinnikov, N.G. Pavlovskaya, A.V. Pilipenko, and I.A. Troshkin, who developed the measuring equipment and participated in experimental runs.

The work was supported by the International Science and Technology Center, project no. 490-96.

REFERENCES

1. D. D. Sentman and E. M. Wescott, Phys. Plasmas **2**, 2514 (1995).
2. D. S. Holden, C. P. Munson, and J. C. Devenport, Geophys. Res. Lett. **22**, 889 (1995).
3. R. S. Massey and D. N. Holden, Radio Sci. **30**, 1645 (1995).
4. U. S. Inan, S. C. Reising, G. J. Fishman, *et al.*, Geophys. Res. Lett. **23**, 1017 (1996).
5. G. J. Fishman, P. N. Bhat, R. Mallozzi, *et al.*, Science **264**, 1313 (1964).
6. K. B. Eack, W. H. Beasley, D. W. Rust, *et al.*, J. Geophys. Res. **101**, 29637 (1966).
7. A. V. Gurevich, G. M. Milikh, and R. A. Roussel-Dupre, Phys. Lett. A **165**, 463 (1992).
8. A. V. Gurevich, G. M. Milikh, and R. A. Roussel-Dupre, Phys. Lett. A **187**, 197 (1994).
9. R. A. Roussel-Dupre and A. V. Gurevich, J. Geophys. Res. **101**, 2297 (1996).
10. L. P. Babich, I. M. Kutsyk, E. N. Donskoy, and A. Yu. Kudryavtsev, Phys. Lett. A **245**, 460 (1998).
11. L. P. Babich, E. N. Donskoy, I. M. Kutsyk, *et al.*, IEEE Trans. Plasma Sci. **28**, 101 (2001).
12. J. S. Townsend, *Motion of Electrons in Gases* (Oxford, 1925).
13. E. N. Donskoy, Vopr. Atom. Nauki Tekh., Ser.: Mat. Model. Fiz. Prots., No. 1, 3 (1993).
14. K. F. Zelenskiĭ, I. A. Troshkin, V. A. Tsukerman, *et al.*, Pis'ma Zh. Tekh. Fiz. **5**, 239 (1979) [Sov. Tech. Phys. Lett. **5**, 95 (1979)].
15. L. P. Babich, E. N. Donskoy, T. V. Loĭko, *et al.*, Prib. Tekh. Éksp., No. 4, 82 (2000) [Instr. Exp. Tech. **43**, 510 (2000)].

Translated by G. Merzon

Doklady Physics, Vol. 47, No. 1, 2002, pp. 12–15. Translated from Doklady Akademii Nauk, Vol. 382, No. 1, 2002, pp. 41–44.

PHYSICS

On a Mechanism Providing an Increase in Oil Recovery from Strata

L. A. Nazarov*, L. A. Nazarova*, A. N. Ryashentsev, N. P. Ryashentsev**†, and Corresponding Member of the RAS V. M. Fomin****

Received July 20, 2001

INTRODUCTION

Observations of the seismic activity for a rock massif after quasi-static (filling a water storage [1]) and dynamic (high-intensity explosions [2] and earthquakes [3]) actions show that, in a number of cases, the quantity of energy released considerably exceeds that determined by external sources. This testifies to the fact of involving into the process the potential energy accumulated in the massif. Good examples are an increase in the oil-well production rate and, sometimes, a reanimation of oil wells [3]. A number of mechanisms are proposed for explaining these facts, e.g., an increase in the collector penetrability due to intense cracking [4], the initiation of resonance processes in a multiphase medium by unsteady waves [5], and a reduction in the fluid viscosity in a dynamic field [6].

In this paper, we propose a mechanism for an increase in oil recovery that is based on the concept of a rock-massif block structure [7]: an external action induces a local redistribution of stresses in the medium, which can result in increasing contour pressure and stratum pressure.

1. INITIAL HYPOTHESES AND FORMULATION OF THE PROBLEM

It is well known that the interblock-contact strength is considerably weaker than that of the blocks involved [7, 8]. Therefore, under a certain external action, the equilibrium inside a massif is likely to be disturbed precisely in such a weak link. This assumption is also confirmed by the fact that the majority of sources of seismic events are localized in the vicinity of tectonic breaks [9].

Let the deformation of an interblock damage be described by the function

$$\tau(R, \sigma_n) = K_t R H(R_p - R) + [\tau_p - K_d(R - R_p)]H(R - R_p), \quad (1.1)$$

where R is the relative displacement of edges (i.e., slip), τ and σ_n are the tangential and normal stresses, K_t is the tangential stiffness, K_d is the tangent of the descending-branch slope, $\tau_p = \sigma_n \tan\varphi + \tau_c$, φ is the analog of the viscous friction, τ_c is the cohesion, $R_p = \dfrac{\tau_p}{K_t}$, and H is the Heaviside function. The stress–strain state of the medium is such that the current state of the contact (R_*, τ_*) is close to the ultimate one (R_p, τ_p): $\dfrac{\Delta R}{R_p} \ll 1$ $(\Delta R = R_p - R_* > 0)$. If an external action leads to violating the ultimate state, then the residual slip can be estimated as $\Delta R\left(1 + \dfrac{K_d}{K_t}\right)$ [10].

In the case of underground nuclear explosions, the relative displacement of blocks is known to reach 20 mm [11]. Intense vibrators can generate a signal whose amplitude amounts to a value on the order of 0.01 mm at a depth of 1–2 km [12]. We take this value as an estimate for ΔR and find a stress state such that the mechanism proposed can be realized for a reasonably typical massif block structure.

Let a horizontal stratum L of a thickness h be located at a depth z_2 in the half-space $z \geq 0$. Let a part of the overlying layer with a thickness D_1 have a slantingly laminar structure with a slope angle of $90° - \alpha$ (Fig. 1), and let the environment be elastic. We select the calculation domain $D\{z_1 \leq z \leq z_3, 0 \leq x \leq x_1\}$ and formulate the following conditions on ∂D:

$$\begin{aligned} u_x = 0, \quad \sigma_{xz} = 0, \quad \text{for} \quad x = 0; \\ \sigma_{xx} = q\sigma_V(z), \quad \sigma_{xz} = 0, \quad \text{for} \quad x = x_1; \\ \sigma_{zz} = \sigma_V(z_1), \quad \sigma_{xz} = 0, \quad \text{for} \quad z = z_1; \\ u_z = 0, \quad \sigma_{xz} = 0, \quad \text{for} \quad z = z_2. \end{aligned} \quad (1.2)$$

Here, u_i are the displacements, σ_{ij} are the stress-tensor

† Deceased.

* *Institute of Mining, Siberian Division, Russian Academy of Sciences, Krasnyĭ prosp. 54, Novosibirsk, 630091 Russia*
E-mail: naz@misd.nsc.ru

** *Institute of Theoretical and Applied Mechanics, Siberian Division, Russian Academy of Sciences, Institutskaya ul. 4/1, Novosibirsk, 630090 Russia*
E-mail: fomin@itam.nsc.ru

components ($i, j = x, z$), $\sigma_V = \gamma g z$, γ is the density, g is the free-fall acceleration, and q is the lateral-resistance coefficient that characterizes the ratio between the horizontal stress and the vertical stress σ_V outside the zone in which the effects of the object under investigation are noticeable.

In D, the equilibrium conditions

$$\sigma_{ij,\,j} - \gamma g \delta_{iz} = 0 \tag{1.3}$$

and Hooke's law

$$\sigma_{ij} = \frac{E}{1+\nu}\left(\frac{\nu}{1-2\nu}\varepsilon\delta_{ij} + \varepsilon_{ij}\right) \tag{1.4}$$

are valid. Here, $\varepsilon_{ij} = 0.5(u_{i,j} + u_{j,i})$ are the components of the strain tensor, $\varepsilon = u_{i,i}$, E is the Young modulus, ν is the Poisson ratio, δ_{ij} is the Kronecker delta, and the summation is performed over the repeated subscript.

The tangential deformation of interblock contacts is described by formula (1.1), while σ_n and the normal displacements in these contacts are continuous.

The set of equations (1.1)–(1.4) determining the initial stress field σ_{ij}^0 in the massif is formulated for the plane-strain model [13] that fittingly describes the fault ($q < 1$) tectonic regime characteristic for many oil fields [14].

The set of equations (1.1)–(1.4) is solved by the finite-element method. The following calculation-domain sizes were chosen: $z_1 = 1500$ m, $z_2 = 2000$ m, $z_3 = 2500$ m, $h = 50$ m, and $x_1 = 1000$ m. The zone D_1 involving ten thin layers (each 5 m thick) separated by discontinuities is located in the middle of overlying layer D (Fig. 1). The physical properties of rocks are presented in the table. For interblock contacts, we used the values $K_t = 3$ GPa/m, $K_d = 0.2K_t$, $\varphi = 25°$, and $\tau_c = 0.5$ MPa.

In Fig. 2, we display the calculation results for the distribution of ΔR along a slanting fault for various values of α (the dashed and solid lines are used for $q = 0.3$ and $q = 0.275$, respectively). These results show that the break zone in the vicinity of the stratum is in the almost-ultimate state ($\Delta R \approx 0.06$ mm). This fact presents a principal possibility to violate the equilibrium of the environment by the action of a group of vibrators, thereby inducing a redistribution of stresses in the vicinity of stratum, increasing pressure within the stratum and, thus, its fluid recovery.

2. ANALYSIS OF CHANGES IN WELL PRODUCTION

Without posing to thoroughly investigate filtration processes, we qualitatively analyze changes in the fluid-flow rate in the case of an induced local stress redistribution.

At the time moment $t = 0$, a stratum is opened by a well located at a distance x_0 from the middle of the break zone. The filtration process is described by the equations of mass conservation

$$(m\rho)_{,t} + (\rho w_i)_{,i} = 0, \tag{2.1}$$

of state

$$\frac{\rho}{\rho_0} - 1 = \frac{p - p_0}{C}, \tag{2.2}$$

and by the Darcy law

$$w_i = -\frac{k}{\eta} p_{,i}. \tag{2.3}$$

Here, w_i are the velocity components; ρ, η, and C are the fluid density, viscosity, and compressibility; p is pressure; k is the penetrability; m is the porosity; and the subscript 0 marks the initial values of the corre-

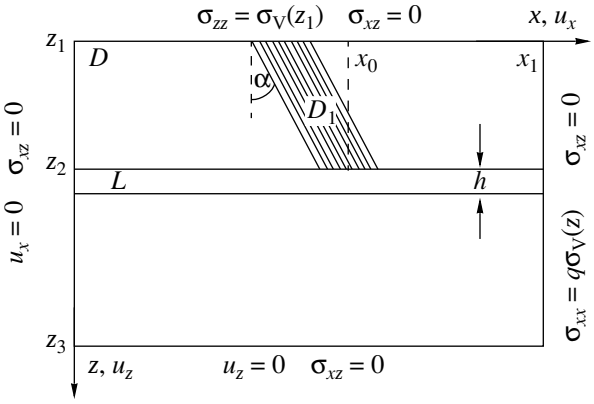

Fig. 1. Structure of the calculation domain and boundary conditions.

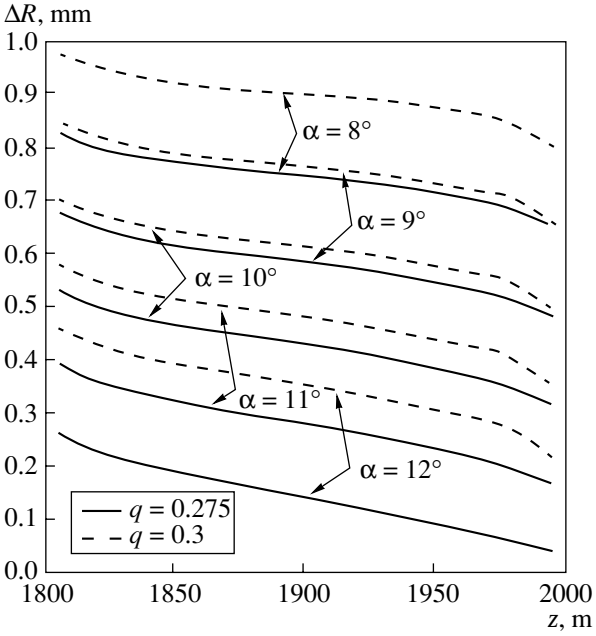

Fig. 2. Distribution of ΔR along a fault for various lateral-resistance coefficients.

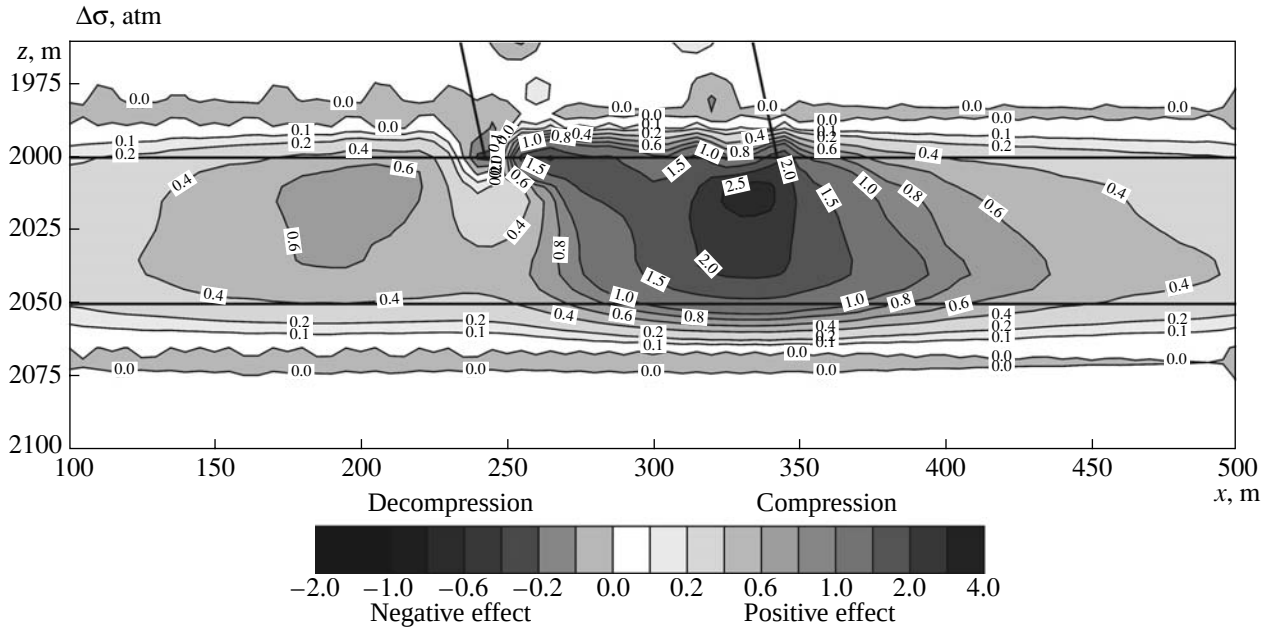

Fig. 3. Pressure increment in a stratum, which is induced by a redistribution of stresses in the massif.

sponding quantities. In the case under consideration, the right-hand side of Eq. (1.2) has the form of $mp_{,i}H(h - |z - z_2|)$; i.e., the change in the stress–strain state of the massif due to filtration processes in the stratum is taken into account.

For (2.1)–(2.3), we formulate the boundary conditions

$$w_z(t, x, z_2) = w_z(t, x, z_2 + h) = 0, \quad (2.4)$$

$$p(t, 0, z) = p_0, \quad (2.5)$$

$$p(t, x_1, z) = s(z), \quad (2.6)$$

and the initial condition

$$p(0, x, z) = \frac{(1 + \nu)\sigma^0_{ii}(x, z)}{3}, \quad (2.7)$$

where $s(z) = (1 + \nu)(1 + q)\dfrac{\sigma_V(z)}{3}$ is the mean stress in the virgin massif (the positive values correspond to compression). Condition (2.6) realizes the Khristianovich hypothesis about the pressure distribution in an intact stratum.

Physical properties of rocks

Domain	E, GPa	ν	γ, kg/m^3
D	20	0.25	2500
D_1	18	0.25	2500
L	15	0.23	2200

Sets (1.1)–(1.4) and (2.1)–(2.7) were solved using the procedure and codes developed in [15].

Let a shift of certain contacts in the break zone occur at $t = t_p$ (it does not matter what the reason was), which induces a redistribution of stresses in the massif. We denote the new state as σ^1_{ij}. Thus, the pressure in the stratum varies jumpwise:

$$p(t_p, x, z) \longrightarrow p(t_p, x, z) + \Delta\sigma(x, z),$$

where $\Delta\sigma = \sigma^1_{ii} - \sigma^0_{ii}$. Along with this, we assume that the stratum penetrability decreases: $k = k_0\left(1 - \dfrac{\Delta\sigma}{K}\right)$, where $K = \dfrac{(1 - m)E}{1 - 2\nu + mC}$ is the collector compressibility.

The calculations were carried out for $k_0 = 5 \times 10^{-14}$ m^2, $\eta = 0.03$ Pa s, $m = 0.2$, $p_0 = 10^5$ Pa, $q = 0.275$, $\rho_0 = 850$ kg/m^3, and $C = 3$ GPa (whereas $K = 24.6$ GPa). In Fig. 3, we display the distribution of $\Delta\sigma$ for the case when a slip by $\Delta R = 0.06$ mm took place for six contacts in the middle of D_1. As is seen, the redistribution is of a rather local nature, and in the case of thick strata, the realization of the mechanism proposed is unreasonable.

In Fig. 4, we show a relative increase in the well production for $t > t_p$ (and for the same calculation parameters):

$$\Delta\overline{Q} = \frac{Q_p(t) - Q(t_p)}{Q(t) - Q(t_p)} - 1.$$

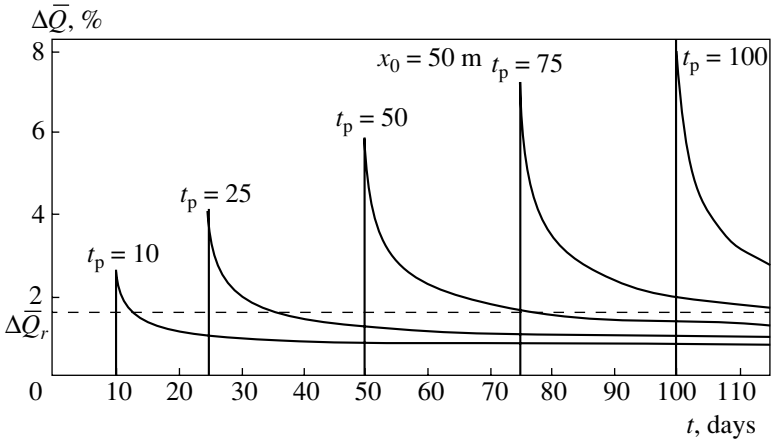

Fig. 4. Relative change in the fluid flow rate.

Here, Q_p and Q are the fluid flow rate in the case with and without an additional action onto the massif. We can note two features in the behavior of $\Delta\bar{Q}$: an

increase with time t_p and

a reasonably fast tendency to reach a certain steady value $\Delta\bar{Q}_r$, which characterizes the residual effect after such a forced change in the pressure inside the stratum.

The calculations showed that the effect of the local redistribution of stresses decreased by ΔQ with removing the well from the break zone.

Remark 1. The analysis is carried out in the two-dimensional formulation. It is evident that in the actual (three-dimensional) situation, it is necessary to treat by external sources the corresponding parts of the massif over the area of stratum bedding.

Remark 2. A forced shift in interblock contacts can also lead to a negative effect. For example, if in the model under consideration a slip of two edge contacts is induced, then virtually everywhere in the stratum we observe $\Delta\sigma < 0$. Therefore, the preliminary analysis of the stress–strain state of the massif is necessary not only to reveal weak zones, but also to estimate how consequences of a disturbance of the equilibrium state in these zones affect the filtration process.

Remark 3. The numerical analysis showed that, for the upthrust tectonic regime with its high ($q > 1$) horizontal stresses, the break-zone state (for the massif structure given here) with $\Delta R \sim 0.05$ mm can take place only for rather low values of φ, which are virtually absent. Therefore, in this case, the realization of the proposed mechanism is very problematic.

ACKNOWLEDGMENTS

This work was supported by Schlumberger Oilfield Services, an international company in the oil and gas industry, and by the CRDF Foundation, contract RGO-679-A.

REFERENCES

1. K. M. Mirzoev and S. Kh. Negmatullaev, Prognoz Zemletryaseniĭ, No. 4, 365 (1983).
2. A. A. Eremenko and N. I. Sklyar, Fiz.-Tekh. Probl. Razrab. Polezn. Iskop., No. 1, 14 (1999).
3. E. V. Kraus, O. L. Kuznetsov, E. M. Simkin, *et al.*, in *New Data on Seismology and Seismogeology of Uzbekistan* (Fan, Tashkent), pp. 292–302.
4. V. A. Chernykh, Fiz.-Tekh. Probl. Razrab. Polezn. Iskop., No. 1, 126 (1990).
5. V. N. Nikolaevskiĭ, *Geomechanics and Fluidodynamics* (Moscow, 1996).
6. G. G. Vakhitov and É. M. Simkin, *Uses of Physical Fields for Recovery Oil from Strata* (Nedra, Moscow, 1985).
7. M. A. Sadovskiĭ, L. G. Bolkhovitinov, and V. F. Pisarenko, *Deformation of Medium and Seismic Process* (Nauka, Moscow, 1987).
8. J. C. Jaeger and N. G. W. Cook, *Fundamentals of Rock Mechanics* (Methuen, London, 1969).
9. M. L. Zoback, J. Geophys. Res. **97**, 11 703 (1992).
10. L. A. Nazarov and L. A. Nazarova, Dokl. Akad. Nauk **365**, 193 (1999) [Dokl. Phys. **44**, 184 (1999)].
11. G. G. Kocharyan and A. A. Spivak, Fiz.-Tekh. Probl. Razrab. Polezn. Iskop., No. 1, 71 (2001).
12. N. P. Ryashentsev, Yu. S. Ashchepkov, L. A. Nazarov, *et al.*, Preprint No. 31 IGD SO AN SSSR (Inst. of Mining, Siberian Division, Academy of Sciences of the USSR, Novosibirsk, 1989).
13. L. A. Nazarova, Fiz.-Tekh. Probl. Razrab. Polezn. Iskop., No. 1, 28 (1999).
14. E. V. Artyushkov, *Physical Tectonics* (Nauka, Moscow, 1993).
15. L. A. Nazarov and L. A. Nazarova, Fiz.-Tekh. Probl. Razrab. Polezn. Iskop., No. 2, 35 (1999).

Translated by V. Bukhanov

Doklady Physics, Vol. 47, No. 1, 2002, pp. 16–20. Translated from Doklady Akademii Nauk, Vol. 382, No. 1, 2002, pp. 45–49.

PHYSICS

Characteristic Temperature and Polymorphism of Ca, Ti, Fe, Co, Zr, Sn, and La in the Debye Approximation

N. N. Sirota

Presented by Academician O.A. Bannykh May 21, 2001

Received May 24, 2001

Structural polymorphism of matter is a widespread phenomenon in nature. It manifests itself in all aggregate states of substances under the variation of generalized forces: temperature, pressure, magnetic- and electric-field intensity, etc.

The temperature polymorphism of a chemical element (single-component monoatomic substance) is observed in the case if, along with a basic modification stable at a low temperature, the chemical element has an energetically close unstable modification (with a lower atomization energy). With increasing temperature T, even at a constant pressure p, the element undergoes a transition from the region of the thermodynamic stability of the low-temperature modification I to the region of the equilibrium existence of another modification II. In the case of further increasing temperature, the subsequent modifications III and IV can arise, if they actually exist.

Note that the appearance of various modifications upon changing other generalized forces, including, e.g., pressure p, magnetic-field intensity H, and electric-field intensity E (at T = const), corresponds to other types of polymorphism, e.g., baric, magnetic, etc., which we here ignore.

Polymorphous structural transitions are, as a rule, enantiomorphous phase transitions of the first order (for p = const).

The polymorphism phenomenon can be treated from the structural standpoint and starting from an analysis of the role of the components for the temperature dependence of the free energy and the corresponding thermodynamic characteristic functions [1–4].

Below, we restrict our consideration of the lattice dynamics of chemical elements as Debye solids, assuming other components of the free energy (electronic and magnetic) to be negligibly small. In the accepted Debye approximation, the crystal-lattice dynamics of each of the modifications is described by the Debye phonon spectrum with the density of states $g(\nu) = \frac{gN}{\nu_m^3}\nu^2$, which is the quadratic function of atomic oscillations with frequency ν (the maximum frequency ν_m) and the corresponding characteristic temperature $\theta = \frac{h\nu_m}{k}$.

The Debye approximation is valid only for crystals possessing no strongly pronounced anisotropy and with the dimensionality (including the exponent n at the maximum frequency ν_m^n of the Debye phonon spectrum) not strongly differing from three.

In the approximation accepted, the critical temperature $T_{K_{ikj}}$ of the polymorphic transition for the i, k modification of the element j corresponds to the intersection point for the curves of the Helmholtz free energy $\Delta F_{ikj} = 0$. At moderate temperatures, the quantity $T_{K_{ikj}}$, specified from the condition $\Delta F_{ikj} = 0$, practically does not differ from the quantity $T_{K_{ikj}}$, determined from the condition of the equality to zero of the Gibbs free energy $\Delta G_{ikj} = 0$.

The free energy F and the internal energy U of the modifications ikj are summed from the temperature-independent atomization energies U_{at} including the energies of atomic zeroth oscillations and temperature-dependent fractions of U_T and F_T.

At $T = T_{\text{cr}}$, the differences in the free energies of modifications I and II are

$$F_{\text{I}} - F_{\text{II}} = U_{\text{atI}} - U_{\text{atII}} - T_{\text{cr}}\int_0^{T_{\text{cr}}} (U_{\text{I}}(T) - U_{\text{II}}(T))\frac{dT}{T} = 0. \quad (1)$$

At $T = T_{\text{cr}}$, the difference in the temperature-dependent fractions of the free energies of modifications I and II is equal to the difference in their atomization energies at $T = 0$:

$$F(T)_{I,\,T_{\text{cr}}} - F(T)_{\text{II},\,T_{\text{cr}}} = U_{\text{atI}} - U_{\text{atII}} = \Delta U_{0\text{tr}}. \quad (2)$$

Note that $\Delta U_{0\text{tr}} \ll U_{\text{at}}$.

Moscow State University of Environmental Engineering, ul. Pryanishnikova 19, Moscow, 127550 Russia

1028-3358/02/4701-0016$22.00

Correspondingly, the difference of the entropy for the modifications I and II at $T = T_{cr}$ is equal to the phase-transition heat related to T_{cr}, which is assumed to be the difference of the internal energies

$$S_I - S_{II} = \frac{U_I - U_{II}}{T_{cr}} = \frac{U_{atI} - U_{atII}}{T_{cr}} + \frac{U_I(T) - U_{II}(T)}{T_{cr}} = \frac{\Delta U_{tr}}{T_{cr}},$$

where $\Delta U_{tr} = U_{0tr} + \Delta U(T)$.

If the entropy S_I of the low-temperature modification I, T_{cr}, and the heat of the polymorphous transition $U_{tr} = U_I - U_{II}$ are known, the entropy S_{II} of the subsequent high-temperature modification is

$$S_{II} = S_I + \frac{\Delta U_{tr}}{T_{cr}}. \quad (3)$$

The entropy of the Debye solid is a tabulated function of the ratio $\frac{\theta}{T}$. Consequently, the found values of $S_{I,T_{cr}}$ and $S_{II,T_{cr}}$ at $T = T_{cr}$ determine the characteristic temperature of the modification II and, correspondingly, the temperature dependences $F_{II}(T)$ and $U_{II}(T)$.

The characteristic temperatures of Debye solids are independent of temperature. They are quantitatively related to the atomization energy, as well as to the crystal structure. In contrast to Debye solids, the characteristic temperatures of actual crystals are functions of temperature and depend on the type of the actual phonon spectrum. For example, according to Alers [5], the characteristic temperature θ for copper, which is calculated according to elastic constants within the range from $T = 0$ to $T = 25$ K, varies from 345 to 307 K. According to data of [6] for germanium within the range from $T = 0$ to $T = 300$ K, the value of θ determined from the calorimetric measurements varies from 375 K at $T = 0$ K, passes through the minimum equal to 257 K at $T = 20$ K, and reaches 378 K at $T = 300$ K.

In calculations of the thermodynamic properties of polymorphic modifications II and III, it turns out to be possible to reduce the number of necessary initial data employing the equation connecting the atomic interaction energy U and the volume V per one atom, e.g.,

$$U = -ae^{-\beta v} + be^{-\gamma v}, \quad (4)$$

which follows from the condition

$$\left(\frac{\partial U}{\partial V}\right)_{V_0} = 0,$$

$$b = a\frac{b}{\gamma}e^{-(\beta-\gamma)V_{at}}, \quad a = -\frac{\gamma U_0}{\gamma-\beta}e^{\beta V_0},$$

$$U = \frac{U_0}{\gamma-\beta}[\gamma e^{-\beta(V-V_0)} - \beta e^{-\gamma(V-V_0)}]. \quad (5)$$

The magnitude of the bulk elastic modulus B is equal to

$$-\left(\frac{V\partial^2 U}{\partial V^2}\right)_{V_0} = \gamma\beta U_0 V_0. \quad (6)$$

Since $U_{at} = U_0 V_0$, then

$$B = \gamma\beta U_{at}. \quad (7)$$

The bulk elastic modulus is proportional to the atomization energy multiplied by the product of the coefficients βγ.

The characteristic temperature of the crystal modification in the certain approximation can be expressed in terms of the bulk elastic modulus B (A is the atomic number):

$$\theta' = \frac{\hbar}{k}\sqrt{N}\alpha\sqrt{\frac{\beta\gamma}{V}}\sqrt{\frac{U_{at}}{A}}. \quad (8)$$

Assuming $\beta\gamma = 9.35$, we obtain

$$\theta' = 14.7\frac{\alpha}{V^{1/2}}\sqrt{\frac{U_{at}}{A}}. \quad (9)$$

The ratio of the characteristic temperatures for the modifications I and II will be

$$\frac{\theta'_{II}}{\theta'_I} = \frac{\alpha_{II}}{\alpha_I}\left[\frac{(\beta\gamma)_{II}}{(\beta\gamma)_I}\frac{V_I}{V_{II}}\right]^{1/2}\sqrt{1 - \frac{\Delta U_{0tr}}{U_{atI}}}, \quad (10)$$

where $\Delta U_{0tr} = U_{atI} - U_{atII}$.

For the employed values of β and γ ($\beta\gamma = 9.35$), the inverse values of α are $\alpha_1^{-1} = 0.999$ for A_1, $\alpha_2^{-1} = 0.998$ for A_2, $\alpha_4^{-1} = 0.741$ for A_4, and $\alpha_5^{-1} = 0.915$ for A_5. For A_3, the value of α_3 depends on the ratio $\frac{c}{a}$ and is close in its magnitude to α_1 and α_2.

Introducing the coefficient α (depending on the type A_i, $i = 1, 2, ..., 5$ of the crystal structure) for given values of β and γ makes it possible to take into account and to correlate their relation to the structure of a crystal having the coefficient κ of filling the unit-cell of the volume V'_0 with atoms of a diameter of δ:

$$\kappa = \frac{\pi\delta^3 n}{6V'_0}, \quad (11)$$

where n is the number of atoms in the unit cell. The filling coefficient is $\kappa_1 = 0.74$ for A_1 structures, $\kappa_2 = 0.68$ for A_2, and $\kappa_4 = 0.34$ for A_4. For A_3 and A_5, the coefficients κ depend on the ratio $\frac{c}{a}$. The coefficient α relates to the inverse value of the effective packing coefficient $\kappa_{eff} \approx \kappa + \frac{1-\kappa}{q}$ for $q \geq 3$, and is proportional to the

Table 1. Initial data employed in calculations

Element	Element	Atomic mass	Structure type	a, c, Å [7]	$\frac{c}{a}$	V, cm^3 [7]	σ, Å	U_{at}, kJ/mol [8]	U_{tr}, kJ/mol [8]	T_{cr}, K [7]	S_{298}, J/(K mol) [7]	$\theta_{S_{298}}$, K	θ, K [8]
20	Ca	40.078	A_1	5.5884		25.86	3.951	178.2 (194.1)	0.150	573	41.42	218.2	220
			A_2	4.480		27.064	3.8797	178.05		723			
			A_3	3.97	1.6347	30.788	3.97	177.99					
				6.49									
22	Ti	47.88	A_3	2.9511	1.5873	10.55	2.9511	469.9	4.0	1155	30.63	342.1	430
				4.6843									
			A_2	3.3065		10.88	2.8634	465.4					
26	Fe	55.847	A_2	2.86645		7.0	2.4823	416.3	0.905	1183	27.28	395.4	
			A_1	3.6468		7.3	2.5783	415.39	0.692	1663			
			A_2	2.9322		7.588	2.5393	414.70					
27	Co	58.933	A_1	3.5441		6.62	2.5057	424.7	0.44	690	30.04	350.7	445
			A_3	2.507	1.623	6.67	2.507	424.26					
				4.069									
40	Zr	91.224	A_3	3.2321	1.5927	14.02	3.2321	608.8	3.84	1135	38.99	240.8	237–310
				5.1477									
			A_2	3.616		14.231	3.1315	605.14					
50	Sn	118.71	A_4	6.4892		20.477	2.81	302.10	2.47	286.4	44.14	195.3	212
			A_5	5.8316	1.833	16.24	2.354	299.63			51.55		
				3.1813									
57	La	138.9055	A_3	3.77	1.6127	22.497	3.77	431.0	0.4	583	56.9	116.4	142
				12.144									
			A_1	5.296		22.355	3.7443	430.6	3.19	1137			139
			A_2	4.2		23.27	3.6892	427.41					

probability integral:

$$\alpha \approx \Phi(x) = \frac{2}{\sqrt{2\pi}}\int_0^x e^{-\frac{t^2}{2}}dt \quad \text{for } x \approx 4\kappa.$$

The variation of the characteristic temperature calculated by relations (8), (9) while passing from modification II to modification I is determined not only by a change in both the molar volume and the atomization energy but also by the change in the exponents β and γ.

According to relation (9), the change in the characteristic temperature at the polymorphous transition from modification I to modification II depends not only on the variation in the atomization energy, the molar volume, and the coefficient α but also on the variation in the product βγ. In this case, we assume that the relationship $\left[\frac{(\beta\gamma)_{II}}{(\beta\gamma)_I}\right]$ is proportional to $\left(\frac{\theta'_{II}}{\theta'_I}\right)^n$ for $(\beta\gamma)_{II} = (\beta\gamma)_I$ and $n = 0$. For other values of $(\beta\gamma)_{II}$ and $(\beta\gamma)_n$, $n = 2$ or $n = 4$,

$$\theta_i = 14.7\frac{\alpha_i}{V_i^{1/2}}\sqrt{\frac{U_{at_i}}{A}}\left(\frac{\theta'_{i-1}}{\theta'_i}\right)^n. \quad (12)$$

The values of the lattice parameters a and c, molar volume V, atomization energy U_{at}, experimental values of the characteristic temperatures θ, standard entropy S_{298} and the value θ_{298} determined according to them, the heat ΔU_{tr}, and temperatures T_{cr} of polymorphous transitions are given in Table 1.

The calculated values of θ_{ikj} (and, for comparison, the values of θ'_{ikj} obtained for $\alpha_{ij} = 1$) and the values of

Table 2. Determined values: θ', θ, θ*, $F_{T=T_{cr}}(\theta)$, $S_{T=T_{cr}}(\theta)$, $\Delta U_0(\theta)$, $\Delta S_{T=T_{cr}}(\theta)$, $\Delta U_0(\theta^*)$, $\Delta S^*_{T=T_{cr}}(\theta^*)$, and values of α, *n*, and βγ used in calculations

Element		T_{cr}, K	α	*n*	βγ	(βγ)*	θ', K	θ, K	θ*, K	$F_{T=T_{cr}}$, kJ/mol	$S_{T=T_{cr}}$, J/(K mol)	ΔU_0, kJ/mol	ΔU_0^*, kJ/mol	$\Delta S_{T=T_{cr}}$, J/(K mol)	$\Delta S^*_{T=T_{cr}}$, J/(K mol)
Ca	A_1		1.0000	2	6.150		192.75	192.75		22.235	60.76				
	A_2	573.0	1.0020		5.830		188.72	180.89		22.980	62.23	0.745		1.47	
	A_2	723.0	1.0020	2	5.830		188.72	180.89		33.021	68.37				
	A_3		1.0001		4.330		176.57	154.57		35.442	72.04	2.421		3.67	
Ti	A_3		1.0090	4	6.150		452.38	452.38		40.809	56.82				
	A_2	1155.0	1.0020		5.825	5.84	440.26	394.91	396.20	44.419	60.37	3.609	3.528	3.54	3.46
Fe	A_2		1.0020	0	6.150		480.66	480.66		40.830	55.88				
	A_1	1183.0	1.0000		6.150	6.07	469.23	469.23	466.27	41.429	56.47	0.599	0.785	0.59	0.76
	A_1	1663.0	1.0000	0	6.150		469.23	469.23		71.062	65.15				
	A_2		1.0020		5.930	6.21	460.78	460.78	462.37	71.840	65.66	0.778	0.631	0.51	0.42
Co	A_1		1.0000	2	6.150		485.01	485.01		16.131	42.38				
	A_3	690.0	1.0003		6.150	6.00	483.08	479.25	473.03	16.293	42.67	0.162	0.348	0.30	0.64
Zr	A_3		1.0085	4	6.150		323.45	323.45		48.206	64.86				
	A_2	1135.0	1.0020		5.940	5.48	318.01	297.16	285.35	50.624	67.20	2.418	3.505	2.33	3.38
Sn	A_4		1.3495	2	5.045		221.15	221.15		6.203	40.12				
	A_5	286.4	1.0930		5.045	3.72	200.31	164.32	155.78	7.850	47.41	1.647	1.961	7.28	8.62
La	A_3		1.0020	2	6.150		174.53	174.53		23.990	63.41				
	A_1	583.0	1.0000		5.950	5.97	173.10	170.29	170.60	24.380	64.15	0.390	0.362	0.73	0.68
	A_1	1137.0	1.0000	4	5.950		173.10	170.29		66.523	82.09				
	A_2		1.0020		5.111	4.88	169.38	155.25	151.79	68.984	84.37	2.461	3.027	2.28	2.81

Note: The value of θ* corresponds to the experimental value of $\frac{\Delta U_{tr}}{T_{cr}} = \Delta S^*_{T=T_{cr}}$. For Sn, $\theta_{A_5} = 200.31$, $\Delta S_{T_{cr}, A_4, A_5} = 2.37$ at $n = 0$.

θ* corresponding to ΔS^* determined according to $\frac{\Delta U_{tr}}{T_{cr}}$ (see Table 1) are presented in Table 2. According to the values θ_{ikj} obtained, the values of the internal energy U_{ikj} of the modifications *i* and *k* for chemical elements *j*, the free energies F_{ikj}, and the differences $\Delta F(T)_{ikj,\, T=T_{cr}} = \Delta U_{0ikj}$ at $T = (T_K)_{ikj}$ are determined. The values of θ_{expt} and θ_{calcd} and those of $\Delta S_{T_{cr}expt}$ and $\Delta S_{T_{cr}calcd}$ are plotted for comparison in Figs. 1 and 2.

While calculating the characteristic temperatures of iron modifications I(A_2), II(A_1), and III(A_2) reduced to the state of the Debye solids, we have used lattice constants according to [7] but not normalized to $T \longrightarrow 0$. The values of θ experimentally determined according to [8] are also taken for A_2. The modifications indicated were considered as independent phases with the functions $F(T)$ also independent of each other, as distinct, e.g., from [9–11], in which $F_I(T)$ and $F_{III}(T)$ were taken as unique common function $F(T)$. In [9, 10], the role of the magnetic contribution of the free energy was taken into account. In [11], the analysis of temperature variations of polymorphic modifications was carried out for iron alloys by the method of geometric thermodynamics.

In the present paper, apart from the geometric vibrational component, other possible components of the free energy were not taken into account. Other possible approaches [12–14] to the polymorphism problem were not considered either.

As follows from the results of this paper, apart from the similarity in the number of cases of characteristic temperatures used with experimental ones, the Debye approximations result in certain inconsistencies of thermodynamic properties at $T = T_{cr}$. The characteristic

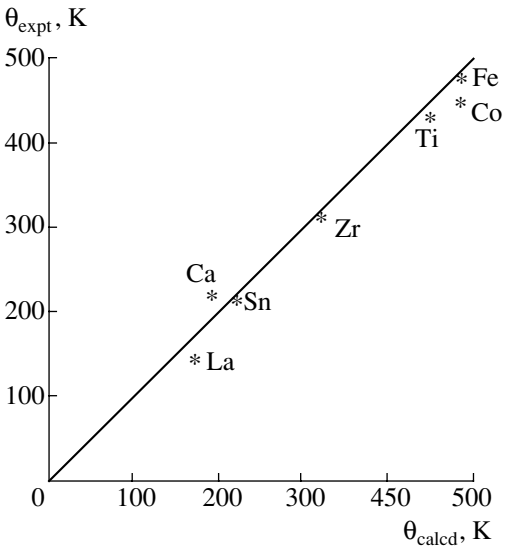

Fig. 1. Calculated and experimental [8] values of θ for low-temperature modifications.

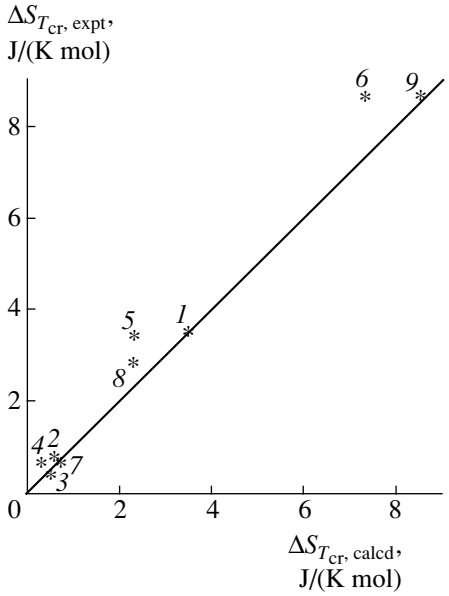

Fig. 2. Calculated and experimental [8] values of $\Delta S_{T_{cr}}$ for polymorphous transitions: (*1*) $Ti(A_3A_2)$; (*2*) $Fe(A_2A_1)$; (*3*) $Fe(A_1A_2)$; (*4*) $Co(A_1A_3)$; (*5*) $Zr(A_3A_2)$; (*6*) $Sn(A_4A_5)$; (*7*) $La(A_3A_1)$; (*8*) $La(A_1A_2)$; (*9*) $Sn(A_4A_5$ for $n = 2.5$).

temperatures calculated according to the experimental data for the entropy of different modifications, as a rule, slightly differ from the characteristic temperatures found on the basis of other experimental data. This fact emphasizes the principle importance of the allowance for the difference phonon spectra, as well as the role of other components of thermodynamic functions except the harmonic vibrational ones.

Along with the arguments given above, the results of this paper testify to the fact that the Debye approximation allows the clear description of the polymorphism of chemical elements having crystal structures free of strongly pronounced anisotropy to be presented and quantitative relations of atomization energy, atomic mass, and molar volume with the Debye characteristic temperature of modifications to be established.

As also follows from both the thermodynamic analysis and the results of this paper, in the Debye approximation the characteristic temperatures of a high-temperature modification are always lower than those of the low-temperature modification. Correspondingly, the stability determinants and other properties of the polymorphic modifications specified by the characteristic temperature also differ from each other.

The use of a novel analytical expression for the Debye characteristic temperature simplifies the structurally-thermodynamic consideration of the polymorphism phenomenon and the estimates of a number of properties for modifications of chemical elements.

REFERENCES

1. A. R. Verma and P. Krishna, *Polymorphism and Polytypism in Crystals* (Wiley, New York, 1966).
2. F. Seits, *Modern Theory of Solids* (McGrow Hill, New York, 1940; Gos. Izd. Tekh. Teor. Lit., Moscow, 1949).
3. N. N. Sirota, Cryst. Res. Technol. **17**, 661 (1982).
4. N. N. Sirota, Cryst. Res. Technol. **22**, 1343 (1987).
5. J. Alers, in *Physical Acoustics. Principles and Methods*, Vol. 3, Part B: *Lattice Dynamics*, Ed. by W. Mason (Academic, New York, 1965; Mir, Moscow, 1968).
6. P. Flubacher, A. J. Leadbetter, and J. A. Morrison, Philos. Mag. **4** (39), 273 (1939).
7. J. Emsley, *The Elements* (Clarendon, Oxford, 1991; Mir, Moscow, 1993).
8. *Metals: Handbook*, Ed. by G. V. Samsonov (Metallurgiya, Moscow, 1976).
9. C. Zener, Trans. Am. Inst. Min. Metal. Eng. **203**, 619 (1955).
10. R. J. Weiss and K. J. Tauer, Phys. Chem. Solids **4**, 135 (1958).
11. N. N. Sirota, Izv. Sekt. Fiz.-Khim. Anal. Inst. Obshch. Neorg. Khim. Akad. Nauk SSSR **19**, 182 (1949).
12. K. F. von Herzsfeld, *Kinetische Theorie der Wärme* (Druck and Verlag von Frieder, Braunschweig, 1925; Gos. Nauch. Tekh. Izd., Moscow, 1945).
13. B. T. Geĭlikman, *Statistical Theory of Phase Transitions* (Gos. Izd. Tekh. Teor. Lit., Moscow, 1954).
14. I. P. Bazarov, É. V. Gevorkyan, and V. V. Kozhekov, *Statistical Theory of Polymorphic Transformations* (Mosk. Gos. Univ., Moscow, 1978).

Translated by T. Galkina

Doklady Physics, Vol. 47, No. 1, 2002, pp. 21–24. Translated from Doklady Akademii Nauk, Vol. 382, No. 1, 2002, pp. 50–53.

PHYSICS

Plasma-Dust Structures at Cryogenic Temperatures

Academician V. E. Fortov, L. M. Vasilyak, S. P. Vetchinin, V. S. Zimnukhov, A. P. Nefedov†, and D. N. Polyakov

Received August 9, 2001

Among numerous methods for producing plasmas exhibiting strong Coulomb interaction [1], dust plasma presently attracts particular attention [2–4]. This is explained by the fact that it allows an extremely high parameter of nonideality ($\gamma = Z^2e^2n^{1/3}/kT \sim 10^5$) to be obtained, due to a significant charge Z of macroparticles, which reaches $\sim 10^4$–10^5. Such a value of the charge can be provided by both a high mobility of electrons (for example, in a high-frequency discharge or glow discharge [2, 3]) and the action of photoelectron emission or thermal emission [3, 5, 6], as well as by radioactive decay [7]. In this case, in a number of experiments, the interparticle Coulomb interaction turns out to be so strong that it causes the appearance of ordered dust structures (plasma liquids and plasma crystals). In them, the interparticle interaction causing structural ordering exceeds by orders of magnitude the thermal motion characterized by the energy kT, which destroys the structure.

In the present paper, we propose a method (alternative to the charge one) that makes it possible to increase the nonideality of the dust plasma. This method is based on decreasing the kinetic energy of dust particles down to cryogenic temperatures. Note that this allows a nonideal plasma in cryogenic discharges to be obtained [8] by laser cooling of ions in electrostatic traps [9] and electron cooling of ions in accelerating rings [10], as well as two-dimensional crystals on the liquid-helium surface [11].

In this study, we experimentally obtained dust structures in both glow-discharge plasma and high-frequency-discharge plasma at liquid-nitrogen temperature (77 K). The scheme of our experiment is similar to that considered in [12]. Dust structures consisting of magnesium oxide particles 3–5 μm in diameter, which had been introduced from above (i.e., from the anode side), were observed in striations of the positive column of a low-pressure glow discharge in a quartz discharge tube (2 cm in diameter) immersed into a cryostat filled with liquid nitrogen. Using laser illumination, also from above, we observed the dust structures through an optical window of the cryostat. Outside the discharge tube, we mounted two copper-foil rings spaced 4 cm from each other, between which the capacitive high-frequency discharge was ignited at a frequency of 13.6 MHz. Air at a pressure below 0.1 Torr served as a plasma-forming gas. The pressure was measured at room temperature by a thermocouple manometer placed in the upper part of the tube. The air density in the lower part of the tube, which was immersed in the liquid nitrogen, is approximately four times higher.

It should be noted that both glow discharge and high-frequency discharge are insufficiently studied at cryogenic temperatures. At the same time, as was shown in our experiments, they possess a number of interesting features. Visually, even the shape of the striations in the glow discharge at 77 K is absolutely distinct compared to that at room temperature. Probably, the shape of the striations is most significantly affected by metastable atoms and molecules accumulated in the discharge and ionization processes associated with them. Thermophoresis forces caused by temperature gradients also play an important role [12].

At liquid-nitrogen temperature, the dust structures in glow-discharge striations are observed in the form of threads and are similar to those detected for the same currents (~1 mA) at room temperature. Interparticle distances are nearly the same and attain approximately 200 to 250 μm [13]. In contrast to room temperatures, there are many particles that rapidly rotate around immovable threads located near the tube axis; no ring structures being observed. With an increase of the discharge current to 3 mA, the dust structures disappear. A rather extended structure (about 30 cm in length) consisting of long dust threads that occupy almost the entire volume of the glow-discharge positive column arises in a narrow range of pressures between 0.04 and 0.05 Torr, both above and below the level of liquid nitrogen. The experiments performed have shown that, along with well-known causes (the shape of the electrostatic potential, gravity force, and ion-friction force), the dynamics and stability of cryogenic dust plasma are significantly affected by longitudinal thermophoresis forces [12]. The forces are proportional to temperature gradients and (as shown in [12]), for the micron-size

† Deceased.

Institute for Thermal Physics of Extremal States, Institute of High Temperatures Scientific Association (IVTAN), Russian Academy of Sciences, Izhorskaya ul. 13/19, Moscow, 127412 Russia

1028-3358/02/4701-0021$22.00

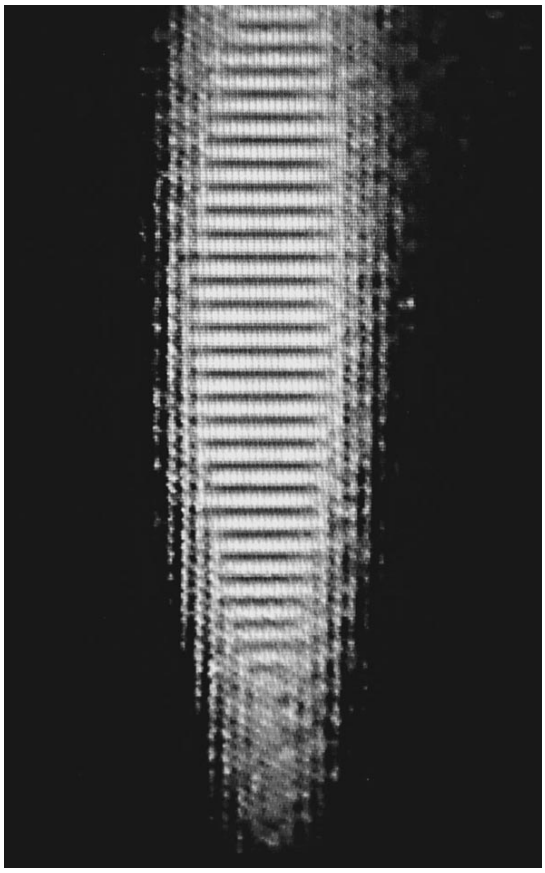

Layering of a dense dust structure at a cryogenic temperature. The size of a luminous region is 2 mm.

particles, exceed ion-friction forces appear because by almost one order of magnitude. These forces appear because the momentum transferred to a macroparticle by molecules passing from the side of the more heated gas exceeds the total momentum of cold molecules. The cryogenic dust structure turns out as though it were in an electrostatic trap. In this trap, the vertical stability is provided by the electric field of the glow discharge (that balances the gravity force of macroparticles) and by the thermophoresis force. This force acts both downwards along the direction of the thermal flow from the upper zone unoccupied by liquid nitrogen and upwards due to the heat release in the cathode region. With decreasing pressure, the dust structure is partitioned into several parts, 4–5 cm in length.

Previously, such extended dust structures were never observed in experiments. However, the structure is unstable with respect to longitudinal low-frequency disturbances. With laser illumination, these disturbances are directly observed by the unaided eye in the form of longitudinal density waves. The entire extended structure is divided into transverse layers (with different densities) about 0.7 mm thick. Probably, this is a result of spontaneous dust-acoustic instability, similar to ion sound in conventional plasmas [14]. It is worth noting that, in contrast to experiments at room temperatures when the dust-acoustic instability was observed, in our case, the entire extended structure at a distance about 30 cm is partitioned into transverse layers. The development of the dust-sound instability is a result of total plasma-flow instability when plasma ions pass through the charged dust with drift velocities exceeding the sound velocity in the dust itself. With decreasing temperature of heavy particles, the development of such an instability is simplified due to the lowered dust-acoustic speed.

The second series of experiments at cryogenic temperatures was performed with a capacitive high-frequency discharge. Since the electrodes are isolated from plasma by the glass tube walls, such a discharge is entirely controlled by the ambipolar diffusion. Experiments carried out at room temperature have shown that particles are located just below the lower ring and are confined in the vertical ambipolar electric field. The plasma localized between the rings represents an electrostatic trap for negatively charged macroparticles. The particles form a cone consisting of threads about 2 cm in length and ~2 mm in diameter. At liquid-nitrogen temperatures, the particle density in this structure abruptly changes. There appears a very dense plasma-dust structure with the same size, which is located in the middle between the rings to which the high-frequency power is transmitted. Interparticle distances in the structure are poorly distinguished even at a high magnification. Around this structure extended along the tube axis, we observed vertical threads consisting of particles having a density typical of the conventional glow discharge. The surface of the dust structure not only intensely scatters but also reflects the laser radiation.

The degree of particle ordering depends on gas pressure. Although we failed to observe the mutual arrangement of the particles in individual layers, we could see that the reconstruction of the structure occurred with an increase in gas pressure. The reconstruction of the structure (from cubic to hexagonal) with increasing pressure was previously observed by us in a glow discharge at room temperature [13]. With decreasing pressure, the dense structure is layered in spite of the fact that the ionization in this region remains uniform. We can observe well-pronounced dark and light thin transverse stripes with a thickness of about 150 μm, with sharp boundaries along the entire length of the structure (see figure). However, unlike the glow discharge, the dust particles in the dark stripes are almost entirely absent. In the lower part of the dust structure, we observed damped density waves traveling upward with a velocity of about 2 cm/s. The damping is associated with the collisional dissipation, which is significantly higher in the dust plasma than in the dust-free plasma. Layering seems to be caused by acoustic instability; however, dust sound is only excited in the dense structure, without affecting rare threads of surrounding macroparticles. Previously, the appearance of thin dust layers with sharp boundaries was not observed in studies

of dust plasmas. This phenomenon is apparently associated with the development of nonlinear processes. In addition, the nonlinear dust-acoustic vibrations (similar to nonlinear ion-acoustic waves) may also give rise to the appearance of sharp boundaries in the dust density. However, the nonlinear processes, as in the case of ion-acoustic vibrations in plasmas, are limited by the effects of spatial dispersion.

For the dust sound, the dependence of the phase velocity on the wavelength is the same as for the ion sound and results from the dispersion equation [14]:

$$\omega = \frac{KC_s}{(1 + K^2D^2)^{1/2}}. \quad (1)$$

Here, $C_s = Z(kT\varepsilon/m_d)^{1/2}$ is the speed of the dust sound, $\varepsilon = n_d/n_i$, n_i is the ion density, m_d is the mass of a dust particles, n_d is their density, and D is the Debye radius. With increasing the wave number, the phase velocity ω/K decreases. In this case, nonlinear dust-acoustic waves of cnoidal type can propagate along the structure. They correspond to an electric-field wave having a steep leading front and result in the formation of dust layers. In our conditions, the Debye radius $D \approx 20$ μm is determined by the ion temperature, the KD parameter is $KD \approx 0.4$, and the wavelength $\lambda \approx 300$ μm is significantly smaller than in other experiments performed with dust plasmas. At the same time, the experimental value of $C_s \approx 2$ cm/s exceeds by a factor of two or three the speed of the dust sound measured at room temperature. This is associated with the higher density of dust structures observed at cryogenic temperatures. Despite of the fact that the dust-acoustic vibrations in nonisothermal plasma is excited by ion drift, the thickness of the dust layers cannot be smaller than the ion mean free path in the charged dust, since otherwise the macroparticles in the layers cannot maintain their charge.

The formation of very dense dust structures is seemingly explained by the fact that, at cryogenic temperatures, the Debye screening radius D decreases and the mutual Coulomb repulsion of charged particles at distances $r \geq D$, which is determined by the exponential part of the Debye potential $(Z^2e^2/r)\exp(-r/D)$, is significantly weakened. In this case, dust particles can approach each other more closely, and their attraction associated with the mutual polarization of ion clouds surrounding them is revealed to a greater extent. The formation of ordering structures (in which interparticle distance considerably exceeds the Debye radius) can be explained by the attraction associated with ion fluxes impinging onto dust particles [15]. At the same time, at low temperatures in very dense structures under consideration, the dust particles strongly shade each other, and the ion mean free path becomes shorter than the size of the structure. Under these conditions, the attraction of dust particles by the action of pure electrostatic forces is possible.

Under the conditions of our experiment (at gas temperature $T = 77$ K and the power of ~0.5 W transferred to the high-frequency discharge), the electron concentration evaluated from the conductivity of the discharge is on the order of 10^9 cm^{-3}. The dust concentration in the dense structure can be estimated from the quasi-neutrality condition

$$Z\varepsilon = 1 - \frac{n_e}{n_i} \quad (2)$$

and the expression for the dust-sound speed C_s entering into formula (1). Using the measured value of C_s and assuming that the negative charge in the dense dust structure is mainly concentrated on the macroparticles, i.e, at $Z\varepsilon \sim 1$, we obtain that $Z \approx 3 \times 10^3$ and the density of macroparticles in the structure n_d cannot exceed 10^6 cm^{-3}. In this case, the ion mean free path in the charged dust $\lambda = (n_d\sigma)^{-1} \sim 0.01$ cm, where σ is the cross section for Coulomb scattering of an ion on a charged dust particle. The parameters of nonideality γ and of the Debye interaction $\Gamma = \gamma\exp(-r/D)$ attain the values of 10^4 and ~10^3, respectively. This indicates that the Coulomb system is strongly nonideal, and its nonideality parameter significantly exceeds the critical value $\gamma \approx 170$ for which a Coulomb crystal is formed.

It is worth noting that, despite the fact that in the high-frequency discharge the dense structure with sharp boundaries is surrounded by a dust structure consisting of rare threads, it does not absorb additional particles when environmental conditions are changed. Neither radial thermophoresis forces [12] nor ion entrainment forces associated with the ion ambipolar flow toward the walls are capable of destroying the dense structure. With decreasing pressure, there appear in it instabilities (similar to density waves) giving rise only to its partition into thin layers.

Thus, at cryogenic temperatures, we have managed to obtain superdense ordered plasma-dust structures that were previously unobserved in a high-frequency low-pressure discharge at room temperatures. The formation of dense structures is most likely related to the pure electrostatic interaction between charged dust particles. Instabilities inherent in these structures (probably associated with longitudinal dust-sound vibrations) give rise to their separation into thin transverse layers with well-pronounced boundaries and are observed when lowering gas pressure. In such structures, the dust-sound speed is several times higher than in dust formations previously investigated at room temperatures.

REFERENCES

1. V. E. Fortov and I. T. Yakubov, *Physics of Nonideal Plasma* (Atomizdat, Moscow, 1994).
2. G. E. Morfill, H. Thomas, and M. Zuric, in *Advances in Dusty Plasmas* (World Sci., Singapore, 1997), pp. 99–142.

3. A. P. Nefedov, O. F. Petrov, and V. E. Fortov, Usp. Fiz. Nauk **167**, 1215 (1997) [Phys. Usp. **40**, 1163 (1997)].
4. *Colloidal Plasma Science*, Ed. by P. K. Shukla and L. Stenflo, Phys. Scr. **89** (2001).
5. A. P. Nefedov, O. F. Petrov, and V. I. Molotkov, Pis'ma Zh. Éksp. Teor. Fiz. **72**, 313 (2000) [JETP Lett. **72**, 218 (2000)].
6. A. P. Nefedov, O. F. Petrov, and S. A. Khrapak, Fiz. Plazmy **24**, 1109 (1998) [Plasma Phys. Rep. **24**, 1037 (1998)].
7. V. E. Fortov, A. P. Nefedov, V. I. Vladimirov, *et al.*, Phys. Lett. A **258**, 305 (1999).
8. E. I. Asinovskiĭ, V. E. Fortov, A. V. Kirillin, and V. V. Markovets, in *Proceedings of the International Conference on Phenomena in Ionized Gases, Nagoya, 2001*, Vol. 3, p. 87.
9. T. H. E. Dubin and T. M. O'Neil, Rev. Mod. Phys. **71**, 87 (1999).
10. A. Rahman and J. P. Schiffer, Phys. Rev. Lett. **57**, 1133 (1986).
11. V. B. Shikin, Usp. Fiz. Nauk **158**, 127 (1989) [Sov. Phys. Usp. **32**, 452 (1989)].
12. V. V. Balabanov, L. M. Vasilyak, S. P. Vetchinin, *et al.*, Zh. Éksp. Teor. Fiz. **119**, 86 (2001) [JETP **92**, 86 (2001)].
13. L. M. Vasilyak, S. P. Vetchinin, A. P. Nefedov, *et al.*, Teplofiz. Vys. Temp. **38**, 701 (2000).
14. V. I. Molotkov, A. P. Nefedov, V. M. Torchinskiĭ, *et al.*, Zh. Éksp. Teor. Fiz. **116**, 902 (1999) [JETP **89**, 477 (1999)].
15. V. N. Tsytovich, Usp. Fiz. Nauk **167**, 57 (1997) [Phys. Usp. **40**, 53 (1997)].

Translated by Yu. Vishnyakov

Doklady Physics, Vol. 47, No. 1, 2002, pp. 25–28. Translated from Doklady Akademii Nauk, Vol. 382, No. 1, 2002, pp. 54–57.

PHYSICS

Unsteady Viscous Fluid Flow between Rotating Parallel Walls with Allowance for Thermal Slip along One of Them

Yu. I. Yalamov and A. A. Gurchenkov

Presented by Academician R.F. Ganiev April 4, 2001

Received April 19, 2001

This paper deals with oscillations in viscous incompressible fluid filling an infinitely long slot. Both the fluid and the slot rotate as a solid with an angular velocity $\boldsymbol{\omega}_0 = \text{const}$. Oscillations in the fluid are induced by both vibrations of the upper plate, which are not torsional, and a temperature gradient. This gradient is applied to the lower plate at the initial time moment. We have determined the velocity field in the flow and the vectors of tangential stresses acting from the fluid upon the upper and lower plates of the slot. Various motions of the upper plate are investigated, and the corresponding velocity fields formed in the flow are found.

We consider a flow of a viscous incompressible fluid with the density ρ and the kinematic viscosity ν, which fills in the slot Q. Both the fluid and the slot uniformly rotate as a solid with an angular velocity $\boldsymbol{\omega}_0$. The fluid is placed in a field of mass forces having the potential U. We introduce a Cartesian coordinate system $Oxyz$ with basis vectors $\mathbf{e}_x$, $\mathbf{e}_y$, and $\mathbf{e}_z$. The system is fixed in the upper plate Q_0 so that the plane Oxz coincides with the plane Q_0 and the y-axis being directed into the fluid is normal to Q_0. The equations of motion for the flow, which are written in the system $Oxyz$ rotating with the angular velocity $\boldsymbol{\omega}_0$, have the form

$$\boldsymbol{\omega}_0 \times (\boldsymbol{\omega}_0 \times \mathbf{r}) + 2\boldsymbol{\omega}_0 \times \mathbf{V} + \frac{\partial \mathbf{V}}{\partial t} + (\mathbf{V}\nabla)\mathbf{V}$$

$$= -\frac{1}{\rho}\nabla P + \nu\Delta\mathbf{V} + \nabla U, \qquad (1)$$

$$\text{div}\mathbf{V} = 0 \text{ in } Q.$$

Here, t, $\mathbf{r}$, $\mathbf{V}$, and P are time, the radius vector with respect to the pole 0, the fluid velocity, and pressure, respectively.

We now consider the boundary conditions and initial conditions of the problem. In the rotating system, the fluid is initially at rest so that

$$\mathbf{V}(\mathbf{r}, t) = 0 \text{ at } \mathbf{r} \in Q, \quad t < 0.$$

Computer Center, Russian Academy of Sciences, ul. Vavilova 40, GSP-1, Moscow, 117967 Russia

At the time moment $t \geq 0$, the upper plate begins to move with the velocity $\mathbf{u}(t)$ and the nonslip condition takes the form $\mathbf{V}(0, t) = \mathbf{u}(t)$. At the same time, the lower plate being at rest is specified by a temperature gradient ∇T. Since the temperature varies along the surface Q_l, the Knudsen layer with a width on the order of the mean free path λ of medium molecules is formed in the fluid. Within this layer, the medium begins to slip with the velocity $\mathbf{V}_T$, where $\mathbf{V}_T$ is such that the total momentum flux through the surface Q_l is zero. Therefore, the medium velocity $\mathbf{V}$ should be specified on the outer boundary of the Knudsen layer as a boundary condition.

It is noteworthy that the slip of a viscous phase along solid nonuniformly heated boundaries was not taken into account in all papers devoted to solving hydrodynamical equations in an oscillating fluid. In this paper, we for the first time allow for the thermal slip and analyze the results based on the exact solution to the hydrodynamic problem, which has primary significance.

The phenomenon of thermal gas slip along a nonuniformly heated surface has been known for a long time. It has been considered in many papers, for example, in [1–4]. In addition, the theoretical results were reliably verified in numerous experiments. It was shown that the velocity of the thermal slip along a nonuniformly heated surface is proportional to the temperature gradient, the proportionality coefficient depending on intermolecular gas–solid interaction. For the velocity of the thermal gas slip along a flat surface, the expression

$$v_T = k_{TSL}\nu_g\frac{\nabla T}{T}$$

has been derived. Here, k_{TSL}, ν_g, ∇T, and T are the thermal-slip coefficient, the dynamic viscosity, the temperature gradient, and the average gas temperature, respectively.

Papers devoted to the effects of thermal slip in temperature-inhomogeneous liquids appeared somewhat later (see, e.g., [5–7]). Moreover, the experiments [8] carried out by McNab and Meison in various liquids containing large latex particles have shown that thermal

1028-3358/02/4701-0025$22.00

slip occurs only if the temperature gradient is maintained on a solid surface in contact with a liquid. In this case, the formula for the velocity of the thermal slip turns out to be identical for both liquid and gas. However, in the case of a liquid, the coefficient of thermal slip is $k_{TSL} = 0.13$. Thus, the velocity of the thermal slip in a liquid is described by the expression

$$v_T = 0.13\nu_l \frac{\nabla T}{T},$$

where ν_l is the dynamic viscosity of the liquid.

As is well known, kinematic viscosity of gases exceeds that of liquids by an order of magnitude; i.e., $\nu_l = 0.1\nu_g$. Moreover, being proportional to the mean free path of molecules, the coefficient of thermal slip in gas is larger than the corresponding coefficient in liquid by an order of magnitude as well. Therefore, in gas, the velocity of the thermal slip is by two orders of magnitude larger than in liquid.

At $\nabla T \sim 10$ K/cm, the velocity of thermal slip in gases $V_T \sim 10^{-4}$ cm/s. However, in the case of the temperature gradient $\nabla T \sim 10^4$ K/cm, the velocity of the thermal slip in liquid exceeds that in gas by an order of magnitude. With allowance for this remark, the boundary conditions specified on the surface Q_l take the form

$$\mathbf{V}(\mathbf{r}, t) = \mathbf{V}_T \text{ at } \mathbf{r} \in Q_l.$$

Here, we took into account the fact that the Knudsen layer is thin ($\lambda \ll |\mathbf{r}|$). Therefore, the velocity $\mathbf{V}$ on the outer boundary of this layer can be calculated for the surface of the plate Q_l.

The complete system of equations describing a perturbed flow of a viscous fluid has the form

$$\begin{gathered}\boldsymbol{\omega}_0 \times (\boldsymbol{\omega}_0 \times \mathbf{r}) + 2\boldsymbol{\omega}_0 \times \mathbf{V} + \frac{\partial \mathbf{V}}{\partial t} + (\mathbf{V}\nabla)\mathbf{V} \\ = -\frac{1}{\rho}\nabla P + \nabla U + \nu\Delta\mathbf{V}; \\ \operatorname{div}\mathbf{V} = 0 \text{ in } Q; \\ \mathbf{V}(\mathbf{r}, t) = \mathbf{u}(t) \text{ at } \mathbf{r} \in Q_0, \quad t \geq 0; \\ \mathbf{V}(\mathbf{r}, t) = \mathbf{V}_T(t) \text{ at } \mathbf{r} \in Q_l, \quad t \geq 0; \\ \mathbf{V} = 0 \text{ at } \mathbf{r} \in Q, \quad t < 0.\end{gathered} \tag{2}$$

The solution to system (2) is sought as

$$\begin{gathered}P = \frac{1}{2}\rho(\boldsymbol{\omega}_0 \times \mathbf{r})^2 + \rho U + \rho p(y, t), \\ \mathbf{V} = V_x(y, t)\mathbf{e}_x + V_z(y, t)\mathbf{e}_z.\end{gathered} \tag{3}$$

As a result, system (2) splits into two following subsystems:

$$\begin{gathered}\frac{\partial \mathbf{V}}{\partial t} + 2\omega_{0y}(\mathbf{e}_y \times \mathbf{V}) = \nu\frac{\partial^2 \mathbf{V}}{\partial y^2}, \quad 0 \leq y \leq l, \\ \mathbf{V}(0, t) = \mathbf{u}(t), \quad t \geq 0; \quad \mathbf{V}(l, t) = \mathbf{V}_T(t), \quad t \geq 0; \\ \mathbf{V}(y, 0) = 0, \quad 0 \leq y \leq l;\end{gathered} \tag{4}$$

$$\begin{gathered}\frac{\partial p}{\partial y} = 2\mathbf{V}(\boldsymbol{\omega}_0 \times \mathbf{e}_y), \\ P(0, t) = P_0(t), \quad \omega_{0y} = \boldsymbol{\omega}_0 \cdot \mathbf{e}_y.\end{gathered} \tag{5}$$

The velocity field formed in the fluid is determined from equations (4), and the pressure field is found from the velocity field (5).

The solution to system (4) is sought as

$$\mathbf{V} = \mathbf{W}\sin 2\Omega t - (\mathbf{W} \times \mathbf{e}_y)\cos 2\Omega t, \tag{6}$$

where $\mathbf{W} = W_x(y, t)\mathbf{e}_x + W_z(y, t)\mathbf{e}_z$ is a new unknown function. Furthermore, it is convenient to introduce the notation $\Omega = \omega_{0y}$ and $\mathbf{u}(t) = \mathbf{u}_1(t)\mathbf{V}_T(t) = \mathbf{u}_2(t)$.

Substituting (6) into (4) yields the following homogeneous heat-conduction equation for determining $\mathbf{W}$:

$$\mathbf{W}_t = \nu\mathbf{W}_{yy}, \quad 0 \leq y \leq l. \tag{7}$$

This equation is solved by using both the initial condition $\mathbf{W}(y, 0) = 0$ and the boundary conditions

$$\begin{gathered}\mathbf{W}(0, t) = \mathbf{u}_1(t)\sin 2\Omega t + (\mathbf{u}_1(t) \times \mathbf{e}_y)\cos 2\Omega t, \\ \mathbf{W}(l, t) = \mathbf{u}_2(t)\sin 2\Omega t + (\mathbf{u}_2(t) \times \mathbf{e}_y)\cos 2\Omega t.\end{gathered}$$

Integrating Eq. (7), we arrive at the relation

$$\begin{gathered}\mathbf{W} = \mathbf{W}(0, t)\left(1 - \frac{y}{l}\right) + \mathbf{W}(l, t)\frac{y}{l} \\ -\frac{2}{l}\sum_{n=1}^{\infty}\frac{\sin\lambda_n y}{\lambda_n}\int_0^t \dot{\mathbf{W}}_{0,t}(\tau)\exp(-\nu\lambda_n^2(t-\tau))d\tau,\end{gathered} \tag{8}$$

where $\lambda_n = \dfrac{\pi n}{l}$.

Substituting (8) into (6), we obtain the desired velocity field

$$\begin{gathered}\mathbf{V} = u_1(t)\left(1 - \frac{y}{l}\right) + \mathbf{u}_2(t)\frac{y}{l} \\ -\frac{2}{l}\sum_{n=1}^{\infty}\frac{\sin\lambda_n y}{\lambda_n}\int_0^t \dot{\mathbf{T}}_{0,l}(\tau)\exp(-\nu\lambda_n^2(t-\tau))d\tau,\end{gathered}$$

where

$$\dot{\mathbf{T}}_{0,l}(\tau) = \frac{\partial}{\partial\tau}\mathbf{T}_{0,l}(\tau),$$

$$\begin{aligned}\mathbf{T}_{0,l}(\tau) &= \mathbf{T}_1(\tau, t-\tau) - (-1)^n\mathbf{T}_2(\tau, t-\tau),\\ \mathbf{T}_{1,2}(\tau, t-\tau) &= \mathbf{u}_{1,2}(\tau)\cos 2\Omega(t-\tau)\\ &\quad + (\mathbf{u}_{1,2}(\tau)\times\mathbf{e}_y)\sin 2\Omega(t-\tau).\end{aligned} \tag{9}$$

The pressure field

$$\begin{aligned}P(y,t) &= 2(\boldsymbol{\omega}_0\times\mathbf{e}_y)\left\{\mathbf{u}_1(t)\left(y-\frac{y^2}{2l}\right)+\frac{\mathbf{u}_2(t)y^2}{2l}\right.\\ &\left.+\frac{2}{l}\sum_{n=1}^{\infty}\frac{1}{\lambda_n^2}\cos\lambda_n y\int_0^t\dot{\mathbf{T}}_{0,l}(\tau)\exp(-\nu\lambda_n^2(t-\tau))d\tau\right\}\end{aligned} \tag{10}$$

is calculated by solving equation (5) with its right-hand side obtained with allowance for expression (9).

We now consider features of the velocity field (9). When studying the perturbed motion of a mechanical object, we can employ an approach widely used in structural dynamics. According to this approach, only the first several tones of the system vibrations are taken into account, while higher harmonics are omitted. Such a procedure is possible, because the coefficients that characterize inertial bonds between the body motion and wave motions in the fluid decrease sharply for higher harmonics compared to the fundamental (lower) tone.

For $n = 1$ and $\lambda_1 = \dfrac{\pi}{l}$, the velocity field for a viscous fluid can be represented as

$$\begin{aligned}\mathbf{v}(y,t) &= \mathbf{u}_1(t)\left(1-\frac{y}{l}\right)+\frac{\mathbf{u}_2(t)y}{l}\\ &-\frac{2}{\pi}\sin\lambda_1 y\int_0^t\dot{\mathbf{T}}_{0,l}(\tau)\exp(-\nu\lambda_1^2(t-\tau))d\tau,\end{aligned}$$

where

$$\begin{aligned}\dot{\mathbf{T}}_{0,l}(\tau) &= \dot{\mathbf{u}}(\tau)\cos 2\Omega(t-\tau)\\ &+\mathbf{u}(\tau)\times\mathbf{e}_y\sin(2\Omega(t-\tau)+2\Omega[\mathbf{u}(\tau)\sin 2\Omega(t-\tau)\\ &-\mathbf{u}(\tau)\times\mathbf{e}_y\cos 2\Omega(t-\tau)],\\ \mathbf{u}(\tau) &= \mathbf{u}_1(\tau)+\mathbf{u}_2(\tau).\end{aligned} \tag{11}$$

We consider the case $\nu = 10^{-2}$ cm^2 s^{-1}, $l = \pi$ cm, and $2\Omega = 10^{-2}$ s^{-1}. In addition, $\mathbf{u}_1(\tau) = \mathbf{e}_x u_1 = \text{const}$ and $\mathbf{u}_2(\tau) = u_2\mathbf{e}_x = \text{const}$, where $\mathbf{e}_x$ is the basis vector of the Ox-axis. In this case, the velocity field (11) can be represented as

$$\begin{aligned}\mathbf{v}(y,t) &= \left[u_1\left(1-\frac{y}{\pi}\right)+\frac{u_2 y}{\pi}\right]\mathbf{e}_x-(u_1+u_2)\frac{\sin y}{\pi}\\ &\times\{[1-(\sin 10^{-2}t+\cos 10^{-2}t)\exp(-10^{-2}t)]\mathbf{e}_x\\ &-[1+(\sin 10^{-2}t-\cos 10^{-2}t)\exp(-10^{-2}t)]\mathbf{e}_z\}.\end{aligned}$$

For the time $T = \dfrac{2\pi}{\Omega} = 200\pi$ s, the natural fluid oscillations are damped; therefore, the velocity profile takes the form

$$\begin{aligned}\mathbf{v}(y) &= \left[u_1\left(1-\frac{y}{\pi}\right)+\frac{u_2 y}{\pi}-\sin y\frac{u_1+u_2}{\pi}\right]\mathbf{e}_x\\ &+\frac{u_1+u_2}{\pi}\sin y\mathbf{e}_z.\end{aligned} \tag{12}$$

Below, we consider the limiting cases.

1. Let $u_2 \ll u_1$; i.e., the velocity of the upper plate considerably exceeds the velocity of the thermal fluid slip along the lower plate Q_l. In this case, the velocity profile has the form

$$\mathbf{v}(y) = u_1\left(1-\frac{y}{\pi}-\frac{\sin y}{\pi}\right)\mathbf{e}_x+u_1\left(\frac{\sin y}{\pi}\right)\mathbf{e}_z.$$

As is seen from this expression, near the upper plate ($y \longrightarrow 0$), the fluid velocity coincides with the velocity of the plate motion $\mathbf{u}_1 = u_1\mathbf{e}_x$; i.e., the nonslip condition is satisfied. At the same time, at the lower wall ($y \longrightarrow \pi$) the fluid velocity vanishes. This fact also corresponds to the nonslip condition, because in the rotating coordinate system the lower plate is motionless.

2. Let $u_1 \ll u_2$; i.e., the velocity of the thermal fluid slip along the lower plate is much higher than velocity of the upper plate. In this case, the velocity profile can be represented as

$$\mathbf{v}(y) = u_2\left(\frac{y}{\pi}-\frac{\sin y}{\pi}+\frac{u_1}{u_2}\right)\mathbf{e}_x+u_2\left(\frac{\sin y}{\pi}\right)\mathbf{e}_z.$$

Evidently, the fluid velocity $\mathbf{v} = \mathbf{u}_1 = u_1\mathbf{e}_x$ as $y \longrightarrow 0$, which corresponds to the nonslip condition at the upper plate. At the same time, $\mathbf{v} = u_2\mathbf{e}_x$ as $y \longrightarrow \pi$; i.e., the boundary condition specified at the lower wall is satisfied.

In conclusion, we note that the velocity field (9), which is obtained with allowance for the thermal slip of a temperature-nonuniform viscous fluid, represents the exact solution to the time-dependent Navier–Stokes equations in a rotating coordinate system. This velocity field can be used in order to take into account force actions occurring in the case of fluid flows in channels of different shapes, in solving filtration problems, and

in modeling various physical phenomena in a flowing fluid.

ACKNOWLEDGMENTS

This work was supported by the Russian Foundation for Basic Research, project no. 00–01–00629.

REFERENCES

1. I. N. Ivchenko and Yu. I. Yalamov, Izv. Akad. Nauk SSSR, Mekh. Zhidk. Gaza, No. 6, 59 (1969).
2. I. N. Ivchenko and Yu. I. Yalamov, *Izv. Akad. Nauk SSSR, Mekh. Zhidk. Gaza*, No. 6, 139 (1968).
3. Yu. I. Yalamov and A. A. Yushkanov, in *Physics of Aerodispersive Systems and Physical Kinetics* (Izd. MOPI im. N.K. Krupskoi, Moscow, 1978), Vol. 2.
4. Yu. I. Yalamov, M. N. Gaidukov, and A. A. Yushkanov, Inzh.-Fiz. Zh. **29**, 489 (1975).
5. Yu. I. Yalamov and A. S. Sanasaryan, Zh. Tekh. Fiz. **45**, 1063 (1975) [Sov. Phys. Tech. Phys. **20**, 668 (1975)].
6. Yu. I. Yalamov and A. S. Sanasaryan, Inzh.-Fiz. Zh. **28**, 1061 (1975).
7. Yu. I. Yalamov and A. S. Sanasaryan, Zh. Tekh. Fiz. **47**, 1063 (1977) [Sov. Phys. Tech. Phys. **22**, 634 (1977)].
8. G. S. McNab and A. M. Meison, J. Colloid Interface Sci. **44** (2), 39 (1972).

Translated by Yu. Verevochkin

Doklady Physics, Vol. 47, No. 1, 2002, pp. 29–33. Translated from Doklady Akademii Nauk, Vol. 382, No. 2, 2002, pp. 176–180.

PHYSICS

Gas-Bubble Dynamics under Excitation by Compression and Rarefaction Pulses in a Liquid

A. A. Aganin* and Corresponding Member of the RAS M. A. Il'gamov**

Received May 10, 2001

INTRODUCTION

Since 1990, nonlinear oscillations of a gas bubble in intense ultrasonic fields are of increasing interest, because one-bubble sonoluminescence, promising for chemistry and physics, was discovered at that time. Now, there are many papers on this problem (see [1, 2]), where much attention is given to the study of harmonic, subharmonic, and ultraharmonic resonances characterized by an increase in oscillation amplitude, period doubling, bifurcations, chaos, and other features.

Here, we consider bubble oscillations for a bubble radius being by two or more orders of magnitude smaller than its resonant value, which corresponds to medium characteristics and conditions of excitation. Such oscillations rapidly become steady-state. In consideration of small-bubble oscillations, were focused on the explanation of both mechanisms of one-bubble sonoluminescence and various associated effects, in particular, on reaching the maximum bubble compression [1, 3].

The Rayleigh–Plesset equation

$$\left(1-\frac{u_b}{c_l^0}\right)r_b u_b' + \frac{3}{2}\left(1-\frac{u_b}{3c_l^0}\right)u_b^2 = \left(1+\frac{u_b}{c_l^0}+\frac{r_b}{c_l^0}\frac{d}{dt}\right)\frac{p_b-p_{ex}}{\rho_l^0} \quad (1)$$

is widely used to describe bubble dynamics. Here, r_b and u_b are the radius of the bubble and the velocity of its surface, c_l^0 and ρ_l^0 are the unperturbed sound velocity in the liquid and the density thereof, and p_{ex} is the liquid pressure at a distance far from the bubble. In addition,

$$p_b = p_g - 4\mu_l\frac{u_b}{r_b} - 2\frac{\sigma}{r_b}, \quad (2)$$

where p_g is the gas pressure at the bubble surface; μ_l and σ are the viscosity and surface-tension coefficient of the liquid, respectively.

If pressure variation in the bubble is uniform and adiabatic, then

$$p_g = p_g^0\left(\frac{r_b^0}{r_b}\right)^{3\gamma}, \quad p_g^0 = p_l^0 + 2\frac{\sigma}{r_b^0}. \quad (3)$$

Here, p_g^0 and p_l^0 are the equilibrium gas pressures in the bubble and in the liquid, respectively, which both correspond to the initial bubble radius r_b^0, and γ is the adiabatic exponent.

EFFICIENCY OF BUBBLE COMPRESSION BY COMPRESSION AND RAREFACTION PULSES

Figure 1 shows the response of an air bubble to pressure variation in water according to model (1)–(3),

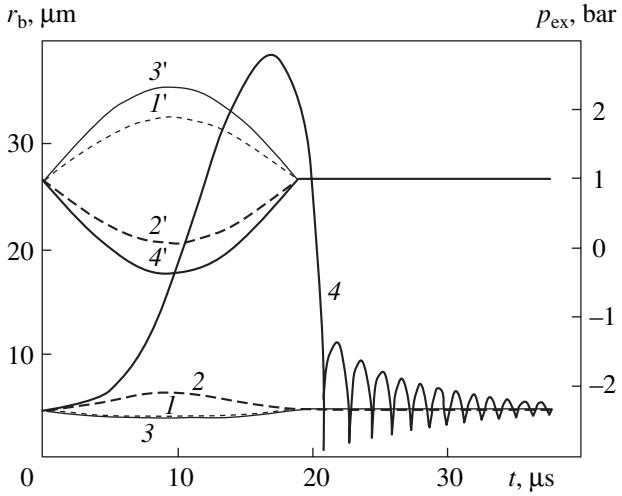

Fig. 1.

* *Institute of Mechanics and Machine Building, Kazan Scientific Center, Russian Academy of Sciences, ul. Lobachevskogo 2/31, Kazan, 420111 Tatarstan, Russia*

** *Presidium of Ufa Scientific Center, Russian Academy of Sciences, ul. K. Marksa 6, Ufa, 450000 Bashkortostan, Russia*

1028-3358/02/4701-0029$22.00

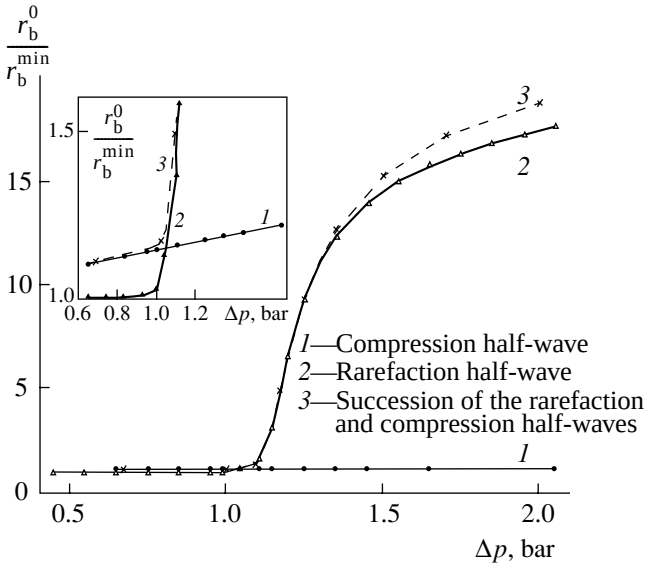

Fig. 2.

where

$$p_{ex} = \begin{cases} p_l^0 \pm \Delta p \sin \omega t \ \text{ at } \ t_n \le t < t_n + \dfrac{T}{2} \\ p_l^0 \ \text{ at } \ t_n + \dfrac{T}{2} \le t < t_{n+1}, \end{cases} \qquad (4)$$

$t_0 = 0$, $t_n = t_{n-1} + T$, $n = 0$, and $T = \dfrac{2\pi}{\omega}$. The calculations were carried out at $\mu_l = 0.001$ kg/(m s), $\omega = 2\pi \times 26.5$ kHz, $c_l^0 = 1498$ m/s, $r_b^0 = 4.5$ μm, $p_l^0 = 1$ bar, $\rho_l^0 = 998$ kg/m^3, $\sigma = 0.0727$ kg/s^2, and $\gamma = 1.4$. Curves *1*–*4* represent bubble responses $r_b = r_b(t)$ to pressure variation $p_{ex} = p_{ex}(t)$ (curves *1*'–*4*'), where the curves numbered by *i*' and *i* correspond to each other. Curves *1*', *2*', *1*, *2* and *3*, *4*, *3*', *4*' are obtained at $\Delta p = 0.9$ and 1.35 bar, respectively.

With the enhancement of a compression pulse [positive sign in relation (4)], the growth of pulse amplitude causes only a small quantitative variation of the bubble response, whereas during rarefaction [negative sign in relation (4)], a strong quantitative and qualitative change of the bubble response occur. Namely, at relatively low pressure Δp, the bubble responds by compression (curve *1*) to excitation by the compression half-wave (curve *1*') and by expansion (curve *2*) to excitation by the rarefaction half-wave (curve *2*'). With increasing Δp, this feature takes place only for the compression pulse (curves *3*' and *3*). So, being excited by the rarefaction half-wave (curve *4*'), the bubble responds first by expansion, which is typical for curve *2*, and then by a series of short-term successively attenuated compressions, the first of which is the strongest (curve *4*). In particular, the rarefaction half-wave of amplitude $\Delta p = 1.35$ bar compresses the bubble up to the maximum values of pressure, density, and temperature that are 10^4, 10^3, and 10 times higher, respectively, than those caused by the compression half-wave of the same amplitude.

Figure 2 shows the maximum bubble compression characterized by the dimensionless parameter $\dfrac{r_b^0}{r_b^{min}}$, where r_b^{min} is the minimum bubble radius, versus pressure amplitude ranging in the interval $0.4 < \Delta p < 2.1$ bar. Curves *1* and *2* correspond to excitation by compression and rarefaction pulses of the form (4), respectively. We can see that with increasing amplitude of the compression pulse a decrease in the minimum bubble radius is very slow (curve *1*). Under the effect of the rarefaction pulse, a bubble decrease with respect to its initial dimension can be noticed only at the amplitude $\Delta p \approx 1$ bar (the inset in Fig. 2). At $\Delta p \approx 1.05$ bar, the rarefaction pulse brings the ratio $\dfrac{r_b^0}{r_b^{min}}$ to the level reached under the effect of the compression pulse (before, it was below this level). Beginning from $\Delta p \approx 1.1$ bar, curve *2* steeply deflects upwards so that, in the region $1.3 < \Delta p < 2.1$ bar, the maximum bubble decrease reached under the effect of the rarefaction pulse by more than a factor of ten exceeds a similar decrease reached under the effect of the compression pulse. With increasing Δp, this difference grows.

It is noteworthy that, when forming converging spherical shock waves in a bubble, its compression caused by the rarefaction pulse becomes much more efficient in the sense of obtaining the maximum values of gas pressure, density, and temperature in the bubble center. In particular, if the shock-wave effect is taken into account by using the model with a complete description of gas compressibility both in the bubble and in the liquid around it [4]. In this case, bubble compression caused by the rarefaction pulse with $\Delta p = 1.35$ bar and characterized by an increase in pressure, density, and temperature in the bubble center turns out to be ~10^8, ~10^4, and ~10^2 times, respectively, more efficient compared to the case of the compression pulse.

BUBBLE DYNAMICS AND ITS QUASI-STATIC PORTRAIT

To understand features of bubble dynamics, it is useful to analyze its varying static-equilibrium states, i.e., its "quasi-static portrait." As is known, certain equilibrium states represent attraction centers of a dynamic system. According to relations (1)–(3), these states are determined by the equation $p_b - p_{ex} = 0$, which, after

substitution of the relation $p_{ex} = p_l^0 - \Delta p \sin\omega t$ entering into (4), takes the form

$$\left[\left(\frac{r_b^0}{r_b}\right)^{3\gamma} - 1\right] + a\left[\left(\frac{r_b^0}{r_b}\right)^{3\gamma} + \frac{r_b^0}{r_b}\right] + \frac{\Delta p}{p_l^0}\sin\omega t = 0, \quad a = \frac{2\sigma}{p_l^0 r_b^0}. \tag{5}$$

If Eq. (5) is satisfied, the system, in contrast to the case of its loading by the pressure $p_{ex} = p_l^0 + \Delta p \sin\omega t$, does not have static-equilibrium states with all external actions. This fact becomes more evident at $\sigma = 0$, when equation (5) takes the form

$$\frac{r_b}{r_b^0} = \left(1 - \frac{\Delta p}{p_l^0}\sin\omega t\right)^{-\frac{1}{3\gamma}},$$

showing that the static-equilibrium states exist only if $\frac{\Delta p}{p_l^0}\sin\omega t < 1$. At $\sigma \neq 0$, the static-equilibrium states exist under the condition

$$\frac{\Delta p}{p_l^0}\sin\omega t < 1 + \frac{3\gamma - 1}{3\gamma} a\left(\frac{a}{3\gamma(1+a)}\right)^{\frac{1}{3\gamma-1}} = \frac{p^*}{p_l^0}, \tag{6}$$

where p^* is the critical value of the pressure amplitude Δp (the Blake threshold [5]) such that excess over it leads to liquid discontinuity.

Figure 3 shows the quasi-static portrait of bubble-radius variation for certain excitation amplitudes from the interval $0.45 \le \Delta p \le 1.5$ bar. Curves *1**–*7** situated in the region $r_b \le r_b^0$ correspond to the responses to the compression pulses, while curves *1*–*7* lying in the region $r_b \ge r_b^0$ conform to the responses to the rarefaction pulses. The quasi-static portraits of the responses to the compression pulses change rather insignificantly (curves *1**–*7**). The portraits of bubble responses to the rarefaction pulses of the amplitude Δp not exceeding 1 bar (curves *1*–*3*) behave in a similar way. Following a further increase in Δp up to $p^* \approx 1.106$ bar, the maximum bubble radius r_b^{max} in the portrait tends rapidly to infinity (between curves *4* and *5*). A higher Δp leads to expansion of the interval within which r_b^{max} tends to infinity (curves *5*–*7*).

In the zones mentioned, condition (6) is violated. Values of both Δp and the initial bubble radius r_b^0 at which the bubble expands strongly can be easily estimated by using equation (5) under the condition $\frac{r_b - r_b^0}{r_b^0} \ll 1$. A solution to the corresponding linear equation has the form

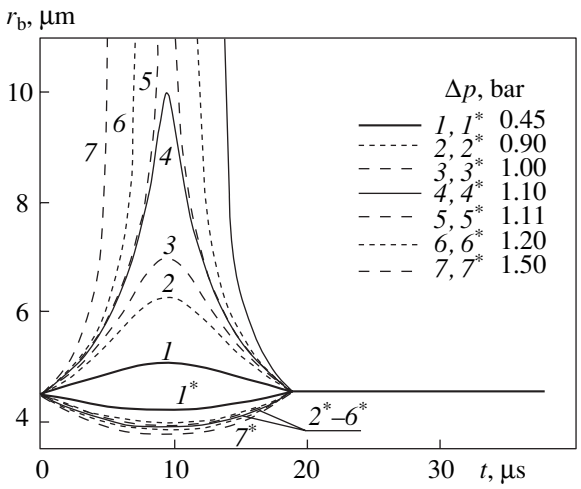

Fig. 3.

$$\frac{r_b - r_b^0}{r_b^0} = \frac{\Delta p}{(3\gamma - 1)a p_l^0 - 3\gamma(\Delta p - p_l^0)}.$$

It grows unboundedly at

$$\frac{\Delta p}{p_l^0} = 1 + \frac{3\gamma - 1}{3\gamma} a.$$

After dividing its second term by two, the relation written above would become close in its value to relation (6). Using this relation, we can determine the critical amplitude $(\Delta p)_{cr}$ at the given radius r_b^0 and the critical radius $(r_b^0)_{cr}$ at the given amplitude Δp

$$(\Delta p)_{cr} \approx p_l^0 + \frac{3\gamma - 1}{3\gamma}\frac{\sigma}{r_b^0}, \quad (r_b^0)_{cr} \approx \frac{(3\gamma - 1)\sigma}{3\gamma(\Delta p - p_l^0)} \quad (\Delta p > p_l^0), \tag{7}$$

which are such that an excess over them leads to strong bubble expansion.

Below, we use the quasi-static portrait to explain features of the bubble responses plotted in Figs. 1 and 2. Being affected by the compression pulse throughout the interval $1.3 < \Delta p < 2.1$ bar or by the rarefaction pulse of the amplitude Δp lower than 1 bar, the static-equilibrium bubble states change slowly. For the most part, the difference between dynamic and quasi-static bubble

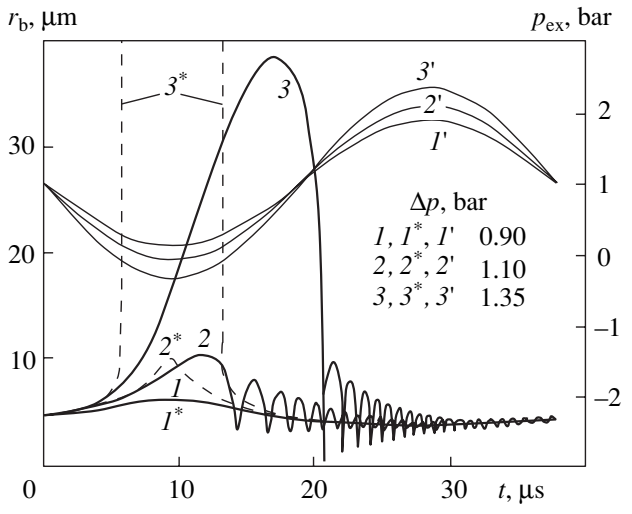

Fig. 4.

states, which include a degree of compression, arises because the quasi-static bubble radius first tends rapidly to infinity and then returns rapidly from infinity to the region r_b^0. In addition, this difference depends on the length of the time interval between these two instants. Because the quasi-static bubble radius tends to infinity at $\Delta p \geq 1.106$ bar and, following a further increase in Δp, the above-mentioned interval expands (Fig. 3, curves *4–7*), the maximum bubble compression grows initially abruptly and then more smoothly (Fig. 2, curve *2*).

Figure 4 shows dynamic (solid curves *1–3*) and quasi-static (dashed curves *1*–3**) radii of a bubble excited with the amplitudes Δp = 0.9, 1.1, and 1.35 bar, respectively, (curves *1'–3'*) as functions of time. The other input data are the same as before. At relatively small amplitudes Δp, the regime of bubble oscillations is close to the quasi-static one (curves *1* and *1** practically merge). While Δp increases up to 1.1 bar, the difference between dynamic and quasi-static behavior grows rather rapidly (curves *2* and *2**). Damped vibrations with respect to the varying static-equilibrium state arise in the transient region between r_b^{max} and r_b^{min}. Being calculated by the dynamic model, r_b^{max} forms with increasing time lag and, up to $\Delta p \approx 1.1$ bar, is a little larger than that according to the quasi-static model. At $\Delta p \approx 1.106$ bar, the quasi-static value of r_b^{max} grows abruptly so that, following a further increase in Δp, the difference between radii becomes more considerable (curves *3* and *3**). Their similar behavior is observed only within a relatively short initial time interval.

We now consider loading by the succession of rarefaction and compression half-waves of the form $p_{ex} = p_f^0 - \Delta p \sin \omega t$. Here, the bubble is excited, in turn, by rarefaction and compression half-waves, the latter of which is not taken into account in relation (4). Having compared curves *2* and *4* (Fig. 1) describing the effect of the rarefaction alone with solid curves *1* and *3* (Fig. 4) corresponding to alternation of the rarefaction with the compression, we can conclude that the compression half-wave following the rarefaction half-wave has an insignificant effect. This conclusion is confirmed as well in Fig. 2, where, in the region $\Delta p < 1.35$ bar, curve *2* taking into account the action of the rarefaction half-wave is only close to curve *3* constructed with allowance for alternation of the rarefaction and compression half-waves. According to Fig. 2, the effect of the compression half-wave grows gradually with increasing Δp.

CONCLUSIONS

1. At the given initial bubble radius r_b^0, an increase in pressure of the amplitude Δp with respect to the average liquid pressure p_l^0 causes higher bubble compression than a decrease in pressure of the same amplitude Δp if $\Delta p < (\Delta p)_{cr}$ or $r_b^0 < (r_b^0)_{cr}$, where $(\Delta p)_{cr}$ and $(r_b^0)_{cr}$ are determined by expressions (7). This conclusion can be drawn from data presented in Figs. 1 and 2.

2. A pressure decrease in the liquid by Δp and its subsequent increase up to the average level under the condition $\Delta p > (\Delta p)_{cr}$ cause strong bubble expansion. In this case, due to subsequent inertial compression of the bubble, maximum values of pressure, density, and temperature attained in it are 10^4, 10^3, and 10 times, respectively, higher than those caused alone by the pressure increase in the liquid by the same Δp. These estimates are obtained under the assumption of volume-uniform adiabatic gas compression. Being carried out for the bubble center with allowance for spherical shock waves, the similar estimation yields 10^8, 10^6, and 10^2, respectively.

3. If pressure in the liquid varies according to the sine law throughout its period, bubble compression increases only a little compared to the case of the rarefaction half-wave. The difference can be noticed only at $\frac{\Delta p}{p_l^0} > 1.4$ (Fig. 2). Therefore, an experimental setup intended for obtaining strong gas compression should mainly provide a decrease in pressure.

For p_l^0 and Δp being higher by some orders of magnitude than those considered above, the item under consideration should be studied additionally.

4. At $r_b^0 < (r_b^0)_{cr}$ and (or) $\Delta p < (\Delta p)_{cr}$, expansion and compression of micron-size bubbles can be approximately determined from the quasi-static equation (5).

ACKNOWLEDGMENTS

This work was supported by the Russian Foundation for Basic Research, project no. 99–01–00234.

We are grateful to I.Sh. Akhatov, R.I. Nigmatulin, V.A. Simonenko, and V.Sh. Shagapov for their participation in discussion of the results.

REFERENCES

1. M. A. Margulis, Usp. Fiz. Nauk **170**, 263 (2000).
2. U. Parlitz, V. Englisch, C. Scheffczyk, and W. Lauterborn, J. Acoust. Soc. Am. **88**, 1061 (1990).
3. R. I. Nigmatulin, I. Sh. Akhatov, N. K. Vakhitova, and R. T. Lahey, J. Fluid Mech. **414**, 47 (2000).
4. A. A. Aganin, R. I. Nigmatulin, M. A. Il'gamov, and I. Sh. Akhatov, Dokl. Akad. Nauk **369**, 182 (1999) [Dokl. Phys. **44,** 734 (1999)].
5. F. G. Blake, Tech. Memo., No. 12 (1949).

Translated by Yu. Verevochkin

Doklady Physics, Vol. 47, No. 1, 2002, pp. 34–38. Translated from Doklady Akademii Nauk, Vol. 382, No. 2, 2002, pp. 181–185.

PHYSICS

Excitation of Singly Charged Yttrium Ions in Electron–Atom Collisions

Yu. M. Smirnov

Presented by Academician V.V. Osiko October 8, 2000

Received May 22, 2001

1. Production of excited ions in electron–atom collisions is a complex process involving the ionization of an atom and the excitation of the ion produced. For these stages to be simultaneous, the incident electron energy must be sufficiently high. This process corresponds to the reaction equation (in the case of single ionization)

$$A + e \longrightarrow A^{+*} + e' + e''. \quad (1)$$

Here, A is an atom; e and e' are incident and scattered electrons, respectively; and e'' is an electron knocked out from the atom. Excited particles are marked by an asterisk.

Processes similar to (1) are of interest for a series of branches of fundamental science (theory of atomic structure, atomic spectroscopy, physics of atomic and electron collisions, astrophysics), as well as for intensely developed intermediate branches at the boundary between fundamental and applied science (lasers, plasma chemistry, special radiation sources). Ionic metal-vapor lasers (MVL) are the most typical example. Principal directions of developing current metal-vapor lasers involve the use of high-temperature active media and the improvement of performance characteristics of MVL, namely, the elevation of their efficiency and output-radiation power, the extension of the range of operating conditions, etc.

All MVL, among them ionic MVL, can be classified according to two basic criteria: the technique of introducing active-medium atoms into the discharge and the method of exciting the atoms. Thermal evaporation is the most evident method of such introduction. However, this method requires the entire discharge tube to be heated up to a sufficiently high temperature. Sometimes, this procedure encounters insurmountable technical difficulties. In order to avoid them, a variety of approaches were proposed. To date, three basic methods for introducing high-temperature atoms into an active volume have been proposed: (1) cathode sputtering (MVL on transitions of copper, silver, gold, etc. [1]), (2) laser evaporation (MVL on transitions of titanium [2], etc.), and (3) the use of metal halides (for example, $MnCl_2$ vapor laser [3]). In the last case, doubled pulses are employed. Namely, the first and second pulses are used, respectively, to dissociate a halide and to excite metal atoms formed by the dissociation. The use of halides instead of pure metals allows the discharge-tube temperature to be lowered by several hundred degrees (for certain compounds, by 1000°C) compared to the evaporation of pure metals.

As to the most advanced methods of exciting ionic MVL, we can refer to (i) hollow-cathode discharge [1, p. 175], (ii) transverse high-frequency discharge [1, p. 194], and (iii) excitation by both transverse and longitudinal electron beams [4]. Longitudinally electron-pumped metal-vapor lasers are rather efficient; however, their realization meets certain technical difficulties that can be overcome by using runaway electrons. In particular, the electron energy can be lowered from several hundred to several kiloelectron-volt. In this case, the longitudinal magnetic field providing the relativistic-beam confinement need not be used. Moreover, difficulties associated with the conjugation of a high-voltage accelerator with a high-temperature laser chamber are eliminated, since the kiloelectron-volt-energy electron beam is formed inside the laser tube. As was concluded in [4, p. 981], the efficiency and the energy release for a kiloelectron-volt electron-pumped laser are tens or hundreds of times as high as those for gas-discharge systems, and such a laser can efficiently operate on atoms and ions within a wide wavelength range.

The presence of fast electrons, whose collisions with atoms of metals are basically responsible for the filling of high-lying laser levels of the ions produced, is a specific feature of all the metal-vapor lasers indicated above. Reference data on atomic constants specifying inelastic electron–atom collisions, including process (1), are urgent for developing and improving ionic metal-vapor lasers. As was pointed out in the reviews [1, 5], there is a considerable deficiency of such data for most atoms and ions. Theoretical calculations of the excitation cross sections for ionic states in process (1) are very laborious. Moreover, as a rule, the accuracy of the

Moscow Power Institute (Technical University), Krasnokazarmennaya ul. 14, Moscow, 111250 Russia

1028-3358/02/4701-0034$22.00

calculation results obtained cannot be determined *a priori*. However, experimental data on the cross sections of simultaneous excitation and ionization for most atoms became available after the method of extended crossed beams had been developed [6]. In the present work, this method was employed for studying the excitation of odd triplet levels of a singly charged yttrium ion in collisions of electrons with yttrium atoms.

2. The technique and instrumentation for the application of extended crossed beams have previously been discussed in a series of papers [6–8]. Thus, a detailed description of these methods seems to be unnecessary in this paper. Below, we point out only basic experimental conditions specific for investigations involving yttrium atoms. In order to produce the atomic beam, we evaporated metallic yttrium with a total impurity content of 0.18% (the basic impurities were Ta, Mo, Cu, Gd, and Tb) from a cup-shaped copper crucible cooled with circulating water. The use of a crucible of the Knudsen cell type turned out to be impossible, because there were no materials sufficiently resistant to the long-term action of melted yttrium. The power needed for melting and evaporation of the yttrium was transported to the metal surface by an electron beam. The temperature of the molten zone was 1870 K. In this case, the concentration of yttrium atoms within the region of intersection for atomic and electron beams was 4.3×10^9 cm^{-3} and could be increased by an order of magnitude when investigating faint lines.

The ground $4d5s^2a^2D$ state of an yttrium atom has two levels with $J = \frac{3}{2}$ and $J = \frac{5}{2}$, the former being the ground level. Under our experimental conditions, the difference 530.5 cm^{-1} in the energy of these levels is on the order of *kT*. Owing to this fact, thermal filling of the level with $J = \frac{5}{2}$ can occur. At the temperature indicated above, in the assumption of thermodynamic equilibrium, the populations estimated for these levels turn out to be equal, because the statistical weight of the higher lying level is greater than that of the lower lying level. This fact was taken into account in theoretical papers by Peterkop that were devoted to calculating excitation cross sections for a series of metal atoms (see, e.g., [9]). This allows the more correct comparison of theoretical and experimental values for the cross sections. The interval between the ground level and the closest higher lying $5s^25pz^2P^\circ_{1/2}$ level attains 10^4 cm^{-1} so that the thermal population of this level is negligibly low. It is worth noting that the population of several low lying atomic levels has been considered to date in none of theoretical papers devoted to studying the process of simultaneous excitation and ionization.

The relative and absolute values of the excitation cross sections for YII are measured with errors from 10 to 15% and ±25 to ±35%, respectively, depending on the spectral-line intensity. The error sources were thoroughly analyzed in [7], where additional information on the experimental conditions was presented. The author of [7] intentionally maintained the experimental conditions as stable as possible in order to provide the more correct comparison of the results obtained for various objects under investigation.

3. We recorded the optical emission spectrum of yttrium atoms within the wavelength range from 212 to 780 nm in the case of bombarding them by a monoenergetic electron beam with an energy of 50 eV. Out of 360 spectral lines observed, almost 120 lines were classified as belonging to the spectrum of a singly charged yttrium ion. Among them, 45 spectral lines lying within the range from 319 to 690 nm arose as a result of the excitation of odd triplet levels of YII. In the case of an even initial level, these levels are excited more efficiently. Moreover, allowed transitions from these levels of YII to the metastable terms a^3P, a^3D, and a^3F take place. Such transitions are of interest from the standpoint of the development of *r–m* lasers [5]. For all these lines, we measured, within the energy range from 0 to 200 eV, the dependence of the excitation cross sections on the energy of incident electrons (i.e., the optical excitation functions).

The measurement results complemented with relevant spectroscopic data are presented in Table 1. There, the wavelength λ, the kind of transition, the total-moment quantum number *J* of the electron shell, the energies E_{low} and E_{up} (with respect to the ground level of a singly charged yttrium ion) of the lower and upper levels, the cross sections Q_{50} and Q_{max} corresponding to the energy of exciting electrons of 50 eV and in the maximum of the optical excitation function (OEF), respectively, and the position $E(Q_{max})$ of the maximum are listed. In the OEF column, the numbers of OEFs are indicated in accordance with their numbering in Fig. 1. Each OEF is normalized to unity in its maximum and has an individual origin on the ordinate axis. The scales for the abscissa and ordinate axes are linear and logarithmic, respectively.

In the case of a singly charged yttrium ion, the four odd triplet terms, z^3P°, z^3D°, z^3F°, and y^3P°, within the range from 23400 to 32300 cm^{-1} have a fairly low energy for its excitation from the $5s^2a^1S_0$ ground state. The first term and the following three terms belong to the $5s5p$ and $4d5p$ configurations, respectively. The configuration mixing for all the levels under consideration is rather weak. Namely, the least content of the basic component amounts to 74% for the $z^3F^\circ_2$ level, while the content of the same component for the $z^3F^\circ_4$ level attains 100% [10, p. 256]. The higher lying $4d6p^3D^\circ$ triplet state closest to these terms corresponds to 64000 cm^{-1}, and no radiative transitions from this state were observed in this study.

The scheme of the low lying triplet states of YII together with the transitions observed is presented in

Table 1. Excitation cross sections for a singly charged yttrium ion

λ, nm	Transition	J	E_{low}, cm^{-1}	E_{up}, cm^{-1}	Q_{50}, 10^{-18} cm^2	Q_{max}, 10^{-18} cm^2	$E(Q_{max})$, eV	OEF
319.561	a^3D–$y^3P°$	1–1	840	32124	2.00	2.32	34	5
320.027	a^3D–$y^3P°$	2–2	1045	32283	2.34	2.76	36	6
320.332	a^3D–$y^3P°$	1–0	840	32048	3.24	3.81	32	4
321.668	a^3D–$y^3P°$	2–1	1045	32124	4.28	4.97	34	5
324.227	a^3D–$y^3P°$	3–2	1449	32283	7.20	8.48	36	6
349.608	a^1S–$z^3D°$	0–1	0	28595	1.09	1.21	35	7
354.900	a^3D–$z^3D°$	2–3	1045	29213	1.73	1.82	40	9
358.451	a^3D–$z^3D°$	1–2	840	28730	1.65	1.90	36	8
360.073	a^3D–$z^3D°$	3–3	1449	29213	4.93	5.19	40	9
360.192	a^3D–$z^3D°$	1–1	840	28595	3.82	4.24	35	7
361.104	a^3D–$z^3D°$	2–2	1045	28730	4.15	4.77	36	8
362.870	a^3D–$z^3D°$	2–1	1045	28595	1.30	1.45	35	7
366.461	a^3D–$z^3D°$	3–2	1449	28730	2.00	2.30	36	8
371.029	a^3D–$z^3F°$	3–4	1449	28394	10.2	12.0	37	2
377.433	a^3D–$z^3F°$	2–3	1045	27532	7.88	9.27	37	11
378.869	a^3D–$z^3F°$	1–2	840	27227	5.46	6.00	37	10
381.834	a^3D–$z^3F°$	2–2	1045	27227	1.55	1.71	37	10
383.289	a^3D–$z^3F°$	3–3	1449	27532	2.18	2.56	37	11
387.828	a^3D–$z^3F°$	3–2	1449	27227	0.49	0.54	37	10
393.066	a^1D–$z^3D°$	2–2	3296	28730	0.87	1.00	36	8
395.159	a^1D–$z^3D°$	2–1	3296	28595	0.34	0.38	35	7
412.490	a^1D–$z^3F°$	2–3	3296	27532	0.39	0.46	37	11
417.753	a^1D–$z^3F°$	2–2	3296	27227	2.04	2.24	37	10
419.927	a^3D–$z^3P°$	1–2	840	24647	0.57	0.60; 0.60	34; 44	3
420.469	a^1S–$z^3P°$	0–1	0	23776	0.95	1.09	35	2
423.573	a^3D–$z^3P°$	2–2	1045	24647	3.67	3.87; 3.87	34; 44	3
430.962	a^3D–$z^3P°$	3–2	1449	24647	6.76	7.11; 7.11	34; 44	3
435.872	a^3D–$z^3P°$	1–1	840	23776	2.04	2.34	35	2
439.801	a^3D–$z^3P°$	2–1	1045	23776	3.31	3.80	35	2
442.258	a^3D–$z^3P°$	1–0	840	23445	1.81	2.35	30	1
468.232	a^1D–$z^3P°$	2–2	3296	24647	0.81	0.85; 0.85	34; 44	3
478.658	a^3F–$z^3D°$	3–3	8328	29213	0.51	0.55	40	9
485.486	a^3F–$z^3D°$	2–1	8003	28595	1.03	1.14	35	7
488.368	a^3F–$z^3D°$	4–3	8743	29213	1.86	1.96	40	9
490.012	a^3F–$z^3D°$	3–2	8328	28730	1.56	1.79	36	8
508.742	a^3F–$z^3F°$	4–4	8743	28394	0.84	0.98	37	12
520.041	a^3F–$z^3F°$	2–2	8003	27227	0.30	0.33	37	10
520.572	a^3F–$z^3F°$	3–3	8328	27532	0.67	0.79	37	11
532.078	a^3F–$z^3F°$	4–3	8743	27532	0.25	0.29	37	11
549.740	a^3P–$y^3P°$	2–2	14098	32283	0.66	0.78	36	6
554.461	a^3P–$y^3P°$	1–0	14018	32048	0.26	0.31	32	4
661.373	a^3P–$z^3D°$	2–3	14098	29213	0.84	0.89	40	9
679.541	a^3P–$z^3D°$	1–2	14018	28730	0.81	0.93	36	8
685.822	a^3P–$z^3D°$	1–1	14018	28595	0.20	0.22	35	7
689.598	a^3P–$z^3D°$	2–1	14098	28595	0.31	0.35	35	7

Fig. 2, the term splitting being not shown. A singly charged yttrium ion has the low lying even (metastable) $4d5sa^1D_2$, $4d5sa^3D$, $4d^2a^3P$, and $4d^2a^3F$ states and also three singlet levels with the $4d^2$ configuration within the energy range from 14800 to 25100 cm^{-1}. The $5s5pz^3P_1^\circ$ level would be expected to be combined with the $5s^2a^1S_0$ ground level, even though the multiplicity would change, because the $5p \longrightarrow 5s$ transition occurs in this case. The $5s^2a^1S_0$–$4d5pz^3D_1^\circ$ transition is seemingly significantly less probable, since it occurs as a two-electron $4d5p \longrightarrow 5s^2$ transition and, moreover, it is a transition accompanied by a change of the multiplicity and has $\Delta L = -2$. Nevertheless, the excitation cross section for this transition turns out to be even slightly larger than that for the former and less highly forbidden transition. On the other hand, the transitions from all the odd triplet levels under consideration to $4d5sa^3D$ levels are quite allowed transitions, because they correspond to $5p \longrightarrow 4d$ and $5p \rightarrow 5s$ transitions for the higher lying z^3P° term and for the following three terms, respectively. Indeed, as is seen from Table 1, the largest from measured cross sections exactly corresponds to transitions to a^3D levels. Transitions to both a^3P and a^3F levels are characterized by slightly smaller excitation cross sections, because the $5p \longrightarrow 4d$ transition is less probable than the $5p \longrightarrow 5s$ transition.

Experiments based on observation of the optical radiation of excited atoms make it possible to directly measure the excitation cross sections Q_{ki} for spectral lines. However, a different quantity, namely, the excitation cross section q_k for an energy level, is used in theory and in many practical applications. The relation between these quantities has the form

$$q_k = \sum Q_{50} - \sum Q' \qquad (2)$$

where $\sum Q_{50}$ is the total cross section of the spontaneous radiative transitions from a k level and $\sum Q'$ is the total cross section of the cascade transitions to the k level from all higher lying levels. In the present paper, all the cross-section values correspond to an electron energy of 50 eV.

The data on the excitation cross sections for the spectral lines listed in Table 1 were used to calculate q_k according to relationship (2). We do not present here cumbersome information related to the individual cross sections for each of the cascade transitions. The results obtained are listed in Table 2, in which $\frac{\sum Q'}{\sum Q_{50}}$ is the contribution (percent) into the total cross section for each of the levels under consideration. As is seen, this contribution ranges from 13 to 59%. The $z^3P_0^\circ$ level is the only exception for which the contribution of the

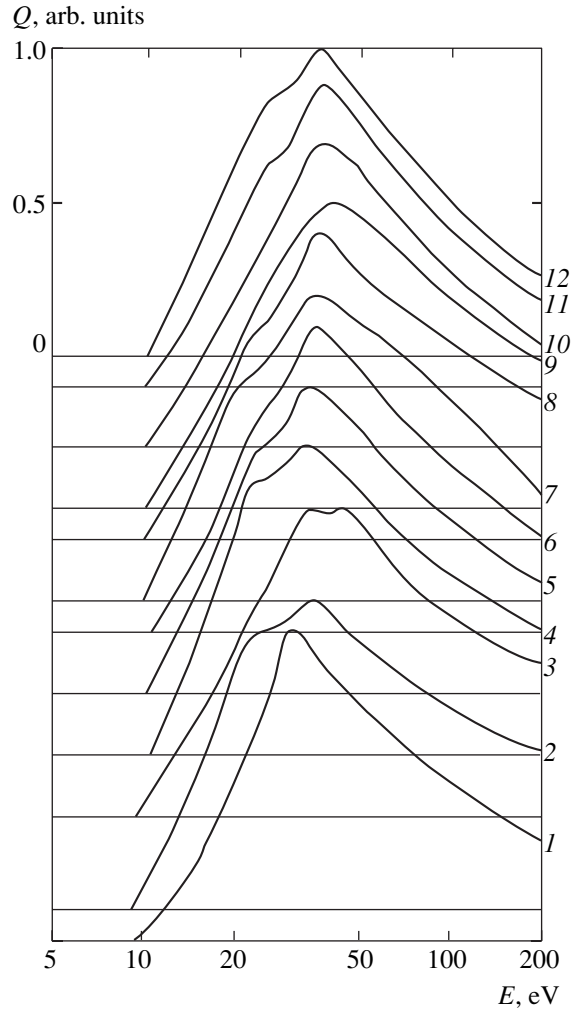

Fig. 1. Optical excitation functions for YII.

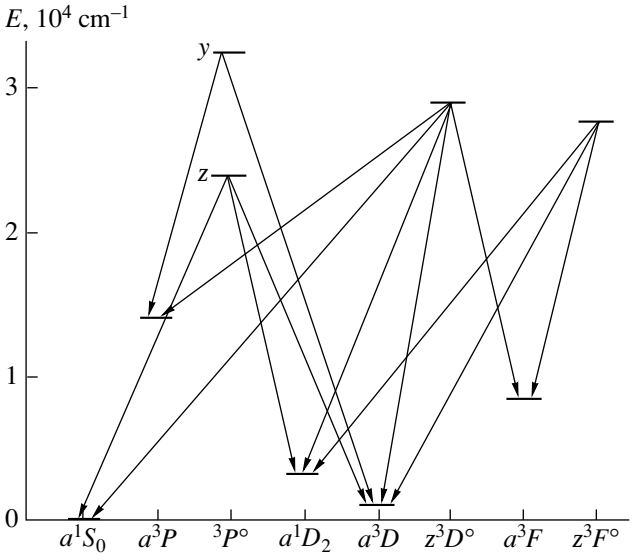

Fig. 2. Scheme of the triplet states of YII and the transitions observed.

Table 2. Excitation cross sections for the energy levels of YII and the cascade-filling contribution

Level	J	E_{up}, cm^{-1}	$\sum Q_{50}$, 10^{-18} cm^2	$\sum Q'$, 10^{-18} cm^2	q_k, 10^{-18} cm^2	$\frac{\sum Q'}{\sum Q_{50}}$, %
$5s5p\ z\ ^3P°$	0	23445	1.81	2.02	(–0.21)	112.0
	1	23776	6.30	3.53	2.77	56.0
	2	24647	11.8	5.99	5.81	50.7
$4d5p\ y^3P°$	0	32048	3.50		3.50	
	1	32124	6.28	1.34	4.94	21.4
	2	32283	10.20	6.01	4.19	59.0
$4d5p\ z^3D°$	1	28595	8.09	2.71	5.38	33.5
	2	28730	11.04	2.64	8.40	23.9
	3	29213	9.87	4.82	5.05	48.8
$4d5p\ z^3F°$	2	27227	9.84	1.79	8.05	18.2
	3	27532	11.37	1.52	9.85	13.4
	4	28394	11.04	3.43	7.61	31.1

cascade transitions slightly exceeds the total measured excitation cross section. The main reason for this anomaly is that we have not determined the cross section of the relatively strong a^3P_1–$z^3P_0^\circ$ transition with a wavelength of 1.06 nm, which could not be observed under the experimental conditions of the present work.

4. Thus, we have obtained experimental data concerning the cross sections for the electron-impact excitation of the odd triplet levels of YII and certain features in the behavior of these cross sections. The results presented in this paper can be used for calculating and estimating characteristics of plasmas containing yttrium and its compounds, as well as for solving other problems of fundamental physics.

REFERENCES

1. I. G. Ivanov, E. L. Latush, and M. F. Sem, *Ion Lasers Operating on Metal Vapors* (Énergoatomizdat, Moscow, 1990).
2. H. Ninomiya and K. Hirata, J. Appl. Phys. **66**, 2219 (1989).
3. V. K. Isakov, M. M. Kalugin, and S. E. Potapov, Pis'ma Zh. Tekh. Fiz. **2**, 747 (1976) [Tech. Phys. Lett. **2**, 292 (1976)].
4. S. V. Arlantsev, B. L. Borovich, V. V. Buchanov, and N. I. Yurchenko, Kvant. Élektronika **23** (11), 977 (1996).
5. G. G. Petrash, Izv. Vyssh. Uchebn. Zaved., Fiz., No. 8, 18 (1999).
6. Yu. M. Smirnov, *Physics of Electron and Atomic Collisions* (Izd. Fiz. Tekhn. Inst. Akad. Nauk SSSR, Leningrad, 1985).
7. Yu. M. Smirnov, J. Phys. II (France) **4** (1), 23 (1994).
8. Yu. M. Smirnov, Dokl. Ross. Akad. Nauk **359**, 610 (1998) [Phys. Dokl. **42**, 173 (1998)].
9. R. K. Peterkop, Izv. Akad. Nauk Latv. SSR, Ser. Fiz. Tekh. Nauk, No. 4, 3 (1988).
10. A. E. Nilsson, S. Johansson, and R. L. Kurucz, Phys. Scr. **44** (3), 226 (1991).

Translated by V. Chechin

Doklady Physics, Vol. 47, No. 1, 2002, pp. 39–43. Translated from Doklady Akademii Nauk, Vol. 382, No. 3, 2002, pp. 320–324.

PHYSICS

Electrokinetic and Magnetic Properties of Cubic Titanium Monoxide with a Double-Defect Structure

A. A. Valeeva, A. A. Rempel', and A. I. Gusev

Presented by Academician G.P. Shveĭkin May 30, 2001

Received June 7, 2001

Titanium monoxide TiO_y cubic ($B1$-type) basis structure is a unique compound that has no analogs. Possessing a wide region of homogeneity from $TiO_{0.70}$ to $TiO_{1.25}$, TiO_y monoxide contains from 10 to 15 at. % of structural vacancies in titanium and oxygen sublattices. We can understand the actual structure of titanium monoxide representing its content with allowance for structural vacancies in each of the sublattices, i.e., in the form of $Ti_xO_z \equiv TiO_y$ or $Ti_x\blacksquare_{1-x}O_z\square_{1-z} \equiv TiO_y$, where $y = z/x$, □ and ■ are the structural vacancies of oxygen and titanium sublattices, respectively. Even $TiO_{1.00}$ monoxide, which formally has a stoichiometric composition, contains of 16.7 at.% vacancies in the titanium and oxygen sublattices; therefore, its actual content is $\sim Ti_{0.833}O_{0.833}$.

Synthesis of TiO_y monoxide is a complicated problem, inasmuch as its content is already unstable at 700–800 K. Even under controllable partial oxygen pressure, it can disproportionate with the formation of Ti_2O ($TiO_{0.50}$) or of Ti_3O_2 ($TiO_{0.67}$) and a cubic oxide or of cubic dioxide and Ti_2O_3 ($TiO_{1.50}$), as well as of other phases of Ti_nO_{2n-1} homologous series ($n = 2 - 10$ is an integer). At temperatures ~700, ~1000, and ~1100 K, various superstructures are formed in TiO_y. Only four of them are reliably described in the literature. The type and symmetry of superstructures depend on the actual initial content of titanium monoxide. The temperature measurements of kinetic and magnetic properties of TiO_y, which had been carried out in the 1960s and 1970s, showed that the chemical and phase content changed in the course of the measurements. This fact caused ambiguity in the results obtained. For example, the temperature coefficient $d\rho/dT$ of the resistivity ρ for disordered TiO_y monoxide with $y \approx 1$ is positive in certain studies [3–5] and negative in [6]. An experimental result with which all the authors agree is the negative sign of both the thermal electromotive force and Hall coefficient for TiO_y with $y > 0.85$ [3–6]. Unreliability of experimental data has caused the appearance of a number of papers devoted to the calculation of the TiO_y electronic structure. But the calculation results, among them those based on the first principles, are also contradictory. According to [7–10], O2p- and Ti3d-bands in the electronic energy spectrum of the cubic titanium monoxide are separated by a broad (several electronvolts) forbidden gap. The presence of the gap is confirmed by experimental studies of X-ray photoemission spectra, bremsstrahlung spectra, and UV photoemission spectra [9] of disordered TiO_y monoxide. However, according to the results of another group of calculations [11–13], there exists no p–d gap in the TiO_y electronic spectrum.

Thus, the experimental and theoretical data are contradictory, and it is unclear up to now whether titanium monoxide exhibits metallic or semiconductor properties.

In this paper, experimental results are obtained for the first time on the electrical conductivity (resistivity) and magnetic susceptibility of TiO_y monoxide within the entire homogeneity region of the cubic phase.

The samples of the nonstoichiometric cubic TiO_y monoxide with various oxygen contents ($0.920 \le y \le 1.262$) were synthesized by the solid-phase sintering of powder mixtures of metallic titanium and titanium dioxide in vacuum (at a pressure of 0.0013 Pa and temperature of 1770 K) for 70 h. The diffraction analysis was performed with the $CuK_{\alpha_{1,2}}$-emission line on the basis of Siemens D-500 and STADI-P (STOE) automated diffractometers. In order to attain the disordered state, the samples synthesized were annealed for 3 h in evacuated quarts ampoules at a temperature of 1330 K. Then, the ampoules with the samples were thrown into water so that the quenching rate was ~200 K s^{-1}. The reflections of only the cubic disordered TiO_y phase with a $B1$ structure (in the samples with $y \ge 1.112$) or the reflections of the disordered TiO_y and of the monoclinic ordered Ti_5O_5 phase [14] (in the samples with $y \le 1.087$) were observed on the X-ray diffraction patterns.

Institute of Solid-State Chemistry, Ural Division, Russian Academy of Sciences, ul. Pervomaĭskaya 91, GSP-145, Yekaterinburg, 620219 Russia

1028-3358/02/4701-0039$22.00

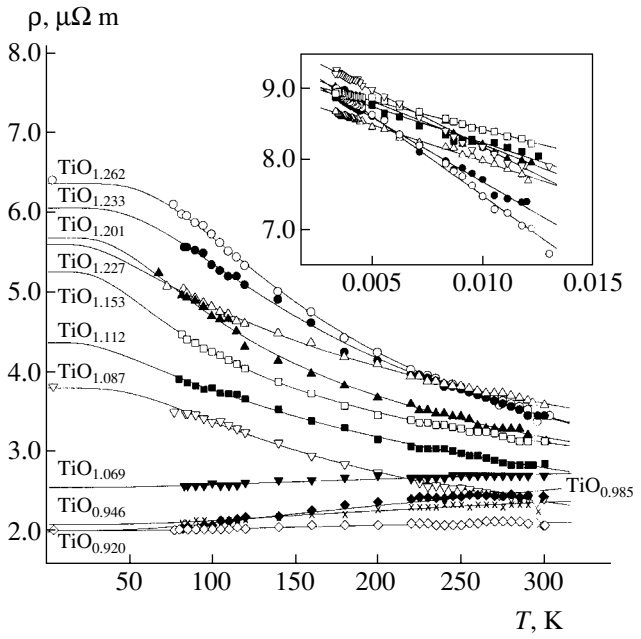

Fig. 1. Temperature dependence of the resistivity ρ for the disordered cubic TiO_y monoxides with various oxygen content. The approximations of experimental results by function (2) for TiO_y monoxides with $y \le 1.069$ and by function (7) for TiO_y monoxides with $y \ge 1.087$ are shown by solid lines. In the insert, the temperature dependence for the conductivity of $TiO_{1.262}$–$TiO_{1.087}$ monoxides is plotted in the coordinates $\ln\{[\sigma(T) - \sigma(0)]/T^{1/2}\} - 1/T$.

The resistivity ρ was measured by the four-probe method within the range 77 to 300 K; the resistivity of $TiO_{1.262}$, $TiO_{1.087}$, and $TiO_{0.920}$ was also measured at 4.2 K. An In–Ga paste was applied to the contact sample surfaces to provide reliability of electrical contact.

The magnetic susceptibility χ of the TiO_y monoxide ($0.920 \le y \le 1.262$) was measured within the temperature range from 4 to 400 K in the magnetic fields with an intensity of 8.8, 25, 30, and 50 kOe, using a MPMS-XL-5 (Quantum Design) vibrating-coil magnetometer. In addition, the susceptibility of $TiO_{0.946}$, $TiO_{1.069}$, $TiO_{1.087}$, and $TiO_{1.262}$ was measured within the temperature interval from 300 K up to the temperature of the disorder ⟷ order transition onset (about 1000 K) by the Faraday method, using a pendulum magnetic balance of the Domenicalli type.

The chemical and phase content of the samples was controlled before and after the measurements.

The measurements of TiO_y magnetization in magnetic fields with an intensity up to 50 kOe at temperatures of 4, 130, and 300 K show that the samples of titanium monoxide studied exhibit no residual magnetization and contain no ferromagnetic impurities.

The temperature dependences of the resistivity $\rho(T)$ for TiO_y titanium monoxide of various contents are shown in Fig. 1. Within the temperature range under study, the resistivity ρ increases as a result of the transition from $TiO_{0.920}$ to $TiO_{1.262}$.

The resistivities of $TiO_{1.069}$, $TiO_{0.985}$, $TiO_{0.946}$, and $TiO_{0.920}$ increase with temperature, although the resistance temperature coefficient is small. In materials with electronic conduction within the range $T < 300$ K, the temperature dependence of the mean free time $\bar{\tau}$ associated with scattering by phonons is well described by the semiempirical Bloch–Grüneisen formula

$$\frac{1}{\bar{\tau}} = \frac{4\pi\lambda k_B \theta_D}{\hbar}\left(\frac{2T}{\theta_D}\right)^5 \int_0^{\theta_D/2T} \frac{x^5 dx}{\sinh^2 x}. \quad (1)$$

Here, λ is the constant of the electron–phonon interaction and θ_D is the characteristic Debye temperature. Since the resistivity is $\rho = m/ne^2\bar{\tau}$, the temperature dependence of the resistivity with allowance for the residual resistivity $\rho(0)$ can be represented as

$$\rho(T) = \rho(0) + \frac{4\pi m\lambda k_B \theta_D}{ne^2\hbar}\left(\frac{2T}{\theta_D}\right)^5 \int_0^{\theta_D/2T} \frac{x^5 dx}{\sinh^2 x}$$
$$\equiv \rho(0) + \frac{4\pi m\lambda k_B \theta_D}{ne^2\hbar}\left(\frac{2T}{\theta_D}\right)^5 \quad (2)$$
$$\times \left[-\left(\frac{\theta_D}{2T}\right)^5 \coth\left(\frac{\theta_D}{2T}\right) + 5\int_0^{\theta_D/2T} x^4 \coth x dx\right].$$

In various temperature ranges, the integral in relation (2) has various forms. For $T < 80$ K and $\theta_D \sim 400$–500 K, $\theta_D/2T > 3.14$; in this case the integral $\int_0^{\theta_D/2T} (x^5/\sinh^2 x)dx$ is calculated as

$$\int_0^{\theta_D/2T} \frac{x^5 dx}{\sinh^2 x} = x^5(1 - \coth x)\Big|_0^{\theta_D/2T}$$
$$+ 10\int_0^{\theta_D/2T} x^4[\exp(-2x) + \exp(-4x)$$
$$+ \ldots + \exp(-2nx)]dx.$$

At $T > 80$ K and $\theta_D \sim 400$–500 K, $\theta_D/2T < 3.14$ and, therefore, the integral $\int_0^{\theta_D/2T} x^4 \coth x dx$ is found as a series

$$\int_0^{\theta_D/2T} x^4 \coth x dx = \sum_{k=0}^{\infty} 2^{2k} B_{2k} x^{4+2k}/[(4 + 2k)(2k)!],$$

where B_{2k} are the Bernoulli numbers.

Experimental dependences $\rho(T)$ for $TiO_{1.069}$, $TiO_{0.985}$, $TiO_{0.946}$, and $TiO_{0.920}$ oxides are well approximated by function (2) (Fig. 1), the value of θ_D being equal to 480, 400, 470, and 470 K, respectively. According to the data of [4], θ_D = 350–410 K for equiatomic $TiO_{1.00}$ monoxide and increases with a decrease in the annealing temperature. For the ordered monoclinic Ti_2O_5 monoxide, θ_D = 500 K [10].

The resistivity of TiO_y monoxides with $y \geq 1.087$ decreases very rapidly with a temperature increase from 4.2 to 300 K. A small resistivity value ($\sim 10^{-6}$ Ω m) for all titanium monoxides is characteristic for metals, whereas the negative temperature coefficient $d\rho/dT$ of the resistivity for TiO_y monoxides with $y \geq 1.087$ is one of the main attributes of the dielectric behavior. Within the range 4.2–300 K, the change of resistivity caused by this effect is $\Delta\rho$ = 20–50%. This fact makes it impossible to consider $\Delta\rho$ as a small correction in the relaxation-time approximation.

The conductivity σ is proportional to the product of the carrier concentration N multiplied by their mobility u; i.e.,

$$\sigma(T) = en_{e,h}(u_e + u_h). \quad (3)$$

If the carriers obey the Boltzmann statistics and the energy bands are parabolic, which is practically valid near the band edges [15], the carrier concentration is

$$n_e = 2(m^*)^{3/2}(k_B T/2\pi\hbar^2)^{3/2}\exp(-\Delta E/2k_B T), \quad (4)$$

where m^* is the effective mass of the charge carriers; ΔE is the energy parameter, which has a meaning of the activation energy and, in the case of intrinsic conduction, is equal to the energy gap E_g between the valence band and the conduction band. In the case of the Boltzmann distribution, the carrier mobility is inversely proportional to the temperature:

$$u \sim AT^{-p}. \quad (5)$$

Since all the samples of titanium monoxide have a nonzero residual resistivity, we can represent, with allowance for (4) and (5), the conductivity of TiO_y ($y \geq 1.087$) oxides in the form

$$\sigma(T) = \sigma(0) + 2(k_B m/2\pi\hbar^2)^{3/2}T^{(3/2-p)}\exp(-\Delta E/2k_B T). \quad (6)$$

The constant contribution $\sigma(0)$ has a meaning of the nonintrinsic conductivity of the system and implies that the conductivity is nonzero at T = 0 K.

The numerical analysis of experimental dependences $\sigma(T)$ shows that they are well described by function (6) with $p \approx 1$; i.e.,

$$\sigma(T) = \sigma(0) + BT^{1/2}\exp(-\Delta E/2k_B T). \quad (7)$$

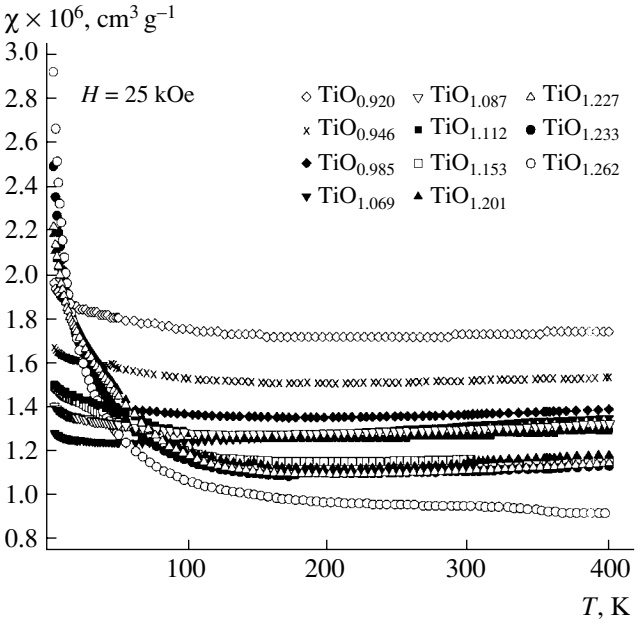

Fig. 2. Magnetic susceptibility χ of disordered cubic TiO_y monoxides with a various oxygen content within the temperature range from 4.2 to 400 K (H = 25 kOe).

The parameter p = 1 is characteristic for polyatomic semiconductors in which scattering occurs not only by acoustic phonons but also by optical phonons.

The representation of the temperature-dependent contribution to conductivity (7) for TiO_y ($y \geq 1.087$) monoxides in the coordinates $\ln\{[\sigma(T) - \sigma(0)]/T^{1/2}\} - 1/T$ (see insert in Fig. 1) shows that the linear dependence is observed in the entire temperature range under study. The activation energy ΔE for the monoxides from $TiO_{1.087}$ to $TiO_{1.233}$ is small and equals 0.015–0.030 eV. It equals 0.043 eV only for $TiO_{1.262}$. If the intrinsic conduction appears near 300 K and above, we cannot definitely claim whether the value found for ΔE is the forbidden gap of the semiconductor in itself or is the activation energy of the impurity level. Analysis of the magnetic susceptibility allows us to elucidate this question.

Two regions with an opposite change of the quantity χ as a function of temperature can be separated in $\chi(T)$ temperature curves for all TiO_y samples (Figs. 2 and 3). The decrease in the susceptibility at T < 150–200 K is characteristic for the paramagnetic contribution, which is described by the modified Curie law $\chi(T) = \chi(0) + C/(T + \Delta)$ with the temperature-independent paramagnetic contribution $\chi(0)$ and $\Delta > 0$. At temperatures above 150–200 K the susceptibility $\chi(T)$ along with the contribution $\chi(0) + C/(T + \Delta)$ also includes a quadratic or more complicated temperature function.

The Curie paramagnetism per unit volume of the material is equal to $\chi_V = Nn\mu_{eff}^2/3k_B T$, where N is the number of atoms per unit volume, n is the relative concentration of atoms having the magnetic moment, μ_{eff} =

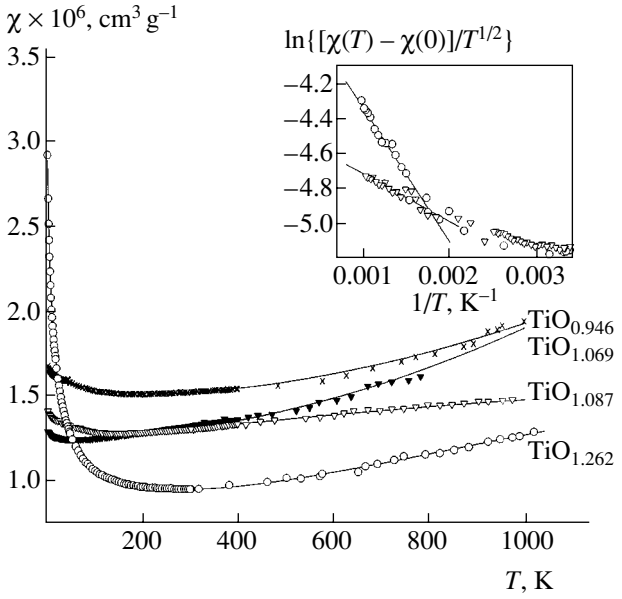

Fig. 3. Magnetic susceptibility of $TiO_{0.946}$, $TiO_{1.069}$, $TiO_{1.087}$, and $TiO_{1.262}$ monoxides within the temperature range from 4.2 K to the temperature of the disorder ↔ order transition onset (near 1000 K). The dependence $\chi(T)$ is described by the functions: $TiO_{0.946}$ – $\chi(T) \times 10^6 = 1.410 + 22.9/(T + 88.6) + 4.930 \times 10^{-7}T^2$; $TiO_{1.069}$ – $\chi(T) \times 10^6 = 1.237 + 0.54/(T + 8.5) + 6.591 \times 10^{-7}T^2$; $TiO_{1.087}$ – $\chi(T) \times 10^6 = 1.196 + 0.012T^{1/2}\exp(-353/T) + 14.9/(T + 71.8)$, $\Delta E = 0.061$ eV; $TiO_{1.262}$ – $\chi(T) \times 10^6 = 0.847 + 0.034T^{1/2}\exp(-1004/T) + 24.1/(T + 7.8)$, $\Delta E = 0.173$ eV.

$p\mu_B$ is the effective magnetic moment, and μ_B is the Bohr magneton. Since $N = N_A d/M$ (N_A is Avogadro's number, d is the density, and M is the molecular mass), the measured magnetic susceptibility per mass unit is $\chi = \chi_V/d = (nN_A/M)(p\mu_B)^2/(3k_BT) \equiv C/T$, whence $p^2 = (CM/n)(3k_B/N_A\mu_B^2)$ or, with allowance for values of N_A, μ_B, and k_B, $p \approx \sqrt{8CM/n}$, the Curie constant C having the dimensionality $cm^3\ K\ g^{-1}$. If the concentration of atoms n that have a magnetic moment is unknown, then the average magnetic moment is $p_{aver} \approx \sqrt{8CM}$.

The calculations using the determined values of the constant C have shown that the magnitude of the magnetic moment μ_{eff} averaged over all atoms is 0.015–0.225 of Bohr magneton. The low magnitude of μ_{eff} is indicative of the fact that the Curie contribution into the susceptibility is, most probably, of impurity origin. In TiO_y monoxide, the majority of Ti^{2+} ions likely have paired electrons, or else there exists the exchange cation–cationic interaction. By virtue of a high concentration of delocalized electrons, we did not succeed in determining the presence in TiO_y monoxide of ions with an uncompensated magnetic moment by the EPR method. Since the ferromagnetic impurities in TiO_y samples are absent, the presence of a small effective magnetic moment can be caused by Ti^{2+} and Ti^{3+} ions having an impurity nature. The content of such impurity ions, judging from the value of p, ranges from 2 to 8 at. %. Most distinctly, the Curie paramagnetism is observed for TiO_y titanium monoxides with a relatively high oxygen content $y > 1.2$ (Fig. 3).

The dependence $\chi(T)$ of TiO_y titanium monoxides with $y \le 1.069$ (Fig. 3) in the entire temperature range under study is described well by the function $\chi(T) = \chi(0) + C/(T + \Delta) + bT^2$. The presence of the quadratic term bT^2 is characteristic for the Pauli paramagnetism of conduction electrons, which agrees well with the metallic type of conduction for these monoxides.

The temperature dependences of the susceptibility for monoxides TiO_y with $y \ge 1.087$ are more complicated, which is clearly distinguishable in the high-temperature region (Fig. 3). If the charge-carrier concentration in TiO_y with $y \ge 1.087$ at $T > 300$ K is described by formula (4), then, in this case, in agreement with the Curie formula $\chi_p(T) = n_e(\mu_B)^2/k_BT$, the fraction of the magnetic susceptibility dependent on temperature will have a paramagnetic contribution

$$\chi_p(T) = 2(m^*/2\pi\hbar^2)^{3/2}(k_B)^{1/2}(\mu_B)^2T^{1/2} \times \exp(-\Delta E/2k_BT) \equiv AT^{1/2}\exp(-\Delta E/2k_BT), \quad (8)$$

where $A = 2(m_0/2\pi\hbar^2)^{3/2}(k_B)^{1/2}(\mu_B)^2q^{3/2} = 3.008 \times 10^{-9}q^{3/2}$ [$K^{-1/2}$], $q = m^*/m_0$, and m_0 is the electron mass. Formula (8) describes the dimensionless susceptibility per unit volume. Taking into account that $A_m = A/d$ and also the features of $\chi(T)$ dependences that were indicated above, we may approximate within the entire temperature range under study the mass susceptibility of TiO_y monoxides with $y \ge 1.087$ by the function

$$\chi(T) = \chi(0) + A_mT^{1/2}\exp(-\Delta E/2k_BT) + C/(T + \Delta). \quad (9)$$

This function takes into account the temperature-independent contribution of $\chi(0)$, the paramagnetic Pauli contribution for the electron system with the energy gap, and the paramagnetic Curie contribution.

The coefficients A_m in dependence (9) for $TiO_{1.087}$ and $TiO_{1.262}$ monoxides are 0.012×10^{-6} and 0.034×10^{-6} $cm^3\ g^{-1}\ K^{-1/2}$; the densities of $TiO_{1.087}$ and $TiO_{1.262}$ are 4.97 and 4.82 g cm^{-3}. The effective mass of carriers expressed in terms of m_0 is equal to $m^* = 4.799 \times 10^5(A_md)^{2/3}m_0$. With allowance for this fact, the effective mass of carriers in $TiO_{1.087}$ and $TiO_{1.262}$ is equal to $\sim 7m_0$ and $\sim 14m_0$. A rather large effective mass confirms the correctness in the application of the Boltzmann distribution for the description of carrier concentration in TiO_y monoxides with $y \ge 1.087$.

The values of ΔE found from the $\chi(T)$ curves (9) for $TiO_{1.087}$ and $TiO_{1.262}$ monoxides are equal to 0.061 and

0.173 eV. The values of ΔE determined for these monoxides from the temperature dependences of the conductivity are 0.029 and 0.043 eV. We may assume that the values of ΔE found from the low-temperature dependences of the conductivity correspond to the activation energy of impurity levels, whereas the values of ΔE derived for the wider temperature range from the magnetic susceptibility define the forbidden gap in the case of the intrinsic conduction. The small magnitude of the forbidden gap allows us to consider the TiO_y titanium monoxide with $y \geq 1.087$ as a narrow-gap semiconductor.

Thus, the totality of the kinetic and magnetic data obtained allows us to assume that with elevation of the oxygen content in the electronic structure of the disordered cubic TiO_y, a narrow gap appears between the valence band and the conduction band. In accordance with this conclusion and depending on the oxygen content, TiO_y monoxide can behave as a *d*-metal or as a semiconductor.

ACKNOWLEDGMENTS

The authors are grateful to N.A. Kirsanov, A.V. Korolev, and R. Henes for their help in performing the experiment.

REFERENCES

1. A. I. Gusev and A. A. Rempel', *Structural Phase Transitions in Nonstoichiometric Compounds* (Nauka, Moscow, 1988).
2. A. I. Gusev and A. A. Rempel', *Nonstoichiometry, Disorder and Order in Solids* (Ural. Otd. Ross. Akad. Nauk, Yekaterinburg, 2001).
3. A. D. Pearson, J. Phys. Chem. Solids **5**, 316 (1958).
4. S. P. Denker, J. Appl. Phys. **37**, 142 (1966).
5. M. I. Aĭvazov, I. A. Domashnev, A. G. Sarkisyan, and T. V. Rezchikova, Izv. Akad. Nauk SSSR, Neorg. Mater. **6**, 745 (1970).
6. M. D. Banus, T. B. Reed, and A. J. Strauss, Phys. Rev. B. **5**, 2775 (1972).
7. M. Schoen and S. P. Denker, Phys. Rev. **184**, 864 (1969).
8. A. Neckel, Intern. J. Quantum. Chem. **23**, 1317 (1983).
9. S. R. Barman and D. D. Sarma, Phys. Rev. B **49**, 16141 (1994).
10. C. Leung, M. Weinert, P. B. Allen, and R. M. Wentzcovitch, Phys. Rev. B **54**, 7857 (1996).
11. D. R. Jennison and A. B. Kunz, Phys. Rev. Lett. **39**, 418 (1977).
12. J. K. Burdett and T. Hughbanks, J. Am. Chem. Soc. **106**, 3101 (1984).
13. G. Hobiger, P. Herzig, R. Eibler, *et al.*, J. Phys.: Condens. Matter **2**, 4595 (1990).
14. A. A. Valeeva, A. A. Rempel', and A. I. Gusev, Pis'ma Zh. Éksp. Teor. Fiz. **71**, 675 (1990) [JETP Lett. **71**, 460 (2000)].
15. I. M. Tsidil'kovskiĭ, *Zero-Gap Semiconductors: A New Class of Materials* (Nauka, Moscow, 1986).

Translated by T. Galkina

Doklady Physics, Vol. 47, No. 1, 2002, pp. 44–46. Translated from Doklady Akademii Nauk, Vol. 382, No. 3, 2002, pp. 325–328.

PHYSICS

Thermooptical Excitation of Plate Vibration by Modulated Radiation of an Unstable-Cavity Laser

M. L. Lyamshev

Presented by Academician F.V. Bunkin May 17, 2001

Received June 26, 2001

In recent years, much attention was paid to investigating the chaotic generation of lasers. For example, scenarios and characteristics of chaotic generation in an unstable cavity of a fast-flow laser with spatially inhomogeneous pumping were studied in [1]. A scheme of optical information chaos on the basis of lasers that synchronously operate in a chaotic regime with chaotic pumping was considered in [2]. Both scaling and fractal dimension are important characteristics of nonlinear systems with dynamic chaos [3]. The existence of scaling properties for harmonic radiation in laser plasmas under the action of high-power pumping was indicated in [4]. The mode structure for the radiation of an unstable-cavity laser was demonstrated to be fractal [5]. The fractal dimensions of the radiation-intensity distribution for lasers with narrow slit-shaped and circular apertures were found to be $D = 1.6$ and 1.3, respectively.

Plates are often used as target samples for studying mechanisms of laser-radiation interaction with a material. Characteristics of plate vibrations are a source of useful information on relevant physical processes [6, 7]. It is of interest to analyze features of plate-vibration excitation by unstable chaotic laser radiation. This is important for elucidating potentialities of the photoacoustic diagnostics of a radiation fractal structure for an unstable-cavity laser by detecting plate vibrations. Below, we consider the thermooptical excitation of vibrations (flexural waves) in a thin plate by laser radiation with a harmonically modulated intensity and a random fractal spatial distribution of intensity fluctuations over the laser-beam cross section. It is worth noting that the effect of spatial and temporal intensity fluctuations of laser radiation on the sound excitation in a liquid was previously studied in [8]. However, the character of the distribution was not specified there. Recently, the sound excited in liquid by chaotic laser radiation was considered in [9].

We now assume that a laser beam with harmonically modulated intensity impinges onto a thin plate orthogonally to its surface. The following equation holds for the displacement $u(x, y)$ of a plate executing forced flexural vibrations [10]:

$$[\Delta^2 - k^4]u(x, y) = \frac{F(x, y)}{g}. \quad (1)$$

Here,

$$\Delta \equiv \frac{\partial^2}{\partial x^2} + \frac{\partial^2}{\partial y^2}, \quad g = \frac{Fh^3}{3(1-\sigma^2)}, \quad k^4 = \frac{3\omega^2\rho(1-\sigma^2)}{Eh^2},$$

g is the flexural stiffness, E is the Young modulus, σ is the Poisson's ratio, $2h$ is the thickness, ρ is the plate-material density, k is the wave number of the propagating flexural waves (vibrations), ω is the circular modulation frequency for the laser-radiation intensity, and $F(x, y)$ is a function that characterizes an external force caused by the laser-radiation action on the plate. The time-dependent factor is omitted everywhere.

Without a loss of generality, we assume that the plate is opaque with respect to laser radiation and this radiation is absorbed in a thin near-surface plate layer.

Based on these arguments, we can write the following expression for $F(x, y)$ [11]:

$$F(x, y) = -\frac{F\alpha\mu m}{C_p} I_0 f(x, y). \quad (2)$$

Here, I_0 is the laser-radiation intensity, $f(x, y)$ is the function characterizing the intensity distribution over the plate surface, α is the coefficient of volumetric thermal expansion, C_p is the specific heat, E is the Young's modulus of the plate material, m is the modulation coefficient ($0 \le m \le 1$), and μ is the coefficient of the laser-radiation absorption by the plate.

Using the reciprocity theorem, we can write the solution to Eq. (1) in the form

$$u(x, y) = -\frac{E\alpha\mu m}{C_p g} I_0 g \times \int_S f(x_0, y_0) G(x_0, y_0/x, y) ds(x_0, y_0). \quad (3)$$

Institute of General Physics, Russian Academy of Sciences, ul. Vavilova 38, Moscow, 117942 Russia
E-mail: lyamshev@kapella.gpi.ru

1028-3358/02/4701-0044$22.00 © 2002 MAIK "Nauka/Interperiodica"

Here, $G(x_0, y_0/x, y)$ is the solution to the boundary value problem on a field of a point source (point force), which is located at the plate point $r(x, y)$ at which the solution to Eq. (1) should be found. In other words, G is Green's function for an infinite plate [12].

Furthermore, we analyze the field of excited flexural waves in the Fraunhofer zone with respect to the laser-beam radius. In this case, for finding plate displacements, it suffices to know the Green's function asymptotic behavior. It is of the form [10]

$$G(x_0, y_0/x, y) = -\frac{\exp(ikR)}{\sqrt{32\pi ik^5 R}}\exp(ik_x x_0 + ik_y y_0), \quad (4)$$

where $R = \sqrt{x^2 + y^2}$, (x, y) are the coordinates of the observation point; (x_0, y_0) are the source-point coordinates; and $k^2 = k_x^2 + k_y^2$, where k_x and k_y are the wave-vector components.

We assume that the spatial distribution of the laser-radiation intensity is characterized by a random statistically homogeneous function $f(x, y)$ so that $\langle f(x, y)\rangle = 0$.

Substituting the asymptotic form of Green's function (4) into solution (3) and multiplying the expression obtained by the complex-conjugate one, we find the mean-square displacement $\langle|u(x, y)|\rangle$ of the plate:

$$\langle|u(x, y)|^2\rangle = \frac{E^2\alpha^2\mu^2 m^2}{C_p^2 g^2 \times 32\pi R k^5} I_0^2 \iint_{S\,S} \langle f(x', y') f(x'', y'')\rangle$$
$$\times \exp[-ik_x(x' - x'') - ik_y(y' - y'')]dx'dy'dx''dy''.$$

After the replacement of coordinates $x_1 = \frac{x' + x''}{2}$, $y_1 = \frac{y' + y''}{2}$, $\xi = x' - x''$, $\eta = y' - y''$, and integration over the coordinates x_1 and y_1, the expression for the mean-square displacements takes the form

$$\langle|u(x, y)|^2\rangle = \frac{E^2\alpha^2\mu^2 m^2}{C_p^2 g^2 \times 32\pi R k^5} I_0^2 S$$
$$\times \iint_{\xi\,\eta} B(\xi, \eta)\exp[-ik_x\xi - ik_y\eta]d\xi\, d\eta. \quad (5)$$

Here, $B(\xi, \eta) = \langle f(x', y') f(x'', y'')$ is a normalized correlation function for the laser-radiation intensity fluctuations, $\xi = |x' - x''|$, $\eta = |y' - y''|$, and S is the spot area of the laser beam on the plate surface. The integration with respect to ξ and η is performed over the entire area of the laser-radiation action. In the case when $B(\xi, \eta)$ rapidly drops at the periphery of the laser-beam cross section, the integration can be extended to the interval from $-\infty$ to $+\infty$.

Properties of statistical fractals are often characterized by structure (correlation) functions and by their spectra, whose specific feature is that they are described by power laws. This fact follows from the scale invariance of the fractal structures [3].

For wave problems, an important characteristic of statistical fractals is the power-law shape of the fluctuation spectrum that has the form

$$\Phi(q) \sim q^{\delta}. \quad (6)$$

Here, for objects with a fractal surface, the exponent δ is determined by the expression [13]

$$\delta = D - 2d, \quad (7)$$

where D is the fractal dimension and d is the embedded-space dimension.

We now find the mean-square plate displacements for the case when the laser aperture in the x-direction is of the narrow-slit form. The correlation function for fluctuations of the laser-radiation intensity can be represented in the form of the product

$$B(\xi, \eta) = B_1(\xi)B_2(\eta). \quad (8)$$

Here, $B_2(\eta) \approx 1$, since the fluctuation distribution of the laser-radiation intensity may be treated as completely correlated.

In this case, taking into account the fact that, for the transverse dimensions of the laser spot, $k_y\eta \ll 1$, we arrive at

$$\int_{-\infty}^{+\infty} B_2(\eta)\exp(ik_y\eta)d\eta \simeq \eta_0, \quad (9)$$

where η_0 is the transverse dimension of the laser spot on the plate surface.

We choose the normalized correlation function in the longitudinal direction in the form (see, e.g., [14])

$$B_1(\xi) = \frac{1}{2^{\nu-1}\Gamma(\nu)}\left(\frac{\xi}{\xi_0}\right)^{\nu} K_{\nu}\left(\frac{\xi}{\xi_0}\right), \quad (10)$$

where $\Gamma(\nu)$ is the gamma function, $k_{\nu}\left(\frac{\xi}{\xi_0}\right)$ is the Macdonald function, and ξ_0 is the correlation radius for laser-radiation intensity fluctuations in the longitudinal direction. We note that $B_1(0) = 1$, $B_1(\infty) = 0$, and $B_1(\xi)_{\xi < \xi_0} \sim \left(\frac{\xi}{\xi_0}\right)^{\nu}$; i.e., the correlation function is of the power-law form. Thus, this function can be used to describe the fractal spatial structure of intensity fluctuations for unstable laser radiation.

Substituting expressions (8), (9), and (10) into formula (5), we obtain after integration

$$\langle |u(x, y)|^2 \rangle = \frac{E^2 \alpha^2 \mu^2 m^2}{16\pi^2 k^5 R C_p^2 g^2} I_0^2 S \eta_0 \cdot \Phi_1(k_x), \quad (11)$$

where $\Phi_1(k_x)$ is the spatial spectral power density for intensity fluctuations of laser radiation in the horizontal direction:

$$\Phi_1(k_x) = \frac{\Gamma\left(\nu + \frac{1}{2}\right)}{\sqrt{\pi}\Gamma(\nu)} \frac{\xi_0}{(1 + k_x^2 \xi_0^2)^{\nu + \frac{1}{2}}}. \quad (12)$$

For $k_x \xi_0 > 1$, the spectral density $\Phi_1(k_x)$ is seen to be of the power-law (fractal) form

$$\Phi_1(k_x) \sim k_x^{-(2\nu + 1)}. \quad (13)$$

We now consider the circular-aperture case. Expression (5) for the plate mean-square displacements can be represented in the form

$$\langle |u(x, y)|^2 \rangle = \frac{\pi E^2 \alpha^2 \mu^2 m^2}{8k^5 R C_p^2 g^2} I_0^2 S \Phi(k_\perp), \quad (14)$$

where

$$\Phi(k_\perp) = (2\pi)^{-2} \int_{-\infty}^{+\infty} B(\rho) \exp(-ik_\perp \rho) d\rho. \quad (15)$$

Here, $k_\perp$ is the wave number for a so-called resonance harmonic in the spatial spectrum of the fluctuation power $k_\perp \sim k$ of the laser-radiation intensity. We represent the correlation function $B(\rho)$ in form (9), replacing ξ by ρ and ξ_0 by ρ_0, where ρ_0 is the correlation radius for the laser-radiation fluctuations.

For spectral density (15), we have

$$\Phi(k_\perp) = \nu \rho_0^2 [\pi(1 + k_\perp^2 \rho_0^2)^{\nu + 1}]^{-1}. \quad (16)$$

For $k_\perp \rho_0 > 1$, we obtain

$$\Phi(k_\perp) \sim k_\perp^{-2(\nu + 1)}. \quad (17)$$

In order to calculate the plate mean-square displacements, we need to specify a particular value of the parameter ν for each of the cases under consideration.

Under the conditions of the numerical experiment [5], the embedded-space dimension is $d = 2$. If we employ the fractal dimensions $D = 1.6$ and 1.3 obtained in the numerical experiment [5], we find from expressions (6), (7), (12), and (16) that $\nu = 0.7$ and 0.35 for the slit-shaped and circular apertures, respectively.

We now analyze in greater detail expressions (11), (12), (14), and (16), which characterize the plate mean-square displacements and fluctuation spectra of the laser-radiation intensity for lasers with slit-shaped and circular apertures, respectively. We assume that the modulation frequency ω is sufficiently high and the conditions $k_x \xi_0 > 1$ or $k_\perp \rho_0 > 1$ are met. For the cases of slit-shaped and circular apertures, we analyze the frequency dependence of the plate mean-square displacements as plate vibrations excited by radiation of an unstable-cavity laser. Note that the relation $k \sim \omega^{1/2}$ holds for the wave number k of the flexural waves (vibrations) of the plate [see formula (1)]. Using equations (6), (7), (12), and (16); the values D_1 and D_2 of the fractal dimensions; and the value of the parameter ν, we obtain $\langle |u(x, y)|^2 \rangle \sim \omega^{-3.7}$ and $\langle |u(x, y)|^2 \rangle \sim \omega^{-3.85}$ for lasers with slit-shaped and circular apertures, respectively. As is evident from expression (4) for Green's function, in the case of stable laser radiation, we have $|u(x, y)|^2 \sim \omega^{-2.5}$.

Thus, in the cases of stable and chaotic laser radiation, the frequency dependences for the plate mean-square displacements excited by modulated laser radiation are different and can serve as characteristics of radiation instability and fractal structure. Properly choosing and varying the modulation frequency of laser radiation, its characteristics, and, in particular, the laser-spot size on the plate surface, as well as plate parameters, we can diagnose the fractal structure of chaotic laser radiation by observing the frequency dependence of plate vibrations excited by this laser radiation.

REFERENCES

1. A. Yu. Loskutov, A. V. Mushenkov, A. I. Odintsov, *et al.*, Kvant. Élektron. (Moscow) **29**, 127 (1999).
2. A. P. Napartovich and A. G. Sukhorukov, Kvant. Élektron. (Moscow) **25**, 85 (1998).
3. M. Schroeder, *Fractals, Chaos, and Power Laws* (Freeman, New York, 1990).
4. V. P. Silin, Kvant. Élektron. (Moscow) **26**, 11 (1999).
5. G. P. Karman and J. P. Woerdman, Opt. Lett. **23**, 1909 (1998).
6. M. Tyunina and S. Leppavneris, J. Appl. Phys. **87**, 8132 (2000).
7. G. Busse, M. L. Lyamshev, and Ĭ. Shtanullo, Akust. Zh. **42**, 35 (1996) [Acoust. Phys. **42**, 28 (1996)].
8. F. V. Bunkin, *Selected Papers* (Nauka, Moscow, 1999).
9. M. L. Lyamshev, Pis'ma Zh. Tekh. Fiz. **26**, 35 (2000) [Tech. Phys. Lett. **26**, 341 (2000)].
10. P. M. Morse and K. U. Ingard, *Theoretical Acoustics* (McGrow-Hill, New York, 1968).
11. M. L. Lyamshev, *Laser Thermooptical Sound Excitation* (Nauka, Moscow, 1989).
12. M. L. Lyamshev, Akust. Zh. **10**, 247 (1964) [Sov. Phys. Acoust. **10**, 205 (1964)].
13. H. D. Bale and P. W. Schmidt, Phys. Rev. Lett. **53**, 596 (1984).
14. Y. P. Zhao, G. C. Wang, and T. M. Lu, Phys. Rev. B **58**, 7300 (1998).

Translated by V. Tsarev

Doklady Physics, Vol. 47, No. 1, 2002, pp. 47–50. Translated from Doklady Akademii Nauk, Vol. 382, No. 2, 2002, pp. 186–189.

TECHNICAL PHYSICS

Stratification of Solid Solution in the Field of Residual Stresses

N. M. Vlasov and Corresponding Member of the RAS I. I. Fedik

Received August 7, 2001

Alloying elements in an alloy are quite sensitive to the level and character of the residual-stress distribution. The substitutional impurities, whose atoms have large atomic radii (compared to the host metal), migrate towards the tensile-stress region. At the same time, the corresponding impurities of small atomic radii migrate towards the compressive-stress region. Thus, the stratification of a solid solution containing substitutional impurities of various kinds and, as a consequence, a change in the thermophysical and strength characteristics of the material occur. If the concentration of substitutional impurities exceeds the solubility limit at a given temperature, new-phase nuclei are formed. Their further growth occurs at the expense of the diffusion feed by impurity atoms. The growing precipitations capture the substitutional impurities from the solid solution, thus depleting it. At the macroscopic level, the formation of concentration inhomogeneities or the appearance of a new phase are observed.

The goal of this paper is to analyze both the stratification kinetics and depletion of a solid solution containing substitutional impurities in the field of residual stresses of a cylindrical shell (e.g., the shell of a fuel element). A system of stresses is considered as a model, whose coordinate dependence admits the exact analytical solution to the diffusion equation in an external force field.

Residual stresses are a particular case of internal stresses. They are characterized by self-equilibrium, which is implied as the presence of tensile and compressive stresses under the condition of the zero value of their integral characteristic. A complex coordinate dependence of residual stresses results in strong mathematical difficulties while solving diffusion equations with allowance for these stresses. The residual stresses in a cylindrical shell are a nice exception from the general rule.

The logarithmic coordinate dependence of the first invariant of the stress tensor substantially simplifies the equation of diffusion in a force field [1]. Such stresses are formed, e.g., in the following manner: the edges of a shell cut are drawn apart at the angle ω, and a required material is placed within. Under such manipulation, in the vicinity of the outer-shell surface the material is in the compressive state, whereas in the vicinity of the inner surface it is in the tensile state. Nonzero components of the stress tensor allow us to easily write out the first invariant for the tensor of these stresses (plane deformation) [2]:

$$\sigma_{ll} = \frac{\mu\omega(1+\nu)}{2\pi(1-\nu)}\left\{1 + 2\ln\frac{r}{R} + \frac{2\left(\frac{r_0}{R}\right)^2}{1-\left(\frac{r_0}{R}\right)^2}\ln\frac{r_0}{R}\right\}. \quad (1)$$

Here, μ is the shear modulus, ν is the Poisson's ratio, ω is the angle of rotation for the shell-cut edges, and r_0 and R are the outer and inner shell radii.

In the case of other equal conditions, the sign of the quantity σ_{ll} depends on the angle of rotation for the shell-cut edges. In the accepted model of residual stresses, it is conventionally considered that $\omega < 0$ ($\sigma_{ll} > 0$ and $\sigma_{ll} < 0$ on the inner and outer shell surfaces, respectively). The potential of interaction with the field of residual stresses for an impurity atom is determined by the well-known relation

$$V = -\frac{\sigma_{ll}}{3}\delta v, \quad (2)$$

where δv is the change in the material volume after incorporating an impurity atom. If $\delta v > 0$ (the substitutional impurity increases the crystal-lattice parameter), then the potential V becomes negative for $\sigma_{ll} > 0$. This corresponds to the attraction of similar impurities to the tensile region of residual stresses. Needless to say that the choice of the sign for the potential V, which characterizes the attraction or repulsion of impurity atoms, is of a conditional nature. The equilibrium concentration of the substitutional impurities exponentially depends on the potential V:

$$C_p = C_0\exp\left(-\frac{V}{kT}\right). \quad (3)$$

Research-Industrial Enterprise "Luch," Podol'sk, Moscow oblast, 142100 Russia

1028-3358/02/4701-0047$22.00

Here, C_0 is the average concentration of impurity atoms, k is the Boltzmann constant, and T is the absolute temperature. In the tensile region ($\sigma_{ll} > 0$), $C_{eq} > C_0$ for $\delta v > 0$ and $C_{eq} < C_0$ for $\delta v < 0$ (substitutional impurities reduce the crystal-lattice parameter). In the compression region $C_{eq} < C_0$ for $\delta v > 0$ and $C_{eq} > C_0$ for $\delta v < 0$. Physically, this implies that the substitutional impurities with a large atomic radius migrate from the compression region into the tensile zone, whereas the diffusion flow of impurities with a small atomic radius has the opposite direction. The final result of such a migration of alloying elements is a stratification of this solid solution. The inhomogeneous field of the impurity-atom concentration produces concentration stresses of the opposite sign with respect to residual stresses. The calculation of the concentration stresses is performed by analogy with the temperature stresses [3]. The change in the crystal-lattice parameter at the expense of the unit impurity-atom concentration is put into correspondence with the linear-expansion coefficient. For a substantial concentration of the substitutional impurities and at the later stages of the diffusion process, the concentration stresses damp the stratification of a solid solution. However, for a low concentration of impurity atoms and at the early stages of the process, this effect can be ignored.

The stratification kinetics for the solid solution of substitutional impurities is described by the unsteady diffusion equation in the field of the potential V under the corresponding initial and boundary conditions:

$$\frac{1}{D}\frac{\partial C}{\partial t} = \Delta C + \frac{\nabla(C\nabla V)}{kT}, \quad r_0 < r < R,$$
$$C(r, 0) = C_0, \quad C(r_0, t) = C_{eq}^1, \quad C(R, t) = C_{eq}^2, \tag{4}$$

where D is the diffusion coefficient for impurity atoms and C_{eq}^1 and C_{eq}^2 are the equilibrium concentrations of the substitutional impurities for $r = r_0$ and $r = R$, respectively. Without a loss of generality, we consider the diffusion migration of substitutional impurities of a large radius ($\delta v > 0$). In this case, $C_{eq}^1 > C_{eq}^2$, since in the model accepted the inner and the outer regions of the cylindrical shell are in the tension-state and compression-state regions, respectively. The physical meaning of the initial and boundary conditions related to problem (4) is completely evident. At the initial time moment, the impurity concentration is equal to its average value.

The boundary conditions for $r = r_0$ and $r = R$ imply that the equilibrium concentration of impurity atoms, which corresponds to the potential V, is instantaneously established and maintained at these boundaries. This is caused by the fact that the maximum and minimum values of σ_{ll} are attained precisely at the boundaries of the cylindrical shell.

The logarithmic coordinate dependence of the potential V considerably simplifies problem (4). In this case, the constants entering into relation (1) play no part, since the diffusion of impurity atoms depends on the gradient of the potential V ($\Delta V = 0$, since V is a harmonic function). With allowance for the arguments stated above, problem (4) is formulated mathematically in the form

$$\frac{1}{D}\frac{\partial C}{\partial t} = \frac{\partial^2 C}{\partial r^2} + \frac{1+\alpha}{r}\frac{\partial C}{\partial r}, \quad r_0 < r < R,$$
$$C(r, 0) = C_0, \quad C(r_0, t) = C_{eq}^1, \quad C(R, t) = C_{eq}^2, \tag{5}$$
$$\alpha = \frac{\mu\omega(1+\nu)\delta v}{3\pi(1-\nu)kT} < 0.$$

The dimensionless problem parameter α determines the contribution of residual stresses into the total diffusion flow of substitutional impurities. For $|\alpha| \ll 1$, the field of residual stresses should be considered as a weak perturbation of the substitutional-impurity flow caused by the concentration gradient. If $|\alpha| \gg 1$, the residual stresses play a decisive role. For $|\alpha| \approx 1$, the diffusion flows of the substitutional impurities caused by both concentration gradients and the potential V are comparable with each other. The estimates show that the magnitude of $|\alpha|$ is close to unity. Indeed, for $\mu = 5 \times 10^{10}$ Pa, $\omega = 0.1$ rad, $\nu = 0.3$, $\delta v = 10^{-29}$ m^3, and $kT = 10^{-20}$ J, we arrive at $|\alpha| \approx 1$. Furthermore, we take $\alpha = -1$, since $\omega < 0$ and $\delta v > 0$. The solution to equation (5) for $\alpha = -1$ describes the concentration field of substitutional impurities with allowance for the effect of residual stresses [4]:

$$C - C_0 = \frac{R(C_{eq}^1 - C_0) - r_0(C_{eq}^2 - C_0) + r(C_{eq}^2 - C_{eq}^1)}{R - r_0}$$
$$+ \frac{2}{\pi}\sum_{n=1}^{\infty}\frac{1}{n}[(-1)^n(C_{eq}^2 - C_0) - (C_{eq}^1 - C_0)] \tag{6}$$
$$\times \sin\frac{\pi n(r - r_0)}{R - r_0}\exp\left[-\frac{\pi^2 n^2 Dt}{(R - r_0)^2}\right].$$

The solution obtained shows that the residual stresses transform the diffusion equation with cylindrical symmetry into an equation with plane symmetry. Physically, it implies that the diffusion process changes not only quantitatively but also qualitatively. This results in a higher formation rate for the concentration profile of substitutional impurities that immediately follows from the form of equation (5). In fact, for $\frac{\partial C}{\partial r} < 0$, the change rate $\frac{\partial C}{\partial r}$ of the impurity concentration for $\alpha = -1$ exceeds the corresponding value $\frac{\partial C}{\partial r}$ for $\alpha = 0$. The diffusion flows caused by both the concentration gradients and the potential V have the opposite

direction: the term $\frac{\partial V}{\partial r}$ is responsible for transferring the substitutional impurities with a large atomic radius into the region of the tensile stresses, while the term $\frac{\partial C}{\partial r}$ provides the impurity migration in the direction opposite to the gradient of the potential V. In the case of the equality of diffusion flows, dynamic equilibrium takes place, which is defined by relation (3). The profile of the substitutional-impurity concentration linearly depends on the radial coordinate. This is a consequence of the model accepted ($\alpha = -1$), since $\exp\left(\ln\frac{r}{R}\right) = \frac{r}{R}$. The equilibrium concentration of substitutional impurities is formed as $\frac{Dt}{(R-r_0)^2} > 1$, when the contribution of the second term in expression (6) is sufficiently small.

We now consider the kinetics of the new-phase growth with allowance for the field of residual stresses of the cylindrical shell. If the concentration of the substitutional impurities in the region of maximum residual stresses exceeds the solubility limit, then on the inner shell surface a new-phase nucleus [with a characteristic size R_0 ($r_0 < R_0 \ll R$)] is formed. As far as $R_0 \ll R$, diffusion processes in an unbounded matrix are considered for the description of kinetics of the new-phase growth. At the moving boundary of precipitations, the concentration of substitutional impurities changes jumpwise: $C = C_1$ for the new phase and $C = C_2$ in the surrounding matrix ($C_1 > C_2$, $C_2 < C_0$, where C_0 is the average concentration of impurity atoms). This fact implies that the interphase boundary instantaneously captures impurities from the solid solution and transfers them into the new phase with a higher concentration. The kinetics of the diffusion new-phase growth in the vicinity of the inner surface of the cylindrical shell is mathematically formulated as [5]

$$\begin{gathered}\frac{1}{D}\frac{\partial C}{\partial t} = \frac{\partial^2 C}{\partial r^2} + \frac{1+\alpha}{r}\frac{\partial C}{\partial r},\\ C(R,t) = C_2, \quad C(r,0) = C_0(r \geq R_0),\\ C(\infty,t) = C_0,\\ (C_1 - C_2)\frac{dR}{Dt} = D\left(\left|\frac{dC}{dr}\right| + \left|\frac{C\alpha}{r}\right|\right)_{r=R},\end{gathered} \tag{7}$$

where R_0 is the radius of a precipitation nucleus and R is the current radius of the new phase.

For a cylindrical shell with a positive dilatation on the inner surface in the presence of substitutional impurities with a large atomic radius ($\alpha = -1$), problem (7) takes the more simple form

$$\begin{gathered}\frac{1}{D}\frac{\partial C}{\partial t} = \frac{\partial^2 C}{\partial r^2},\\ C(R,t) = C_2, \quad C(r,0) = C_0(r \geq R_0),\\ C(\infty,t) = C_0,\\ (C_1 - C_2)\frac{dR}{dt} = D\left(\frac{dC}{dr} + \frac{C}{r}\right)_{r=R}.\end{gathered} \tag{8}$$

If the new-phase growth kinetics is limited by the diffusion of impurity atoms, then the change in the precipitation size obeys the law $R(t) = \beta\sqrt{Dt}$, where β is the dimensionless problem parameter. Its value is found from the equation of the mass balance at the interphase boundary. In the approximation of an immobile interphase boundary, we obtain the quadratic equation for the determination of the parameter β:

$$\beta^2 - \frac{2\beta}{\sqrt{\pi}}\left|\frac{C_2 - C_0}{C_1 - C_2}\right| - \left|\frac{2C_2}{C_1 - C_2}\right| = 0. \tag{9}$$

Other approximations (e.g., introducing the new variable $\frac{r}{2\sqrt{Dt}}$) only complicate the equation for the determination of the parameter β [6]. If we set $\alpha = 0$ in problem (7), then, under the same initial and boundary conditions, we obtain

$$\begin{gathered}\frac{1}{D}\frac{\partial C}{\partial t} = \frac{\partial^2 C}{\partial r^2} + \frac{1}{r}\frac{\partial C}{\partial r},\\ C(R,t) = C_2, \quad C(r,0) = C_0(r \geq R_0),\\ C(\infty,t) = C_0,\\ (C_1 - C_2)\frac{dR}{dt} = D\left(\frac{dC}{dr}\right)_{r=R}.\end{gathered} \tag{10}$$

In this case, the growth of a new-phase precipitation is caused only by the concentration gradient for impurity atoms. From the equation of mass balance for the interphase boundary, we obtain the transcendental equation that determines parameter β_1, which characterizes the new-phase growth kinetics according to the relation $\beta_1\sqrt{Dt}$:

$$\beta_1 = \frac{2}{\sqrt{\pi}}\left|\frac{C_2 - C_0}{C_1 - C_2}\right|\frac{K_1\left(\beta_1\frac{\sqrt{\pi}}{2}\right)}{K_0\left(\beta_1\frac{\sqrt{\pi}}{2}\right)}. \tag{11}$$

Here, $K_0(x)$ and $K_1(x)$ are modified Bessel functions of the second kind and of the zero and first orders, respectively. Solving equations (9) and (11), we are able to

reveal the contribution of the residual-stress field into the kinetics of the process of the new-phase growth. For atomic concentrations $C_0 = 2 \times 10^{-4}$, $C_2 = 10^{-4}$, and $C_1 = 3 \times 10^{-4}$, we obtain

$$\beta^2 - \frac{\beta}{\sqrt{\pi}} - 1 = 0, \quad \beta_1 = \frac{1}{\sqrt{\pi}} \frac{K_1\left(\beta_1 \frac{\sqrt{\pi}}{2}\right)}{K_0\left(\beta_1 \frac{\sqrt{\pi}}{2}\right)}. \qquad (12)$$

Since $\frac{K_1(x)}{K_0(x)} > 1$, we have $\beta_1 > \frac{1}{\sqrt{\pi}}$. On the other hand, it follows from $\beta = \frac{1}{\beta} + \frac{1}{\sqrt{\pi}}$ that $\beta > \frac{1}{\sqrt{\pi}}$. Therefore, without numerical analysis of relations (12), deriving the expected inequality $\beta > \beta_1$ seems to be impossible.

Numerically solving equation (12) yields $\beta = 1.3$ and $\beta_1 = 0.8$. This implies that the residual stresses promote the growth rate of new-phase nuclei. Using other values of boundary concentrations for impurity atoms will result only in refinement of the numerical values for parameters β and β_1. When the characteristic size of the precipitate is increased, the depletion of the solid solution of substitutional impurities occurs, and the new-phase growth becomes slower. Bulk variations of the new phase result in the appearance of stresses at the interphase boundary. Generally speaking, these stresses change the kinetics of the diffusion process. However, under small bulk changes of the new phase and at early stages of the process, this effect can be ignored.

Thus, the substitutional impurities with a large atomic radius are redistributed in the field of residual stresses. In this case, the enrichment of the tensile-stress zone and the depletion of the compressive-stress region occur. Simultaneously with this process, the diffusion migration of the substitutional impurities with a small atomic radius occurs. In the equilibrium state, the field of residual stresses redistributes these impurities as well, the profile of their concentration being also linearly dependent on the radial coordinate. At the same time, however, there exists an essential difference: the substitutional impurities of small atomic radius enrich the region of compressive stresses and deplete the zone of tensile stresses. At the macroscopic level, a stratification of the solid solution containing substitutional impurities of various types is observed. This stratification is most noticeable at the boundaries of the cylindrical shell. If the concentration of substitutional impurities in the near-boundary region of the shell exceeds the solubility limit, new-phase nuclei are formed. Their diffusion growth is followed by the depletion of the solid solution containing substitutional impurities throughout the entire volume bounded by the shell. In the macroscopic scale, formation of the concentration inhomogeneities or the new-phase precipitations is observed. In these processes, the residual stresses play the decisive role.

REFERENCES

1. N. M. Vlasov and I. I. Fedik, Dokl. Akad. Nauk **375**, 334 (2000) [Dokl. Phys. **45**, 623 (2000)].
2. A. I. Lur'e, *Theory of Elasticity* (Nauka, Moscow, 1970).
3. I. I. Fedik, V. S. Kolesov, and V. N. Mikhaĭlov, *Temperature Fields and Thermal Stresses in Nuclear Reactors* (Énergoatomizdat, Moscow, 1985).
4. A. V. Bitsadze and D. F. Kalinichenko, *Equations of Mathematical Physics: Collection of Problems* (Mir, Moscow, 1980; Nauka, Moscow, 1985).
5. N. M. Vlasov and V. A. Zaznoba, Dokl. Akad. Nauk **363**, 472 (1998) [Dokl.–Phys. **43**, 761 (1998)].
6. B. Ya. Lyubov, *Diffusion Processes in Heterogeneous Solid Media* (Nauka, Moscow, 1981).

Translated by T. Galkina

Doklady Physics, Vol. 47, No. 1, 2002, pp. 5–8. Translated from Doklady Akademii Nauk, Vol. 382, No. 1, 2002, pp. 34–37.

PHYSICS

A Mathematical Model for the Formation of Inhomogeneous Structures in Thermally Oxidized Silicon Layers

Corresponding Member of the RAS G. Ya. Krasnikov, N. A. Zaĭtsev, and I. V. Matyushkin

Received June 27, 2001

The need in modern microelectronics for the reproducible production of thin (2–5 nm) silicon dioxide layers used as gate insulators stimulates particular attention to processes accompanying the formation of the boundary layer in the Si–SiO_2 system [1]. After termination of the thermal oxidation of silicon, the boundary layer naturally becomes the junction-layer [2]. Hence, the features characterizing the boundary-layer formation strongly affect the structure and the impurity distribution in the junction layer. In addition, the evolution of the boundary layer eventually gives rise to the formation of the random Zachariasen network characteristic of bulk silicon dioxide.

Note that due to the high characteristic temperature of the oxidation process (1273–1373 K), it is a rather complicated task to study the boundary layer in the course of thermal oxidation. Therefore, it is of primary importance to develop a theoretical scheme or a model for the description of the boundary layer. In this paper, we consider a general mathematical model for the oxidation of silicon, which takes into account the polymerization processes occurring in this layer.

In our paper [2], we proposed to divide the boundary layer into an active zone and a polymerization zone. In the active zone directly adjoining the Si–SiO_2 interface, low-molecular-weight silicon–oxygen clusters are formed due to the intense heat release in the course of chemical reactions. These clusters are monomer units for further polymerization reactions. Owing to thermally activated diffusion, the monomers also arrive at the polymerization zone. In this zone, the local viscosity elevates with distance from the Si–SiO_2 interface due to the increase in the number of 8-, 9-, and 10-unit polymer molecules. The formation of ring molecules and of the polymer network limits the further prolongation of the polymeric-molecule chain. As a result, the local viscosity undergoes a jumplike increase, and the chemical reactions corresponding to the growth in the chain length are impeded due to steric causes.

AOOT Research Institute of Molecular Electronics and Micron Plant, Zelenograd, Moscow, 103460 Russia

1. EQUATIONS OF THE MODEL

We consider an arbitrary cross section in the polymerization zone. In the course of the polymerization process, the Si–SiO_2 interface continuously shifts deeper into the semiconductor (say, for definiteness, to the left) and the horizontal coordinate of this cross section increases. We assume that there exists a steady inflow j of the monomer to the given cross section. Let the monomer concentration and the $(i+1)$-unit polymer concentration in a layer be x_0 and x_i, respectively. Assuming the cross section of a certain finite thickness to be, as a whole, homogeneous, we can write out all proceeding chemical reactions until n-unit polymers will be formed ($n \le N = 8$):

$$\begin{gathered} x_0 + x_0 \xrightarrow{k_0} x_1, \\ x_1 + x_0 \xrightarrow{k_1} x_2, \\ \dots \\ x_{N-1} + x_0 \xrightarrow{k_{N-1}} x_N. \end{gathered} \tag{1}$$

Here, k_0, k_1, …, k_{N-1} are the reaction-rate constants characterizing the rates of corresponding chemical reactions. The reactions are assumed to be irreversible, and their rates are calculated according to the acting-mass law (bimolecular reaction). The reaction rate constants are considered to be different. To take into account the limitation imposed on the growth of the chain length, we assume that $k_N = 0$. Then, we can write out

$$\begin{gathered} \frac{dx_0}{dt} = j(x_0, t) - k_0 x_0^2 - k_1 x_0 x_1 - \dots - k_{N-1} x_{N-1} x_0, \\ \frac{dx_1}{dt} = k_0 x_0^2 - k_1 x_1 x_0, \\ \dots \\ \frac{dx_n}{dt} = k_{n-1} x_{n-1} x_0 - k_n x_n x_0, \\ \dots \\ \frac{dx_N}{dt} = k_{N-1} x_{N-1} x_0. \end{gathered} \tag{2}$$

1028-3358/02/4701-0005$22.00

The reaction rate is limited by the diffusion of reagents. This assumption stems from the viscoelastic properties of the growing SiO_2 layer, which is verified in a number of studies [3]. It is well known [4] that the reaction-rate constant k_d of a diffusion-driven reaction obeys the following relationship:

$$k_d = \frac{2RT}{3\eta}\frac{(r_a + r_b)^2}{r_a r_b}. \quad (3)$$

Here, η is the viscosity of the medium, r_a is the reagent molecular size (related to the number of monomer units), r_b is the monomer molecular size, R is the universal gas constant, and T is temperature. Thus, in our case, $k_i = k_d(r_a(i))$, k_i increasing with i. Ignoring unity compared to i, we can write out

$$k_i = \frac{2RT}{3\eta}(i+1). \quad (4)$$

It should be noted that the parameter k_0 should actually be given by another expression, since the monomer–monomer interaction seems to be controlled by the reaction kinetics rather than by diffusion. The boundary-layer viscosity, in turn, depends on the problem parameters, i.e., on the concentration of polymer molecules. As is known from the physics of polymers [5], the viscosity of a polymer melt consisting of n-unit molecules is proportional to n^3. Therefore, we use in our case this dependence valid for large n ($n > 30$) as an approximation, i.e.,

$$\eta = \eta_0\left(1 + \frac{\sum_{n=1}^{N-1} x_n(t)n^3}{\sum_{n=1}^{N-1} x_n(t)}\right). \quad (5)$$

In Eqs. (2) of our model, we have introduced the monomer flux $j(x_0, t)$ incoming from outside to the cross section under study. Generally speaking, this flux depends on both time (since the farther the cross section from the interface, the smaller the diffusion-induced flow from the active zone) and the monomer concentration. It is evident that the time dependence of the flux j is a monotonically decreasing function that vanishes when the given cross section passes from the polymerization zone to the domain of already formed SiO_2 layers. The derivation of an explicit formula for $j(x_0, t)$ seems to be a very complicated task. Therefore, we use furthermore a number of model dependences having the aforementioned property.

2. ANALYSIS OF THE MODEL IN THE LINEAR CASE

We now introduce a simplifying assumption supposing the boundary-layer viscosity to have a constant value. Although this assumption is hardly justified from the physical standpoint, it is certainly of interest to consider this case as providing an opportunity to find an explicit solution to be used as a starting approximation. Thus, Eqs. (2) form an autonomous homogeneous set of the second order. We perform a change of variables: $d\xi = x_0(t)dt$. For correctness of this change, we also assume that $k_0x_0 \gg k_ix_i$ ($i > 0$); i.e., the amount of a monomer decreases mainly due to its dimerization. Then, we have an equation with respect to $x_0(\xi)$, another one with respect to $x_1(\xi)$, and $N - 1$ equations with respect to $x_i(t)$, $i > 1$:

$$\frac{dx_1}{d\xi} = f(\xi) - k_1x_1,$$
$$\frac{dx_i}{d\xi} = k_{i-1}x_{i-1} - k_ix_i, \quad i = 2, 3, \ldots, N-1. \quad (6)$$

Here, $f(\xi)$ is expressed by the term k_0x_0 written out in the new variable ξ. At first, we solve the linear homogeneous system, i.e., that containing $f(\xi) = 0$. Its n roots are $\lambda_i = -k_i$, and the kth component of ith eigenvector $\mathbf{u}_i$ is given by the expression

$$u_{ik} = \begin{cases} 0, & k < i \\ \prod_{l=i+1}^{k} \frac{k_l}{k_l - k_i}, & k > i \\ 1, & k = i. \end{cases} \quad (7)$$

For example, the values $\lambda_n = -k_n$ and $\lambda_1 = -k_1$ correspond, respectively, to the vectors (0, 0, 0, …, 0, 1) and

$$1, \frac{k_1}{k_2 - k_1}, \frac{k_1k_2}{(k_2 - k_1)(k_3 - k_1)}, \ldots,$$
$$\frac{k_1 \times \ldots \times k_n}{(k_2 - k_1) \times \ldots \times (k_n - k_1)}.$$

The general solution to the homogeneous equation has the form

$$x_i(\xi) = \sum_{k=1}^{n} C_k u_{ik} \exp(-k_i\xi). \quad (8)$$

We note that the first component of $\mathbf{x}(\xi)$ depends only on the first of the constants C_k. This makes the use of the Cauchy formula for the solution to the inhomogeneous system easier. Thus, we obtain the following formula:

$$\mathbf{x}(\xi) = C_1\mathbf{u}_1\exp(-k_1\xi) + \int_0^{\xi} f(\xi')\exp(k_1(\xi' - \xi))d\xi' + \sum_{k=2}^{n} C_k\exp(-k\xi)\mathbf{u}_k. \quad (9)$$

Under the initial condition $x_i(0) = 0$, $x_1(0) = 0$, we have $C_1 = C_k = 0$. We now go back to the function $x_0(\xi)$.

It is evident that

$$dt = \frac{dx_0}{j(x_0) - k_0 x_0^2},$$
$$d\xi = x_0 dt = \frac{1}{2}\frac{d(x_0^2)}{j\left(\sqrt{x_0^2}\right) - k_0 x_0^2}. \quad (10)$$

If j = const and $x_0(0) = c$, then we find

$$x_0(t) = \sqrt{\frac{j}{k_0}}\frac{1 - \exp(-bt)}{1 + \exp(-bt)}, \quad b = 2\sqrt{jk_0}\frac{j + ck_0}{j - ck_0}, \quad (11)$$

$$f(\xi) = k_0 x_0(\xi)$$
$$= \sqrt{k_0 j(1 - \exp(-2k_0\xi)) + k_0 c^2 \exp(-2k_0\xi)}. \quad (12)$$

In particular, it follows from (12) that the rate of the decrease in the amount of the monomer is strongly affected by its initial concentration, since the parameter c enters into the exponent of the exponential terms. The same remark is applicable to the effect of the flux j.

3. CALCULATION RESULTS

It is quite difficult to experimentally determine the reaction-rate constants for the increase in the chain length, especially if we take into account specific features of each n-unit polymer. We have assumed that T = 1273 K and $\eta_0 = 10^9$ kg/(m s) [4, 6]. To specify the initial conditions for Cauchy problem (2), we need to know $c = x_0(0)$, whereas we have $x_i(0) = 0$, $i > 0$ for other x_i. The concentration x_0 is assumed to have the dimension of cm^{-3}, and we took c equal to 2.2×10^{22} cm^{-3}. Such a choice of the dimension (the alternative choice is [cm^{-2}]) allows us to preserve the habitual dimensions for both constants of chemical reactions and flux j. Moreover, there is an additional parameter τ responsible for the flux-decrease rate according, e.g., to the relationship

$$j = j_0 \exp\left(-\frac{t}{\tau}\right). \quad (13)$$

For the steady-state case, we assume that τ = 300 s. The parameter j_0 was taken to be proportional to the initial monomer concentration c. In our opinion, the relation between these two parameters determines in many respects the adequacy of an arbitrary model describing the thermal oxidation.

Based on the above considerations, we performed our calculation using dimensionless parameters. The concentrations, time, and flux were normalized, respectively, to the value of c, to one second, and to the value of $[x_0(0)/c]$; the reaction rates were expressed in terms of the parameter

$$Q = \frac{2RT}{3\eta_0}. \quad (14)$$

The set of equations written out in the dimensionless form demonstrates that variations of the quantities c and Q are equivalent; i.e., they cause the same changes in dynamics of the curves (expressed in dimensionless variables). The calculations were performed using the conventional Runge–Kutta method of the fourth order of accuracy with the step corresponding to 1/10 s.

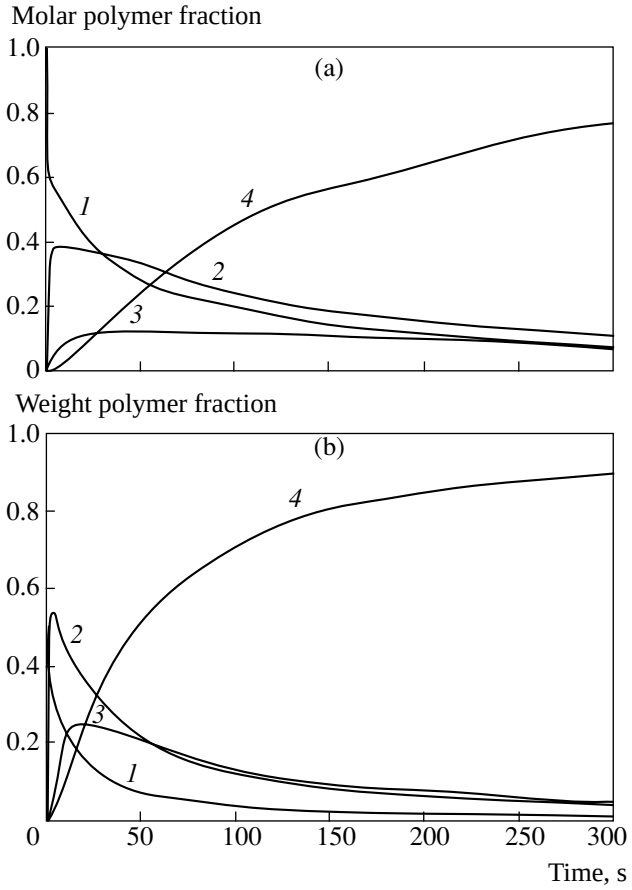

(a) Molar fractions of polymers and (b) weight fractions of polymer molecules in a certain cross section; c =1, Q =1: (*1*) monomers; (*2*) 2-, 3-, 4-unit polymers; (*3*) 5-, 6-, 7-unit polymers; (*4*) 8- and 9-unit polymers.

In the figure, we present typical results for the exponential decay of the monomer flux j. The horizontal axis corresponds to time (expressed in seconds), whereas the vertical axis corresponds to the molar or weight fraction of polymer chains having different lengths (in arbitrary units). Such a representation allows us to account for the excluded-volume problem; i.e., the chosen cross section is permanently supplied with the substance and simultaneously expands. The

molar W and weight U fractions are calculated according to the relationships

$$W_\alpha = \frac{\sum_{i \in \alpha} x_i}{\sum_{0 \le i \le N} x_i}, \quad (15)$$

$$U_\alpha = \frac{\sum_{i \in \alpha} (i+1)x_i}{\sum_{0 \le i \le N} (i+1)x_i}. \quad (16)$$

Here, α is a set of indices with respect to which the aggregation takes place. We considered the following sets {0}, {1, 2,3}, {4, 5, 6}, and {7, 8}. As should be expected, the general pattern corresponds to the following behavior of the curves: the fraction of monomer decreases (except, maybe, the initial segment of the curves); the fraction of 8- and 9-unit polymers increases monotonically; and the fractions of 2-, 3-, and 4-unit molecules and 5-, 6-, 7-unit rings have more or less pronounced peak (the moments corresponding to the peaks of molar and weight fractions can be not coincident). Note that the fractions of 2-, 3-, and 4-unit polymers steeply increase during the first seconds; on the contrary, the monomer fraction rapidly decreases. The most interesting features are the settled ratios of fractions between the polymers of different lengths at large times and the settled ratios of fractions between different polymers in a given cross section, i.e., at fixed t corresponding to the termination of the oxidation process.

The model was analyzed for different values of parameters. As a result, in the case of more intense chain-prolongation processes ($Q = 10$), all peaks turn out to be clearly pronounced; the fraction of 8- and 9-unit polymers tends to 90–95%. The quasisteady mode is attained faster. We can note a rapidly attained (for about 1 s) local dip in the monomer fraction, which exists until the formation of a local peak has been completed for about 16 s. When the monomer flux increases by a factor of 100 ($j_0 = 10\ c$) compared to the situation presented in the figure, the monomer fraction drastically decreases. The peaks also become more clearly pronounced, and the ratio of peak heights for fractions of 2-, 3-, 4-unit and 5-, 6-, 7-unit polymers changes. We also have considered the case when the flux j linearly decreases in time down to zero and then remains there identically zero:

$$j(t) = \begin{cases} j_0\left(1 - \frac{t}{\tau}\right), & 0 \le t \le \tau \\ 0, & \tau \le t \le 3\tau. \end{cases} \quad (17)$$

The behavior of molar fractions turns out to be more complicated. The decrease in the molar fraction of 8- and 9-unit polymers down to 63% seems to be the most important feature. The fraction of 2-, 3-, and 4-unit polymers increases; moreover, it exceeds the fraction of 5-, 6-, and 7-unit polymers. At the same time, the weight fraction of 8- and 9-unit polymers equals 80%. Finally, in the absence of the diffusion-induced monomer flux ($j = 0$), the 2-, 3-, and 4-unit polymers dominate (80%), whereas the fraction of 8- and 9-unit polymers is rather small (below 5%).

Thus, the case of the exponential attenuation of the flux (see figure) is nearest to the actual physics of the process under study. The computer simulation demonstrates that the diffusion-induced monomer flux from the active zone to the polymerization zone strongly affects the relation between the fractions of polymer molecules with different lengths even in the case when growing silicon layers are relatively thick. Bearing in mind that the active zone naturally transforms with time to the polymerization zone, we may conclude that this result is rather interesting.

4. CONCLUSION

Electrophysical properties of the Si–SiO_2 system are determined in many aspects by the structural features of thermally oxidized silicon layers. As it was shown in [1], the junction region in the silicon–silicon dioxide system is a mixture consisting of 3–10-unit structural rings. Currently, there is no mathematical model providing an opportunity to find the percentage of these rings in different cross sections of the junction layer. In addition, the mechanisms underlying the formation of rings with different sizes are also far from being well understood.

The mathematical model developed in this paper, which describes the formation of inhomogeneous structures in thermally oxidized silicon layers, gives an answer to the questions posed above. This fact has significant practical importance, providing an opportunity to control the structure of the junction layer and, hence, parameters of Si–SiO_2 system and of semiconductor devices based on this system.

REFERENCES

1. G. Ya. Krasnikov and N. A. Zaĭtsev, *Physical and Technological Basis Determining the Quality of Super-Large Integrated Circuits* (Mikron-Print, Moscow, 1999).
2. N. A. Zaĭtsev, Izv. Akad. Nauk SSSR, Neorg. Mater. **20**, 2067 (1984).
3. Frounchi Masoud, J. Appl. Polym. Sci. **64**, 971 (1997).
4. I. A. Semiokhin, B. V. Strakhov, and A. I. Osipov, *Kinetics of Chemical Reactions* (Mosk. Gos. Univ., Moscow, 1995).
5. A. Yu. Grosberg and A. R. Khokhlov, *Statistical Physics of Macromolecules* (Nauka, Moscow, 1989).
6. A. I. Priven', Fiz. Khim. Stekla **24** (2), 97 (1998).

Translated by K. Kugel'

Doklady Physics, Vol. 47, No. 1, 2002, pp. 51–60. Translated from Doklady Akademii Nauk, Vol. 382, No. 2, 2002, pp. 190–198.

TECHNICAL PHYSICS

New Synthesized Windows

V. F. Kravchenko

Presented by Academician Yu.V. Gulyaev May 24, 2001

Received May 25, 2001

1. INTRODUCTION

In [1–10], the application of atomic functions to solving problems of signal digital processing was considered, and the efficiency of the atomic functions compared to the classical methods of [11, 12] was proven. In the present paper, we present for the first time new weight functions (windows) proposed and substantiated by the author. Introducing such nonstandard windows is a timely solution to urgent problems that arose recently, being associated with the appearance of a new class of ground-based and airborne radar stations [14] capable of simultaneously searching for and tracking numerous targets. That is why they are called multifunctional radar stations [15]. Noticeable progress in radar engineering, brought about by the use of antenna arrays with phase and digital methods of beam formation, as well as by the application of modern computers, has still received little attention in Russian and foreign scientific literature. A broad list of windows is presented in [11]. As follows from [11], the windows constructed are represented in the form of products, sums, and convolutions of simple windows, as well as in the form of separate parts of windows known previously. As a rule, these windows exhibit moderate physical characteristics, and some of them do not even satisfy necessary practical requirements. In this connection, constructing new windows on the basis of atomic functions and operations of convolution and correlation is of great practical importance.

2. OPERATIONS OF CONVOLUTION AND CORRELATION

The principal idea of the method proposed consists in the following. Atomic functions considered in [4] are closely connected with other atomic functions, e.g.,

$$\hat{\mathrm{up}}(x) = \mathrm{cup}(x) = \frac{1}{2\pi}\int_{-\infty}^{\infty}\exp(ixt) \times \prod_{k=1}^{\infty}\left(\frac{\sin(t\times 2^{-k})}{t\times 2^{-k}}\right)^2 dt. \quad (1)$$

Institute of Radio Engineering and Electronics, Russian Academy of Sciences, Mokhovaya ul. 18, Moscow, 103907 Russia

This atomic function is the self-convolution of the function $\mathrm{up}(x)$:

$$\hat{\mathrm{up}}(x) = \mathrm{cup}(x) = \mathrm{up}(x) * \mathrm{up}(x). \quad (2)$$

The role of this function consists in the fact that integrals of the products of shifts by $\frac{k}{2^n}$ of the functions $\mathrm{up}(x)$, $\mathrm{Fup}_n(x)$, and other atomic functions are expressed in terms of $\hat{\mathrm{up}}(x) = \mathrm{cup}\left(\frac{k}{2^n}\right)$. For understanding further results, we briefly describe basic operations of convolution and correlation, which are based on the results of [13]. When constructing windows, it is helpful to apply operations called convolutions that allow us to obtain the third, daughter, or hybrid function $\hat{\mathrm{up}}(x)$, which is based on the two parent atomic functions $\mathrm{up}_1(x)$ and $\mathrm{up}_2(x)$, in accordance with the rule

$$\hat{\mathrm{up}}(x) = \int_{-\infty}^{\infty}\mathrm{up}_1(\tau)\mathrm{up}_2(x-\tau)d\tau. \quad (3)$$

Employing the sign $*$ for the convolution operation, we can write out formula (3) in a more convenient form:

$$\hat{\mathrm{up}}(x) = \mathrm{up}_1(x) * \mathrm{up}_2(x). \quad (4)$$

Assuming $x - \tau = y$ in expression (3), we obtain

$$\int_{-\infty}^{\infty}\mathrm{up}_2(y)\mathrm{up}_2(x-y)dy = \hat{\mathrm{up}}(x).$$

From here, it follows that the convolution operation has the same commutation property as a usual multiplication:

$$\mathrm{up}_1(x) * \mathrm{up}_2(x) = \mathrm{up}_2(x) * \mathrm{up}_1(x). \quad (5)$$

The validity of the combinative properties is also substantiated quite simply:

$$\mathrm{up}_1(x) * [\mathrm{up}_2(x) * \mathrm{up}_3(x)] = [\mathrm{up}_1(x) * \mathrm{up}_2(x)] * \mathrm{up}_3(x).$$

Figure 1a demonstrates the convolution of the functions $\mathrm{up}_1(x)$ and $\mathrm{up}_2(x)$. The method of deriving the daughter function $\hat{\mathrm{up}}(x)$ ($\mathrm{cup}(x)$) from the parent functions $\mathrm{up}_1(x)$ and $\mathrm{up}_2(x)$ shows that this function inherits

1028-3358/02/4701-0051$22.00

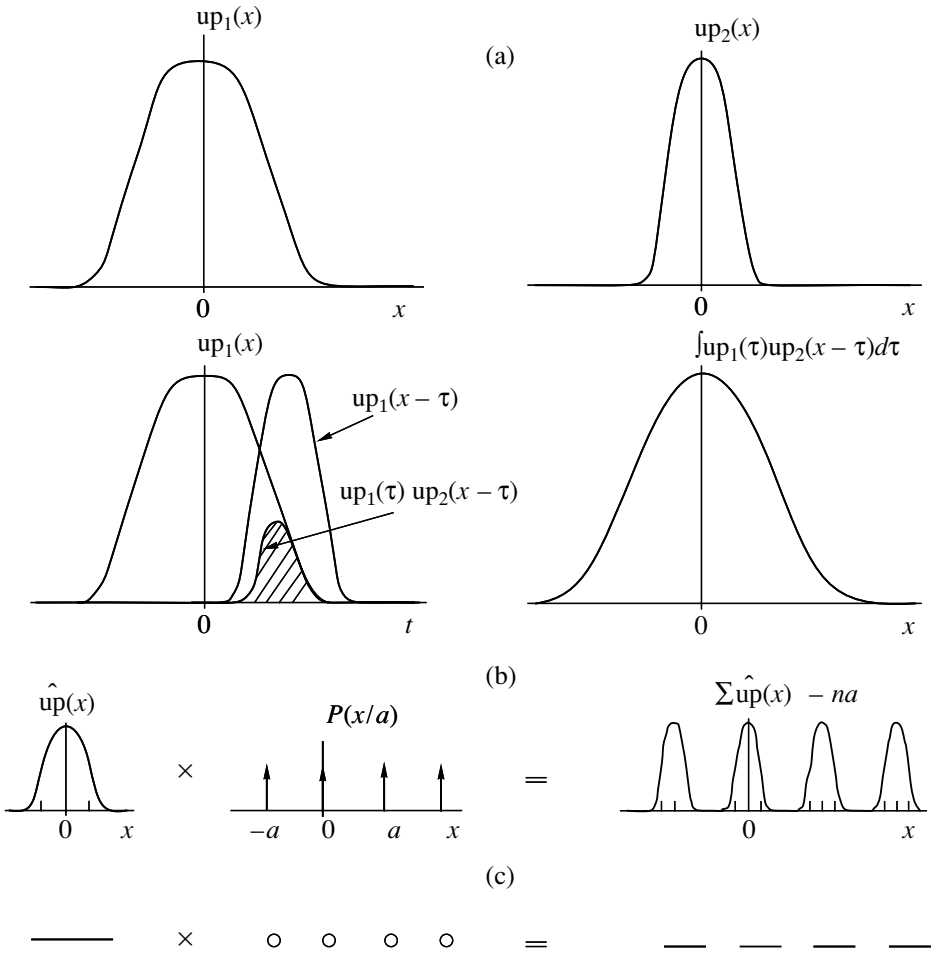

Fig. 1. (a) Convolution of the functions $up_1(x)$ and $up_2(x)$ and (b) convolution of the function $\hat{up}(x)$ (bell) and the lattice function $P(x/a)$ (plot of the functions); (c) plot of the carriers.

parental attributes. These attributes consist in the fact that the carrier has an extension. In the limiting case, the convolution of the function $\hat{up}(x)$, whose carrier is zero, does not change this function:

$$\begin{aligned}\hat{up}(x) * \delta(x) &= \delta(x) * \hat{up}(x) = \hat{up}(x),\\ \hat{up}(x) * \delta(x) &= \int_{-\infty}^{\infty} \hat{up}(x)\delta(x-\tau)d\tau\\ &= \int_{-\infty}^{\infty} \hat{up}(\tau)\delta(\tau - x)d\tau = \hat{up}(x).\end{aligned} \quad (6)$$

Here, the first integral is the convolution and the second integral is the selective property of the δ-function. For functions shifted from the origin of the chosen coordinate system, we have:

$$\hat{up}(x - x_1) * \delta(x - x_2) = \hat{up}(x - (x_1 + x_2)). \quad (7)$$

The convolution of a "good" function $\hat{up}(x)$ with a unit function $\mathbf{l}(x)$, which has a carrier $\mathrm{supp}\,\mathbf{l}(x) = [-\infty, \infty]$, yields the unit function normalized to the area under the function $\hat{up}(x)$

$$\hat{up}(x) * \mathbf{l}(x) = \int_{-\infty}^{\infty} \hat{up}(\tau)\mathbf{l}(x-\tau)d\tau = \int_{-\infty}^{\infty} \hat{up}(\tau)d\tau. \quad (8)$$

A case of convolution of the function $\hat{up}(x)$ with the lattice function

$$\hat{up}(x) * P\left(\frac{x}{a}\right) = \sum_{n=-\infty}^{\infty} \hat{up}(x - na) \quad (9)$$

is basic in applications. In Figs. 1b and 1c, the lattice function is shown that has repeated the function $\hat{up}(x)$ at position points of the δ-function. In addition to the integral operation of the convolution, there exists one more operation of the same type, which is called corre-

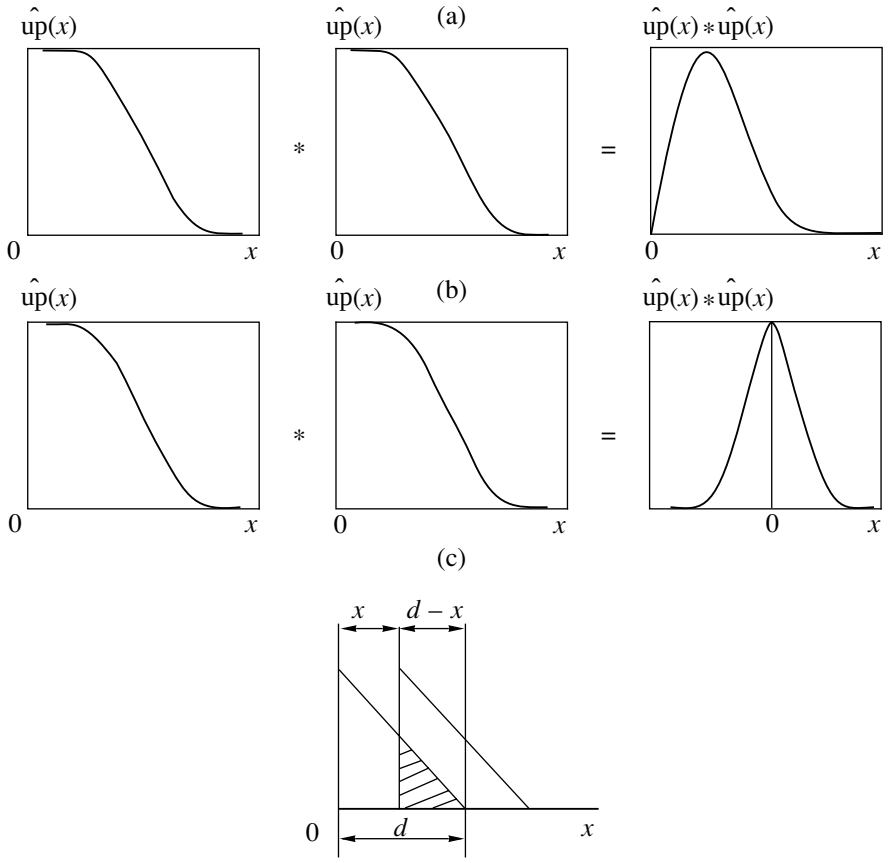

Fig. 2. Convolution and correlation: (a) convolution; (b) correlation; (c) extension (equal to $d - |x|$) of the autocorrelation region.

lation (or cross-correlation) and which makes it possible to obtain a third function from two others:

$$\hat{up}(x) = up_1(x) \bar{*} up_2(x) = \int_{-\infty}^{\infty} up_1^*(\tau) up_2(x+\tau) d\tau. \quad (10)$$

Here, the asterisk in the superscript implies complex conjugation. It follows from Eq. (10) that, in contrast to the convolution, the functions $up_1(x)$ and $up_2(x)$ do not commute. However, a particular case for the operation $\bar{*}$ is a variant called the autocorrelation when $up_1(x) \equiv up_2(x)$. In the case when $up_1^*(x) = up_2(x)$ [the function $up_1(x)$ is real-valued], we arrive at

$$\hat{up}(x) = up_1(x) \bar{*} up_2(x)$$
$$= \int_{-\infty}^{\infty} up_1(\tau) up_2(x+\tau) d\tau = up_1(x) * up_2(-x). \quad (11)$$

Hence, the autocorrelation for a real-valued function can be changed by the convolution of the original function obtained from the former one by means of inversion. If there exists the correlation of the finite function $\hat{up}(x)$, whose carrier is d, then the extension of the correlation region under the given shift x is equal to the difference $d - x$ (Fig. 2c); the correlation function can be written out as

$$\hat{up}(x) = up_1(x) \bar{*} up_2(x)$$
$$= (d-x)\langle up_1^*(\tau) up_2(x+\tau)\rangle,$$

where the average value is calculated over the correlation region. When the set of quantities $\{x_i\}$, $i = 1, 2, \ldots, R$ is given, the autocorrelation is determined by the expression

$$\hat{up}(n) = \sum_{j=1}^{R-n} x_{n+j} x_j = (R-n)\langle x_{n+j} x_j\rangle.$$

With allowance for formulas (4) and (11) for the function $up_1^*(x) = up_1(x)$, we obtain

$$\hat{up}(x) = up_1(x) \bar{*} up_1(x) = up_1(x) * up_1(-x)$$
$$= up_1(-x) * up_1(x) = \hat{up}(-x).$$

It is worth mentioning that the autocorrelation of a real-valued function exhibits the property of symmetrization of the finite function. This implies that the output function is even: $\hat{up}(x) = \hat{up}(-x)$. We note that for a

Table 1. Basic physical parameters for new synthesized Kravchenko windows and classical windows

Window	Equivalent noise band, bin	Correlation of overlapping segments (50% overlap), %	Parasitic amplitude modulation, dB	Maximum transformation loss, dB	Maximum decrease level for side lobes, dB	Side-lobe decrease rate, dB/octave	Band at the 6-dB level, bin	Coherent amplification
Kravchenko								
K	2.34	0.8	0.6	4.3	–47	–∞	3.05	0.31
K_1	2.9	0.06	0.4	5	–69.8	–∞	3.82	0.25
K_2	3.35	0.004	0.3	5.55	–93.2	–∞	4.45	0.21
K_3	3.75	2.9×10^{-4}	0.24	5.98	–116.4	–∞	4.90	0.19
K_4	4.11	2.1×10^{-5}	0.2	6.34	–139.8	–∞	5.41	0.17
K_{Ξ_2}	1.89	4.95	0.9	3.67	–34	–∞	2.51	0.5
K_{Ξ_3}	2.14	2.1	1.35	4.66	–51	–∞	2.05	0.5
K_{Ξ_4}	2.35	0.9	1.8	5.5	–68	–∞	1.78	0.5
K_{Ξ_6}	2.73	0.7	2.7	7.1	–102	–∞	1.5	0.5
Kaiser–Bessel								
$a = 3.0$	1.8	7.4	1.02	3.56	–69	–6	2.39	0.4
$a = 3.5$	1.93	4.8	0.89	3.74	–82	–6	2.57	0.37
Hamming	1.36	23.5	1.78	3.1	–43	–6	1.81	0.54
Blackman–Harris (four-term)	2	3.8	0.83	3.85	–92	–6	2.72	0.36

real-valued and even function $\hat{up}(x)$, operations of convolution and autocorrelation are undistinguished. For $\hat{up}^*(x) = \hat{up}(x) = \hat{up}(-x)$, we obtain that $\hat{up}(x) * \hat{up}(x) = \hat{up}(x) \bar{*} \hat{up}(x)$.

3. SYNTHESIZING NEW WINDOWS

Based on atomic functions, we now are studying new synthesized windows under the following parameters: $w(nT) = 0, |n| > \frac{N}{2}$, N is even, $w(nT) = w(-nT)$. To compare characteristics of new synthesized windows, we make use of the system of physical parameters introduced in [11]. It is well known that in practice (at $T = 1$), the following windows are widely used [11, 12].

1. The Kaiser–Bessel window

$$w(n) = \frac{I_0\left(\alpha\sqrt{1-\left(\frac{2n}{N-1}-1\right)^2}\right)}{I_0(\alpha)}, \quad 0 \le n \le N-1,$$

where I_0 is the Bessel function of the zero order, $\alpha = 2, 2.5, 3, 3.5$.

2. The Hamming window

$$w(n) = 0.54 - 0.46\cos\left(2\pi\frac{n}{N-1}\right), \quad 0 \le n \le N-1.$$

3. The Blackman–Harris (four-term) window

$$w(n) = 0.35875 - 0.48829\cos\left(\frac{2\pi}{N}n\right) + 0.14128\cos\left(\frac{2\pi}{N}2n\right) - 0.01168\cos\left(\frac{2\pi}{N}3n\right), \quad 0 \le n \le N-1.$$

Using theoretical results, we consider the window K [$up(x) * up(x)$, which is new and synthesized by the author] (see Table 1 and Fig. 3a) and determine its physical parameters. The calculation was performed for $N = 50$.

1. The equivalent noise band is $k_1(K) = 50 \times 0.0468 = 2.34$.

2. The correlation for the 50% overlap is $k_2(\mathrm{K}) = \frac{3.68}{446} = 0.8\%$.

3. The parasitic amplitude modulation is $k_3(\mathrm{K}) = -10\log\left|\frac{W(\pi/2)}{W(0)}\right|^2 = 0.6$.

4. The maximum transformation loss is $k_4(\mathrm{K}) = 10\log(2.34) + 0.6 = 4.3$ dB.

5. The maximum level of the side-lobe decrease is equal to $k_5(\mathrm{K}) = -47$ dB.

6. The asymptotic rate for the side-lobe decrease is $k_6(\mathrm{K}) = -\infty$.

7. The window width at the 6-dB level is $k_7(\mathrm{K}) = 3.05$.

8. The coherent amplification is $k_8(\mathrm{K}) = 0.31$.

For comparison, we present the calculated data for the K_2 [up(x) ∗ up(x) ∗ up(x) ∗ up(x)] synthesized window (Table 1, Fig. 3b).

9. The equivalent noise band is $k_1(\mathrm{K}_2) = 50 \times 0.0017 = 3.35$.

10. The correlation for the 50% overlap is $k_2(\mathrm{K}_2) = \frac{0.0125}{306} = 0.004\%$.

11. The parasitic amplitude modulation is $k_3(\mathrm{K}_2) = -10\log\left|\frac{W(\pi/2)}{W(0)}\right|^2 = 0.3$.

12. The maximum transformation loss is $k_4(\mathrm{K}_2) = 10\log(3.35) + 0.3 = 5.55$ dB.

13. The maximum level of the side-lobe decrease is equal to $k_5(\mathrm{K}_2) = -93.2$ dB.

14. The asymptotic rate for the side-lobe decrease is $k_6(\mathrm{K}_2) = -\infty$.

15. The window width at the 6-dB level is $k_7(\mathrm{K}_2) = 4.45$.

16. The coherent amplification is $k_8(\mathrm{K}) = 0.21$.

4. A NUMERICAL EXPERIMENT

Analysis of numerical results for synthesizing Kravchenko windows (Table 1) and classical Kaiser–Bessel, Hamming, and Blackman–Harris (four-term solution) windows has shown that the Kravchenko windows exceed the well-known windows in their physical parameters.

New windows exhibit a low parasitic amplitude modulation and a high decrease level for side lobes, which essentially depends on the degree of the convolution operation within the range from –47 to –139.8 dB. The other group of windows, i.e., the Kravchenko windows, are composed of convolutions of atomic functions $\Xi_n(x)$. We now give the basic physical parameters for the K_{Ξ_2} and K_{Ξ_4} windows (Table 1).

17. The equivalent noise bands are $k_1(\mathrm{K}_{\Xi_2}) = 50 \times 0.0178 = 1.89$ and $k_1(\mathrm{K}_{\Xi_4}) = 50 \times 0.047 = 2.35$.

Table 2. Basic physical parameters of new synthesized windows for Kravchenko–Hamming (KH), Kravchenko–Kaiser–Bessel (KKB), and Kravchenko–Blackman–Harris (KBH) windows

Window	Equivalent noise band, bin	Correlation of overlapping segments (50% overlap), %	Parasitic amplitude modulation, dB	Maximum transformation loss, dB	Maximum decrease level for side lobes, dB	Side-lobe decrease rate, dB/octave	Band at the 6-dB level, bin	Coherent amplification
KH	2.14	2.06	0.74	4.05	−71.2	−∞	2.78	0.35
KH_1	2.68	0.21	0.46	4.74	−96	−∞	3.5	0.27
KH_2	3.17	0.016	0.17	5.1	−120	−∞	4.1	0.23
KH_3	3.6	0.0012	0.026	5.8	−143	−∞	4.77	0.2
KKB	2.44	0.58	0.56	4.43	−50.2	−∞	3.2	0.29
KKB_1	2.97	0.042	0.38	5.1	−75.4	−∞	3.9	0.24
KKB_2	3.4	0.003	0.29	5.6	−100	−∞	4.45	0.21
KKB_3	3.81	2.3×10^{-4}	0.24	6	−123.6	−∞	4.9	0.19
KBH	2.55	0.31	0.5	4.6	−44.2	−∞	3.37	0.28
KBH_1	3.05	0.023	0.36	5.2	−68.7	−∞	3.97	0.25
KBH_2	3.46	0.0026	0.233	5.6	−115.8	−∞	5.09	0.21
KBH_3	3.85	1.9×10^{-4}	0.23	6	−116.2	−∞	5.1	0.19

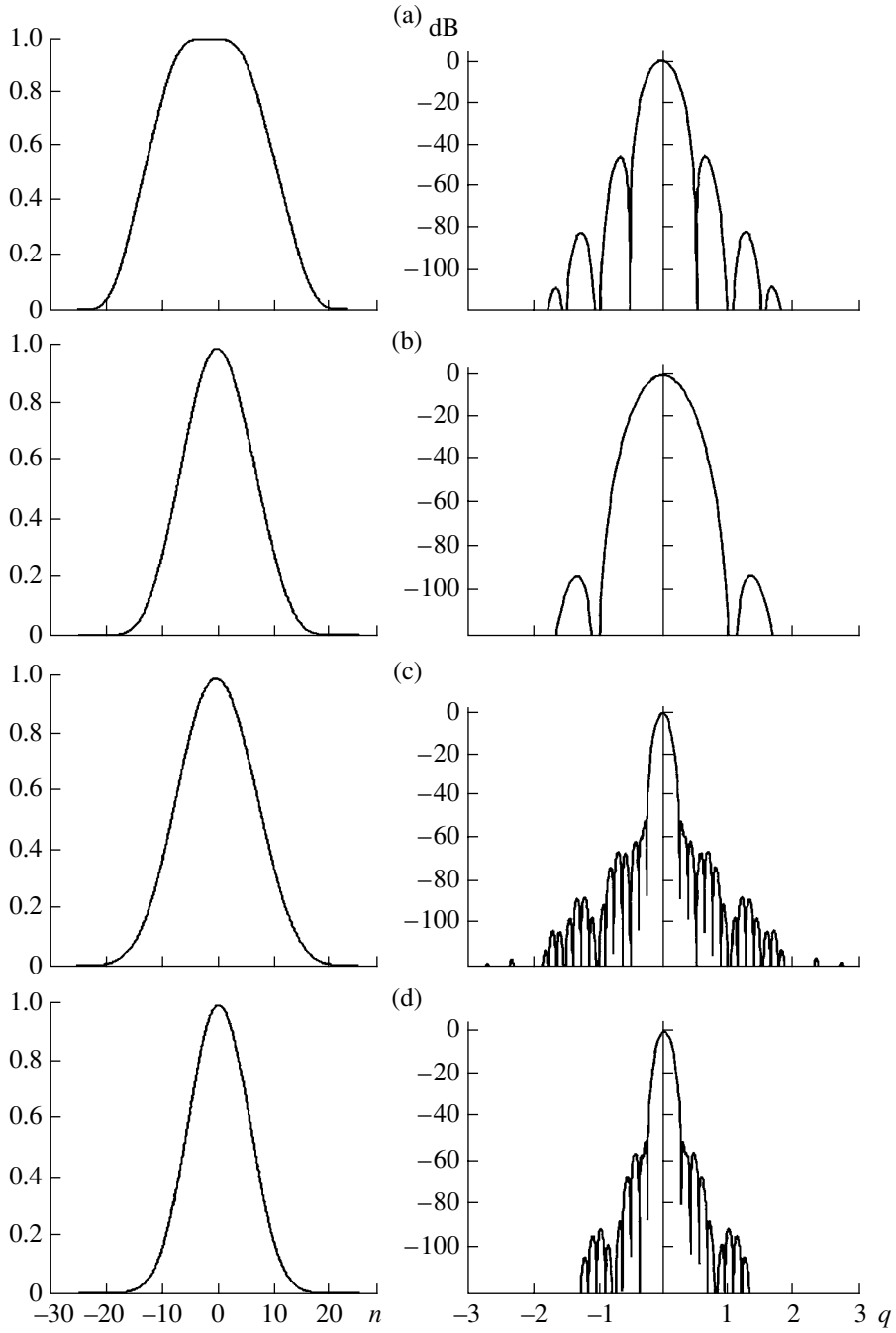

Fig. 3. Synthesized Kravchenko windows: (a), (b) Kravchenko windows (K, K_2); (c), (d) Kravchenko–Hamming windows (KH, KH_2); (e), (f) Kravchenko–Kaiser–Bessel windows (KKB, KKB_2); (g), (h) Kravchenko–Blackman–Harris windows (KBH, KBH_2). The functions are on the left, the logarithm of the Fourier transform for the corresponding window is on the right; n is the count number, $n \in \left[-\frac{N}{2}, \frac{N}{2}\right]$, $N = 50$ is the total number of counts; $\theta = \frac{2\pi}{N}$ is the normalized frequency.

18. The correlations for the 50% overlap are $k_2(K_{\Xi_2}) = 4.95\%$ and $k_2(K_{\Xi_4}) = 0.9\%$.

19. The parasitic amplitude modulations are $k_3(K_{\Xi_2}) = -10\log\left|\frac{W(\pi/2)}{W(0)}\right|^2 = 0.9$ and $k_3(K_{\Xi_4}) = 1.8$.

20. The maximum transformation losses are $k_4(K_{\Xi_2}) = 10\log(1.89) + 0.9 = 3.67$ dB and $k_4(K_{\Xi_4}) = 5.5$ dB.

21. The maximum levels of the side-lobe decrease are equal to $k_5(K_{\Xi_2}) = -34$ dB and $k_5(K_{\Xi_4}) = -68$ dB.

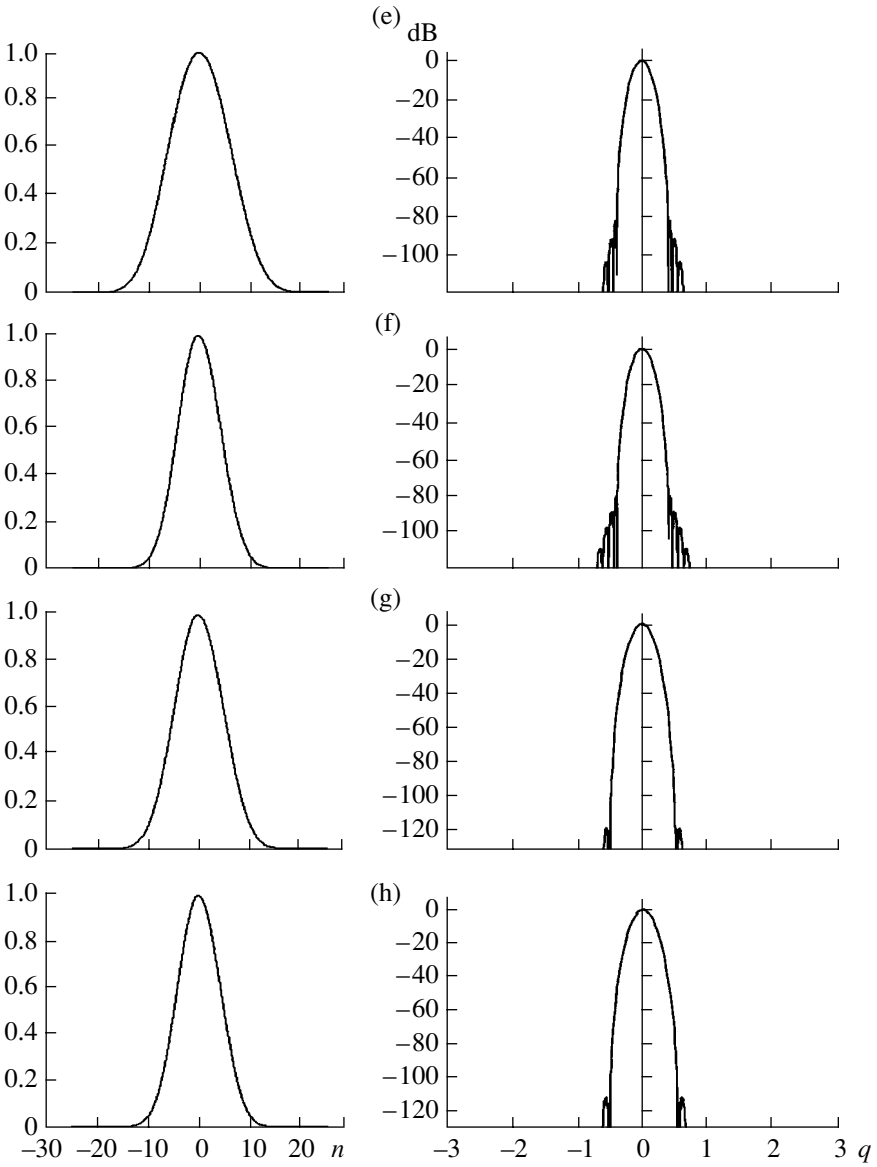

Fig. 3. (Contd.)

22. The asymptotic rates for the side-lobe decrease are $k_6(K_{\Xi_2}) = -\infty$ and $k_6(K_{\Xi_4}) = -\infty$.

23. The window widths at the 6-dB level are $k_7(K_{\Xi_2}) = 2.51$ and $k_7(K_{\Xi_4}) = 1.5$.

24. The coherent amplifications are $k_8(K_{\Xi_2}) = 0.5$ and $k_8(K_{\Xi_4}) = 0.5$.

We should emphasize the high selectivity of this group of Kravchenko windows: with the increase in the degree of the convolution operation, the transmission band (according to the 6-dB level) reduces from 2.51 bin [K_{Ξ_2} window] to 1.5 bin [K_{Ξ_6} window]. In addition to the good selectivity, the latter K_{Ξ_6} window also has a high level for the decrease of side lobes (−102 dB) and a low correlation factor for overlapping segments (exceeding this parameter for classical windows by an order of magnitude). Thus, this window can be applied for filtering signals with a small distance between equal-intensity spectral lines (e.g., in the application of radars for a group of targets). If we need windows with a very low correlation factor, a small value of the parasitic amplitude modulation, and a high level of the side-lobe decrease (down to –143 dB), it is possible to use the synthesized Kravchenko–Hamming (KH) windows, Kravchenko–Kaiser–Bessel (KKB) windows, and Kravchenko–Blackman–Harris (KBH) windows (Table 2 and Fig. 3). All the synthesized windows have an infinite rate of the side-lobe decrease. The

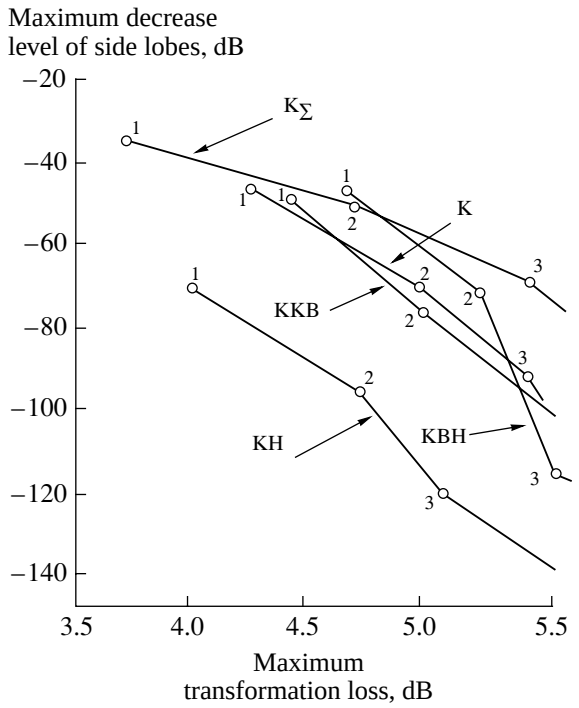

Fig. 4. Diagram for the relation between the transformation loss and the maximum level of the side-lobe decrease for new synthesized Kravchenko windows.

basic physical characteristics of the new synthesized windows are presented in Table 2 and in Fig. 3.

From the standpoint of practical applicability of the windows, the diagram for the dependence of the transformation loss and the maximum level of the side-lobe decrease is of the most interest (Fig. 4). As follows from this diagram, most optimal new synthesized windows are situated in its lower left corner. These windows have a low level of the side lobes, although the transformation loss is slightly enhanced. The latter parameter can be considerably improved by passing to the extension or compression of windows on the basis of properties of atomic functions. To do this, we employ a number of particular mathematical transformations. We transform the x-axis into the t-axis according to the formula $t = \frac{T}{X}x$. Then, we analyze how the basic physical parameters of new synthesized windows can change under these transformations (Tables 3 and 4). When extending the windows, the following physical effects are observed in the time region: the equivalent noise band narrows for all windows, the same occurs for the band corresponding to the 6-dB level, and the maximum transformation loss considerably decreases. In this case, the following disadvantages should be indicated: the correlation of overlapping segments increases, and the parasitic amplitude modulation deteriorates. These effects arise at the constant maximum level of the side-lobe decrease. Thus, the windows investigated compare well with known classical windows, and even exceed them for a number of parameters.

The results of this study were reported at the First International Workshop on Mathematical Modeling of Physical Processes in Inhomogeneous Media (Mexico, Guanajuato, March 20–22, 2001) [8] and at the Fourth International Symposium on Physics and Engineering

Table 3. Parameters of the new synthesized Kravchenko window with allowance for time variations

Relative extension of the weight function (window) in the time region, %	Equivalent noise band, bin	Correlation of overlapping segments (50% overlap), %	Parasitic amplitude modulation, dB	Maximum transformation loss, dB	Maximum decrease level for side lobes, dB	Side-lobe decrease rate, dB/octave	Band at the 6-dB level, bin	Coherent amplification
0	2.34	0.8	0.6	4.3	−47	−∞	3.05	0.31
5	2.22	1.42	0.67	4.13	–	–	2.92	0.32
10	2.1	2.35	0.74	3.96	–	–	2.78	0.34
15	1.98	3.72	0.83	3.8	–	–	2.61	0.36
20	1.87	5.64	0.94	3.66	–	–	2.46	0.39
25	1.75	8.24	1.07	3.5	–	–	2.3	0.41
30	1.64	11.6	1.22	3.38	–	–	2.15	0.44
35	1.52	15.7	1.42	3.24	–	–	2	0.47
40	1.42	20.5	1.67	3.2	–	–	1.83	0.51

Table 4. Parameters of new synthesized windows of Kravchenko–Hamming and Kravchenko–Blackman–Harris with allowance for time variations

Relative extension of the window in the time region, %	Equivalent noise band, bin	Correlation of overlapping segments (50% overlap), %	Parasitic amplitude modulation, dB	Maximum transformation loss, dB	Maximum decrease level for side lobes, dB	Side-lobe decrease rate, dB/octave	Band at the 6-dB level, bin	Coherent amplification
Kravchenko–Hamming window								
0	2.68	0.21	0.46	4.74	–96	–∞	3.5	0.27
5	2.55	0.4	0.51	4.57	–	–	3.37	0.28
10	2.42	0.74	0.57	4.41	–	–	3.2	0.3
15	2.3	1.32	0.64	4.26	–	–	3	0.31
20	2.1	2.25	0.72	4.05	–	–	2.85	0.33
25	2.02	3.7	0.82	3.88	–	–	2.64	0.36
30	1.88	5.7	0.94	3.68	–	–	2.48	0.38
35	1.75	8.6	1.1	3.52	–	–	2.3	0.41
40	1.62	12.4	1.28	3.38	–	–	2.15	0.44
Kravchenko–Blackman–Harris window								
0	3.4	0.003	0.29	5.6	–100	–∞	4.45	0.21
5	3.24	0.01	0.32	5.43	–	–	4.29	0.22
10	3.1	0.03	0.36	5.27	–	–	4.07	0.23
15	2.9	0.08	0.4	5.03	–	–	3.84	0.25
20	2.73	0.2	0.45	4.8	–	–	3.6	0.26
25	2.56	0.43	0.51	4.6	–	–	3.39	0.28
30	2.39	0.92	0.59	4.34	–	–	3.17	0.3
35	2.21	1.82	0.68	4.13	–	–	2.93	0.32
60	1.39	21.5	1.8	3.24	–	–	1.78	0.52

of Millimeter and Submillimeter Waves (Kharkov, Ukraine, June 4–9, 2001) [9].

ACKNOWLEDGMENTS

The author is grateful to Academician Yu.V. Gulyaev, Academician of the National Academy of Sciences of Ukraine V.L. Rvachev, Corresponding Member of the RAS V.I. Pustovoĭt, as well as to Professors E.G. Zelkin, V.A. Kashin, I.K. Lifanov, V.I. Merkulov, H. Peres-Meana, A.A. Potapov, V.I. Ponomarev, A.V. Sokolov, and Ya.S. Shifrin for discussing the results of this work.

REFERENCES

1. V. F. Kravchenko, M. A. Basarab, V. I. Pustovoĭt, and H. Perez-Meana, Dokl. Akad. Nauk **377**, 183 (2001) [Dokl. Phys. **46**, 9 (2001)].
2. V. F. Kravchenko, M. A. Basarab, and H. Perez-Meana, Radiotekh. Élektron. **46** (5) (2001).
3. A. A. Goncharenko, V. F. Kravchenko, and V. I. Ponomarev, *Remote Probing Inhomogeneous Media* (Mashinostroenie, Moscow, 1991).
4. V. F. Kravchenko, V. A. Rvachev, and V. L. Rvachev, Radiotekh. Élektron. **40**, 1385 (1995).
5. V. F. Kravchenko, V. A. Rvachev, and V. L. Rvachev, Dokl. Akad. Nauk SSSR **306**, 78 (1989) [Sov. Phys. Dokl. **34**, 430 (1989)].
6. Yu. V. Gulyaev, V. F. Kravchenko, and V. L. Rvachev, Dokl. Akad. Nauk **342**, 29 (1995).
7. V. F. Kravchenko, M. A. Basarab, and H. Perez-Meana, Telecommun. and Radio Eng. **56**, 3 (2001).
8. V. F. Kravchenko, M. A. Basarab, and H. Perez-Meana, in *Proceedings of I International Workshop on Mathematical Modeling of Physical Processes in Inhomoge-*

neous Media, Guanajuato, Mexico, March 20–22, 2001 (Gto., Mexico, 2001), p. 5.

9. V. F. Kravchenko and M. A. Basarab, in *Proceedings of IV International Symposium on Physics and Engineering of Millimeter and Submillimeter Waves, Kharkov, Ukraine, 2001* (Kharkov, 2001).
10. V. F. Kravchenko and M. A. Basarab, Élektromag. Volny Élektron. Sistemy **6** (4), 3 (2001).
11. F. Harris, Proc. IEEE Trans. **66**, 60 (1978).
12. D. Dudgeon and R. Mersereau, *Multidimensional Digital Signal Processing* (Prentice-Hall, USA, Englewood Cliffs, 1984; Mir, Moscow, 1988).
13. S. L. Sobolev, *Selected Problems in Theory of Functional Spaces and Generalized Functions* (Nauka, Moscow, 1989).
14. V. I. Merkulov, A. I. Perov, V. N. Sablin, *et al.*, *Radar Meters of Ranges and Velocities* (Radio i Svyaz', Moscow, 1999), Vol. 1.
15. S. Z. Kuz'min, *Digital Radiolocation* (Kvits, Kiev, 2000).

Translated by G. Merzon

Doklady Physics, Vol. 47, No. 1, 2002, pp. 61–63. Translated from Doklady Akademii Nauk, Vol. 382, No. 3, 2002, pp. 329–331.

TECHNICAL PHYSICS

Method of Almost Complete Operator Inversion in the Theory of Connected Strip–Slotted Transmission Lines

A. S. Aref'ev*, V. A. Neganov*, and E. I. Nefedov**

Presented by Academician O.M. Belotserkovskiĭ April 24, 2001

Received June 21, 2001

1. INTRODUCTION

Problems concerning natural waves for a series of both screened strip transmission lines and slotted transmission lines can be formulated in the form of vector integral equations of the first kind with respect to electric-current density components on strips or electric-field intensity components on slots. The kernel elements of these integral equations implicitly contain both logarithmic and Cauchy singularities. Employing the projection-operator technique to this equation is always accompanied by a change from the singular kernel to a regular one and, therefore, introduces an incorrectness into the statement of the problem [1].

The method of partial integral-operator inversion [2], which leads to an integral equation of the second kind, makes it possible to avoid the incorrectness. However, this method is associated with considerable analytic transformations of integral equations. This imposes certain constraints on the class of problems being solved by this method. In particular, the constraint imposed on the domain of definition for the integral equation of the first kind has remained significant. Indeed, most electrodynamic problems solved to date were defined only on an interval of the real axis.

2. A METHOD PROPOSED

In this paper, we extend the method of partial operator inversion (which is more correctly referred to as a method of almost complete operator inversion) to the case of connected plane transmission lines. The generalization is based on formulas for the partial inversion of both the Cauchy singular integral and an integral having a logarithmic singularity, which are defined on a combination of intervals

$$V = \bigcup_{m=1}^{L} V_m,$$

where $V_m = (v_{m1}, v_{m2})$. We also assume that $V \subset (-1, 1)$. We define the following system of functions on V:

$$T_i^{(m)}(v) = \begin{cases} T_i(a_m + b_m v), & v \in V_m \\ 0, & v \in V \backslash V_m. \end{cases} \quad (1)$$

Here, $i = 0, 1, \ldots$; $m = 1, 2, \ldots, L$, T_i are the Chebyshev polynomials of the first kind; and

$$a_m = -\frac{v_{m2} + v_{m1}}{v_{m2} - v_{m1}}, \quad b_m = \frac{2}{v_{m2} - v_{m1}}.$$

The system of functions $T_i^{(m)}$ is orthogonal on V with the weight coefficient Q^{-1}, which is defined on each of the intervals V_m by the relationship

$$Q^{-1}(v) = (1 - (a_m + b_m v)^2)^{-1/2}.$$

It is also evident that the system $T_i^{(m)}$ is complete in a space of functions that are quadratically integrable on V with a measure corresponding to the weight of Q^{-1}.

We now consider the Cauchy singular integral

$$\frac{1}{\pi}\int_V \frac{\varphi(v')}{v' - v} dv' = f(v), \quad v \in V. \quad (2)$$

We suggest that the function φ belongs to the class H^* of functions satisfying the Hölder condition [3] and, possibly, having integrable singularities at the ends of intervals V_m. We expand kernel (2) into the singular $K^{[S]}$ and regular $K^{[R]}$ parts:

$$(v' - v)^{-1} = K^{[S]}(v', v) + K^{[R]}(v', v), \quad (3)$$

* *Povolzhskaya State Academy of Telecommunication and Informatics, ul. L'va Tolstogo 23, Samara, 443099 Russia*

** *Institute of Radio Engineering and Electronics, Russian Academy of Sciences (Fryazino Branch), pl. Vvedenskogo 1, Fryazino, Moscow oblast, 141120 Russia*

1028-3358/02/4701-0061$22.00

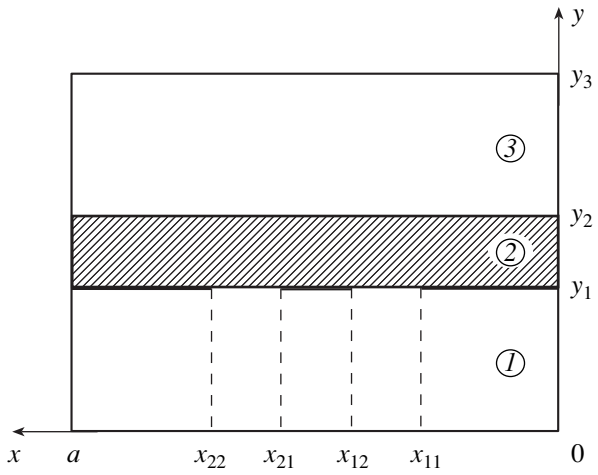

Cross section of the coplanar waveguide.

assuming that

$$K^{[S]}(v', v) = (v' - v)^{-1} \sum_{m=1}^{L} T_0^{(m)}(v') T_0^{(m)}(v).$$

We then define an integral operator S on H^*,

$$S(v)\varphi = \frac{1}{\pi}\int_V K^{[S]}(v', v)\varphi(v')dv', \quad v \in V,$$

and a projection operator P given by the relationship

$$P(v)\psi = 2(\pi Q(v))^{-1} \sum_{m=1}^{L} b_m \sum_{n=1}^{\infty} T_n^{(m)}(v)$$
$$\times \int_V Q(v') U_{n-1}^{(m)}(v')\psi(v')dv', \quad v \in V.$$

Here, the functions $U_n^{(m)}$, in much the same way as functions $T_n^{(m)}$, can be expressed in terms of the Chebyshev polynomials of the second kind. Using the expansion

$$\varphi(v) = Q^{-1}(v) \sum_{m=1}^{L} \sum_{n=0}^{\infty} \varphi_n^{(m)} T_n^{(m)}(v), \quad v \in V,$$

we can easily prove the validity of the equality

$$P(v)S(v')\varphi = \varphi(v) - Q^{-1}(v) \sum_{m=1}^{L} \varphi_0^{(m)} T_0^{(m)}(v).$$

Then, expanding integral (2) with the help of expansion (3) and applying the operator P to the result obtained, we arrive at the following relationship:

$$\varphi(v) = (\pi Q(v))^{-1}\Bigg[\sum_{m=1}^{L} T_0^{(m)}(v)\Bigg(\pi b_m \sum_{k=1}^{L} \frac{\varphi_0^{(k)}}{b_k}$$
$$- \int_V \mathrm{sgn}(v' - v)\sqrt{(a_m + b_m v')^2 - 1}$$
$$\times K^{[R]}(v', v)\varphi(v')dv'\Bigg)$$
$$- \int_V Q(v')K^{[S]}(v', v) f(v')dv\Bigg], \quad v \in V. \tag{4}$$

Similarly, for the integral with a logarithmic singularity,

$$\frac{1}{\pi}\int_V \ln|v' - v|\xi(v')dv' = g(v'), \quad v \in V, \tag{5}$$

we obtain

$$\xi(v) = (\pi Q(v))^{-1}\Bigg[\sum_{m=1}^{L} T_0^{(m)}(v)\Bigg(\frac{-b_m^2}{\ln(2b_m)}$$
$$\times \int_V T_0^{(m)}(v')g(v')Q^{-1}(v')dv'$$
$$+ \frac{b_m}{\ln(2b_m)}\int_V (1 - T_0^{(m)}(v'))\ln\Big(|a_m + b_m v'|$$
$$+ \sqrt{(a_m + b_m v')^2 - 1}\Big)\xi(v')dv'$$
$$- \int_V \mathrm{sgn}(v' - v)\sqrt{(a_m + b_m v')^2 - 1}$$
$$\times K^{[R]}(v', v)\xi(v')dv'\Bigg)$$
$$+ \int_V Q(v')K^{[S]}(v', v)g'(v')dv'\Bigg], \tag{6}$$
$$v \in V.$$

It seems natural to refer to relationships (4) and (6) as formulas for partial inversion of integrals (2) and (5).

We now employ the procedures of partial operator inversion proposed above in order to evaluate spectral parameters of a coplanar waveguide. The cross section of the waveguide is shown in the figure. Three infinitely thin strips made of a perfect conductor are deposited

onto an insulating substrate (region *2*). The structure is placed into a rectangular metallic screen, the wall losses being ignored.

The integral equation of the first kind for the coplanar waveguide coincides with the equation describing a screened slotted transmission line [4]. However, the domain of definition in the former case is a combination of intervals on the *x*-axis, which correspond to the slots.

Isolating the singularity of kernel [4] and making the change of variables

$$v = \cos\frac{\pi x}{a}, \qquad v' = \cos\frac{\pi x'}{a},$$

we arrive at integrals (2) and (5). Then, the method of partial operator inversion, which is based on transformations (2), (4) and (5), (6), should be applied to the equation obtained. Furthermore, using projection basis (1), we should solve the boundary value problem numerically.

When calculating, we took the following values of the parameters: $y_1 = y_3 - y_2 = 0.225a$, $y_2 - y_1 = 0.05a$, $x_{11} = 0.375a$, $x_{12} = 0.425a$, $x_{21} = 0.45a$, and $x_{22} = 0.55a$. The values of the permittivity and of the permeability for the dielectric layers and the normalized wave number were $\varepsilon^{(1)} = \varepsilon^{(3)} = 1$, $\varepsilon^{(2)} = 9.35$, $\mu^{(i)} = 1$ ($i = 1, 2, 3$), and $ka = 1.7$, respectively.

The data listed in Tables 1 and 2 illustrate the convergence in the spectral parameters for the method of partial operator inversion. Here, we have chosen the rates γ/k of wave slowing-down for the first and second natural waves of the coplanar waveguide as spectral parameters (γ is the wave propagation constant). The parameters *N* and *M* are the number of terms taken into account in the representation of the field components at each slot and in the kernel of the integral equation of the second kind.

Thus, we have presented in this paper the procedures of partial inversion for the singular Cauchy integral and the integral having a logarithmic singularity, both being defined on a combination of intervals. The method allowed us to construct a well convergent mathematical model of a coplanar waveguide. This method can easily be extended to the case of an arbitrary finite number of slotted transmission lines or strip transmission lines placed in the same plane inside a rectangular screen.

Table 1

N	γ/k ($M = 400$)	
1	2.085282847	0.56073294
2	2.087857031	0.55166405
3	2.087794630	0.55149564
4	2.087782304	0.55148941
5	2.087781984	0.55148843
6	2.087781985	0.55148836

Table 2

M	γ/k ($N = 7$)	
25	2.08775881	0.55142105
50	2.08777951	0.55148013
100	2.08778148	0.55148736
200	2.08778193	0.55148823
400	2.08778199	0.55148835

REFERENCES

1. A. F. Verlan' and V. S. Sizikov, *Integral Equations: Methods, Algorithms, and Codes* (Naukova Dumka, Kiev, 1986).
2. V. A. Neganov, E. I. Nefedov, and G. P. Yarovoĭ, *Strip–Slot Structures of Super-High and Ultra-High Frequencies* (Nauka, Moscow, 1996).
3. F. D. Gakhov, *Boundary-Value Problems* (Nauka, Moscow, 1977, 3rd ed.; Reading, Mass., Addison-Wesley, 1966).
4. V. A. Neganov and E. I. Nefedov, Dokl. Akad. Nauk SSSR **284**, 1127 (1985) [Sov. Phys. Dokl. **30**, 889 (1985)].

Translated by V. Chechin

Doklady Physics, Vol. 47, No. 1, 2002, pp. 64–66. Translated from Doklady Akademii Nauk, Vol. 382, No. 3, 2002, pp. 332–334.

TECHNICAL PHYSICS

Physical Nature of the Effects of Thermomagnetic and Thermomechanical Treatment of Ferromagnets

V. V. Gubernatorov and T. S. Sycheva

Presented by Academician N.A. Vatolin June 1, 2001

Received June 26, 2001

In spite of the fact that effects of thermomagnetic and thermomechanical treatments were discovered long ago [1, 2] and are widely used in industry, their physical nature is not clarified until now.[1] To date, two models that explain the rise in μ_{max} and B_r after thermomagnetic and thermomechanical treatments are the most popular. One of them relates the rise in μ_{max} with the anisotropy of the shape of precipitated particles [4]. The other explains this rise with the reorienting axes of pairs of nearest atoms of dissolved elements (directional ordering) in an alloy having an ordered arrangement of the component's atoms (superstructure) [5]. At the same time, the atomic mechanism responsible for the reorientation of these axes is not discussed in this case. However, the above models fail to explain numerous experimental data. For example, it is unclear why the above effects are thermally unstable (when annealed without external actions, the effects disappear). The decrease in H_c and P after the thermomagnetic and thermomechanical treatments is associated with the destabilization of the magnetic domain structure [3], but the reasons for this phenomenon remain incomprehensible.

In this study, we have investigated the relation between the effects of thermomagnetic and thermomechanical treatments and strain aging.[2]

From the standpoint of a positive effect of strain aging on the efficiency of thermomagnetic and thermomechanical treatments, the stage of ordering can be the most significant, since atmospheres, segregations, and precipitated particles increase H_c and P (atmospheres and segregations, in addition, lead to a kink in the magnetization curve [7]). For the case of strain aging, the effect of ordering on the efficiency of the thermomagnetic treatment was examined experimentally.

We used samples of Fe–3 wt % Si alloy, which had a size of $0.33 \times 5 \times 100$ mm, a (110)[011] texture, and 2–4-mm grains. After high-temperature annealing at 1000°C for 30 min, they were slowly (0.5°C/min) and rapidly (60–100°C/min) cooled. In the latter case, in contrast to the former one, the material contained fresh defects. This is explained by the fact that, upon slow cooling, the defects hardly appear and, even having appeared, have time to interact with atoms of dissolved chemical elements. Furthermore, the samples were successively subjected to strain aging at 400°C for 10 h and to thermomagnetic treatment at 400°C for 15 min in an alternating magnetic field with a frequency of 50 Hz and an amplitude of 10 kA/m. After each treatment, we measured the magnetic-hysteresis loops and determined H_c (see table).

After various thermal treatments, all the samples exhibited usual (without kinks) magnetization curves. The absence of kinks in the curves indicates that, for an alloy subjected to strain aging in chosen treatment

Effect of thermal treatment on the quantity H_c, A/cm, in (Fe–3% Si) alloy

Treatment	Cooling after high-temperature annealing	
	slow	rapid
High-temperature annealing	0.19	0.26
High-temperature annealing + strain aging	0.19	0.22
High-temperature annealing + strain aging + thermomagnetic treatment	0.18	0.10

[1] Holding of a ferromagnet at a certain elevated temperature and its cooling to a lower temperature in the presence of either an external magnetic field or a uniaxial tensile stress is called thermomagnetic treatment and thermomechanical treatment, respectively. For soft-magnetic alloys that were subjected to either thermomagnetic or thermomechanical treatment in the direction of external actions, the maximum magnetic permeability μ_{max} and the residual induction B_r increase, whereas the coercive force H_c and the specific electromagnetic loss P decrease [3].

[2] Strain aging is interaction between atoms of dissolved elements and fresh defects in a crystal lattice, which were introduced into a material by a certain method, e.g., upon rapid cooling. The redistribution of atoms of dissolved elements under strain aging corresponds to the distribution of defects in the material. Strain aging has four subsequent stages: ordering, formation of atmospheres, formation of segregations, and precipitation [6].

Institute of Metal Physics, Ural Division, Russian Academy of Sciences, ul. S. Kovalevskoĭ 18, Yekaterinburg, 620219 Russia

1028-3358/02/4701-0064$22.00

regimes, only the ordering stage takes place, which determines the effect of thermomagnetic treatment.

The significant positive effect of the thermomagnetic treatment can be caused by the following reasons.

1. In Fe–3%Si alloy at the stage of ordering under strain aging, there appear microvolumes of the type of Guinier–Preston zones (clusters) with an elevated silicon content and the B2 (FeSi) superstructure. The clusters that appeared can have the shape of globules (when the temperature of strain aging is above the Curie point), since such a shape corresponds to a state with a minimum surface energy. The appearance of anisotropic clusters (when the temperature of strain aging is below the Curie point) oriented along the domain magnetization (similar to precipitated particles in [8, 9]) is also possible. The clusters are distributed throughout the volume of the material in accordance with a defect structure (but rather chaotically) and, according to [10], have dimensions on the order of several nanometers.

The lowering of H_c under strain aging is caused by partial relieving internal stresses, which is associated with a decrease in the number of defects and a redistribution of the remaining defects into low-energy configurations, as well as due to the stress relaxation in the process of interaction between defects and atoms of dissolved elements.

2. Under thermomagnetic treatment, the magnetic field reorients the axes of pairs of nearest silicon atoms in clusters so that the angle between the axes and the field direction becomes minimal. We propose one possible mechanism responsible for the reorientation of axes of silicon-atom pairs, namely, the jump of a part of the silicon atoms from central sites of a cubic lattice to its vertices. This process occurs due to the existence of thermal vacancies in the material. The state when silicon atoms are situated in the cube vertices (i.e., directional ordering) is nonequilibrium and, thermally unstable. Therefore, upon heating or cooling in the absence of a magnetic field, silicon atoms in the alloy come back to their previous sites, and the effect of thermomagnetic treatment disappears, which is observed experimentally.

According to [3], the larger the number of pairs of nearest silicon atoms, the higher the effect of thermomagnetic treatment. Therefore, we should expect that its maximum effect would correspond to complete ordering in the case of the stoichiometric alloy composition. However, as was shown for Fe–Ni alloys [11], the maximum effect under thermomagnetic treatment is observed in an alloy containing a significantly lower nickel content compared to the stoichiometric composition. Hence, first, the maximum effect of thermomagnetic treatment is attained when the number of pairs of nearest atoms of a dissolved element is optimal (consequently, when the number of clusters with superstructure is also optimal), which holds for a certain but nonstoichiometric alloy composition. Second, the effect of thermomagnetic treatment depends not only (and in any case, insignificantly) on the reorientation of axes of pairs of a dissolved-element atoms, since the maximum effect of the thermomagnetic treatment with respect to μ_{max} exceeds by a factor of three the effect obtained in the case of reorienting the maximum possible number of pairs [11].

3. Under thermomagnetic treatment, globular clusters formed in the process of strain aging acquire an anisotropic shape, while anisotropic clusters reorient. In both cases, they become extended along the direction of an applied external field, which leads to a decrease in the free energy of the system because of reducing the magnetostatic energy and an increase in μ_{max}. Probably, this is the anisotropy of the shape of clusters oriented along the magnetic field that causes the maximum effect with respect to μ_{max} in [11].

Note that H_c and P can be unchanged or can even rise. This is associated with the chaotic location of clusters, which stabilizes the magnetic domain structure.

4. Estimates for the effect of an external magnetic field on strain aging were performed in [12]. On the basis of these estimates, it is possible to assume that, under thermomagnetic treatment in an alternating magnetic field, the magnetoelastic interaction between clusters, impurities, and defects (inhomogeneities) with moving walls of magnetic domains takes place. The result of this interaction is the redistribution of the inhomogeneities mentioned above throughout the alloy volume. They migrate, forming narrow alternating regions (enriched by clusters, impurities, and defects) that penetrate through the bulk of the sample (or a grain) and are extended along the field direction. The distances between these regions are specified by the amplitude of the domain-wall vibrations under the thermomagnetic treatment. The occurrence of such regions additionally increases μ_{max} and decreases H_c and P because of the destabilization of the magnetic domain structure, since the motion of domain walls in the process of magnetization reversal occurs in pure volumes free of clusters, impurities, and defects.

In addition, upon cooling, the samples undergo uniaxial tension due to the difference in thermal-expansion coefficients of the regions of aggregating inhomogeneities and pure volumes, which will still more strongly reduce H_c and P. As a result, after the high-temperature annealing of a rapidly cooled alloy, H_c is lowered down to a value significantly smaller than that obtained for an alloy cooled slowly (see table).

Probably, similar processes also occur under both thermomagnetic treatment in a constant magnetic field and thermomechanical treatment. In all these cases, the motive force responsible for the processes of formation, redistribution, and modification of cluster shapes, reorientation of axes of pairs of nearest atoms of dissolved elements, as well as redistribution of impurities and defects, is uniaxial tensile stress. In the case of the thermomagnetic treatment in a constant magnetic field, the

cause of uniaxial tensile stress is a positive magnetostriction. The validity of the above statement is confirmed by the transformation of cube-shaped particles of the ordered phase in a lamel under the creep process [13].

Thus, a new concept explaining the effects of thermomagnetic and thermomechanical treatments is proposed. The essence of this concept (in our approach) consists in the fact that, along with existing models, regularities in strain aging and in the interaction between the magnetic-domain walls with both atoms of dissolved elements and defects of the crystal lattice is used.

ACKNOWLEDGMENTS

This work was supported by the Russian Foundation for Basic Research (project no. 99-02-16279).

REFERENCES

1. B. H. Pender and P. L. Jones, Phys. Rev. **1**, 259 (1913).
2. Ya. S. Shur and A. S. Khokhlov, Dokl. Akad. Nauk SSSR **53**, 39 (1946).
3. V. A. Zaĭkova, I. E. Startseva, and B. N. Filippov, *Domain Structure and Magnetic Properties of Electrotechnical Steels* (Nauka, Moscow, 1992).
4. S. Kaya, Rev. Mod. Phys. **25**, 49 (1953).
5. L. Neel, J. Phys. Radiat. **12**, 339 (1951).
6. V. K. Babich, Yu. P. Gul', and I. E. Dolzhenkov, *Strain Aging of Steels* (Metallurgiya, Moscow, 1972).
7. V. V. Gubernatorov, A. P. Potapov, B. K. Sokolov, *et al.*, Fiz. Met. Metalloved. **91**, 40 (2001).
8. S. Libovicky, Phys. Status Solidi A **12**, 539 (1972).
9. A. S. Ermolenko, É. N. Melkisheva, and Ya. S. Shur, Fiz. Met. Metalloved. **18**, 540 (1964).
10. E. N. Vlasova and B. V Molotilov, Pretsizion. Splavy, No. 5, 71 (1979).
11. J. F. Dillinger and R. M. Bozorth, Physics (N. Y.) **6**, 280 (1935).
12. V. V. Gubernatorov, A. P. Potapov, A. I. Deryagin, and T. S. Sycheva, Fiz. Met. Metalloved. **92**, 39 (2001).
13. Yu. N. Gornostyrev, N. D. Bakhteeva, N. I. Vinogradova, and O. V. Furzikov, Fiz. Met. Metalloved. **76**, 94 (1993).

Translated by Yu. Vishnyakov

Doklady Physics, Vol. 47, No. 1, 2002, pp. 67–71. Translated from Doklady Akademii Nauk, Vol. 382, No. 3, 2002, pp. 335–340.

TECHNICAL PHYSICS

Mechanism of Deformation and Nucleation of Fatigue Cracks in Aluminum Polycrystals under Alternating Bending

Academician V. E. Panin, T. F. Elsukova, and G. V. Angelova

Received August 16, 2001

1. According to the ideas of physical mesomechanics [1, 2], the surface layers of loaded solids correspond to an important mesoscopic structural level of deformation. In the case of cyclic loading, plastic strain develops mainly in the near-surface layers of a material [3–6]. This fact causes a determining role of the surface in the nucleation and development of fatigue fracture. Investigations of the mechanism of cyclic deformation on the mesoscale level [7–9] show that the main bulk of a specimen experiences only elastic strain under cyclic loading, while its surface layers undergo an alternating tension–compression in the plastic domain. In developing such strain, two effects play a fundamental role. First is the Bauschinger effect, which is accompanied by accumulating a significant degree of plastic strain in the surface layers for a large number of loading cycles. Second is the character of conjugation between the plastically deformed surface layer and an elastically deformed substrate (the effect of strain incompatibility), which leads inevitably to the nucleation of fatigue cracks in the near-surface layer.

This study is devoted to the investigation of the mechanism for developing the fatigue fracture in the surface layer of aluminum polycrystals under cyclic loading.

2. As a material for investigation, we used A6 commercial aluminum. Flat dumb-bell specimens were of $40 \times 8 \times 1$ mm in size of the gage section. For a large-scale observation of the pattern of nucleation and development of the surface strain and fracture, the specimens were previously treated to obtain a coarse-grained structure. Individual surface grains were 8–15 mm long and 2–7 mm wide. The loading was performed by alternating bending, which predominantly provided strain only in surface layers of the specimen. As a quantitative characteristic of fatigue, we took the number N_f of cycles to fracture. For obtaining extended patterns of the strain mechanism in the surface layers at the mesolevel, we used montages of optical images of the deformed-specimen surface, obtained with a scanning optical microscope. In addition, we analyzed fields of displacement vectors, which were obtained employing the TOMSC optical television measuring complex [10].

3. In Fig. 1, we show a typical pattern of slip traces and nucleation of surface cracks in coarse grains *A* and *B* in the surface layer of a flat aluminum specimen for the number $N = 7.6 \times 10^6$ of loading cycles. The following features of developing the plastic strain and the fatigue cracks in the surface layer are typical.

The first plastic shears develop in a coarse grain *A* located near the immobile grip, where a maximum amplitude of bending is set. These shears arise alternatively on the opposite boundaries of the grain *A* and propagate towards one another. The front of shears moves along the grain according to the switching-wave scheme.

When the plastic strain completely envelopes the grain *A*, the shears in the adjacent grain *A* begin to develop along the conjugate directions of maximum tangential stresses τ_{max}. The primary shears along a lengthy axis of the grain *B* develop the most intensely. The shear in the conjugate direction τ_{max} distributed more rarely superimpose onto the primary ones.

The approach of the front of intense primary shears in the grain *B* to the strengthened grain *A* induces the initiation of a strong bending–torsion effect in the near-boundary band *C*. In this zone, a powerful kink band develops; the accommodation shears propagate in this band as the mechanism of material rotation.

For a reasonably large number of loading cycles, the surface tearing-mode shears arise in the band of intense primary shears of the grain *B*. An enhancement of the bending–torsion effect in the kink band *C* forms a powerful concentrator of stresses in this band, which, at first, initiates the tearing-mode shear in the adjacent grain *A* and then the accommodation crack in the kink band itself. The crack in the kink band *C* connects cracks in the grains *A* and *B* nearest to each other. This process is completed by the formation of an extended zigzag surface crack enveloping the entire surface of the specimen.

The directions for all the types of shears in the region of the tips of primary-surface cracks in the grain *B* for their propagation in the kink band *C* are

Institute of Strength Physics and Materials Science, Siberian Division, Russian Academy of Sciences, Akademicheskiĭ pr. 2/1, Tomsk, 634021 Russia

1028-3358/02/4701-0067$22.00

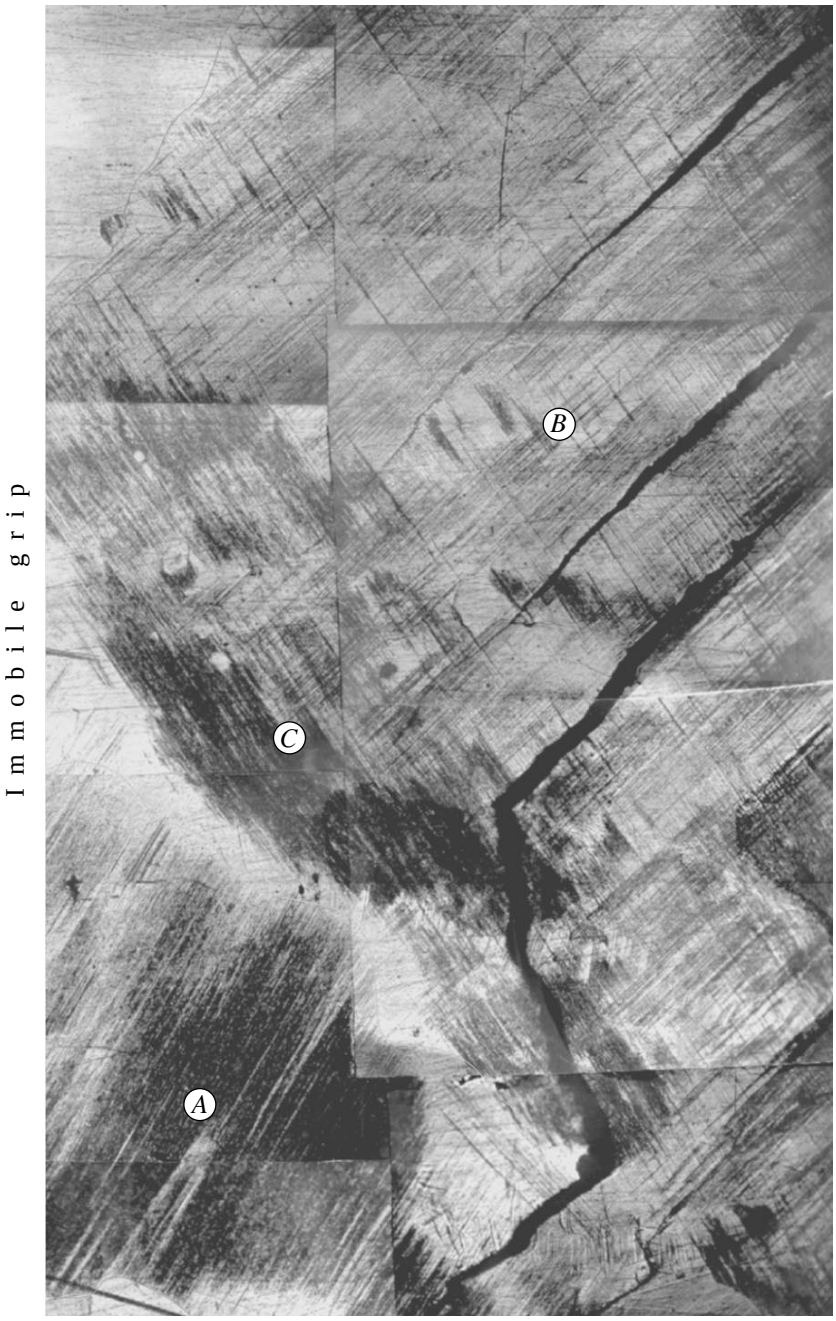

Fig. 1. Development of shears, a kink band *C*, and microcracks in the grains *A* and *B* of aluminum after $N = 7.6 \times 10^6$ loading cycles, 30×.

identified by constructing the fields of displacement vectors. The typical pattern of such a vector field is shown in Fig. 2 for the specimen subjected to alternating bending with a loading-cycle number $N + \Delta N = 3.22 \times 10^6 + 50$. This vector field is characterized by the following features.

The dominating directions of the displacement vectors are the conjugate directions τ_{max} or their vector sums.

Within the presented surface fragment, the strain is developed in strictly specified sites. In each of the sites (*B*, *B*', *C*, and *C*'), the shears manifest themselves mainly along one of the conjugate directions τ_{max} or their vector sum.

In the site *B*, intense primary shears with a vector **a** prevail. In the site *B*', two types of primary conjugate shears develop with the vectors **a** and **b**. In the site *C*, the accommodation shears prevail in the kink band with a vector **c**. The extended zone *C*' of the surface ahead of

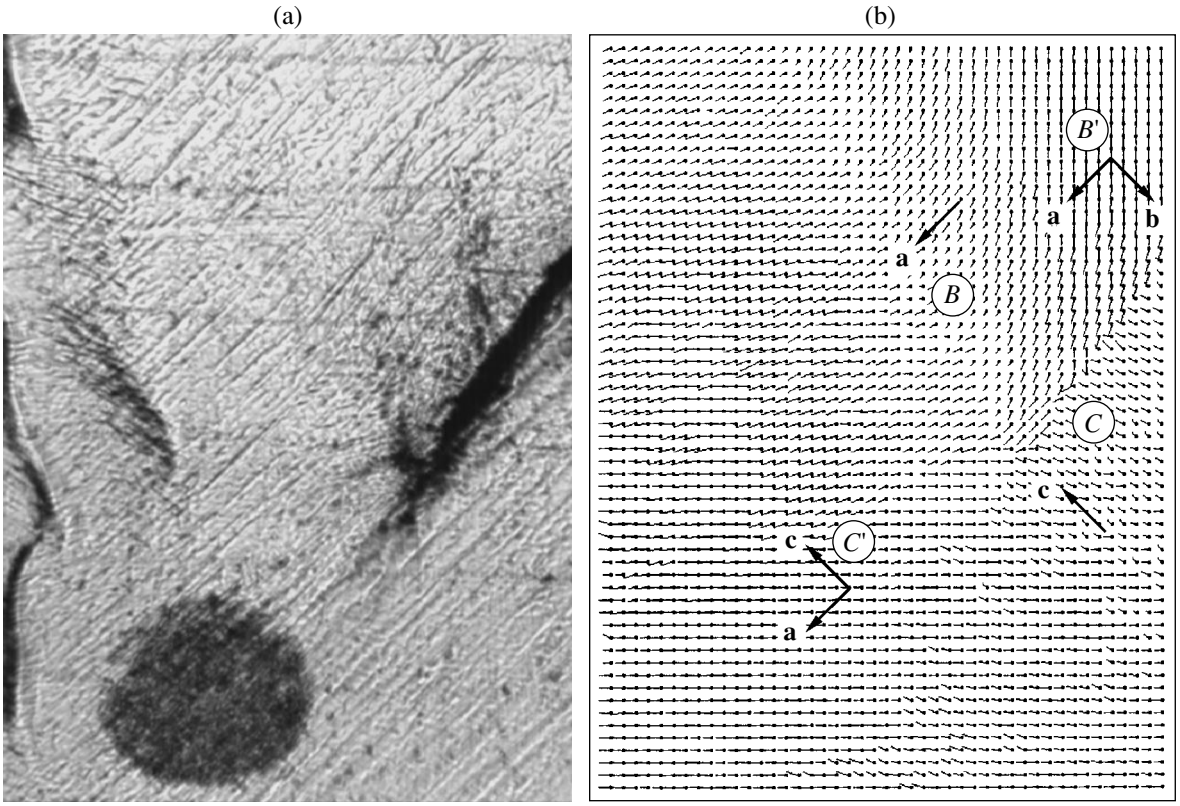

Fig. 2. (a) Microstructure and (b) the corresponding displacement-vector field after $N = 3.22 \times 10^6 + 50$ loading cycles.

the crack tips is characterized by the vector sum of primary shears with the vector **a** and accommodation shears with the vector **c**.

The experimental results displayed in Figs. 1 and 2 make it possible to assume the following mechanism of developing the shears in a surface grain *B* of the specimen under cyclic loading (Fig. 3).

For loading half-cycles inducing plastic compression in the surface layer, intense primary shears are developed in this layer along the τ_{max} direction with the vector **a**. The longitudinal component of these shears causes compression in the surface layer. The transverse component of the compression shears induces local bending of the specimen. In this case, counteracting stresses arise in the elastically deformed substrate, which decelerate the primary shears in the surface layer.

For the loading half-cycles inducing the plastic tension of the surface layer, the shears develop with the vector **b** along the direction conjugate to τ_{max}. Their longitudinal component induces a tension in the surface layer that causes a relaxation of residual compression stresses in this layer. According to the Bauschinger effect, the surface compression shears continue to develop under the subsequent loading. This process is cyclically repeated during the alternating bending.

At the same time, the transverse components of the vectors **a** and **b** are collinear. Thus, the bending stresses caused by the surface compressive and tensile shears

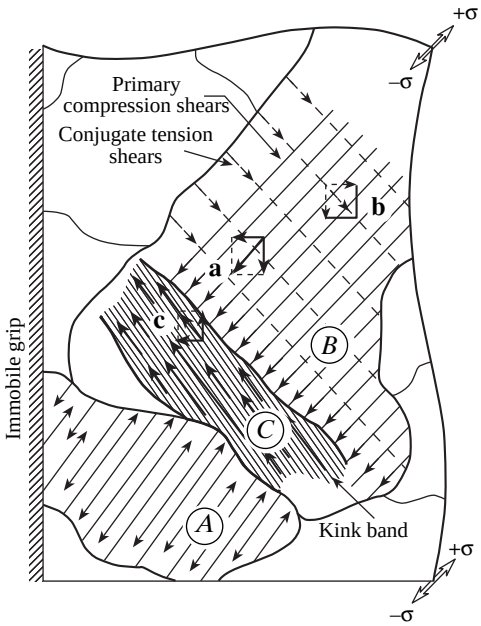

Fig. 3. Scheme of development of "primary compression shears" **a**, "conjugate tension shears" **b**, and localized accommodation slip **c** in the kink band *C* of the surface grain *B*.

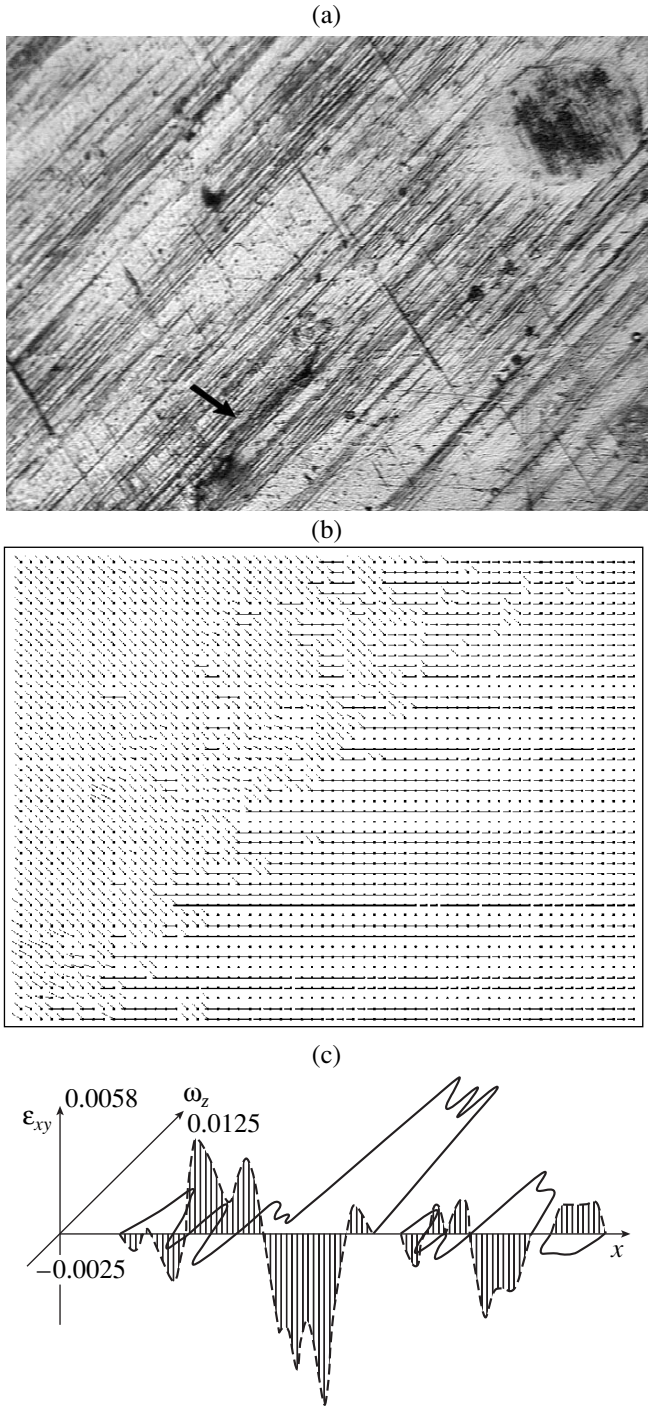

Fig. 4. (a) Microstructure, (b) corresponding displacement-vector field, and (c) distribution of shear component ε_{xy} and rotation component ω_z of the distortion tensor after $N = 5.9 \times 10^6$ cycles of loading. The fatigue crack in the grain is indicated by the arrow.

are summed. This fact forms an intense concentrator of stresses in the bending–torsion zone. The counteracting image forces associated with this concentrator generate the kink band with localization of accommodation shears as the rotation mode of strain. In this case, the local bending stresses relax.

A similar problem was analyzed theoretically in [11] by numerically calculating a stress field generated by the edge of the plastic-shear band near the crystal surface. The results of the theoretical calculations and the above experimental data agree well qualitatively. It should be emphasized that the results displayed in Figs. 1–3 convincingly illustrate the wave nature of the basic act of plastic deformation: intense shears along τ_{max} in the surface layer of a loaded solid generate the kink band as a rotation mode of the plastic-flow wave [2].

The experimental results under consideration and the theoretical estimates make it possible to conclude that the nucleation mechanism for surface tearing-mode shear is associated with the effect of rotation of the plastically deformed surface layer relative to the elastically loaded substrate. Experimentally, such a rotation was discovered, quantitatively measured, and shown in Fig. 4. Here, it can be seen that the displacement-vector field (Fig. 4b) is clearly separated into two macrofragments by the fatigue crack propagated in the direction of the intense primary sliding. It is characteristic that this separation of the grain propagates far ahead of the crack determining the trajectory of its further development. This fact is clearly displayed in Fig. 4c, where we show the strong localization of the shear–rotation on the boundary of fragments ahead of the crack. The theoretical possibility of such a rotation is shown by the example of the model of motion of an infinite series of screw dislocations in the slip plane [12].

The surface shears propagate in a polycrystal along the conjugate directions τ_{max}, which, probably, occurs according to the Bain mechanism [13] by means of a local rearrangement of various atomic configurations in the surface layer. The propagation of the front of such a rearrangement in the shear band is qualitatively similar to the propagation of screw-dislocation pileups in the surface layer. Therefore, the theoretical model [12] most adequately represents the development of shear bands in the surface layers of solids under deformation.

In this model, an infinite series of parallel screw dislocations with the Bürgers vector **b** is considered. The dislocations are located in the *xz* plane along the *z*-axis at equal *h* intervals [12]. The presence of pileups of such dislocations in the *xz* plane causes the initiation of significant microstresses in a medium with the shear modulus μ. In the main, these microstresses are localized in the layer $\Delta y < 2h$. The components σ_{xz} and σ_{yz} of these stress tensors and related rotations ω_{zx} and ω_{yz} have the form

$$\sigma_{xz} = -\frac{b\mu}{2h}\frac{y}{|y|}\left[1 + 2\sum_{\kappa=1}^{\infty} e^{-\frac{2\pi\kappa|y|}{h}} \cos\left(\frac{2\pi\kappa x}{h}\right)\right], \quad (1)$$

$$\sigma_{yz} = \frac{b\mu}{h}\sum_{\kappa=1}^{\infty} e^{-\frac{2\pi\kappa|y|}{h}} \sin\left(\frac{2\pi\kappa x}{h}\right), \quad (2)$$

$$\omega_{zx} = -\frac{b}{4h}\frac{y}{|y|}\left[1 + 2\sum_{\kappa=1}^{\infty} e^{-\frac{2\pi\kappa|y|}{h}} \cos\left(\frac{2\pi\kappa x}{h}\right)\right], \quad (3)$$

$$\omega_{yz} = \frac{b}{2h}\sum_{\kappa=1}^{\infty} l^{-\frac{2\pi\kappa|y|}{h}} \sin\left(\frac{2\pi\kappa x}{h}\right). \quad (4)$$

At distances $y > 2h$, the zero harmonic ($k = 0$) of the component σ_{xy} determines macrostresses in the medium containing a flat pileup of screw dislocations. In passing through the slip plane, this harmonic undergoes a jump $\left|\frac{b\mu}{h}\right|$ and the corresponding rotation-vector component ω_{xz} undergoes a jump $\left|\frac{b}{2h}\right|$.

When passing through the plane of screw-dislocation pileup, the jumps of average shear-stress and rotation fields cause two very important consequences.

1. The jump ω_{zx} is the angle of disorientation of the surface layer in the shear band with the elastically loaded substrate. In other words, the interface between the plastically deformed surface layer and the elastic substrate is the crystal-torsion boundary with an angle $\omega = -\frac{b}{2h}$.

2. The jump of shear stresses $\sigma_{xz} = \frac{b\mu}{h}$ forms a stress concentration on the torsion boundary, which is characterized by the shear–rotation scheme.

The former consequence agrees well with the known experimental result [14], according to which the uniaxial tension of flat whiskers is always accompanied by their twisting. The surface-layer rotation in the shear band relative to an elastically loaded substrate arising in the alternating bending explains the nucleation of the surface fatigue cracks of the longitudinal shear.

The latter consequence is associated with the appearance of the concentration of the shear–bending–torsion stresses in the primary-shear band. These stresses cause corrugation of the primary-shear band and the formation of the kink bands in it (Fig. 1). These bands can have various orientations relative to the primary shears. This fact is due to the strongly inhomogeneous field of internal stresses arising in an elastically deformed heterogeneous substrate.

Following the development of surface cracks in the primary-shear band, similar surface cracks appear in the kink bands (Fig. 1). Then, the main fatigue crack propagates in a zigzag manner along the surface cracks of the longitudinal shear in the primary-shear bands and of the kink band inducing fatigue fracture of the material.

REFERENCES

1. V. E. Panin, Fiz. Mezomekh. **2**, 5 (1999).
2. V. E. Panin, Fiz. Mezomekh. **3**, 6 (2000).
3. V. S. Ivanova and V. F. Terent'ev, *Nature of Metal Fatigue* (Metallurgiya, Moscow, 1975).
4. St. Katsan'da, *Fatigue Fracture of Metals* (Wydawnictwa Naukowo-Techniczne, Warsaw, 1972; Metallurgiya, Moscow, 1976), translated from Polish.
5. V. F. Terent'ev, *Synergetics and Fatigue Fracture of Metals* (Nauka, Moscow, 1989).
6. M. E. Drits, Yu. P. Guk, and L. P. Gerasimova, *Fracture of Aluminum Alloys* (Nauka, Moscow, 1980).
7. V. E. Panin, T. F. Elsukova, G. V. Angelova, and S. V. Sapozhnikov, Fiz. Mezomekh. **1**, 41 (1998).
8. V. E. Panin, T. F. Elsukova, G. V. Angelova, and S. V. Panin, Dokl. Akad. Nauk **365**, 186 (1999) [Dokl. Phys. **44**, 163 (1999)].
9. V. E. Panin, T. F. Elsukova, and G. V. Angelova, Fiz. Mezomekh. **3**, 79 (2000).
10. *Physical Mesomehanics and Computer-Aided Design of Materials*, Ed. by V. E. Panin (Nauka, Novosibirsk, 1995), Vol. 1.
11. S. D. Borisova and I. I. Naumov, Izv. Vyssh. Uchebn. Zaved., Fiz., No. 9, 65 (1999).
12. S. D. Borisova and I. I. Naumov, Izv. Vyssh. Uchebn. Zaved., Fiz., No. 4, 53 (1999).
13. H. Warlimont and L. Delay, *Martensitic Transformations in Copper-, Silver-, and Gold-Based Alloys* (Pergamon, Oxford, 1974; Nauka, Moscow, 1980).
14. S. F. Antipov, I. A. Bataronov, A. I. Drozhzhin, *et al.*, Kristallografiya **34**, 702 (1986) [Sov. Phys. Crystallogr. **34**, 417 (1989)].

Translated by V. Bukhanov

Doklady Physics, Vol. 47, No. 1, 2002, pp. 72–73. Translated from Doklady Akademii Nauk, Vol. 382, No. 3, 2002, pp. 341–342.

TECHNICAL PHYSICS

Fracture of a Composite Material Based on a Uniformly Deformable Polymeric Matrix and Rubber Particles

O. A. Serenko, V. S. Avinkin, and S. L. Bazhenov

Presented by Academician N.F. Bakeev May 30, 2001

Received June 5, 2001

In the case of tension in thermoplastic polymers filled with mineral particles at a certain filler content, an abrupt drop of the material deformability occurs, caused by the transition from plastic to brittle fracture [1–5]. In the present study, we have established that the embrittlement of filled thermoplastics is associated with the formation and propagation of a neck in the matrix polymer under tension. If the matrix polymer is deformed macrouniformly and the neck does not form, then introducing a filler does not result in the embrittlement of the composite material.

In order to prepare composite materials, we used a copolymer of ethylene and vinyl acetate (CEVA) of the 11306-075 trademark. A rubber powder was used as a filler. The powder consisted of about 50, 10, and 10 wt % of isoprene; divinyl; and methylstyrene caoutchoucs, respectively, as well as 30 wt % carbon black. The size of rubber particles was $100 < d < 500$ μm.

Mixing the CEVA with rubber particles was performed in a single-worm laboratory extruder. The concentration of the rubber powder varied within the limits from 1.7 to 88 vol % (2 to 90 wt %). From the mixtures obtained, plates 2 mm thick were prepared by pressing. Two-sided blades with working surfaces of 5×35 mm were cut out from these plates.

Mechanical tests of the composites were carried out with the help of a 2038P-005 dynamometric facility at the deformation rate of 20 mm/min. The CEVA crystalline structure and CEVA-based composites were studied at a heating rate of 10 K/min by the method of differential scanning calorimetry with the use of a TA 4000 thermal analyzer manufactured by the Mettler Company.

Calorimetric analysis has shown that the presence of rubber particles does not change the crystallinity degree or melting temperature of the polymeric matrix. Therefore, the elastic filler does not affect the crystalline structure of the material, and it is identical with the original structure of the unfilled CEVA.

The curves for tension of the original CEVA and composites prepared on its base are displayed in Fig. 1. A characteristic feature of the deformation of the unfilled polymer is the absence of a yield tooth (curve *1*). The copolymer deforms macrouniformly without a neck formation, and the stress in it monotonically increases with deformation. With deformation, plastic strains are developed in the polymer along with reversible strains. After fracture of the unfilled polymer under a deformation of 830%, the residual elongation reaches 650%. After filling the CEVA by rubber particles, the pattern of the tension diagram does not vary. The tension diagram of a composite containing more than 30 vol % of the rubber powder is similar to tension diagrams for rubber (curves *2* and *3*).

Figure 2 exhibits the composite strength as a function of the volume fraction of rubber particles. In the

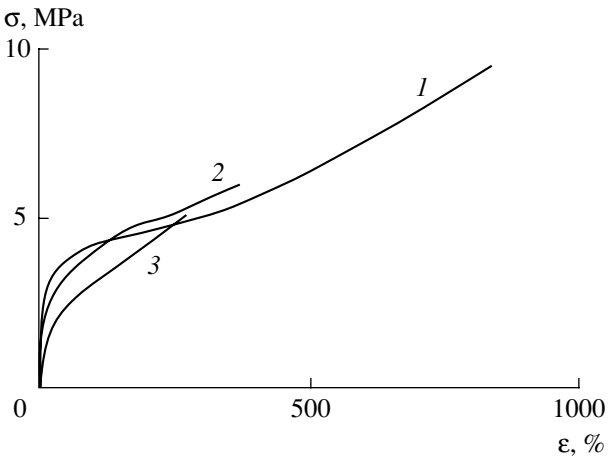

Fig. 1. Deformation diagram for (*1*) a copolymer of ethylene with vinyl acetate and composite materials based on this copolymer and containing (*2*) 26 and 66 vol % of rubber particles.

Enikolopov Institute of Synthetic Polymeric Materials, Russian Academy of Sciences, Profsoyuznaya ul. 70, Moscow, 117393 Russia

1028-3358/02/4701-0072$22.00

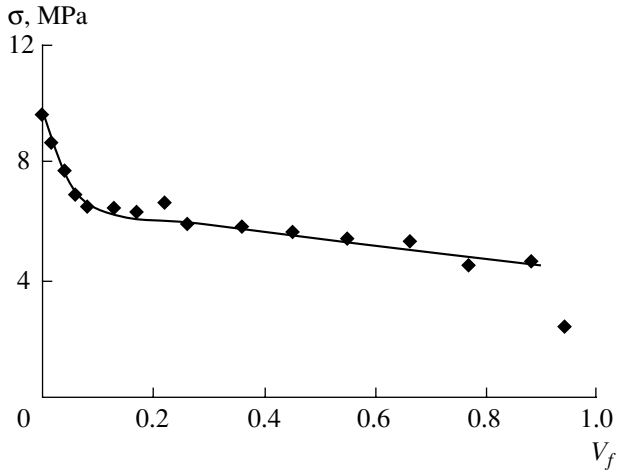

Fig. 2. Strength of a composite material based on the copolymer of ethylene with vinyl acetate as a function of the volume content of rubber particles.

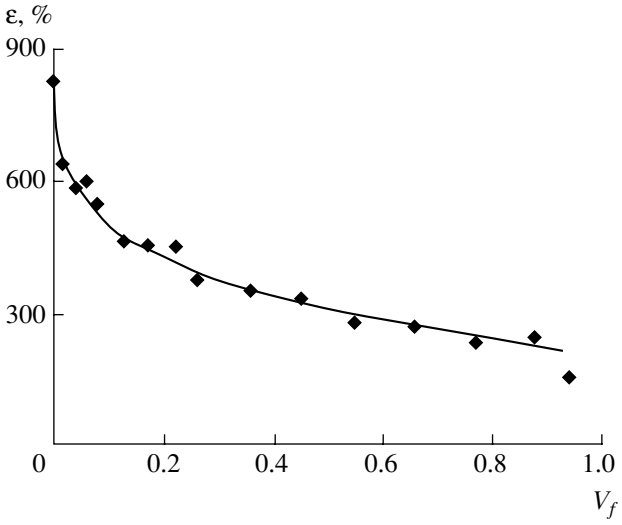

Fig. 3. Dependence of the relative elongation in the case of a rupture of a composite material based on the copolymer of ethylene with vinyl acetate on the volume content of rubber particles.

entire content region, a monotonous decrease of the composite-material strength is observed.

The dependence of the material fracturing deformation on the volume fraction of rubber particles is shown in Fig. 3. The shape of the ε–V_f curve is similar to the strength curve. The material deformability monotonically decreases with increasing filler concentration. Within the entire range of the filling degree, the fracturing deformation exceeds 200%, and the composite material does not become brittle.

The embrittlement is typical for a number of filled polymers, e.g., high-density polyethylene, polypropylene, polycarbonate, polyvinyl chloride, polyethylene, and terephthalate [5]. According to concepts concerning the embrittlement mechanism for polymers developed in [6–8], this phenomenon is associated with the transition from the propagation of a neck along a sample to a fracture in the process of the neck formation [7]. When using a thermoplastic matrix that deforms without formation of a neck, no embrittlement of the material must be observed. This assumption is confirmed by the results of our study.

The absence of the composite-material embrittlement was also observed when studying deformation properties of polytetrafluoroethylene filled with copper particles [8]. Polytetrafluoroethylene is deformed without the neck formation. The deformation properties of the given composite material monotonously decreased with increasing filler content. The behavior of caoutchouc with a rigid mineral filler is similar [7].

Thus, we may conclude that the embrittlement of filled polymers, i.e., the abrupt decrease in the composite-material deformability, is unambiguously associated with the formation and propagation of a neck in the matrix polymer under tension. In the case of a macrouniform deformation of a polymer, introducing an arbitrary amount of a filler into its bulk does not lead to the embrittlement of the given composite material. This conclusion is valid for both vulcanized caoutchoucs being deformed without the neck formation and linear thermoplastic polymers.

REFERENCES

1. V. A. Tochin, E. N. Shchupak, and V. V. Teleshov, Plastmassy, No. 1, 6 (1987).
2. V. A. Topolkaraev, N. V. Gorbunova, I. L. Dubnikova, *et al.*, Vysokomol. Soedin., Ser. A **32**, 2210 (1990).
3. I. L. Dubnikova, A. I. Petrosyan, V. A. Topolkaraev, *et al.*, Vysokomol. Soedin., Ser. A **30**, 2345 (1990).
4. S. Bazhenov, *Plastics Additives* (Chapmen and Hall, London, 1998).
5. S. Bazhenov, J. X. Li, A. Hiltner, and E. Baer, J. Appl. Polym. Sci. **52**, 243 (1994).
6. S. Bazhenov, Polym. Eng. Sci. **35**, 813 (1995).
7. L. E. Nielsen, *Mechanical Properties of Polymers and Composites* (Marcel Dekker, New York, 1974; Khimiya, Moscow, 1978).

Translated by G. Merzon

Doklady Physics, Vol. 47, No. 1, 2002, pp. 74–77. Translated from Doklady Akademii Nauk, Vol. 382, No. 1, 2002, pp. 58–61.

MECHANICS

General Solutions to the Nonlinear Static Problem for Elastic Shells

L. M. Zubov

Presented by Academician I.I. Vorovich June 25, 2001

Received July 18, 2001

Within the framework of the general nonlinear theory of elastic shells, we found families of finite deformations for which the original two-dimensional boundary value problem of statics is reduced to the boundary value problem for a system of ordinary differential equations. These families represent exact solutions to nonlinear equilibrium equations and are applicable to shells with the shape of a helical surface. Shells of revolution and cylindrical (prismatic) shells are special cases of such thin-walled shells. The solutions constructed describe, in particular, severe torsional and bending deformations of helical tubes and self-twisted prismatic shells.

BASIC RELATIONSHIPS

Let σ be the surface of a shell in an original (reference) configuration. The surface is specified in the Gaussian coordinates q^α ($\alpha = 1, 2$). The radius vector $\mathbf{r}$ of a point on the surface σ is $\mathbf{r}(q^1, q^2) = x_1\mathbf{i}_1 + x_2\mathbf{i}_2 + x_3\mathbf{i}_3$, where x_k ($k = 1, 2, 3$) are Cartesian coordinates of the point and $\mathbf{i}_k$ is a fixed orthonormal vector basis. The coefficients of the first and second quadratic forms of the surface σ are determined by the relationships

$$g_{\alpha\beta} = \mathbf{r}_\alpha \cdot \mathbf{r}_\beta, \quad b_{\alpha\beta} = \frac{\partial \mathbf{r}_\alpha}{\partial q^\beta} \cdot \mathbf{n}, \quad \mathbf{r}_\alpha = \frac{\partial \mathbf{r}}{\partial q^\alpha}, \qquad \mathbf{r}^\beta \cdot \mathbf{r}_\alpha = \delta^\beta_\alpha, \quad \mathbf{r}^\beta \cdot \mathbf{n} = 0. \tag{1}$$

Here, $\mathbf{n}$ is the unit normal to σ, and δ^β_α is the Kronecker delta. The surface Σ of the deformed shell is specified in the same coordinates q^α, and the position of a point at Σ is specified by the radius vector

$$\mathbf{R}(q^1, q^2) = X_1\mathbf{i}_1 + X_2\mathbf{i}_2 + X_3\mathbf{i}_3,$$

where X_k are Cartesian coordinates of a point for which the normal to Σ is denoted by $\mathbf{N}$. The coefficients of the quadratic forms for the surface Σ are given by the equations

$$G_{\alpha\beta} = \mathbf{R}_\alpha \cdot \mathbf{R}_\beta, \quad B_{\alpha\beta} = \frac{\partial \mathbf{R}_\alpha}{\partial q^\beta} \cdot \mathbf{N}, \qquad \mathbf{R}_\alpha = \frac{\partial \mathbf{R}}{\partial q^\alpha}, \quad \mathbf{R}^\beta \cdot \mathbf{R}_\alpha = \delta^\beta_\alpha, \quad \mathbf{R}^\beta \cdot \mathbf{N} = 0. \tag{2}$$

For a shell of the Love type, the equilibrium equations in terms of resultant stresses and couples take the form [1–4]

$$\nabla_\alpha(\nu^{\alpha\beta} - \mu^{\alpha\delta}B^\beta_\delta) - B^\beta_\delta\nabla_\alpha\mu^{\alpha\delta} + F^\beta = 0, \quad \beta = 1, 2,$$
$$\nabla_\alpha\nabla_\beta\mu^{\alpha\beta} + B_{\alpha\beta}(\nu^{\alpha\beta} - B^\alpha_\delta\mu^{\delta\beta}) + F = 0, \tag{3}$$
$$F = \mathbf{F} \cdot \mathbf{N}, \quad F^\beta = \mathbf{F} \cdot \mathbf{R}^\beta,$$
$$B^\alpha_\delta = G^{\alpha\gamma}B_{\gamma\delta}, \quad G^{\alpha\gamma} = \mathbf{R}^\alpha \cdot \mathbf{R}^\gamma.$$

Here, $\mathbf{F}$ is the vector of an external force load applied to Σ; $\nu^{\alpha\beta}$ and $\mu^{\alpha\beta}$ are the tensors of resultant stresses and couples, respectively; and ∇_α stands for the covariant derivative in the metric $G_{\alpha\beta}$. The constitutive relations for an elastic shell take the form [1]

$$\chi\sqrt{\frac{G}{g}}\nu^{\alpha\beta} = 2\frac{\partial W}{\partial G_{\alpha\beta}},$$
$$\chi\sqrt{\frac{G}{g}}\mu^{\alpha\beta} = \frac{\partial W}{\partial B_{\alpha\beta}}, \quad \chi = \begin{cases} 1, & \alpha = \beta \\ 2, & \alpha \neq \beta, \end{cases} \tag{4}$$
$$G = G_{11}G_{22} - G_{12}^2, \quad g = g_{11}g_{22} - g_{12}^2.$$

In the case of a homogeneous isotropic shell, the specific (per unit area of the surface σ) strain energy W is a function of the following nine quantities [1]:

$$g^{\alpha\beta}b_{\alpha\beta}, \quad g^{\alpha\beta}G_{\alpha\beta}, \quad g^{\alpha\beta}B_{\alpha\beta}, \quad \frac{b_{11}b_{22} - b_{12}^2}{g}, \quad \frac{G}{g},$$
$$\frac{B_{11}B_{22} - B_{12}^2}{g}, \quad b^{\alpha\beta}G_{\alpha\beta}, \quad b^{\alpha\beta}B_{\alpha\beta}, \quad g^{\alpha\beta}g^{\gamma\delta}G_{\alpha\gamma}B_{\beta\delta}, \tag{5}$$

Rostov State University,
pr. Stachki 194, Rostov-on-Don, 344104 Russia

1028-3358/02/4701-0074$22.00

$$b^{\alpha\beta} \equiv g^{\alpha\kappa} g^{\beta\lambda} b_{\kappa\lambda}, \quad g^{\beta\lambda} \equiv \mathbf{r}^{\beta} \cdot \mathbf{r}^{\lambda}.$$

We assume that the boundary $\delta\Sigma$ of the deformed shell is loaded by a distributed force and a distributed moment with the linear densities $\mathbf{Q} = Q^{\alpha}\mathbf{R}_{\alpha} + Q\mathbf{N}$ and $\mathbf{d} \times \mathbf{N}$, respectively. In this case, the boundary conditions take the form [1]

$$\begin{gathered}\sqrt{\frac{G}{g}} m_{\alpha}(\nu^{\alpha\beta} - 2B^{\beta}_{\delta}\mu^{\alpha\beta}) = \varepsilon(Q^{\beta} - B^{\beta}_{\alpha}d^{\alpha}), \quad \beta = 1, 2,\\ \sqrt{\frac{G}{g}} m_{\alpha} m_{\beta}\mu^{\alpha\beta} = \varepsilon m_{\alpha} d^{\alpha},\\ \sqrt{\frac{G}{g}} m_{\beta}\nabla_{\alpha}\mu^{\alpha\beta} + \frac{d}{ds}\left(\sqrt{\frac{G}{g}}\varepsilon^{-2}\tau^{\delta} m_{\beta} G_{\alpha\delta}\mu^{\alpha\beta}\right)\\ = \varepsilon Q + \frac{d}{ds}(\varepsilon^{-1}\tau^{\delta} d_{\delta}),\\ \mathbf{d} = d^{\alpha}\mathbf{R}_{\alpha} = d_{\beta}\mathbf{R}^{\beta}, \quad \mathbf{m} = m_{\alpha}\mathbf{r}^{\alpha},\\ \boldsymbol{\tau} = \tau^{\delta}\mathbf{r}_{\delta}, \quad \varepsilon = \sqrt{\tau^{\alpha}\tau^{\beta}G_{\alpha\beta}}.\end{gathered} \tag{6}$$

Here, $\mathbf{m}$ and $\boldsymbol{\tau}$ are, respectively, the unit vectors of a normal and a tangent to the boundary contour $\partial\sigma$ of the undistorted shell, and s is the current arc length in the curve $\partial\sigma$.

In what follows, we consider general solutions to equilibrium equations (3). These solutions applicable to shells having a specific geometric shape represent families of the finite deformations for which the original nonlinear system of partial differential equations with the two independent variables q^1 and q^2 is reduced to a system of ordinary differential equations (i.e., equations in unknown functions of a single variable).

TORSION AND TENSION OF A SELF-TWISTED CYLINDRICAL SHELL

We assume that the original shape of a shell is a helical surface. The surface is formed by a screw motion of a plane curve, described by the equations $x_1 = \eta_1(\xi)$ and $x_2 = \eta_2(\xi)$, along the x_3-axis. Introducing the Gaussian coordinates $q^1 = x_3$ and $q^2 = \xi$, we can write out the equation for the surface σ in the form

$$\begin{gathered}\mathbf{r}(q^1, q^2) = \eta_1(\xi)\mathbf{e}_1 + \eta_2(\xi)\mathbf{e}_2 + x_3\mathbf{i}_3,\\ \mathbf{e}_1 = \mathbf{i}_1\cos\psi_0 x_3 + \mathbf{i}_2\sin\psi_0 x_3,\\ \mathbf{e}_2 = -\mathbf{i}_1\sin\psi_0 x_3 + \mathbf{i}_2\cos\psi_0 x_3,\end{gathered} \tag{7}$$

where ψ_0 is a constant.

The shell whose surface is given by Eq. (7) will be referred to as a self-twisted cylindrical shell. For $\psi_0 = 0$, the shell becomes cylindrical and has an arbitrary cross section. With due regard for Eq. (7), we have

$$\begin{gathered}\mathbf{r}_1 = \psi_0(-\eta_2\mathbf{e}_1 + \eta_1\mathbf{e}_2) + \mathbf{i}_3, \quad \mathbf{r}_2 = \eta_1'\mathbf{e}_1 + \eta_2'\mathbf{e}_2,\\ \frac{\partial\mathbf{r}_1}{\partial q^1} = -\psi_0^2(\eta_1\mathbf{e}_1 + \eta_2\mathbf{e}_2), \quad \frac{\partial\mathbf{r}_2}{\partial q^2} = \eta_1''\mathbf{e}_1 + \eta_2''\mathbf{e}_2,\\ \frac{\partial\mathbf{r}_1}{\partial q^2} = \frac{\partial\mathbf{r}_2}{\partial q^1} = \psi_0(\eta_1'\mathbf{e}_2 - \eta_2'\mathbf{e}_1),\\ \mathbf{n} = n_1(\xi)\mathbf{e}_1 + n_2(\xi)\mathbf{e}_2 + n_3(\xi)\mathbf{i}_3.\end{gathered} \tag{8}$$

It follows from (1) and (8) that the coefficients $g_{\alpha\beta}$ and $b_{\alpha\beta}$ of the first and second quadratic forms of the surface σ are independent of the x_3-coordinate. We consider the following deformations of a self-twisted shell:

$$\begin{aligned}X_1 &= \nu_1(\xi)\cos\psi x_3 - \nu_2(\xi)\sin\psi x_3,\\ X_2 &= \nu_1(\xi)\sin\psi x_3 + \nu_2(\xi)\cos\psi x_3,\\ X_3 &= \nu_3(\xi) + \lambda x_3, \quad \lambda, \psi = \text{const}.\end{aligned} \tag{9}$$

Using Eq. (9), we find

$$\begin{gathered}\mathbf{R}_1 = \psi(\nu_1\mathbf{E}_2 - \nu_2\mathbf{E}_1) + \lambda\mathbf{i}_3,\\ \mathbf{R}_2 = \nu_1'\mathbf{E}_1 + \nu_2'\mathbf{E}_2 + \nu_3'\mathbf{i}_3,\\ \mathbf{E}_1 = \mathbf{i}_1\cos\psi x_3 + \mathbf{i}_2\sin\psi x_3,\\ \mathbf{E}_2 = -\mathbf{i}_1\sin\psi x_3 + \mathbf{i}_2\cos\psi x_3,\\ \frac{\partial\mathbf{R}_1}{\partial q^1} = -\psi^2(\nu_1\mathbf{E}_1 + \nu_2\mathbf{E}_2),\\ \frac{\partial\mathbf{R}_2}{\partial q^2} = \nu_1''\mathbf{E}_1 + \nu_2''\mathbf{E}_2 + \nu_3''\mathbf{i}_3,\\ \frac{\partial\mathbf{R}_1}{\partial q^2} = \psi(\nu_1'\mathbf{E}_2 - \nu_2'\mathbf{E}_1),\\ \mathbf{N} = N_1(\xi)\mathbf{E}_1 + N_2(\xi)\mathbf{E}_2 + N_3(\xi)\mathbf{i}_3.\end{gathered} \tag{10}$$

Based on Eqs. (2) and (10) and taking into account that the vectors $\mathbf{E}_1$, $\mathbf{E}_2$, and $\mathbf{i}_3$ form an orthonormal basis, we can easily prove that the quantities $G_{\alpha\beta}$ and $B_{\alpha\beta}$ are independent of the coordinate x_3. The Christoffel symbols $\Gamma^{\beta}_{\delta\lambda} = \mathbf{R}^{\beta} \cdot \dfrac{\partial\mathbf{R}_{\delta}}{\partial q^{\lambda}}$, which enter into the covariant derivatives ∇_{α}, depend only on the coordinate ξ. In the case of an isotropic uniform shell, it follows from (4) and (5) that the tensors $\nu^{\alpha\beta}$ and $\mu^{\alpha\beta}$ are functions of the single variable ξ. We then assume that the loads Q^{β}, Q, and d^{α}, which are applied to the shell edges $\xi = \xi_1$ and $\xi = \xi_2$, as well as the external surface loads F^{β} and F, are independent of the x_3-coordinate. In this case, equilibrium equations (3) and boundary conditions (6) at $\xi = \xi_1$ and $\xi = \xi_2$ compose the nonlinear boundary value problem for a system of ordinary differential equations with the unknown functions $\nu_k(\xi)$ ($k = 1, 2, 3$).

TORSION OF A CYLINDRICAL SHELL WITH A DISLOCATION

In order to consider a prismatic (cylindrical) shell with its generatrices parallel to the x_k-axis, we introduce the circular cylindrical coordinates r, φ, and z: $x_1 = r\cos\varphi$, $x_2 = r\sin\varphi$, and $x_3 = z$, where x_1, x_2, and x_3 are Cartesian coordinates. The cross section of the surface σ at $z = \text{const}$ is described by the function $r(\varphi)$. Introducing the Gaussian coordinates $q^1 = z$ and $q^2 = \varphi$, we have

$$\begin{gathered}\mathbf{r}_1 = \mathbf{i}_3, \quad \mathbf{r}_2 = r'\mathbf{e}_r + r\mathbf{e}_\varphi,\\ g_{11} = 1, \quad g_{12} = 0, \quad g_{22} = r'^2 + r^2, \\ \mathbf{e}_r = \mathbf{i}_1\cos\varphi + \mathbf{i}_2\sin\varphi, \quad \mathbf{e}_\varphi = -\mathbf{i}_1\sin\varphi + \mathbf{i}_2\cos\varphi.\end{gathered} \tag{11}$$

We then denote the cylindrical coordinates of a point on the deformed shell surface Σ by R, Φ, and Z ($X_1 = R\cos\Phi$, $X_2 = R\sin\Phi$, and $X_3 = Z$) and discuss the following deformations of the shell:

$$\begin{gathered}R = R(\varphi), \quad \Phi = \varphi + \psi z + \nu(\varphi),\\ Z = \lambda z + a\varphi + w(\varphi), \quad \psi, a, \lambda = \text{const}.\end{gathered} \tag{12}$$

Formulas (12) describe axial torsion combined with and out-of-plane tension and out-of-plane shear, with ψ being the angle of torsion per unit length. If the shell cross section is a closed curve, then the functions R, ν, and w should be 2π-periodic and, hence, the quantity $2\pi a$ should be coincident with the length of the Bürgers vector for the screw dislocation. From Eqs. (12), we have

$$\begin{gathered}\mathbf{R}_1 = \lambda\mathbf{i}_3 + \psi R\mathbf{e}_\Phi,\\ \mathbf{R}_2 = (a + w')\mathbf{i}_3 + R'\mathbf{e}_R + R(1 + \nu')\mathbf{e}_\Phi,\\ \mathbf{e}_R = \mathbf{i}_1\cos\Phi + \mathbf{i}_2\sin\Phi, \quad \mathbf{e}_\Phi = -\mathbf{i}_1\sin\Phi + \mathbf{i}_2\cos\Phi,\\ G_{11} = \lambda^2 + \psi^2R^2, \quad G_{12} = \lambda(a + w') + \psi R^2(1 + \nu'),\\ G_{22} = (a + w')^2 + R^2(1 + \nu')^2 + R'^2.\end{gathered} \tag{13}$$

It follows from (13) that the quantities $G_{\alpha\beta}$, $B_{\alpha\beta}$, and $\Gamma^\beta_{\delta\lambda}$ are independent of the variable z. Hence, in the case of an isotropic cylindrical shell, Eqs. (3) are reduced to a system of ordinary differential equations in the unknown functions $R(\varphi)$, $\nu(\varphi)$, and $w(\varphi)$.

We now consider the problem of a screw dislocation in the closed circular cylindrical shell whose original cross section has the radius r_0. As is easily verified with the help of formulas (11) and (13), in this case, there exists an isometric deformation (i.e., bending) of the cylindrical surface, which is specified by the relationships

$$\begin{gathered}R(\varphi) = R_0 = \sqrt{r_0^2 - a^2}, \quad \nu(\varphi) = 0, \quad w(\varphi) = 0,\\ \psi = -\frac{a}{r_0(r_0^2 - a^2)}, \quad \lambda = \sqrt{1 - \frac{a^2}{r_0^2}}.\end{gathered} \tag{14}$$

According to (14), this isometric deformation involves the torsion of the cylinder and a decrease in its radius.

BENDING OF A SELF-TWISTED CYLINDRICAL SHELL

We assume that the axis of the helical surface σ of an elastic undistorted shell is parallel to the vector $\mathbf{i}_1$. In this case, the surface σ is specified by the relationships

$$\begin{gathered}\mathbf{r} = x_1\mathbf{i}_1 + \eta_2(\xi)\mathbf{j}_2 + \eta_3(\xi)\mathbf{j}_3,\\ \mathbf{j}_2 = \mathbf{i}_2\cos\psi_0x_1 + \mathbf{i}_3\sin\psi_0x_1,\\ \mathbf{j}_3 = -\mathbf{i}_2\sin\psi_0x_1 + \mathbf{i}_3\cos\psi_0x_1.\end{gathered} \tag{15}$$

From (15), with $q^1 = x_1$ and $q^2 = \xi$, we have

$$\begin{gathered}\mathbf{r}_1 = \mathbf{i}_1 - \psi_0\eta_3\mathbf{j}_2 + \psi_0\eta_2\mathbf{j}_3, \quad \mathbf{r}_2 = \eta_2'\mathbf{j}_2 + \eta_3'\mathbf{j}_3,\\ \mathbf{n} = n_1(\xi)\mathbf{i}_1 + n_2(\xi)\mathbf{j}_2 + n_3(\xi)\mathbf{j}_3.\end{gathered} \tag{16}$$

We describe the shell deformations by the following relations:

$$\begin{gathered}X_1 = u_1(\xi)\cos\omega x_1 - u_2(\xi)\sin\omega x_1,\\ X_2 = u_1(\xi)\sin\omega x_1 + u_2(\xi)\cos\omega x_1,\\ X_3 = u_3(\xi) + lx_1, \quad \omega, l = \text{const}.\end{gathered} \tag{17}$$

As is seen from Eqs. (17), the surface Σ of the deformed shell is a helical surface with the axis parallel to the vector $\mathbf{i}_3$. Using Eqs. (17), we arrive at

$$\begin{gathered}\mathbf{R}_1 = \omega u_1\mathbf{I}_2 - \omega u_2\mathbf{I}_1 + l\mathbf{i}_3,\\ \mathbf{R}_2 = u_1'\mathbf{I}_1 + u_2'\mathbf{I}_2 + u_3'\mathbf{i}_3,\\ \mathbf{N} = N_1(\xi)\mathbf{I}_1 + N_2(\xi)\mathbf{I}_2 + N_3(\xi)\mathbf{i}_3,\\ \frac{\partial\mathbf{R}_1}{\partial q^1} = -\omega^2(u_1\mathbf{I}_1 + u_2\mathbf{I}_2),\\ \frac{\partial\mathbf{R}_1}{\partial q^2} = \omega(u_1'\mathbf{I}_2 - u_2'\mathbf{I}_1),\\ \frac{\partial\mathbf{R}_2}{\partial q^2} = u_1''\mathbf{I}_1 + u_2''\mathbf{I}_2 + u_3''\mathbf{i}_3,\\ \mathbf{I}_1 = \mathbf{i}_1\cos\omega x_1 + \mathbf{i}_2\sin\omega x_1,\\ \mathbf{I}_2 = -\mathbf{i}_1\sin\omega x_1 + \mathbf{i}_2\cos\omega x_1.\end{gathered} \tag{18}$$

It follows from relationships (1), (2), (16), and (18) that the quantities $g_{\alpha\beta}$, $b_{\alpha\beta}$, $G_{\alpha\beta}$, $B_{\alpha\beta}$, and $\Gamma^{\beta}_{\delta\lambda}$ are independent of the x_1 coordinate. Hence, equilibrium equations (3) become ordinary differential equations in the unknown functions $u_k(\xi)$ ($k = 1, 2, 3$).

BENDING AND TORSION OF A HELICAL SHELL

We now consider the helical surface formed by a screw motion of a given plane curve. The curve lies in a plane containing the x_3-axis of revolution and is defined by the equations $x_3 = \zeta(t)$ and $r = \rho(t)$, where r is the distance to the axis of revolution. The equation of the helical surface takes the form

$$\begin{aligned}\mathbf{r} &= \rho(t)\mathbf{e}_r + \zeta(t)\mathbf{i}_3 + l_0\varphi\mathbf{i}_3,\\ \mathbf{e}_r &= \mathbf{i}_1\cos\varphi + \mathbf{i}_2\sin\varphi, \quad l_0 = \text{const},\end{aligned} \tag{19}$$

where φ is the polar angle in the circular cylindrical coordinates (r, φ, x_3). The elastic shell with the surface σ given by Eq. (19) will be referred to as a helical shell. In the case of $l_0 = 0$, the surface becomes a sector of a surface of revolution. Introducing the Gaussian coordinates $q^1 = t$ and $q^2 = \varphi$, we have

$$\begin{aligned}\mathbf{r}_1 &= \rho'\mathbf{e}_r + \zeta'\mathbf{i}_3, \quad \mathbf{r}_2 = \rho\mathbf{e}_\varphi + l_0\mathbf{i}_3,\\ \mathbf{e}_\varphi &= -\mathbf{i}_1\sin\varphi + \mathbf{i}_2\cos\varphi,\\ \mathbf{n} &= n_1(t)\mathbf{e}_r + n_2(t)\mathbf{e}_\varphi + n_3(t)\mathbf{i}_3.\end{aligned} \tag{20}$$

We then analyze a two-parameter family of deformations for which the deformed surface Σ remains helical with its axis parallel to the vector $\mathbf{i}_3$:

$$\begin{aligned}X_1 &= \alpha(t)\cos\kappa\varphi - \beta(t)\sin\kappa\varphi,\\ X_2 &= \alpha(t)\sin\kappa\varphi + \beta(t)\cos\kappa\varphi,\\ X_3 &= \gamma(t) + L\varphi, \quad L, \kappa = \text{const}.\end{aligned} \tag{21}$$

It follows from Eqs. (21) that

$$\begin{aligned}\mathbf{R}_1 &= \alpha'\mathbf{F}_1 + \beta'\mathbf{F}_2 + \gamma'\mathbf{i}_3,\\ \mathbf{R}_2 &= -\kappa\beta\mathbf{F}_1 + \kappa\alpha\mathbf{F}_2 + L\mathbf{i}_3,\\ \mathbf{F}_1 &= \mathbf{i}_1\cos\kappa\varphi + \mathbf{i}_2\sin\kappa\varphi,\\ \mathbf{F}_2 &= -\mathbf{i}_1\sin\kappa\varphi + \mathbf{i}_2\cos\kappa\varphi,\\ \frac{\partial\mathbf{R}_1}{\partial q^1} &= \alpha''\mathbf{F}_1 + \beta''\mathbf{F}_2 + \gamma''\mathbf{i}_3,\\ \frac{\partial\mathbf{R}_1}{\partial q^2} &= -\kappa\beta'\mathbf{F}_1 + \kappa\alpha'\mathbf{F}_2,\\ \frac{\partial\mathbf{R}_2}{\partial q^2} &= -\kappa^2(\alpha\mathbf{F}_1 + \beta\mathbf{F}_2),\\ \mathbf{N} &= N_1(t)\mathbf{F}_1 + N_2(t)\mathbf{F}_2 + N_3(t)\mathbf{i}_3.\end{aligned} \tag{22}$$

As before, it follows from Eqs. (4), (5), (20), and (22) that, if the external loads F^β, F, Q^β, Q, and d^α are independent of the variable φ, then the equilibrium state of the shell is determined by solving the boundary value problem for the system of ordinary differential equations in the unknown functions $\alpha(t)$, $\beta(t)$, and $\gamma(t)$.

It is worth noting that expressions (21) involve the following important particular cases:

(1) $\kappa = 1$, $l_0 = L = 0$ (torsion of a shell of revolution);

(2) $\kappa = -1$, $l_0 = L = 0$ (torsion of a shell of revolution turned inside out);

(3) $\kappa > 0$, $l_0 = L = \beta(t) = 0$ (pure bending of a sector of a shell of revolution); and

(4) $\kappa > 0$, $l_0 = L = 0$ (torsion of a shell of revolution containing a disclination).

DEFORMATION ACCOMPANIED BY A VARIATION IN THE AXIS OF A HELICAL SHELL

We consider the following two-parameter deformations of a helical shell:

$$\begin{aligned}X_1 &= P(t) + K\varphi, \quad K, \theta = \text{const},\\ X_2 &= U(t)\cos\theta\varphi - V(t)\sin\theta\varphi,\\ X_3 &= U(t)\sin\theta\varphi + V(t)\cos\theta\varphi.\end{aligned} \tag{23}$$

In this case, a helical surface σ, which is subjected to such deformations, with its axis parallel to the vector $\mathbf{i}_1$ is transformed into a helical surface Σ with its axis parallel to the vector $\mathbf{i}_1$.

The subsequent arguments concerning the reduction of the problem under consideration to a one-dimensional boundary value problem for the functions $U(t)$, $V(t)$, and $P(t)$ are similar to those given above.

ACKNOWLEDGMENTS

This work was supported by the Russian Foundation for Basic Research, project no. 00-15-96087.

REFERENCES

1. L. M. Zubov, *Methods of Nonlinear Elasticity Theory in Theory of Shells* (Rostovs. Univ., Rostov-on-Don, 1982).
2. W. Pietraszkiewicz, Adv. Mech. **12**, 51 (1989).
3. L. M. Zubov, Izv. Akad. Nauk SSSR, Mekh. Tverd. Tela, No. 2, 128 (1983).
4. K. Z. Galimov, *Principles of Nonlinear Theory of Thin Shells* (Kazan. Univ., Kazan, 1975).

Translated by V. Chechin

Doklady Physics, Vol. 47, No. 1, 2002, pp. 78–84. Translated from Doklady Akademii Nauk, Vol. 382, No. 2, 2002, pp. 199–205.

MECHANICS

Motion of the Earth's Pole

L. D. Akulenko*, S. A. Kumakshev*, and Yu. G. Markov**

Presented by Academician A.Yu. Ishlinskiĭ August 15, 2001

Received August 16, 2001

Using approximate methods of nonlinear mechanics, we construct a theoretical model of the polar motion that satisfies the astrometric data of the International Earth-Rotation Service (IERS). This model is shown to rationally explain the observed characteristics of a complicated oscillatory process executed by the angular-velocity vector with respect to a coordinate system associated with the Earth. On the basis of the IERS data and using the least-squares technique, we determine parameters of the system, determine the trajectory of the pole, and predict its motion. The dynamic model is found to satisfactory describe the overall motion and its fundamental oscillations (free nutation), forced oscillations (annual nutation), and irregular relatively slow drift of the figure-Earth axis (the trend); the model allows further refinement if accessory factors are taken into account.

1. The construction of the mathematical model that satisfies the astrometric data is of interest in natural science and technology. The problem has an age-old history pointing to the lack of a rational approach to its solution; the theories and models available do not account for the essence of the regular mechanical oscillation process [1–3]. The use of only seasonal geophysical factors and an unjustified complication of the model for explaining the mechanism of the moment-of-force action without necessary estimates cannot be considered as conclusive in a mechanical aspect. A very short-term prediction (for 100 days) requires weekly correction, taking into account the IERS operational data (http://hpiers.obspm.fr/eoppc/eop/eopc04/eopc04-xy.gif).

In this paper, we substantiate the possibility of constructing a simple dynamic model using the methods of theoretical and celestial mechanics. The realization proposed for the first-approximation model involves a small number of parameters determined from observations and makes it possible to reliably (from the statistic standpoint) interpret essential characteristics of the pole trajectory and give a reasonably accurate prediction for long-time intervals (from one to a few years).

The principal component of oscillations (free nutation or Chandler wobble) has an amplitude of ~0.″2 and a period $T_1 = 433 \pm 2$ sidereal days. At the Earth's surface, this trajectory is close to a circumference with the center corresponding to the figure axis; the radius is approximately 6.3 m. The characteristics of the oscillations are determined by the inertia tensor of the deformed Earth, with allowance for an "equatorial protuberance" and by the axial-rotation velocity [1–3]; the refined model of the Chandler wobble is constructed in [4]. The amplitude is determined by initial data and, as observations of the last decade show, is quite stable: no noticeable tidal evolution occurs [4].

Frequency analysis testifies to the fact that there is a regular annual component of oscillations with a period $T_h = 365$ sidereal days and an amplitude of ~0.08″. The summation of the Chandler and annual components leads to beats with a period of $T_\Sigma \approx 6$ years. The trajectory represents an either winding or unwinding spiral with minimum ~0.12″ (~3.8 m) and maximum ~0.28″ (~8.8 m) radii. These values are essential and must be taken into account when solving the modern astrometric and navigational problems. The polar-motion prediction is a topical, very interesting, and complicated problem. According to the opinion of specialists, causes and the mechanism of excitation of annual oscillations are not explained; it is customary to relate them to seasonal geophysical phenomena (atmospheric processes and oceanic tides) [1].

Classical investigations in the context of the hard-Earth model were carried out by considering a moment of solar gravitational forces [2, 3]. However, such an approach turned out to be inadequate and did not result in revealing the mechanism of observed oscillations of the angular-velocity vector with respect to the coordinate system associated with the Earth. The authors believe that the annual nutation oscillations can be explained and calculated on the basis of additionally taking into account the daily gravitational tides occur-

* *Institute of Problems of Mechanics, Russian Academy of Sciences, pr. Vernadskogo 101/1, Moscow, 117526 Russia*

** *Moscow Institute of Aviation, Volokolamskoe sh. 4, Moscow, 125080 Russia*

ring in the deformable Earth. The simultaneous analysis of the Euler dynamic and kinematic equations for the inertia tensor deformed with the daily period in the coordinate system associated with the Earth, with allowance for the orbital motion and the figure-axis inclination to the ecliptic plane, makes it possible to establish the presence of the solar moment-of-force action with an annual period relative to the equatorial axes of inertia (see below). The necessary value of the amplitude for this action attains $M_h \approx 10^{20}$ kg m^2 s^{-2} and leads to a relative variation of principal central moments of inertia on the order of 10^{-5}. This is almost two orders of magnitude less than the quasi-steady deformation adopted in the theory of deformable Earth for substantiating the period T_1 of the Chandler wobble [1–4]. The effect of the lunar gravitational-force moment is less by a factor of 20, which is explained by a substantial difference in frequencies for eigenmodes and external actions. Monthly-period mutations of the pole virtually do not manifest themselves.

The axis drift for the figure of the Earth (the trend of ~0.5″ in the direction of ~90° to the west of Greenwich) can be explained by off-diagonal components of the inertia tensor. The relative value of these components is ~10^{-8} and lies outside the limits of accuracy for their determination. The trend variations can be explained by geotectonic processes with time constants on the order of 10^3 years and by the effect of dynamic asymmetry leading to the modulation of Chandler wobbles with a period of about 220 years.

2. For constructing the first-approximation simplified mathematical model, small deformations of the Earth are assumed to proceed mainly in the radial direction. In this case, the equations of rotation with respect to the center of mass can be represented in the form of the classical Euler equations with a variable inertia tensor J [2–6]:

$$J\dot{\boldsymbol{\omega}} + \boldsymbol{\omega} \times J\boldsymbol{\omega} = \mathbf{M}, \quad \boldsymbol{\omega} = (p, q, r)^T,$$
$$J = J^* + \delta J, \quad J^* = \text{const}, \tag{1}$$
$$J^* = \text{diag}(A^*, B^*, C^*), \quad \delta J = \delta J(t), \quad \|\delta J\| \ll \|J^*\|.$$

Here, $\boldsymbol{\omega}$ is the angular-velocity vector in the coordinate system associated with the Earth (the reference system), which approximately coincides with the principal central axes of inertia J^* of the "frozen" Earth with allowance for the equatorial protuberance [2–4]. The small inertia-tensor variations δJ are considered as containing various harmonic components caused by the effect of solar and lunar daily tides and, possibly, other (annual, half-annual, monthly, half-daily, etc.) components. The gravitational actions are taken as the main perturbing external moments of forces $\mathbf{M}$ causing the nutation oscillations.

The Euler kinematic equations setting the orientation of the coordinate system associated with the Earth about the orbital coordinate system are of the form

$$\dot{\theta} = p\cos\varphi - q\sin\varphi - \omega_0(\nu)\sin\psi,$$
$$\dot{\nu} = \omega_0(\nu) = \omega_*(1 + e\cos\nu)^2, \tag{2}$$
$$\dot{\psi} = \frac{p\sin\varphi + q\cos\varphi}{\sin\theta} - \omega_0(\nu)\cot\theta\cos\psi, \quad e = 0.0167,$$
$$\dot{\varphi} = r - (p\sin\varphi + q\cos\varphi)\cot\theta + \omega_0(\nu)\frac{\cos\psi}{\sin\theta}.$$

Here, $\nu(t)$ is the real anomaly, e is the orbital eccentricity, and ω_* is a constant determined by the gravitational and focal parameters. While investigating equations (1) and (2) in the situation corresponding to the polar motion, the terms in equations (2), which are proportional to ω_0, turn out to be essentially higher compared to p and q (by a factor of approximately 300) and are the defining factors for finding $\dot{\theta}$ and $\dot{\varphi}$. In scientific literature, this important property was not noted, while the above-indicated terms were discarded without proof.

The structure of expressions for components of the moment of solar gravitational forces is of the form [7]

$$M_q = 3\omega^2[(A^* + \delta A - (C^* + \delta C))\gamma_r\gamma_p$$
$$+ \delta J_{pq}\gamma_r\gamma_q + \delta J_{pr}(\gamma_r^2 - \gamma_p^2) - \delta J_{rp}\gamma_p\gamma_q], \tag{3}$$
$$\omega = \omega_*(1 + e\cos\nu)^{3/2},$$
$$\gamma_p = \sin\theta\sin\varphi, \quad \gamma_q = \sin\theta\cos\varphi, \quad \gamma_r = \cos\theta.$$

For calculating $M_{p,r}$, we make a cyclic permutation of the subscripts p, q, and r in (3). Analysis of (3) shows that the annual component of mutations of the pole can be caused by the term involving the products $\gamma_p\gamma_r$ and $\gamma_q\gamma_r$ of direction cosines. For their calculation in the first approximation, we integrate equations (2):

$$r = r^0, \quad \varphi \approx rt + \varphi^0, \quad \nu \approx \omega_* t + \nu^0,$$
$$\cos\theta(\nu) = a(\theta^0, \psi^0)\cos\nu,$$
$$\theta(0) = \theta^0 = 66°33', \quad 0.4 \le a \le 1, \quad 0 \le \psi^0 \le 2\pi, \tag{4}$$
$$\cos\theta\sin\theta = b(\theta^0, \psi^0)\cos\nu + d\cos 3\nu + \ldots,$$
$$0.4 \le b \le \frac{4}{3}\pi^{-1}, \quad |d| \ll 1.$$

The second and higher harmonics in ν lead to values that are smaller than the principal ones by a factor of 10^2–10^3, and, therefore, can be ignored. The value of $B^* - A^*$ is also considerably smaller than that of

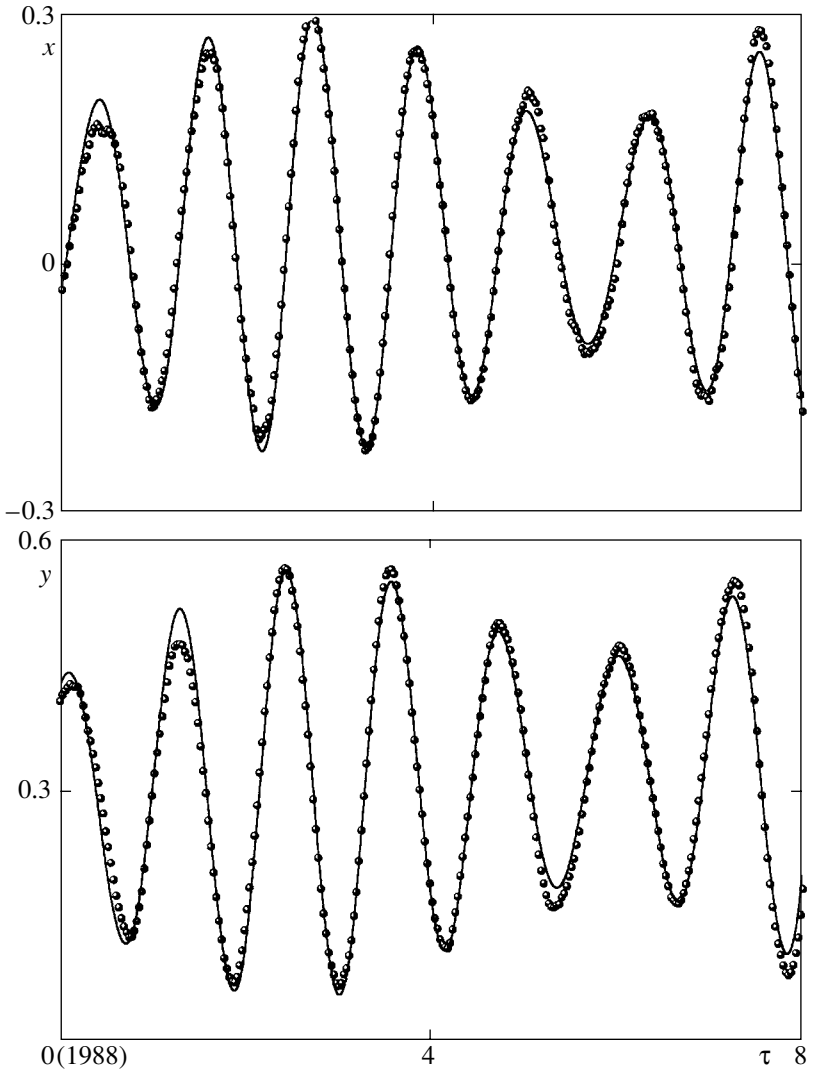

Fig. 1. Interpolation of the pole trajectory for the eight-year interval of 1988–1995 (solid line); here, as in Figs. 2–4, dots correspond to the IERS data.

$C^* - A^*$ (by a factor of approximately 160). After averaging over the fast phase φ, the estimate of terms in equations (1) for p and q leads to a simplified analytical model of the form

$$\begin{gathered}\dot{p} + N_p q = \kappa_q r^2 + 3b\omega_*^2 \chi_p \cos\nu, \\ N_{p,q} \approx N = \frac{2\pi}{T_1} \approx 0.84\omega_*, \\ \dot{q} - N_q p = -\kappa_p r^2 - 3b\omega_*^2 \chi_q \cos\nu, \\ p(0) = p^0, \quad q(0) = q^0.\end{gathered} \tag{5}$$

Here, κ_p and κ_q are the average values of $\frac{\delta J_{pr}}{B^*}$ and $\frac{\delta J_{qr}}{A^*}$, which can be slow functions. The quantities χ_p and χ_q are obtained by averaging over φ for the coefficients of cosν in the components of the moment of solar gravitational forces; as was noted, they are caused by the daily tides. The moments of the lunar gravitational force are ignored due to their relatively low effect on the nutation oscillations.

The right-hand sides of Eqs. (5) contain in an explicit form harmonic action with the annual period, which explains the mechanism of nutation oscillations detected by the IERS observations. Although the sensitivity of the coefficients $\kappa_{p,q}$ is five orders higher than that of $\chi_{p,q}$, the regular mechanism of the annual (moment-of-force) action with the indicated amplitude $M_h \sim 10^{20}$ kg m^2 s^{-2} by means of internal geophysical factors seems to be inconsistent in the mechanical aspect.

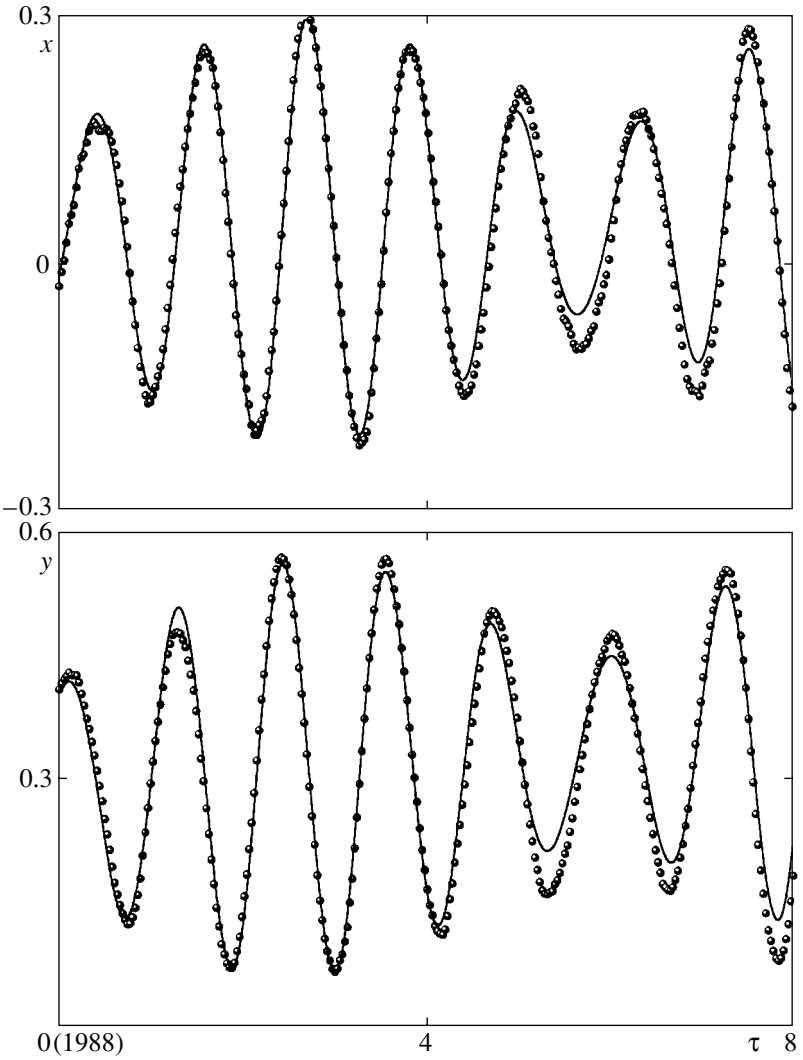

Fig. 2. Interpolation of the pole trajectory for the four-year interval of 1988–1991 and the prediction for 1992–1995 (solid line).

3. The values of the coefficients $\kappa_{p,q}$ and $\chi_{p,q}$ and the initial values p^0 and q^0 are unknown: they should be determined on the basis of observational data. Introducing the variables $x(\tau) = p(t)$ and $y(\tau) = q(t)$, where $\tau = \dfrac{t}{T_h}$ is the time measured in years, we obtain the structure of solution to the set of Eqs. (5) [8]:

$$\begin{aligned} x(\tau) &= c_x - a_x^c \cos 2\pi N\tau + a_x^s \sin 2\pi N\tau \\ &\quad - \frac{N d_x^c \cos 2\pi\tau + d_x^s \sin 2\pi\tau}{1 - N^2}, \\ y(\tau) &= c_y + a_y^c \cos 2\pi N\tau + a_y^s \sin 2\pi N\tau \\ &\quad - \frac{N d_y^c \cos 2\pi\tau - d_y^s \sin 2\pi\tau}{1 - N^2}. \end{aligned} \tag{6}$$

Here, $c_{x,y}$, $a_{x,y}^{c,s}$, and $d_{x,y}^{c,s}$ are the quantities to be calculated by the least-square technique [9] from the IERS measurements [1, 8]. These coefficients are unambiguously related to the unknowns involved in set (5); in this case, it is necessary to take into account the equalities $a_x^{c,s} = a_y^{s,c}$ and $d_x^{c,s} = d_y^{s,c}$ representing the structural property of the model. The parameters introduced can be subjected to a correction of the form $c_{x,y} = c_{x,y}^0 + c_{x,y}^1\tau + \ldots$ in a reasonably long interval $0 \le \tau \le \Theta$ (where, e.g., $\Theta \sim 10$–20 years); a similar correction can be made for $a_{x,y}^{c,s}$ and $d_{x,y}^{c,s}$. The secular terms must take into account the evolution of the parameters of set (1)–(5) for improving the interpolation of the oscillation process [8]. Theoretical model (6) can be refined by taking into account accessory factors but this seems to be unsuitable and unjustified at the given stage.

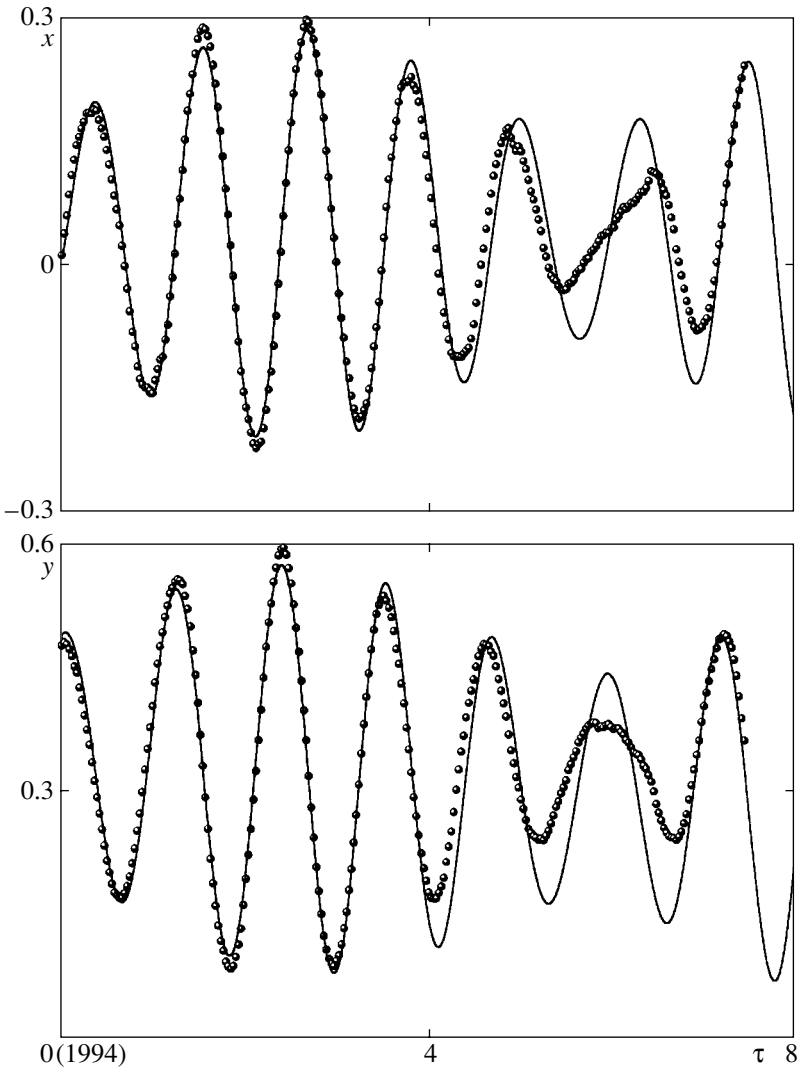

Fig. 3. Interpolation of the pole trajectory for the four-year interval of 1984–1997 and the prediction for 1998–2001 (solid line).

Below, we present the results of calculations on the basis of the method of least squares [9], which was applied independently to the variables $x(\tau)$ and $y(\tau)$ in the form of the six-dimensional approximation according to model (6):

$$x(\tau) = (\xi, f(\tau)), \quad y(\tau) = (\eta, f(\tau)),$$
$$\xi = (\xi_1, \ldots, \xi_6)^T, \quad \eta = (\eta_1, \ldots, \eta_6)^T, \tag{7}$$
$$f(\tau) = (1, \tau, \cos 2\pi N\tau, \sin 2\pi N\tau, \cos 2\pi\tau, \sin 2\pi\tau)^T,$$
$$N = 0.84.$$

First, it is of interest to investigate the efficiency of the interpolation and prediction for the polar motion by means of the simple mathematical model (6) on the basis of the known daily IERS measurement data [1]. In Fig. 1, we show the theoretical curves $x^*(\tau)$ and $y^*(\tau)$ of interpolation for daily measurements on the eight-year time interval $0 \le \tau \le 8$ from 1988 to the end of 1995. The root-mean-square deviations are equal to $\sigma_x = 0.014$ and $\sigma_y = 0.017$, which indicates a satisfactory accuracy of the model constructed (6), (7) corresponding to the optimal values of ξ^*, η^*:

$$\xi^* = (0.041, -0.0004, -0.034, 0.194, -0.023, -0.065)^T, \tag{8}$$
$$\eta^* = (0.300, 0.005, 0.193, 0.033, -0.060, 0.020)^T.$$

The comparison of the coefficients ξ_3^* and η_4^*, ξ_4^* and η_3^*, determining the Chandler components of oscillations, and also ξ_5^* and η_6^*, ξ_6^* and η_5^* (with allowance for the factor $N = 0.84$), corresponding to the annual

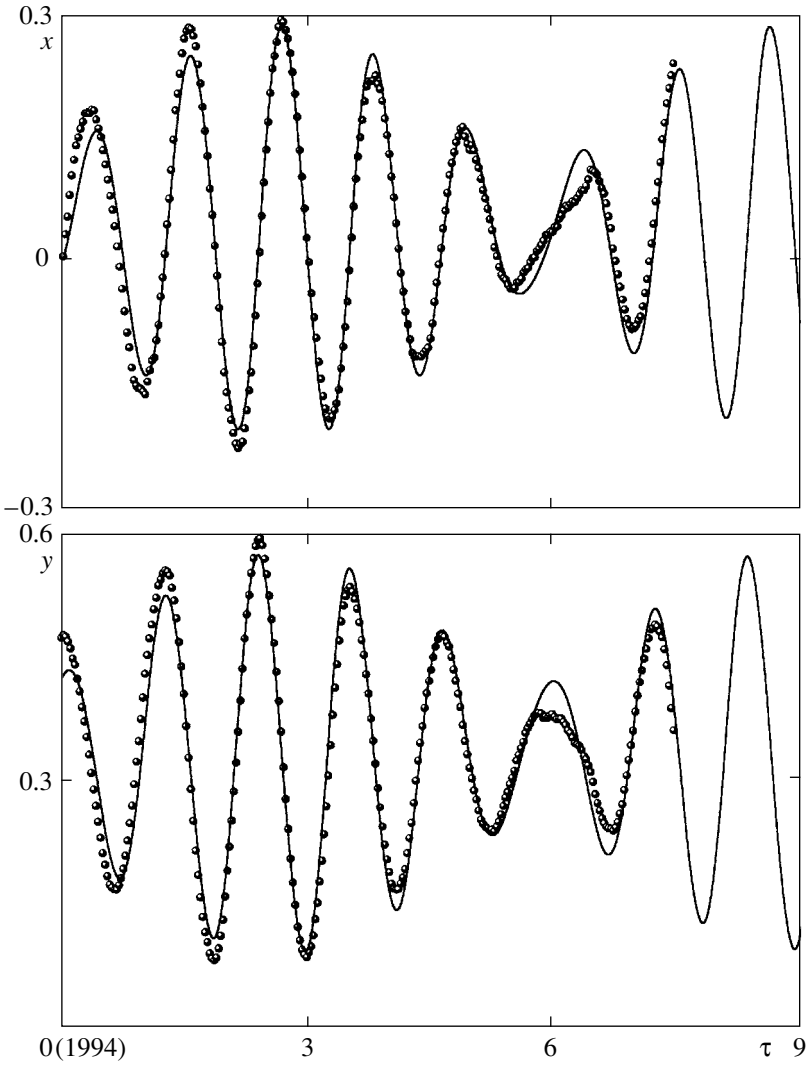

Fig. 4. Interpolation of the pole's trajectory for the seven-year interval 1994–2000 and the prediction for 2001–2002 (solid line).

component in (8), strongly supports the indicated structural property of the model.

In Fig. 2, we display the theoretical curves $x^*(\tau)$ and $y^*(\tau)$ plotted on the basis of the measurement data for the four-year interval $0 \le \tau \le 4$ and give a prediction for $4 \le \tau \le 8$. The comparison with the experimental points confirms the efficiency of the model, i.e., the high accuracy of interpolation and a reasonably reliable prediction. The corresponding optimal vectors ξ^*, η^*, and the root-mean-square errors σ_x, σ_y in the interpolation interval are:

$$\xi^* = (0.039, 0.002, -0.023, 0.182, -0.025, -0.072)^T,$$
$$\sigma_x = 0.012,$$
$$\eta^* = (0.298, 0.007, 0.179, 0.025, -0.068, 0.023)^T, \quad (9)$$
$$\sigma_y = 0.015.$$

Comparison of the values obtained in accordance with (9) for the indicated coefficients corroborates the structural property of the theoretical model.

In Fig. 3, we show the results of interpolation and prediction using model (7) on the basis of the operative daily IERS data from 1994 to mid-2001. The optimal theoretical trajectory $x^*(\tau)$, $y^*(\tau)$ is plotted by interpolation on a four-year interval; the prediction for four years is given beginning from 1988. The optimal parameters ξ^*, η^* and the root-mean-square errors σ_x, σ_y are:

$$\xi^* = (0.036, -0.0005, 0.003, 0.188, -0.037, -0.051)^T,$$
$$\sigma_x = 0.016,$$
$$\eta^* = (0.345, -0.007, 0.193, -0.006, -0.048, 0.027)^T, \quad (10)$$
$$\sigma_y = 0.015.$$

The anomaly of the mutation of the pole from the end of 1999 to mid-2000 is noteworthy, which, in our opinion, can be naturally explained by the gravitational perturbations (parade of planets). In the next time interval, the regular mutations of the pole take place according to model (7). This fact is an indirect confirmation of the adequacy and efficiency of the model. The components of the vectors ξ^*, η^* (10) satisfy the required properties of the model.

In Fig. 4, we display the results of interpolation for the seven-year data of measurements from the beginning of 1999 to the end of 2000. Then, we predict the trajectory for two years from the beginning of 2001 to the end of 2002. The optimal parameters ξ^*, η^* of theoretical model (7) and the root-mean-square errors σ_x, σ_y are:

$$\xi^* = (0.039, 0.0001, 0.015, 0.161, -0.046, -0.076)^T,$$
$$\sigma_x = 0.024, \qquad (11)$$
$$\eta^* = (0.334, 0.0005, 0.162, -0.0139, -0.068, 0.043)^T,$$
$$\sigma_y = 0.025.$$

The coefficients in (11) convincingly satisfy to the fact of the structural property of theoretical model (6), (7).

We also carried out numerous calculations for verifying the efficiency of the model by the interpolation in time intervals from 2 to 20 years and the prediction of the trajectory for 1–5 years. The results obtained testify to the satisfactory accuracy for the interpretation of observations and for the prediction of the pole trajectory by a very simple theoretical first-approximation model. This model admits its natural refinement and complication by taking into account accessory factors to which we can also assign random perturbations.

ACKNOWLEDGMENTS

This work was supported by the Russian Foundation for Basic Research, project nos. 02-01-00252, 02-01-00176, 01-01-06306, and 01-02-17250.

REFERENCES

1. *International Earth-Rotation Service Annual Reports, Central Bureau of IERS* (Observatoire de Paris, Paris, 1991–2000).
2. Yu. N. Avsyuk, *Tidal Forces and Natural Processes* (Moscow, 1996).
3. G. Moritz and A. Müller. *Earth's Rotation. Theory and Observations* (Naukova Dumka, Kiev, 1992).
4. L. D. Akulenko, Yu. G. Markov, and L. V. Rykhlova, Dokl. Akad. Nauk **377**, 618 (2001) [Dokl. Phys. **46**, 261 (2001)].
5. A. A. Il'yushin, *Mechanics of Continuum* (Mosk. Gos. Univ., Moscow, 1990).
6. F. L. Chernous'ko, Izv. Akad. Nauk SSSR, Mekh. Tverd. Tela, No. 1, 22 (1980).
7. V. V. Bondarenko, Yu. G. Markov, and I. V. Skorobogatykh, Astron. Vestn. **32**, 340 (1998).
8. L. D. Akulenko, S. A. Kumakshev, and Yu. G. Markov, Dokl. Akad. Nauk **379**, 191 (2001) [Dokl. Phys. **46**, 508 (2001)].
9. Yu. V. Linnik, *Least-Squares Technique and Principles of the Mathematical-Statistical Theory of Observations* (Pergamon Press, Oxford, 1961; Fizmatgiz, Moscow, 1962).

Translated by V. Bukhanov

Doklady Physics, Vol. 47, No. 1, 2002, pp. 85–88. Translated from Doklady Akademii Nauk, Vol. 382, No. 2, 2002, pp. 206–209.

MECHANICS

Quantum Nature and Dual Character of Fracture Dynamics in Solids

Academician N. F. Morozov and Yu. V. Petrov

Received September 28, 2001

There is no doubt that the fracture process in solids is multistage and multilevel; therefore, its adequate modeling necessitates using advanced modern experimental and computing methods. At the same time, the formulation of principles that could be applicable in engineering practice increasingly becomes an urgent problem. This is explained by the fact that methods and ways used in analyzing a large number of well-known models (mainly numerical), unfortunately, turned out to be accessible almost exclusively only to their authors. However, in practice, it is very important to have clear analytical tools that make it possible to reduce the qualitative analysis of fracture to simple procedures suitable for application in engineering. One of the most well-known examples of such a practical approach is the structural macromechanics of fracture [1–3], as well as the structure–time approach [4] based on the notion of incubation fracture time (which is a natural generalization for application in fracture dynamics). These fracture theories represent the deep structure–time regularities of fracture processes in solids. One of the most important consequences of these approaches is associated with the dual character of dynamic fracture, which can be expressed in certain relations between time parameters of loading and the incubation period preceding the time moment of macroscopic fracture. This results in a novel version of the problem related to testing the dynamic-strength properties of materials. In a certain sense, this situation is similar to what we dealt with in the case of a spatial characteristic linear size in static fracture mechanics. To elucidate the situation, we consider the static and dynamic cases successively.

One of the principal parameters in linear fracture mechanics is the structural linear size d describing a unit fracture cell. The linear size can be represented in the form of a dimensional combination involving the surface energy, the critical stress-intensity factor, the static strength, and the elastic constants of a material:

$$d \sim \frac{\gamma E}{\sigma_c^2}, \quad d \sim \frac{K_{Ic}^2}{\sigma_c^2}. \tag{1}$$

Smirnov Research Institute of Mathematics and Mechanics, St. Petersburg State University, Universitetskaya nab. 7/9, St. Petersburg, 199164 Russia

There exist several suggestions of various authors, which concern the physical nature of the parameter d (interatomic distance in a medium with a regular atomic structure, grain size in a polycrystalline medium, scaling parameter for strength characteristics, etc.). In this study, this parameter is treated as a specific linear size characterizing a unit fracture cell at a given scale level. Note that in the classical Griffith–Irwin approach [5, 6] this characteristic is present in the implicit form.

In the Neuber–Novozhilov approach, the linear size is assumed to be taken into account explicitly. We now consider basic principles of structural fracture macromechanics corresponding to this approach. They can be reduced to the following points similar to those that were enunciated as early as in the beginning of the last century, when principles of classical quantum mechanics were formulated:

(i) all solids consist of structural spatial elements of a finite size;

(ii) an elementary fracture act is the fracture of a single structural element;

(iii) criterion parameters (including the size of a structural element) must be chosen in such a manner that, in ultimate adequate cases, the results of the classical fracture theory could be obtained.

We now apply these principles to formulate an adequate condition for fracturing. We consider a static two-dimensional stress field (e.g., corresponding to the case of plane deformation) and suggest that the fracture occurs along a certain direction Ox, which is assumed to be a symmetry line. In accordance with the aforesaid first principle, we assume that the solid structure is specified in the spatial scale (Fig. 1a) and that the linear size of a single structural component is equal to d. In accordance with the second principle [2], we suggest that the macrofracture has occurred when even only a single structural element failed. The natural condition of fracture can be written out in the form of the condition when a force acting onto a structural element attains a certain critical value:

$$F \le F_c. \tag{2}$$

1028-3358/02/4701-0085$22.00

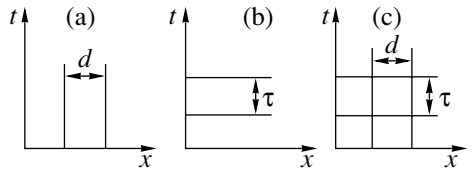

Fig. 1. Fracture structural parameters: (a) linear size; (b) incubation time; and (c) space-and-time fracture cell.

In terms of a uniform stress field that we actually deal with in continuum mechanics, this relationship can be written out in the form

$$\int_{x-d}^{x} \sigma dr \le \sigma_c d. \tag{3}$$

The condition (3) represents the Neuber–Novozhilov force criterion. The stress σ_c can be treated as a specific critical stress introduced instead of the critical force F_c.

To determine σ_c and the linear size d introduced above, it is necessary to apply the third basic principle. Next, using (3), we consider the problem of fracturing a homogeneous sample free of defects. Assuming that, in this case, the fracture is determined by the classical strength criterion $\sigma \le \sigma_B$, we obtain that $\sigma_c = \sigma_B$. We now consider the classical problem of the Griffith crack and the Irwin fracture criterion. First, we substitute the tensile stress corresponding to the crack continuation

$$\sigma = \frac{K_I}{\sqrt{2\pi r}} + O(1), \quad r \longrightarrow 0 \tag{4}$$

into criterion (3). Then, integrating over r ($r = x - d$) from 0 to d and taking into account that $K_I \le K_{Ic}$, we arrive at the following formula for the linear size:

$$d = \frac{2}{\pi}\frac{K_{Ic}^2}{\sigma_c^2}. \tag{5}$$

The physical meaning of the parameter σ_c is beyond question: this is the brittle strength of a defect-free sample. However, there exist different opinions concerning the physical meaning of the parameter d. It would be promising to unambiguously relate d with characteristics of the material internal structure (interatomic distances, physical or geometric parameters of dislocation motions, grains, grain blocks, etc.). Nevertheless, there is no need to do so! Similar to the situation with the actual strength of a polycrystal (e.g., an alloy), σ_c is not directly related to the atomic-lattice strength of a particular single-crystal block that forms the given crystal. Generally speaking, the linear size d also must not be unambiguously determined by the geometric structure of the material. The parameters σ_c and d are equivalent and independent characteristics of the fracture process [7]. Therefore, in our opinion, the treatment of d given in [8] as a scaling parameter that determines the correlation of material strength properties at a given scale level seems to be the most natural. It is much more significant that, in accordance with basic physical principles, such defining parameters introduced into theory must be measurable, i.e., directly or indirectly be determined experimentally. For σ_c and d, this requirement is completely fulfilled.

The above approach admits a natural generalization for the dynamic case. Let, under the previous conditions, the stress state of the medium be spatially uniform and change only with time (Fig. 1b). In addition, let a certain structure also be given in the time scale. We denote the corresponding time size by τ and call it structural (incubation) fracture time. We assume that the fracture takes place provided that a force pulse acting during the time τ attains its critical value

$$J(t) \le J_c. \tag{6}$$

In terms of the continuum mechanics, we have

$$\frac{1}{\tau}\int_{t-\tau}^{t} \sigma(t')dt' \le \sigma_c. \tag{7}$$

Here, τ is the minimum time that is needed for fracturing an element under the action of the stress σ_c.

In the general case of the space-and-time nonuniformity of the dynamic stress field, we have a combination of both previous variants and the corresponding space-and-time unit fracture cell (Fig. 1c). Then, we have the following structure–time criterion:

$$\frac{1}{\tau}\int_{t-\tau}^{t}\frac{1}{d}\int_{0}^{d}\sigma(r, \theta, t')drdt' \le \sigma_c. \tag{8}$$

Here, (r, θ) are the polar coordinates and $\sigma(r, \theta, t)$ is the maximum rupture stress near the crack tip ($r = 0$). Thus, the parameters σ_c, K_{Ic}, and τ form a system of defining parameters in the given fracture theory. Written out in form (8), the dynamic criterion was first put forward in [9].

In the case of a defect-free material, criterion (8) is reduced to the form (7), which is convenient for simulating fracture under the splitting-off condition. Criterion (7) is the efficient means for explaining the time dependence of strength, which makes it possible to pro-

vide a unified description of the static and dynamic branches, as well as a prediction of the geometry of the fracture zone in the splitting-off process [4, 10].

In the case of fracturing near the tip of a symmetrically loaded crack, condition (5) should be taken into account. Then, it follows from (8) that

$$\frac{1}{\tau}\int_{t-\tau}^{t} K_I(t')dt' \le K_{Ic}. \qquad (9)$$

It is shown in [11] that, in the case of dynamic fracture near the macroscopic-crack tip, the structural size τ in criterion (9) can be treated as an incubation time in the well-known criterion of the minimum time, which was proposed and studied in [12–14].

Analysis of fracture with the help of structure–time criteria (7) and (9) presents the possibility to determine ultimate dynamic loads, dynamic fracture strength, and dynamic fracture viscosity as calculated parameters. This is possible, provided that σ_c, K_{Ic}, and τ are used as constants of the material, which are assumed to be independent of both the way and the history (rate) of loading.

In the case of the structure–time approach, the analysis of the available experimental data shows that the corresponding unstable behavior of the dynamic fracture strength σ_d and the dynamic fracture viscosity K_{Id} is a principle feature of the dynamic fracture, which is caused by the discrete structure–time nature of the process [15]. The observed significant data spread of both dynamic fracture strength and the dynamic fracture viscosity, which were measured under various conditions, reflects the space-and-time structure and physical discreteness of the dynamic fracture process. With this fact taken into account, we can also conclude that introducing into the dynamic theory the so-called strain-rate dependences for the critical stress σ_d and the critical-intensity coefficients K_{Id} as functional characteristics of the material under consideration (by analogy with the static ones σ_c and K_{Ic}) is incorrect.

The effects indicated become significant when we pass from slow actions to those having periods compared in their duration to a scale depending on the incubation fracture time. The nature of this period of time is determined by the preliminary relaxation processes of developing microdefects in the material structure. In essence, the structural size and the incubation time are the parameters determining the boundary between the micro- and macrofractures in the space-and-time scale under consideration, which corresponds to the given scale level.

Thus, our analysis of fracture processes indicates that it is necessary to take into account at least two dynamics types, namely, dynamics of elastic-wave propagation and the dynamics of structural-element fracture. Both of them manifest themselves as being dependent on the testing scale level, geometric characteristics of samples, and loading conditions. The first is determined by the ratio between a characteristic length of samples and the loading rate (or by a characteristic wavelength). This ratio provides an efficient tool for the distinction between the static and dynamic models. For example, when the action pulses are short compared to the time interval needed for propagating the stress wave through a sample, it is necessary to take into account inertial effects and to analyze corresponding hyperbolic equations. Note that, when the loading rate is reasonably small or a pulse duration sufficiently exceeds the corresponding incubation time for the fracture process, we can apply the static critical stress and the static fracture viscosity to estimate ultimate loads. The second type of dynamics is associated with the situation when an interval of the load application is on the order of (or less than) the incubation time of the sample material. Then, it is necessary to take into account the dynamic specificity of the fracture process, which can manifest itself, for example, as a dependence of the fracture strength and fracture viscosity on the loading history. In this case, it is appropriate to use the structure–time criterion.

Thus, for studying properties of the material dynamic strength, we may use various combinations of sample sizes (e.g., small-sized samples) and loading parameters, thereby realizing one type of fracture dynamics or another. If the interval of loading time is on the order of (or less than) the incubation time but is larger, in fact, than the interval needed for the stress wave to propagate through the sample, we can investigate the dynamic specificity of the fracture process on the basis of a quasi-static solution to the corresponding boundary value problem. The size of a small sample must be determined by the conditions that provide the quasi-static stabilization of the stress field until the fracture time moment.

The above arguments are of importance when determining the scale level for experimentally observable effects and in choosing a corresponding technique for testing static and dynamic strength properties of materials.

ACKNOWLEDGMENTS

This work was supported by the Russian Foundation for Basic Research (project nos. 99-01-00718, 00-01-00489, 00-15-96023, and TsKP 00-01-05020).

REFERENCES

1. H. Neuber, *Kerbspannungslehre* (Julius Verlag, Berlin, 1937).
2. V. V. Novozhilov, Prikl. Mat. Mekh. **33**, 212 (1969).
3. V. V. Novozhilov, Prikl. Mat. Mekh. **33**, 797 (1969).

4. N. Morozov and Y. Petrov, *Dynamics of Fracture*. (Springer, Berlin, 2000).
5. A. Griffith, Philos. Trans. Roy. Soc. London. Ser. A **221**, 163 (1921).
6. G. Irwin, J. Appl. Mech. **24**, 361 (1957).
7. N. F. Morozov, *Mathematical Problems of Crack Mechanics* (Nauka, Moscow, 1984).
8. R. V. Gol'dshtein and N. M. Osipenko, Dokl. Akad. Nauk SSSR **240**, 829 (1978) [Sov. Phys. Dokl. **23**, 421 (1978)].
9. N. F. Morozov and Yu. V. Petrov, Izv Akad. Nauk SSSR, Mekh. Tverd. Tela, No. 6, 108 (1990).
10. N. F. Morozov, Yu. V. Petrov, and A. A. Utkin, Dokl. Akad. Nauk SSSR **313**, 276 (1990) [Sov. Phys. Dokl. **35**, 646 (1990)].
11. Yu. V. Petrov and N. F. Morozov, ASME J. Appl. Mech. **61**, 710 (1994).
12. J. F. Kalthoff and D. A. Shockey, J. Appl. Mech. **48**, 986 (1977).
13. H. Homma, D. A. Shockey, and Y. Murayama, J. Mech. Phys. Solids **31**, 261 (1983).
14. D. A. Shockey, D. C. Erlich, J. F. Kalthoff, and H. Homma, Eng. Fract. Mech. **23**, 311 (1986).
15. Yu. V. Petrov, Dokl. Akad. Nauk SSSR **321**, 66 (1991) [Sov. Phys. Dokl. **36**, 802 (1991)].

Translated by Yu. Vishnyakov

Doklady Physics, Vol. 47, No. 1, 2002, pp. 89–91. Translated from Doklady Akademii Nauk, Vol. 382, No. 3, 2002, pp. 343–345.

MECHANICS

Cavities and Flow Nonuniqueness behind a Sill in an Open Channel

V. I. Bukreev and A. V. Gusev

Presented by Academician V.M. Titov April 27, 2001

Received May 24, 2001

Many outstanding scientists have analyzed the flow around a sill in an open channel [1]. However, this problem of hydraulics has a number of weakly studied aspects, which include, under certain conditions, the formation of an air cavity behind a sill. Our paper contains experimental data on methods of closure of the cavity free end, which are important for cavity theory [2]. In addition, we show that many different steady-state regimes can be formed with the same external problem parameters, i.e., that the flow under consideration is not unique.

The experiments were carried out in a rectangular open channel with a zero bottom slope. The sill had a rectangular cross section with a length and height equal to 30 and 4.9 cm, respectively. In the transverse direction (6 cm), the sill closed the channel. The force of gravity and surface tension at the water–air interface (73×10^{-3} N/m) represented the most important problem parameters. The discharge Q varied within the range for which the flow behind the sill was supercritical. The flow pattern was visualized by adding an aluminum powder with typical particle dimensions of 10 μm into the water. Photographic recording of particle trajectories was carried out in a dark room so that the part of flow under investigation was illuminated with a 1-cm-thick penlight.

As is well known [1], three typical flow regimes can be observed behind a sharp-crested weir. They are characterized by adhering, free, and depressed nappes, respectively. It is also known that an adhering nappe can become free by injecting air under it without varying any external problem parameters. In this paper, we show that under certain conditions similar phenomena occur behind a broad-crested weir, i.e., that both a depressed-nappe regime and many free-nappe regimes can form with identical problem parameters.

Photographs presented in Fig. 1 for illustration were obtained at $Q = 1.159$ l/s and the above-mentioned values of the other parameters. In Fig. 1a, the nappe is depressed, while in Fig. 1b there is an air cavity existing for an arbitrarily long time.

Flow regimes can be controlled. For example, if the transition to the steady-state conditions is sufficiently slow, then the adhering nappe becomes depressed without the formation of a cavity. At a rapid increase in the flow rate, the flow separates from different points of the downstream sill edge at different moments of time. As a result, conditions arise for air leak-in under the nappe and, thus, for cavity formation. Transition from a steady-state free nappe with cavities of different volumes to a depressed nappe can be realized by a short-term elevation of the free-surface level behind the sill and a subsequent return to the initial steady-state conditions. The reverse transition from the depressed nappe to the free one can be realized by means of air injection or suction.

The cavity stability depends essentially on both the sill length and the height of the nappe fall. Our experiments have shown that, in a certain range of these parameters, sporadic air leakage from the cavity to the atmosphere leads to self-sustained oscillations. In nature, a similar process occurs, for example, in pulsating waterfalls, in which flow regimes are free-nappe and air cavities periodically change their volumes.

Different methods are used in cavity theory to close the cavity free end [2]. Among them, the Riaboushinsky–Weinig calculation scheme [2] based on using a fictitious return jet is preferable. Our experiments (Fig. 2a) qualitatively verify the possibility of a return jet existing in the cavity formed behind a sill. However, actual and fictitious return jets differ from each other (cf. Fig. 2a with the calculating scheme [2]). This is explained by the fact that the fluid viscosity, surface tension, force of gravity, and occurrence of both the free surface and the channel bottom are not taken into account in the calculation scheme. In our experiments, the shape and dimensions of the jet varied with time, while the total cavity volume remained constant for an arbitrarily long time.

Figure 2b verifies the method of introducing a fictitious wall [2] for closure of the free cavity end in the

Lavrent'ev Institute of Hydrodynamics, Siberian Division, Russian Academy of Sciences, pr. Akademika Lavrent'eva 15, Novosibirsk, 630090 Russia

1028-3358/02/4701-0089$22.00

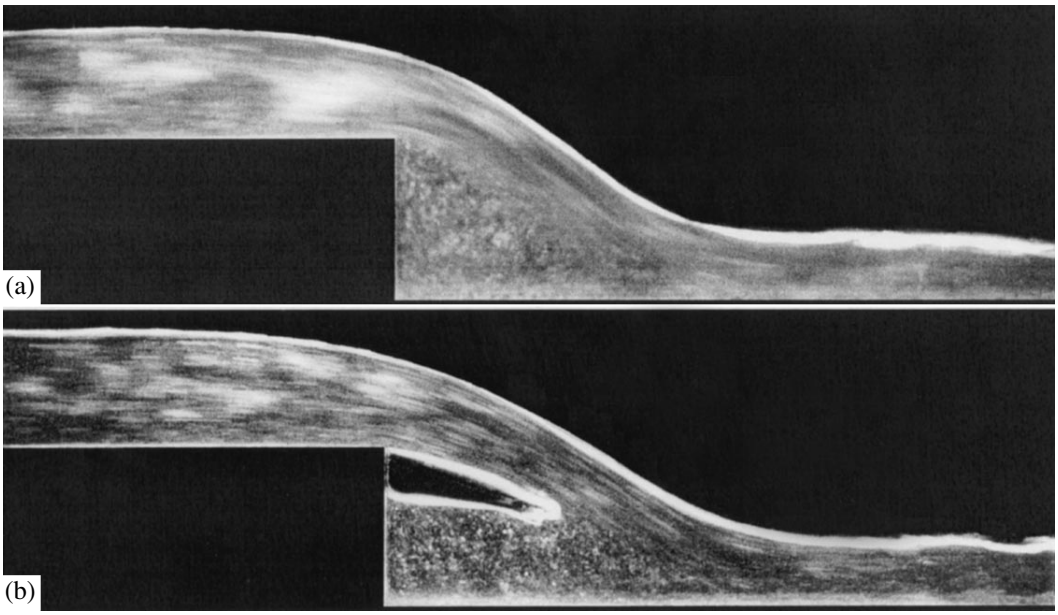

Fig. 1. (a) Depressed and (b) free nappes with identical values of the parameters. The flow is directed from the left to the right.

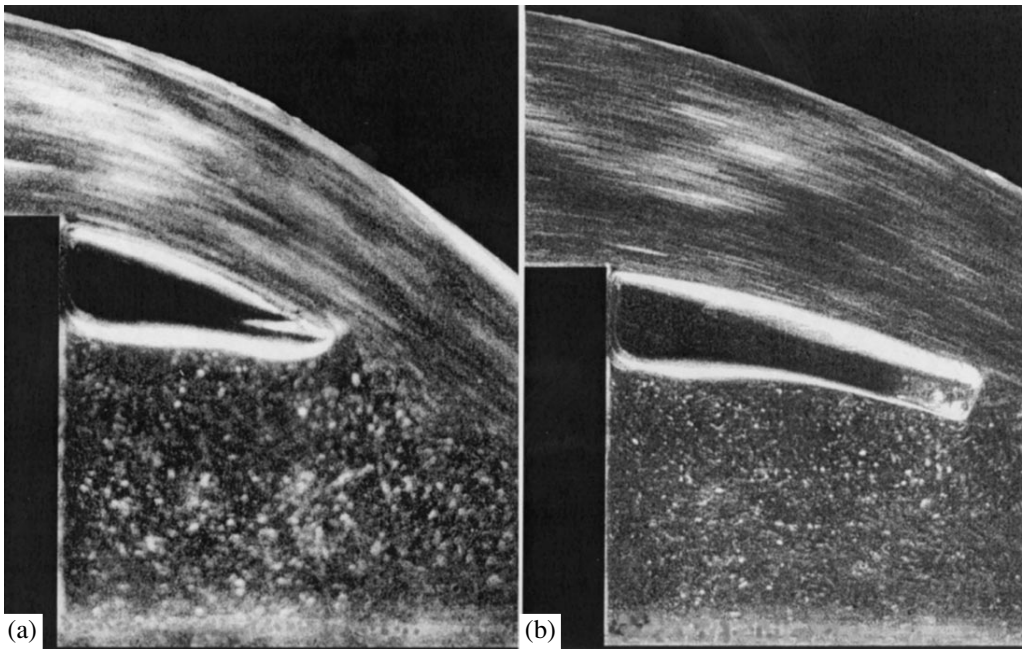

Fig. 2. Examples of closure of the free cavity end at (a) $Q = 0.904$ and (b) 1.473 l/s.

calculation schemes. However, in our experiments, cavities with flat free ends were unstable. Air bubbles were sporadically released from them until the formation of one of the stable configurations was over. Along with stable cavities containing return jets, we observed a stable cavity having its free end in the form of an acute angle slightly smoothed by the surface tension.

According to the classical theory, upper and lower cavity boundaries must be convex towards the side of the surrounding liquid [2]. However, in a flow with a free surface behind a weir, the shape of cavity boundaries is more complicated because of the effect of the force of gravity.

In the regimes possible with identical external parameters, flow features important for practice can be highly different. For example, at a flow rate of 2 l/s and the above-mentioned values of other parameters, the maximum excess pressure exerted on the channel bot-

tom behind the sill varied from 700 Pa (in the regime without a cavity) to 1200 Pa (in the regime with a stable cavity of the largest volume). In these regimes, the discharge coefficient characterizing the flow capacity of a sill considered as a spillway [1] varied from 0.38 (in the first case) to 0.32 (in the second case).

ACKNOWLEDGMENTS

This work was performed under the financial support of the Russian Foundation for Basic Research (project no. 01–01–00846) and in the framework of the Program of Leading Scientific Schools of the Russian Federation (project no. 00-05-98542).

REFERENCES

1. P. G. Kiselev, *Handbook on Hydraulic Design* (Gosénergoizdat, Moscow, 1957).
2. G. Birkhoff and E. H. Zarantonello, *Jets, Wakes, and Cavities* (New York, 1957; Mir, Moscow, 1964).

Translated by Yu. Verevochkin

Doklady Physics, Vol. 47, No. 1, 2002, pp. 9–11. Translated from Doklady Akademii Nauk, Vol. 382, No. 1, 2002, pp. 38–40.

PHYSICS

Dispersion Equations for Guided Modes of a Multilayer Elliptic Fiber Optic Waveguide

V. I. Krivenkov

Presented by Academician E.M. Dianov June 1, 2001

Received June 7, 2001

Modes intrinsic to elliptic optical fibers are nondegenerate in contrast to those of circular optical fibers. In the case of elliptic fibers, the longitudinal-propagation constants for orthogonally polarized modes are different, and under certain conditions a polarization state of guided light can be conserved [1]. This effect provides the basis for many fiber devices, for example, fiber-optic interferometers.

Foundations for the theory of electromagnetic-wave propagation in elliptic fiber-optic waveguides were laid down long ago in [2]. There, approximate dispersion equations for two fundamental (even and odd) modes of a dielectric elliptic air-filled waveguide were formulated. Later on, based on this theory, dispersion equations for guided modes of a two-layer elliptic fiber [3] and of a three-layer fiber with layer boundaries having the form of confocal elliptic cylinders [4] were derived. In addition, a method of evaluating dispersion characteristics of an arbitrary three-layer elliptic optical fiber was developed [5].

A method for solving the problem of natural waves in a multilayer light guide was formulated in [6], with a circular multilayer fiber used as an example. In the present study, employing this method, we have determined both field components and dispersion equations for all guided modes of a multilayer elliptic-fiber light guide having an arbitrary number of confocal elliptic layers. The dispersion equations are presented in the form corresponding to a determinant equal to zero, with its rank being independent of the number of the layers.

We consider an elliptic optic fiber whose permittivity (in elliptic cylindrical coordinates ξ, η, and z, with the z-axis directed along the fiber axis) is written out in the form

$$\varepsilon(\xi) = \begin{cases} \varepsilon_1, & \text{for} \quad 0 = \xi_0 \le \xi < \xi_1 \\ \varepsilon_2, & \text{for} \quad \xi_1 \le \xi < \xi_2 \\ \ldots\ldots\ldots\ldots\ldots\ldots \\ \varepsilon_{N+1}, & \text{for} \quad \xi_N \le \xi < \infty, \end{cases}$$

where $\varepsilon_{N+1} < \max(\varepsilon_1, \varepsilon_2, \ldots, \varepsilon_N)$.

For a guided mode of such a fiber, the dependence of both the electric field strength $\mathbf{E} = (E_\xi, E_\eta, E_z)$ and the magnetic field strength $\mathbf{H} = (H_\xi, H_\eta, H_z)$ on time t and the longitudinal coordinate z takes the form $\exp[j(\omega t - \beta z)]$ (in what follows, the exponential factor is omitted), where ω and β are, respectively, the circular frequency and the constant for the longitudinal propagation of the mode. In this case, Maxwell equations are reduced to the following set:

$$\varepsilon(\xi)\frac{\partial \mathbf{e}}{\partial \xi} = \mathbf{A}(\xi, \eta)\mathbf{h},$$

$$\frac{\partial \mathbf{h}}{\partial \xi} = -\mathbf{A}(\xi, \eta)\mathbf{e},$$

where

$$\mathbf{e} = \sqrt{\varepsilon_0}\begin{pmatrix} E_z \\ jg(\xi, \eta)E_\eta \end{pmatrix}, \quad \mathbf{h} = \sqrt{\mu_0}\begin{pmatrix} H_z \\ jg(\xi, \eta)H_\eta \end{pmatrix},$$

$$\mathbf{A}(\xi, \eta) = \begin{pmatrix} -\gamma\dfrac{\partial}{\partial \eta} & \varepsilon(\xi) - \gamma^2 \\ \varepsilon(\xi)g^2(\xi, \eta) + \dfrac{\partial^2}{\partial \eta^2} & \gamma\dfrac{\partial}{\partial \eta} \end{pmatrix},$$

$$g(\xi, \eta) = k_0\rho\sqrt{\sinh^2\xi + \sin^2\eta}.$$

Here, ρ is the half-distance between the foci of the given elliptic cylindrical coordinate system, $\gamma = \dfrac{\beta}{k_0}$, $k_0 = \omega\sqrt{\varepsilon_0\mu_0}$, and ε_0 and μ_0 are the permittivity and the permeability of free space, respectively.

We now define the functions

$$f_{mn}^{\alpha j}(q, q') = \frac{1}{\pi}\int_0^{2\pi} sc_m^{|j-\alpha|}(\eta, q')\frac{d^j}{d\eta^j}[sc_n^\alpha(\eta, q)]d\eta,$$

Moscow State Academy of Instrument Making and Informatics,
ul. Stromynka 20, Moscow, 107076 Russia

1028-3358/02/4701-0009$22.00

$$V^{(j)}_{\alpha m}(\xi, \xi', q)$$

$$= -(-1)^j \frac{\pi}{2}\left\{ M^{(1)}_{\alpha m}(\xi, q)\frac{d^j}{d\xi^j}[M^{(2)}_{\alpha m}(\xi, q)]_{\xi=\xi'} \right.$$

$$\left. - M^{(2)}_{\alpha m}(\xi, q)\frac{d^j}{d\xi^j}[M^{(1)}_{\alpha m}(\xi, q)]_{\xi=\xi'} \right\},$$

$$K^{\alpha}_m(\xi, \xi', q) = \frac{M^{(3)}_{\alpha m}(\xi, q)}{M^{(3)}_{\alpha m}(\xi', q)}, \quad \delta_{mn} = \begin{cases} 1, & \text{for } m = n \\ 0, & \text{for } m \neq n, \end{cases}$$

$$\alpha, j = 0, 1, \quad m, n = 0, 1, \ldots.$$

Here,

$$sc^0_m(\eta, q) \equiv se_m(\eta, q), \quad sc^1_m(\eta, q) \equiv ce_m(\eta, q),$$

$$M^{(j)}_{0m}(\xi, q) \equiv Ms^{(j)}_m(\xi, q), \quad M^{(j)}_{1m}(\xi, q) \equiv Mc^{(j)}_m(\xi, q),$$

$$j = 1, 2, 3,$$

and $se_m(\eta, q)$, $ce_m(\eta, q)$, $Ms^{(j)}_m(\xi, q)$, and $Mc^{(j)}_m(\xi, q)$ are the angular and radial Mathieu functions [7].

The derived system of equations has a solution satisfying the conventional conditions at $\xi = 0$ and as $\xi \longrightarrow \infty$. We represent this solution in the form

$$\begin{pmatrix} \mathbf{e}(\xi, \eta) \\ \ldots \\ \mathbf{h}(\xi, \eta) \end{pmatrix}$$

$$= \sum_{k=0}^{\infty} \begin{cases} \mathbf{D}_l \sum_{j=0}^{1} \begin{pmatrix} a^j_{lk} V^{(j)}_{\mu, 2k+\nu}(\xi, \xi_{l-1}, q_l) sc^{\mu}_{2k+\nu}(\eta, q_l) \\ b^j_{lk} V^{(j)}_{1-\mu, 2k+\nu}(\xi, \xi_{l-1}, q_l) sc^{1-\mu}_{2k+\nu}(\eta, q_l) \end{pmatrix}, \\ \text{if} \quad \xi_{l-1} \le \xi < \xi_l, \quad l = 1, 2, \ldots, N \\ \mathbf{D}_{N+1} \begin{pmatrix} a_k K^{\mu}_{2k+\nu}(\xi, \xi_N, q_{N+1}) sc^{\mu}_{2k+\nu}(\eta, q_{N+1}) \\ b_k K^{1-\mu}_{2k+\nu}(\xi, \xi_N, q_{N+1}) sc^{1-\mu}_{2k+\nu}(\eta, q_{N+1}) \end{pmatrix}, \\ \text{if} \quad \xi_N \le \xi < \infty, \end{cases}$$

$$\mu, \nu \in \{0, 1\}.$$

Here,

$$\mathbf{D}_l = \left(\begin{array}{c|c} \mathbf{D}^{\eta}_l & \mathbf{D}^{\xi}_l \\ \hline -\varepsilon_l \mathbf{D}^{\xi}_l & \mathbf{D}^{\eta}_l \end{array}\right), \quad \mathbf{D}^{\eta}_l = \begin{pmatrix} 1 \\ -\dfrac{\gamma}{u_l^2}\dfrac{\partial}{\partial\eta} \end{pmatrix},$$

$$\mathbf{D}^{\xi}_l = \begin{pmatrix} 0 \\ \dfrac{1}{u_l^2}\dfrac{\partial}{\partial\xi} \end{pmatrix},$$

$$q_l = -\frac{k_0 \rho^2 u_l^2}{4}, \quad u_l^2 = \gamma^2 - \varepsilon_l,$$

$$l = 1, 2, \ldots, N+1 \quad (u^2_{N+1} > 0),$$

$$a^{1-\mu}_{1k} = b^{\mu}_{1k} = 0, \quad k = 0, 1, \ldots.$$

This solution corresponds to the even modes ${}_eHE_{mn}$ and ${}_eEH_{mn}$ for $\mu = 0$ and to the odd modes ${}_oHF_{mn}$ and ${}_oEH_{mn}$ for $\mu = 1$ with the even ($\nu = 0$) or odd ($\nu = 1$) azimuth index m.

It follows from the continuity condition for the tangential field components that the constants

$$\mathbf{C}_i = \begin{pmatrix} \mathbf{C}_{i0} \\ \hline \mathbf{C}_{i1} \\ \hline \vdots \end{pmatrix}, \quad \mathbf{C}_{1k} = \begin{pmatrix} a^{\mu}_{1k} \\ b^{1-\mu}_{1k} \end{pmatrix}, \quad \mathbf{C}_{ik} = \begin{pmatrix} a^1_{ik} \\ b^0_{ik} \\ b^1_{ik} \\ a^0_{ik} \end{pmatrix},$$

$$i = 2, 3, \ldots, N,$$

$$\mathbf{C}_{N+1,k} = \begin{pmatrix} a_k \\ b_k \end{pmatrix}, \quad k = 0, 1, \ldots$$

satisfy the homogeneous system of equations

$$\mathbf{C}_{l+1} = \mathbf{\Psi}_{l+1}\mathbf{\Phi}_l \mathbf{C}_l, \quad l = 1, 2, \ldots, N-1,$$

$$\mathbf{\Phi}_{N+1}\mathbf{C}_{N+1} = \mathbf{\Phi}_N \mathbf{C}_N.$$

Here,

$$\mathbf{\Phi}_l = (\mathbf{\Phi}^l_{mn}), \quad m, n = 0, 1, \ldots, \quad l = 1, 2, \ldots, N+1,$$

$$\mathbf{\Phi}^l_{mn} = \begin{cases} \left(\begin{array}{c|c} {}^{\mu}\mathbf{P}^{l\mu}_{mn} & {}^{1-\mu}\mathbf{Q}^{l,1-\mu}_{mn} \\ \hline -\varepsilon_l {}^{\mu}\mathbf{Q}^{l\mu}_{mn} & {}^{1-\mu}\mathbf{P}^{l,1-\mu}_{mn} \end{array}\right), & l = 1, N+1 \\ \left(\begin{array}{c|c|c|c} {}^{\mu}\mathbf{P}^{l1}_{mn} & {}^{1-\mu}\mathbf{Q}^{l0}_{mn} & {}^{1-\mu}\mathbf{Q}^{l1}_{mn} & {}^{\mu}\mathbf{P}^{l0}_{mn} \\ \hline -\varepsilon_l {}^{\mu}\mathbf{Q}^{l1}_{mn} & {}^{1-\mu}\mathbf{P}^{l0}_{mn} & {}^{1-\mu}\mathbf{P}^{l1}_{mn} & -\varepsilon_l {}^{\mu}\mathbf{Q}^{l0}_{mn} \end{array}\right), \\ l = 2, 3, \ldots, N, \end{cases}$$

$$\mathbf{\Psi}_l = (\mathbf{\Psi}^l_{mn}), \quad m, n = 0, 1, \ldots, \quad l = 2, 3, \ldots, N,$$

$$\mathbf{\Psi}^l_{mn} = \begin{pmatrix} \delta_{mn} & 0 & 0 & 0 \\ u_l^2 F^{\mu l}_{mn} & u_l^2 \delta_{mn} & 0 & 0 \\ 0 & 0 & \delta_{mn} & 0 \\ 0 & 0 & -\dfrac{u_l^2}{\varepsilon_l} F^{1-\mu, l}_{mn} & -\dfrac{u_l^2}{\varepsilon_l}\delta_{mn} \end{pmatrix},$$

$$
{}^{\alpha}\mathbf{P}_{mn}^{ij} = V_{\alpha, 2n+\nu}^{(j)}(\xi_i, \xi_{i-1}, q_i)
\times \begin{pmatrix} f_{2m+\nu, 2n+\nu}^{\alpha 0}(q_i, q_{i+1}) \\ -\dfrac{\gamma}{u_i^2} f_{2m+\nu, 2n+\nu}^{\alpha 1}(q_i, q_{i+1}) \end{pmatrix},
$$

$$
{}^{\alpha}\mathbf{Q}_{mn}^{ij}
= \frac{f_{2m+\nu, 2n+\nu}^{\alpha 0}(q_i, q_{i+1})}{u_i^2} \frac{d}{d\xi}[V_{\alpha, 2n+\nu}^{(j)}(\xi, \xi_{i-1}, q_i)]_{\xi=\xi_i} \begin{pmatrix} 0 \\ 1 \end{pmatrix},
$$

$$
i = 1, 2, \ldots, N,
$$

$$
{}^{\alpha}\mathbf{P}_{mn}^{N+1, j} = \begin{pmatrix} \delta_{mn} \\ -F_{mn}^{\alpha, N+1} \end{pmatrix}, \quad {}^{\alpha}\mathbf{Q}_{mn}^{N+1, j} = \begin{pmatrix} 0 \\ K_{mn}^{\alpha} \end{pmatrix},
$$

$$
F_{mn}^{\alpha i} = \frac{\gamma}{u_i^2} f_{2m+\nu, 2n+\nu}^{\alpha 1}(q_i, q_i),
$$

$$
K_{mn}^{\alpha} = \frac{\delta_{mn}}{u_{N+1}^2} \frac{d}{d\xi}[K_{2n+\nu}^{\alpha}(\xi, \xi_N, q_{N+1})]_{\xi=\xi_N},
$$

$$
\alpha = \mu, 1-\mu.
$$

The determinant of this system must be equal to zero.

We eliminate the unknowns $\mathbf{C}_2$, $\mathbf{C}_3$, …, $\mathbf{C}_{N+1}$ from this system of equations and set the determinant of the system obtained to zero. As a result, we arrive at the following equation in the unknown phase constant γ:

$$
\det\left(\prod_{l=1}^{N} \mathbf{\Psi}_{l+1}\mathbf{\Phi}_l\right) = 0, \quad \mu, \nu \in \{0, 1\},
$$

where

$$
\mathbf{\Psi}_{N+1} = (\mathbf{\Psi}_{mn}^{N+1}), \quad m, n = 0, 1, \ldots,
$$

$$
\mathbf{\Psi}_{mn}^{N+1} = \begin{pmatrix} F_{mn}^{\mu, N+1} & \delta_{mn} & -K_{mn}^{1-\mu} & 0 \\ \varepsilon_{N+1}K_{mn}^{\mu} & 0 & F_{mn}^{1-\mu, N+1} & \delta_{mn} \end{pmatrix}.
$$

This equation is a dispersion equation for guided modes of the multilayer elliptic-fiber light guide under consideration, with the boundaries having the form of confocal elliptic cylinders. It corresponds to the even modes ${}_eHE_{mn}$ and ${}_eEH_{mn}$ for $\mu = 0$ and the odd modes ${}_oHE_{mn}$ and ${}_oEH_{mn}$ for $\mu = 1$ with the azimuth index $m = 2k + \nu$, $k = 0, 1, \ldots$.

The rank of the determinant in the left-hand side of this equation is virtually equal to the doubled number of terms in the expansion of the mode field components in the angular Mathieu functions. It is especially important that this rank is independent of the number of layers in the fiber under consideration.

REFERENCES

1. A. S. Belanov, E. M. Dianov, and V. I. Krivenkov, Kvantovaya Élektron. (Moscow) **11**, 1273 (1984).
2. L. A. Lyubimov, G. I. Veselov, and N. A. Beĭ, Radiotekh. Élektron. (Moscow) **6**, 1871 (1961).
3. C. Yeh, Opt. Quantum Electron. **8** (8), 43 (1976).
4. S. R. Rengarajan and J. E. Lewis, Radio Sci. **16**, 541 (1981).
5. A. S. Belanov and V. I. Krivenkov, Sov. Lightwave Commun. **1**, 139 (1991).
6. A. S. Belanov, E. M. Dianov, and V. I. Krivenkov, Dokl. Akad. Nauk **364**, 37 (1999) [Dokl. Phys. **44**, 1 (1999)].
7. *Handbook of Mathematical Functions*, Ed. by M. Abramowitz and I. A. Stegun (Dover, New York, 1971; Nauka, Moscow, 1979).

Translated by V. Chechin

Doklady Physics, Vol. 47, No. 1, 2002, pp. 92–94. Translated from Doklady Akademii Nauk, Vol. 382, No. 3, 2002, pp. 346–348.

MECHANICS

On the Theory of Spatial Averaging in Heterogeneous-Continuum Mechanics

V. P. Bushlanov and I. V. Bushlanov

Presented by Academician V.E. Panin June 14, 2001

Received June 14, 2001

The averaged equations in heterogeneous-continuum mechanics, which are derived by spatially averaging equations for single-phase continua, contain unknown integrals over the interphase interface. These integrals are of the following form (we use the terminology and notation introduced in [1]):

$$\langle \psi_i'^k n_i'^k \rangle_{12} = \frac{1}{dS_{12}} \int\limits_{dS_{12}} \psi_i'^k n_i'^k d'S. \qquad (1)$$

Here, $\mathbf{\Psi}_i'^k = \boldsymbol{\sigma}_i'^k, \boldsymbol{\sigma}_i'^k \mathbf{v}_i' - \mathbf{q}_i'^k, \mathbf{x}' \times \mathbf{v}_i'; \sigma_i'^{kn}$ are the stress tensor components; $\mathbf{v}_i'$ is the velocity vector; $\mathbf{q}_i'^k$ is the vector of the heat flow or radiation flux through the interface towards the *i*th phase; and $\mathbf{x}'$ and $\mathbf{n}'$ are the radius-vector of an interface point and the vector of a unit-normal to the interface, respectively. The prime stands for the local parameter of the single-phase medium; the subscript *i* enumerates the phases in the medium; the sign $\langle\cdot\rangle_{12}$ implies averaging over the interface; dS_{12} is the interface area in the volume element dV in which the averaging occurs; and $dS_{12} = s_{12}dV$, where s_{12} is the interface area per unit volume.

The lack of a method for evaluating integrals (1) noticeably hampers the employment of the theory [1]. Relationships (1) are usually applied for a particular model describing the interface shape. This model should be separately substantiated for each of the problems to be considered and, as a rule, significantly differs from the actual situation. Within the framework of the topological hypothesis proposed below, we present here a universal method for solving Eq. (1). The hypothesis uses an interface-area distribution function in terms of the direction angles for normals to the interface [2]. The method is based on Stokes integral formulas extended below to the case of heterogeneous media and on new equations describing the evolution of averaged topological parameters of the interface. These parameters are s_{12} and the tensor $\langle n_i'^p n_i'^q \rangle_{12} \cdot s_{12}$ of the volume density for the interface area.

TOPOLOGICAL HYPOTHESIS

Let $s(t, \mathbf{x}', \theta, \varphi)$ be a distribution function for the interface area per unit volume of a heterogeneous medium [2]. Therefore, the quantity $s(t, \mathbf{x}', \theta, \varphi)d\Omega d'V$ is numerically equal to the interface area per volume element $d'V$, with the direction angles θ and φ of normals to the interface lying in the solid-angle element $d\Omega = \sin\theta d\theta d\varphi$. Here, θ is the angle between a normal and the unit vector $\mathbf{e}_3$ of a Cartesian coordinate system, the angle φ lies in a plane perpendicular to $\mathbf{e}_3$, and $\mathbf{n}' = \{\sin\theta \cdot \cos\varphi, \sin\theta \cdot \sin\varphi, \cos\theta\}$. Since $d'S = s_{12}d'V$, relationships (1) can be written in terms of the distribution function

$$s_{12}\langle \psi_i'^k n_i'^k \rangle_{12} = \frac{1}{dS_{12}} \int\limits_{dS_{12}} \psi_i'^k \int\limits_{\Omega} n_i'^k s(t, \mathbf{x}', \theta, \varphi) d\Omega d'S, \qquad (2)$$

where the domain $\Omega = (0 \le \theta \le \pi, 0 \le \theta \le 2\pi)$. To evaluate the function $s(t, \mathbf{x}', \theta, \varphi)$, we should sum the interface area in a volume element dV with the direction angles θ and φ for normals to the interface lying in the solid-angle element $d\Omega$ and then divide the result obtained by $dVd\Omega$. Such a method was employed, for example, to evaluate the distribution function for packing of spheres [2]. The aforesaid implies that the $\mathbf{x}'$-coordinate of the volume element dV can be substituted for the argument $\mathbf{x}$ of the function $s(t, \mathbf{x}', \theta, \varphi)$ entering into relation (2), which, furthermore, is assumed to always be true. Under this natural assumption, which will be referred to as a topological hypothesis, equality (2) can be written in the form

$$\langle \psi_i'^k n_i'^k \rangle_{12} = s_{12} v^k \langle \psi_i'^k \rangle_{12}, \qquad (3)$$

Department of Structural Macrokinetics, Tomsk Scientific Center, Siberian Division, Russian Academy of Sciences, ul. Vavilova 16–25, Tomsk, 634055 Russia

1028-3358/02/4701-0092$22.00

$$\nu^k(t, \mathbf{x}) = \frac{1}{s_{12}}\int_\Omega n_i'^k s(t, \mathbf{x}, \theta, \varphi)d\Omega = \langle n_i'^k\rangle_{12}. \quad (4)$$

EQUATIONS DESCRIBING THE EVOLUTION OF AVERAGED TOPOLOGICAL PARAMETERS OF THE INTERFACE

In order to derive the desired equations, we use the equation for the function $\Phi(t, \mathbf{x}', \theta, \varphi)$ introduced in [2] (below, the subscript i is omitted):

$$\frac{1}{s_{12}}\left[\frac{\partial}{\partial t}(s_{12}f) + \nabla^k(s_{12}v^k f)\right] = \left\langle\frac{d\Phi}{dt}\right\rangle_{12} + \langle\Phi'(\delta^{pq} - n'^p n'^q)e'pq\rangle_{12}. \quad (5)$$

Here, $f = \langle\Phi'\rangle_{12}$, $v^k = \frac{1}{dV_i}\int_{dV_i} v'^k d'V$, dV_i is a volume element of the ith phase in dV, and $e'^{pq} = \frac{1}{2}(\nabla'^p v'^q + \nabla'^q v'^p)$ are the strain rate tensor components. We also use the expression for $\frac{d\mathbf{n}'}{dt}$ from [2]:

$$\frac{d\mathbf{n}'}{dt} = \mathbf{n}'[\mathbf{n}'(\mathbf{n}'\mathbf{v}')\mathbf{v}'] - (\mathbf{n}'\nabla')\mathbf{v}' - \mathbf{n}'\times\boldsymbol{\Omega}', \quad (6)$$

with $\boldsymbol{\Omega}' = \mathrm{rot}'\mathbf{v}'$, as well as the identity

$$(\mathbf{n}'\nabla')\mathbf{v}' = \mathbf{e}^k n'^p e'^{kp} - \frac{1}{2}\mathbf{n}'\times\boldsymbol{\Omega}', \quad (7)$$

where $\mathbf{e}^k$ are the unit vectors of the Cartesian coordinate system. Then the summation over repetitive indices is implied. Substituting $\Phi = \mathbf{n}'$ and then $\Phi = n'^k n'^i$ into formula (5) and taking into account expressions (6) and (7), as well as the topological hypothesis, we arrive at

$$\frac{1}{s_{12}}\frac{d}{dt}(s_{12}\nu^k) + \nu^k\mathrm{div}\mathbf{v} + \varepsilon^{kp}\nu^p - \nu^k\varepsilon^{kk} + \frac{1}{2}\boldsymbol{\epsilon}^{kpq}\nu^p\omega^q = 0, \quad (8)$$

$$\frac{1}{s_{12}}\frac{d}{dt}(s_{12}\nu^{ik}) + \nu^{ik}\mathrm{div}\mathbf{v} - \varepsilon^{pp}\nu^{ik} + \frac{1}{2}(z^{ik} + z^{ki}) + \frac{1}{2}(z_s^{ik} + z_s^{ki}) = 0,$$
$$z^{ik} = \nu^{ip}\varepsilon^{pk} + \boldsymbol{\epsilon}^{ipq}\nu^{kp}\omega^q, \quad (9)$$
$$z_s^{ik} = \langle n'^i(n'^p e'^{pk} - n'^k n'^p n'^q e'^{pq})\rangle_{12}.$$

Here, $\boldsymbol{\epsilon}^{kpq}$ is the unit antisymmetric Levi-Civita tensor [3], and

$$\varepsilon^{kp} = \langle e'^{kp}\rangle_{12}, \quad \omega^q = \langle\Omega'^q\rangle_{12},$$
$$\nu^{ik} = \langle n'^i n'^k\rangle_{12}, \quad \frac{d}{dt} = \frac{\partial}{\partial t} + (\mathbf{v}\cdot\boldsymbol{\nabla}).$$

It is worth noting that the equation for s_{12} is derived by summing equalities (9) over k for $i = k$, with $\nu^{kk} = 1$. The quantity z_s^{ik} entering into these equalities is zero if the phase is a Newtonian liquid whose surface is free from tangential stresses.

ANALOGS OF STOKES FORMULAS FOR HETEROGENEOUS MEDIA

Stokes formulas [3] for a closed surface dS_{12} have the form

$$\int_{dS_{12}}\mathbf{n}'\mathrm{rot}'\mathbf{F}(\mathbf{x}')d'S = \int_{dL_{12}}\mathbf{F}(\mathbf{x}')d'\mathbf{l},$$
$$\int_{dS_{12}}\mathbf{n}'\times\boldsymbol{\nabla}'\Phi(\mathbf{x}')d'S = \int_{dL_{12}}\Phi(\mathbf{x}')d'\mathbf{l}, \quad (10)$$
$$\int_{dS_{12}}(\mathbf{n}'\times\boldsymbol{\nabla}')\times\mathbf{F}(\mathbf{x}')d'S = -\int_{dL_{12}}\mathbf{F}(\mathbf{x}')\times d'\mathbf{l}.$$

Here, dL_{12} is the multiply connected boundary for dS_{12}, which lies on the surface dS of a volume element dV; $d'\mathbf{l}$ is a vector element of the contour dL_{12}; and the functions $\Phi(\mathbf{x}')$ and $F(\mathbf{x}')$ are defined on the interface. Using the method of additional spatial averaging presented in [4], it is easy to derive the following analogs of formulas (10) for heterogeneous media:

$$s_{12}\langle\mathbf{n}'\mathrm{rot}'\mathbf{F}'\rangle_{12} = \mathrm{div}(s_{12}\langle\mathbf{F}'\times\mathbf{n}'\rangle_{12}),$$
$$s_{12}\langle\mathbf{n}'\times\boldsymbol{\nabla}'\Phi'\rangle_{12} = -\mathrm{rot}(s_{12}\langle\mathbf{n}'\Phi'\rangle_{12}),$$
$$s_{12}\langle(\mathbf{n}'\times\boldsymbol{\nabla}')\times\mathbf{F}'\rangle_{12} = \frac{\partial}{\partial x^k}(s_{12}\langle\mathbf{F}'\times(\mathbf{e}^k\times\mathbf{n}')\rangle_{12}). \quad (11)$$

Comment. If $\Phi(\mathbf{x}')$ and $\mathbf{F}(\mathbf{x}')$ are defined in the entire volume dV_i, which is occupied by the ith phase in dV, as well as at the surface dS_{12}, then Eqs. (11) can be derived without employing the method of additional spatial averaging. Indeed, transforming the volume integral that enters into the identity $0 = \frac{1}{dV}\int_{dV_i}\mathrm{rot}'\boldsymbol{\nabla}'\Phi'd'V$ to a surface integral and using the relationship

$$\alpha\langle\nabla'^k\Phi'\rangle = \nabla^k(\alpha\langle\Phi'\rangle) + s_{12}\langle n'^k\Phi'\rangle_{12}, \quad (12)$$

given in [1] (subscript i is omitted), we arrive at

$$\frac{1}{dV}\int\limits_{dS_{12}+dS_i}\mathbf{n}'\times\nabla'\Phi'dS' = s_{12}\langle\mathbf{n}'\times\nabla'\Phi'\rangle_{12} + \mathrm{rot}(s_{12}\langle n'\Phi'\rangle_{12}) = 0.$$

Two other formulas in the set of equations (11) can be derived in a similar way.

THE APPLICATION OF STOKES FORMULAS AND THE EQUATIONS FOR THE AVERAGED TOPOLOGICAL PARAMETERS

We substitute $\Phi = \mathbf{v}'^k$ into (11) and take account of the topological hypothesis and the equality $s_{12}\nu = -\nabla\alpha$ following from (12) for $\Phi' = 1$. As a result, we obtain

$$\nabla\alpha\times(\langle\nabla'\nu'^k\rangle_{12} - \nabla\vartheta^k) = 0, \tag{13}$$

where $\vartheta^k = \langle\nu'^k\rangle_{12}$.

It follows from (13) that

$$\langle\nabla'^k\mathbf{v}\rangle_{12} = \nabla\vartheta^k + T^k\nabla\alpha,$$
$$\varepsilon^{kp} = \frac{1}{2}(\nabla^k\vartheta^p + \nabla^p\vartheta^k) + \frac{1}{2}(T^k\nabla^p\alpha + T^p\nabla^k\alpha), \tag{14}$$

where $\mathbf{T}$ should be expressed in terms of $\boldsymbol{\omega}$. To do this, we use the equations

$$\boldsymbol{\omega} = \mathrm{rot}\boldsymbol{\vartheta} + \nabla\alpha\times\mathbf{T}, \quad (\boldsymbol{\omega} - \mathrm{rot}\boldsymbol{\vartheta})\nabla\alpha = 0, \tag{15}$$

which follow from formula (14). Assuming the ith phase to be incompressible, so that $\mathrm{div}\mathbf{v}' = 0$, we arrive at

$$\mathbf{T}\cdot\nabla\alpha = -\mathrm{div}\boldsymbol{\vartheta}. \tag{16}$$

Solving Eqs. (15), (16) with respect to $\mathbf{T}$, we obtain [3]

$$\mathbf{T} = -\frac{\nabla\alpha\,\mathrm{div}\boldsymbol{\vartheta} + \nabla\alpha\times(\mathrm{rot}\boldsymbol{\vartheta} - \boldsymbol{\omega})}{(\nabla\alpha)^2}. \tag{17}$$

After the substitution $\mathbf{F} = \mathbf{v}'$ into (11) and on the basis of the identity

$$(\mathbf{n}'\times\nabla')\times\mathbf{v}' = -\mathbf{n}'\mathrm{div}\mathbf{v}' + \mathbf{e}^k n'^p e'^{kp} + \frac{1}{2}\mathbf{n}'\times\boldsymbol{\Omega}',$$

we have

$$\frac{1}{s_{12}}\frac{\partial}{\partial x^p}s_{12}[\boldsymbol{\vartheta}\times(\mathbf{e}^p\times\mathbf{v})] = \mathbf{e}^k\nu^p\varepsilon^{pk} + \frac{1}{2}\mathbf{v}\times\boldsymbol{\omega}. \tag{18}$$

Finally, we express the variable $\boldsymbol{\vartheta}$ in terms of $\mathbf{v}$ and α. According to relation (18), we rewrite Eq. (8) in the form

$$\frac{d\nabla\alpha}{dt} + \nabla\alpha\,\mathrm{div}\mathbf{v} + \frac{\partial}{\partial x^p}[\boldsymbol{\vartheta}\times(\mathbf{e}^p\times\nabla\alpha)] = 0. \tag{19}$$

We now use Eq. (19), the equation $\frac{\partial\alpha}{\partial t} = s_{12}\langle\mathbf{n}'\mathbf{v}'\rangle_{12} = -\boldsymbol{\vartheta}\nabla\alpha$ for the volume content of the ith phase, and the continuity equation $\frac{\partial\alpha}{\partial t} + \mathrm{div}(\alpha\mathbf{v}) = 0$ for the incompressible phase to derive the following relationships:

$$\boldsymbol{\vartheta} = \mathbf{v} + \frac{\mathbf{b}}{\left(\frac{\nabla\alpha}{\alpha}\mathbf{b}\right)}\mathrm{div}\mathbf{v}, \tag{20}$$

$$\mathbf{b} = \nabla b^1\times\nabla b^2 + \nabla b^2\times\nabla b^3 + \nabla b^3\times\nabla b^1,$$
$$\mathrm{div}\mathbf{v} = -\frac{1}{\beta}\left(\frac{\nabla\alpha}{\alpha}\mathbf{b}\right)\mathrm{div}\boldsymbol{\vartheta}, \quad \beta = (\nabla b^1, \nabla b^2, \nabla b^3),$$
$$b^k = \ln\left(\frac{\alpha_k}{\alpha}\right),$$
$$(\mathbf{b}\nabla)\ln\left[\frac{(\alpha^1\alpha^2\alpha^3)^{1/3}}{\left(\frac{\nabla\alpha}{\alpha}\mathbf{b}\right)}\mathrm{div}\mathbf{v}\right] = 0, \quad \alpha^k = \nabla^k\alpha. \tag{21}$$

CONCLUSIONS

Thus, we have shown that integrals (1) over the interface, which enter into the averaged equations [1], can be evaluated by formulas (3), where $s_{12}\mathbf{v} = -\nabla\alpha$. We have derived generalized Stokes formulas (11) and Eq. (9), the latter describing the evolution of the averaged topological parameters s_{12} and ν^{ik} of the interface. The equations obtained are needed for exact evaluations of both the volume density of surface forces (which, as was shown in [4], is proportional to the divergence of the tensor ν^{ik}) and the volume densities for the work and the angular momentum of surface forces. These quantities enter into the averaged equations of conservation for the momentum, energy, and angular momentum, respectively [1]. The variables ε^{kp} in Eqs. (9) are determined from formulas (14) and (17) in terms of $\boldsymbol{\omega}$ and $\boldsymbol{\vartheta}$. The vector $\boldsymbol{\vartheta}$ is found from relation (20), while the quantity $\boldsymbol{\omega}$ is determined by formula (15) and boundary conditions for the stress σ'^{ik} at the interface. In the case of the stress tensor linearly depending on the strain-rate tensor, these conditions can be easily obtained by the method proposed. We also have derived Eq. (21) extending the incompressibility condition to the case of heterogeneous media.

REFERENCES

1. R. I. Nigmatulin, *Principles of Heterogeneous-Medium Mechanics* (Nauka, Moscow, 1978).
2. V. P. Bushlanov, Poverkhnost, No. 10, 88 (2000).
3. G. A. Korn and T. M. Korn, *Mathematical Handbook for Scientists and Engineers* (McGraw-Hill, New York, 1968; Nauka, Moscow, 1984).
4. V. P. Bushlanov, Prikl. Mat. Teor. Fiz. **41** (4), 165 (2000).

Translated by V. Chechin